STRUCTURAL BEHAVIOUR OF
HIGH STRENGTH S690 STEEL
COLD-FORMED CIRCULAR HOLLOW SECTIONS

YIFEI HU

PhD

The Hong Kong Polytechnic University

2019

THE HONG KONG POLYTECHNIC UNIVERSITY

DEPARTMENT OF CIVIL AND ENVIRONMENTAL ENGINEERING

STRUCTURAL BEHAVIOUR OF

HIGH STRENGTH S690 STEEL

COLD-FORMED CIRCULAR HOLLOW SECTIONS

YIFEI HU

A thesis submitted in partial fulfillment of the requirements
for the Degree of Doctor of Philosophy

July 2019

CERTIFICATE OF ORIGINALITY

I hereby declare that this thesis is my own work and that, to the best of my knowledge and belief, it reproduces no material previously published or written, nor material that has been accepted for the award of any other degree or diploma, except where due acknowledgement has been made in the text.

_______________________________________ (Signed)

____________HU YIFEI__________________(Name of student)

ABSTRACT

Motivation

Compared with normal strength steel (NSS), high strength steel (HSS) has a higher strength-to-self-weight ratio, which is highly efficient in heavily loaded structures. Structural hollow sections have been widely applied in various construction projects all over the world, and a circular hollow section (CHS) is one of the most common types of sections used in steel structures because it has a highly desirable architectural appearance and a large resistance against torsion. In general, structural hollow sections are manufactured through hot rolling or cold forming and welding. These manufacturing processes will affect structural performance of these sections to different extents. At present, the use of high strength cold-formed circular hollow sections (CFCHS) is rather limited due to a lack of understanding on their structural performance. Hence, it is necessary to investigate the structural behaviour of these high strength S690 CFCHS as well as to provide effective design rules for their applications.

Objectives and scope of work

In this research project, a systematic experimental and numerical investigation into structural behaviour of high strength S690 CFCHS has been carried out. The scope of work is:

- **Task 1: Residual stresses in S690 CFCHS**

  To examine residual stresses in S690 CFCHS due to i) transverse cold-bending, and ii) longitudinal welding through experimental and numerical studies. Simplified residual stress patterns will be proposed for subsequent studies.

- **Task 2: Stocky columns of S690 CFCHS**

  To examine section resistances of stocky columns of S690 CFCHS under axial compression, and to propose relevant section classification rules.

- **Task 3: CHS T-joints under various loading conditions**

To examine structural performance of T-joints between S690 CFCHS under i) brace axial compression, ii) monotonic brace in-plane bending, and iii) cyclic brace in-plane bending, and to validate current design rules.

Four different cross-sections of CFCHS, namely Sections C1 to C4, were fabricated with S690 steel plates of 6 and 10 mm thick, and a total of 32 CFCHS were prepared for the experimental investigation.

Research methodology and key findings

The research work is based on a series of experimental and numerical investigations, and all the above-mentioned tasks have been completed successfully.

- **Task 1: Residual stresses in S690 CFCHS**

A total of eight CFCHS were tested as follows: i) surface temperature measurements during welding were conducted on four CFCHS with thermocouples, ii) residual stress measurements using the sectioning method were conducted on two CFCHS and two CFCHS-NW (no welding). Numerical models were established and calibrated with measured temperature history at specified points and measured surface residual stresses through coupled thermomechanical analyses. Simplified residual stress patterns were proposed based on these experimental and numerical results.

- **Task 2: Stocky columns of S690 CFCHS**

A total of eight stocky columns of CFCHS were tested, which covered Class 2 to Class 4 sections according to section classification rules provided in EN 1993-1-1. Test results on these stocky columns confirmed that predicted section resistances based on EN 1993-1-1 were readily attained in all these columns. Moreover, the proposed residual stress patterns for S690 CFCHS obtained in Task 1 should be incorporated into numerical models of these stocky columns for accurate prediction of their deformation characteristics.

Current section classification rules for S355 CHS provided in EN 1993-1-1 were found to be generally applicable for S690 CFCHS with notable conservatism.

- **Task 3: T-joints under various loading conditions**

A total of sixteen T-joints between S355 and S690 CFCHS were tested under the following loading conditions: i) brace axial compression, ii) monotonic brace in-plane bending, and iii) cyclic brace in-plane bending. A digital image correlation (DIC) technique was employed to measure surface strain contours of these T-joints under in-plane bending. Various failure modes were identified, and numerical models were established and calibrated against experimental results. In general, these T-joints were found to have large resistances and ductility under various loading conditions. Current reduction factors provided in EN 1993-1-12 were found to be very conservative when applied to T-joints between S690 CFCHS.

Key findings and their significances

Major academic merits of this research project are:

- This is the first research which systematically investigates residual stresses in CFCHS induced by both transverse cold-bending and longitudinal welding. Experimental studies on residual stresses of high strength S690 steel CFCHS have been conducted, and advanced numerical models have been established to simulate deformation characteristic of CFCHS with different steel grades, and geometrical dimensions.
- Generalized finite element models are developed to predict residual stresses in CFCHS through coupled thermomechanical analyses. Simplified residual stress patterns for S355 to S690 CFCHS have been proposed.
- Current design rules for section resistances in EN1993-1-1 have been confirmed to be applicable to S690 CFCHS through experimental and numerical studies.
- Current design rules for T-joints between CHS under monotonic in-plane bending in EN 1993-1-8 have been confirmed to be applicable to T-joints between S690 CFCHS through experimental and numerical studies. Suitable design parameters have been proposed to improve structural efficiency.
- Structural performance of T-joints between S690 CFCHS under cyclic in-plane bending is confirmed through experimental and numerical investigations, and they have a high level of resistance and ductility.

- Application of high strength S690 steels in CFCHS is fully validated through a series of comprehensive experimental and numerical investigations. They are technically ready for wide applications in construction.

PUBLICATIONS

Journal Papers

- T. Y. Ma, **Y. F. Hu**, X. Liu, G. Q. Li and K. F. Chung (2017). Experimental investigation into high strength Q690 steel welded H-sections under combined compression and bending, Journal of Constructional Steel Research, 138, 449-462.
- T. Y. Ma, X. Liu, **Y. F. Hu**, K. F. Chung and G. Q. Li (2018). Structural behaviour of slender columns of high strength S690 steel welded H-sections under compression, Engineering Structures, 157, 75-85.

Conference Papers

- K. Wang, **Y. F. Hu**, T. M. Chan and K. F. Chung (2016) Compression tests on stocky welded H-sections made of Q690 steel materials. Proceeding of the Fourteenth East Asia-Pacific Conference, Ho Chi Minh City, January 2016, p552-568.
- **Y. F. Hu** and K. F. Chung (2017). Numerical Study on Residual Stresses in High Strength Q690 Cold-formed Circular Hollow Sections, Proceedings of the fifteenth East Asia-Pacific Conference on Structural Engineering and Construction (EASEC 15), October 2017, P910-917.
- **Y. F. Hu** and K. F. Chung (2018).Structural tests on high strength S690 steel CHS T-joints subjected to in-plane bending. Proceedings of the International Conference on Engineering Research and Practice for Steel Construction 2018 (ICSC 2018), September 2018.
- K. F. Chung, H. C. Ho, D. A. Nethercot, X. Liu, K. Wang, **Y. F. Hu** and T. Y. Ma (2018). Investigation into structural behaviour of high strength S690 steels and their welded sections. Proceedings of the International Conference on Engineering Research and Practice for Steel Construction 2018 (ICSC 2018), September 2018

ACKNOWLEDGEMENT

First and foremost, I would like to express my sincere gratitude to my supervisor, Professor K. F. Chung, for offering me the opportunity to pursuit my PhD study in 2014. His knowledge and expertise has always been inspiring me. With his valuable guidance and constant encouragement, I have developed a comprehensive understanding on research methodology, communication skills and critical thinking on how to conduct research. His perseverance and rigorous attitude towards research has also driven me to achieve higher goals in my research study.

I would like to express my gratitude to the Department of Civil and Environmental Engineering of The Hong Kong Polytechnic University. It provided me with fine working environment and a well-equipped structural laboratory. I would also like to thank for the technical support during my experimental investigations from experienced technicians, Mr. K. H. Wong, Mr. M. C. Ng and Mr. Y. H. Yiu. Without their kind support and advice, the experiments will not be completed so successfully.

I am grateful to the financial support provided by the Research Committee and the Chinese National Engineering Research Centre for Steel Construction (Hong Kong Branch) of The Hong Kong Polytechnic University.

My sincere thanks also go to my colleagues and friends. Dr. T. M. Chan, Dr. H. C. Ho, Dr. M. H. Shen, Mr. T. Y. Ma, Dr. X. Liu, Dr. K. Wang, Dr. J. Y. Zhu and Mr. J. B. Chen provided useful technical advice to me. I wish to thank Miss Catherine Ng, Dr. J. K. Zhou, Mr. M. Xiao, Mr. Y. C. Wang, Mr. H. Jin, Ms. Y. B. Guo, and Ms. M. F. Zhu for their help and encouragement during my research study in Hong Kong.

Last but not the least, I would like to express my thanks to my family for their encouragement and love.

TABLE OF CONTENTS

LIST OF FIGURES

LIST OF TABLES

XX

LIST OF SYMBOLS

A	Cross-sectional area of a CFCHS
A_0	Original cross-sectional area along the parallel portion of a tensile coupon
a	minimum throat thickness of a fillet weld in tubular joints
a_1, a_2, b and c	Semi-axes of the double ellipsoild
D	Outer diameter of a CFCHS
d_0	Outer diameter of the chord
d_1	Outer diameter of the brace
E	Young's modulus
E_i	Dissipated energy at each cycle
E_i^+ and E_i^-	Dissipated energy in the tension and the compression half-cycle
E_y	Reference dissipated energy
f_f and f_r	Fractions illustrating energy distribution
f_y	Yield strength of steel
f_{y0}	Yield strength of the chord
f_u	Ultimate strength of steel
I	Welding current
k_p	Chord stress function defined by EN 1993-1-8
L	Height of a stocky column of CFCHS or span between two pinned supports of a T-joint between CFCHS
L_0	Gauge length of a standard tensile coupon or length of the chord
L_1	Length of the brace
M_0	Bending moment applied to the chord
$M_{0,end}$	Chord end moment
M_{FE}	Predicted moment resistance from numerical analysis
$M_{pl,0}$	Plastic moment resistance of the chord
$M_{Rd,1}$	Design moment resistance according to CIDECT
$M_{Rd,2}$	Design moment resistance according to EN 1993-18
M_{Test}	Measured moment resistance
N	Applied axial force
N_{CIDECT}	Design axial resistance according to CIDECT

N_{EC3}	Design axial resistance according to EN 1993-1-8
$N_{c,FE}$	Predicted axial resistance from finite element analysis
$N_{c,Rd}$	Design axial resistance
$N_{c,Test}$	Measured axial resistance from test
$N_{pl,0}$	Axial resistance of the chord
n and n_p	Chord stress ratio
P_{Test}	Applied lateral load
P_y	Reference elastic load
Q	Total heat energy input of welding
Q_u	Design strength function defined by CIDECT
$Q_{u,\mathrm{Mean}}$	Mean strength function defined by CIDECT
Q_f	Chord stress function defined by CIDECT
q_f	Volumetric heat flux in the front
q_r	Volumetric heat flux in the rear
r	Bending radius of a transverse cold-bending process or lever arm
r_w	Weld size of a butt-weld in CFCHS
t	Thickness of a steel plate or wall thickness of a CFCHS
t_0	Wall thickness of the chord
t_1	Wall thickness of the brace
U	Voltage of the welding arc
w	Amplitude of local imperfection
x, y and z	Local coordinates
α	Chord length parameter
β	Chord to brace diameter ratio
τ	Ratio of brace wall thickness to chord wall thickness
Δ	Axial shortening of a stocky column of CFCHS or chord indentation of a T-joint between CFCHS
Δ_y	Reference elastic displacement
δ	Vertical displacement at the mid-span of the chord
η	Welding efficiency
η_a	Energy dissipation ratio
ε	Nominal strain

ε_u	Elongation at tensile strength
ε_f	Elongation at fracture
ε_o	Residual strain on the outer surface of a CFCHS
ε_i	Residual strain on the inner surface of a CFCHS
$\varepsilon^{pl}_{\mathrm{true}}$	True plastic strain
θ	Angle measured from the weld seam of a CFCHS or joint rotation in a T-joint between CFCHS, or interstory drift angle
θ_{b1} *and* θ_{b2}	Rotation of the brace
θ_g	Rotation of the chord
θ_{max}	Rotation limit
$\bar{\theta}$	Normalized angle measured from the weld seam, and $\bar{\theta} = \theta/\pi$
χ	Reduction factor in axial resistance for local buckling
σ	Nominal stress
σ_b	Bending residual stress
σ_m	Membrane residual stress
σ_o	Residual stress on the outer surface of a CFCHS
σ_i	Residual stress on the inner surface of a CFCHS
σ_r	Residual stress
σ_{true}	True stress
$\sigma_{p,Ed}$	Maximum compressive stress in the chord excluding the stress due to components parallel to the chord axis

CHAPTER ONE

INTRODUCTION

1.1 RESEARCH BACKGROUND

Since 1970s, structural hollow sections have been widely applied in construction projects around the world, including long span foot bridges, space trusses and roof structures.

Circular hollow sections, or CHS, are often preferred by architects because of their desirable architectural appearance. Structural performance of S235, S275 and S355 steel CHS has been studied by many researchers in the past thirty years. Research outcomes of those studies have been widely published (Wardnenier *et al*., 2002), and developed into various design specifications, such as CIDECT Design Guide1 (Wardnenier *et al*., 2008) and EN 1993-1-8 (CEN, 2005), which are regarded as definitive technical guides for structural design.

CHS are usually manufactured by hot-rolling or cold-forming. Hot-rolling is widely applied for large scale industrial production of seamless steel tubes. Cold-forming of CHS is developed when it becomes possible to manufacture steel strips and plates. Nowadays, there have been various cold-forming methods, as shown in Figure 1.1. It should be noted that both the three-roll bending process and the C-ing press process are suitable for small scale production, while the U-ing press process, the O-ing press process and the spiral tube forming process are more frequently used for massive industrial production. The gas metal arc welding and the submerged arc welding are two welding methods which are widely adopted for longitudinal welding of these cold-formed circular hollow sections (CFCHS). Other welding methods including electric resistance welding and induction welding are also commonly applied in industrial production. These methods do not require welding electrodes as the weld is generated by molten parts of the steel materials caused by resistance heat.

However, the use of high strength steel in construction has not been widely adopted, especially for high strength steel S690 welded tubular hollow sections. The main reasons may be attributed to i) a lack of understanding on manufacturing processes and their effects onto structural behaviour, and ii) insufficient guidance on structural design of S690 tubular structural hollow sections. Therefore, effects of various manufacturing processes onto structural behaviour of CFCHS need to be investigated systematically. Structural performance of high strength S690 tubular structural hollow sections also needs to be assessed. Applicability of existing design rules should be examined.

In order to promote effective use of high strength S690 steel in construction and to develop a good understanding on structural behaviour of high strength S690 steel structural hollow sections, this research project is devised to work on the following issues:

i) Residual stresses in cold-formed circular hollow sections (CFCHS)

Circular hollow sections are manufactured by either a hot-rolling process or a cold-forming process. Different levels of residual stresses are generated during these manufacturing processes. These residual stresses are generally considered to have adverse effects on structural behaviour of these sections in terms of both strength and ductility.

These residual stresses in high strength S690 CFCHS are considered to be one of the key areas of this research project, and they will be studied through experimental and numerical investigations. These residual stresses will be quantified and simplified into residual stress patterns for direct incorporation into numerical models of CFCHS.

ii) Structural behaviour of T-joints between CFCHS

In tubular structures, joint behaviour is very important. For T-joints between CFCHS, they are commonly found in typical roofs, where the brace is mainly i) under compression, ii) under monotonic in-plane bending, iii) under cyclic in-plane bending. Structural behaviour of T-joints between S690 CFCHS subjected to various loading conditions is another key area of this research project.

iii) Structural design on T-joints between CFCHS

EN 1993-1-12 has extended design rules given in EN 1993-1-1 and EN1993-1-8 to cover high strength steels with yield strengths up to S700 by simply specifying additional requirements on ductility of the steel materials, and also reduction factors in calculating joint resistances. These design rules are generally considered to be applicable to design of S690 structural hollow sections with a certain extent of conservatism. This research project will examine these design rules to establish whether these reduction factors are sufficient, and any modification should be made to improve their design efficiency.

1.2 OBJECTIVES AND SCOPE OF WORK

The main objectives of this research work presented in this thesis are:

- Task 1: Residual stresses in S690 CFCHS

To examine residual stresses in S690 CFCHS due to i) transverse cold-bending, and ii) longitudinal welding through experimental and numerical studies. Simplified residual stress patterns will be established and proposed for practical design and subsequent numerical investigations.

- Task 2: Stocky columns of S690 CFCHS

To examine section resistances of stocky columns of S690 CFCHS under axial compression, and to propose relevant section classification rules to EN 1993-1-1.

- Task 3: T-joints between CFCHS under various loading conditions

To examine structural performance of T-joints between S690 CFCHS under i) brace axial compression, ii) monotonic brace in-plane bending, and iii) cyclic brace in-plane bending, and to validate applicability of the current design rules given in EN 1993-1-8.

1.3 RESEARCH METHODOLOGY

The research work is based on a series of experimental and numerical investigations, and details of these investigations are presented as follows:

- Task 1: Residual stresses in S690 CFCHS

Surface temperatures are measured with thermocouples during welding on four CFCHS. Residual stress measurements using the sectioning method are conducted on two CFCHS and two CFCHS-NW (no welding). Numerical models are established and calibrated with temperature history measured at specified points as well as measured surface residual stresses through coupled thermomechanical analyses. Simplified residual stress patterns are proposed which are based on these experimental and numerical results.

- Task 2: Stocky columns of S690 CFCHS

A total of eight stocky columns of S690 CFCHS are tested under axial compression, and they are regarded as Class 2 to 4 sections according to current section classification rules provided in EN 1993-1-1. The proposed residual stress patterns for S690 CFCHS obtained in Task 1 are incorporated into the numerical models of these stocky columns for prediction of their axial resistances and deformation characteristics. A series of parametric studies are conducted to examine applicability of current section classification rules provided in EN 1993-1-1.

- Task 3: T-joints under various loading conditions

A total of sixteen T-joints between S690 CFCHS are tested under the following loading conditions: i) brace axial compression, ii) monotonic brace in-plane bending, and iii) cyclic brace in-plane bending. A digital image correlation (DIC) technique was employed to measure surface strain contours of these T-joints under in-plane bending. Various failure modes are identified, and numerical models are established and calibrated against experimental results. A series of parametric studies are carried out to study various effects onto structural behaviour of these T-joints between CFCHS. Applicability of current reduction factors provided in EN 1993-1-12 are examined.

1.4 SIGNIFICANCE OF THE RESEARCH PROJECT

This is a highly systematic research which investigates residual stresses in high strength S690 CFCHS induced by i) transverse cold-bending, and ii) longitudinal welding through both experimental and numerical investigations. Experimental studies on residual stresses of these S690 CFCHS have been conducted, and advanced numerical models have been established to simulate deformation characteristic of these CFCHS with different steel grades, and geometrical dimensions.

Advanced finite element models are developed to predict residual stresses in these S690 CFCHS through coupled thermomechanical analyses. Simplified residual stress patterns for both S355 and S690 CFCHS have been proposed.

Current design rules for section resistances in EN1993-1-1 have been confirmed to be applicable to these S690 CFCHS through experimental and numerical studies.

Current design rules for T-joints between CHS under monotonic in-plane bending in EN 1993-1-8 have been confirmed to be applicable to these S690 CFCHS through experimental and numerical studies. Suitable design parameters have been proposed to improve design efficiency.

Structural performance of these T-joints between S690 CFCHS under cyclic in-plane bending is also confirmed through experimental and numerical investigations.

Structural behaviour of these S690 CFCHS steels in structural hollow sections is thoroughly examined through a series of comprehensive experimental and numerical investigations. They are technically ready for wide applications in construction with design rules with improved structural efficiency.

1.5 OUTLINE OF THE THESIS

This thesis consists of seven chapters, which are listed as follows:

- *Chapter 1 – Introduction*

This chapter gives an overview on the research background of this research project. The scope of work covered in this research project and the research significance are also presented.

- *Chapter 2 – Literature Review*

This chapter presents a comprehensive review of existing research on high strength CFCHS, including experimental and numerical investigations into residual stresses in S690 CFCHS, stocky columns of S690 CFCHS and T-joints between S690 CFCHS. Current design rules for S690 CFCHS are also reviewed and presented.

- *Chapter 3 – Investigations into Residual Stresses in CFCHS*

This chapter presents a systematic experimental and numerical study into both thermal and mechanical responses in these S690 CFCHS induced by various manufacturing processes. Surface temperature and residual stress measurements on a total of eight S690 CFCHS are conducted. Finite element models are established to simulate i) transverse cold-forming, and ii) longitudinal welding process. Simplified residual stress patterns for these S690 CFCHS are proposed.

- *Chapter 4 – Structural Behaviour of Stocky Columns under Axial Compression*

Structural behaviour of stocky columns of these S690 CFCHS are examined in this chapter. Based on experimental results on a total of eight stocky columns of these S690 CFCHS, finite element models are constructed and calibrated, which incorporate residual stresses due to cold-forming and welding. Parametric studies with finite element models are carried out to examine applicability of current section classification rules in EN 1993-1-1 to high strength CFCHS under axial compression.

- *Chapter 5 – Structural Behaviour of T-joints between CFCHS under Axial Compression*

This chapter presents an experimental results of a total of six T-joints between these S355 and S690 CFCHS under axial compression in brace members. Typical failure modes are identified. Finite element models are established and calibrated against test results on their compression resistances. Parametric studies with the finite element models are conducted to study effects of various geometric parameters. Applicability of current design rules in EN 1993-1-8 and CIDECT Design Guide 1 to T-joints between these CFCHS under brace axial compression are examined.

- *Chapter 6 – Structural Behaviour of T-joints between CFCHS under In-plane Bending*

An experimental investigation of a total of ten T-joints between these S355 and S690 CFCHS under in-plane bending moment are reported. Six of them are tested under monotonic in-plane bending moments while the other four are tested under cyclic in-plane bending moments in brace members. A Digital Image Correlation (DIC) technique is employed to monitor surface strains and to identify fracture initiation in these T-joints. Numerical investigations are also conducted to simulate in-plane bending of these T-joints between CFCHS. Applicability of current design rules in EN 1993-1-8 and CIDECT Design Guide 1 to these T-joints between CFCHS under in-plane bending moments in brace members are examined.

- *Chapter 7 – Conclusions and future work*

This chapter summarizes the conclusions drawn from this research project and discusses relevant research studies to be conducted in the future.

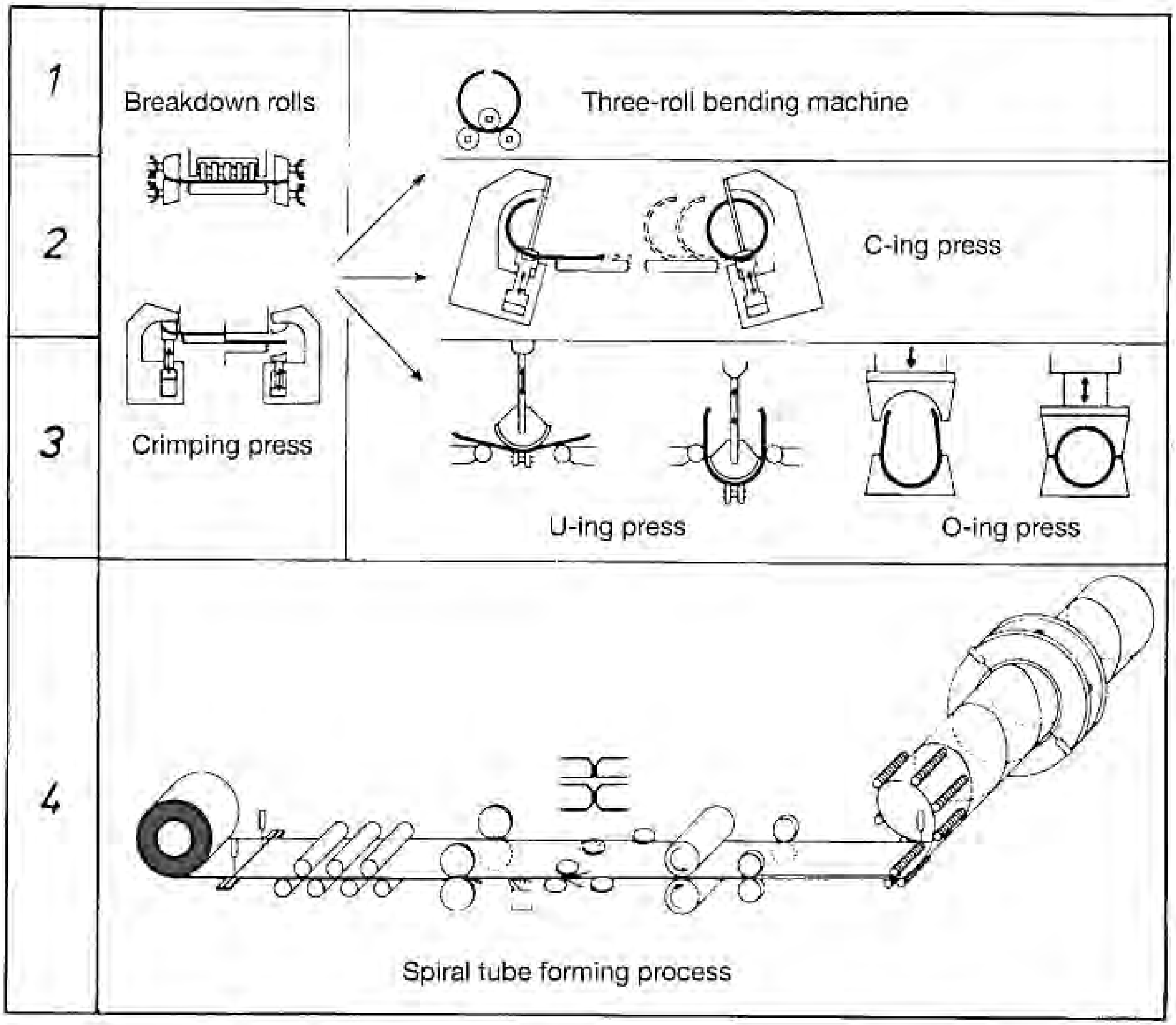

Figure 1.1. Various cold-forming methods of CHS (Brensing and Sommer, 2008)

CHAPTER TWO

LITERATURE REVIEW

2.1 INTRODUCTION

In this chapter, a literature review on existing research on steel circular hollow sections (CHS), especially high strength steel cold-formed CHS (CFCHS) was presented. The literature review consists the followings:

(1) Previous experimental investigations into residual stresses in CHS were reviewed. Various test methods, such as the sectioning method, the hole-drilling method and the neutron diffraction method were introduced. Both advantages and disadvantages of these methods were compared. Available experimental results of residual stresses in normal strength and high strength steel CHS were summarized. Existing residual stress patterns of CHS given in literature were reviewed. Their ranges of applicability were also addressed.

(2) Numerical investigations into various manufacturing processes of CHS, including cold-bending and welding were reviewed. Simulation of transverse cold bending process using nonlinear geometrical and material finite element analyses, and simulation of longitudinal welding process using coupled thermomechanical analyses were introduced.

(3) Current design rules for T-joints between CHS under various loading conditions were reviewed. Design formulae given in EN 1993-1-8 and CIDECT Design Guide 1 were compared. Experimental and numerical evidence for development of current design rules were discussed. Additional rules on application of these design formulae with high strength steel in EN 1993-1-12 were also described.

(4) Previous studies on T-joints between CHS members were summarized while experimental and numerical results of these T-joints subjected to various loading conditions were reviewed. Test results and key findings were compared and analyzed to establish the research needs for the present study.

2.2 EXPERIMENTAL INVESTIGATIONS INTO RESIDUAL STRESSES OF CHS

Residual stress is an important initial imperfection in structural steels, which is always generated in various fabrication processes. Such imperfection will result in premature yielding of steels, and hence, influence structural behaviour of structural steel members.

The formation of residual stresses can be attributed to macroscopic reasons such as manufacturing processes or microstructural effects such as phase transformation (Withers and Bhadeshia 2001). Anderson (2000) has classified residual stresses into three main types. In this study, the Macroscopic Type I residual stress is under investigation, as it has the most significant effect on the structural behavior of steel structures. In a cold-formed CHS, cold-bending and welding will both generate residual stresses. Cold-bending induced residual stresses were studied by Moen *et al*. (2008), which includeded both plastic bending and elastic spring back. The generation of welding-induced residual stresses is examined in Masabuchi (2001).

2.2.1 Measurement techniques

During the past three decades, a large number of experimental investigations have been carried out to study effects of residual stresses on normal strength and high strength steels. Various methods have also been developed for residual stress measurements. These methods are basically divided into destructive methods and non-destructive methods.

Rossini *et al*. (2012) summarized different measurement techniques and compared advantages and disadvantages of each method, as shown in Table 2.1. The penetration and the spatial resolution of each method are presented in Figure 2.1.

In recent years, the advantages of the neutron diffraction method has been recognized. This method can be applied to measure the internal residual stresses of many materials. A neutron is able to penetrate up to 25 mm in steel (Kim *et al*., 2019), which enables to provide through thickness residual stress profiles within the material. However, the cost of the equipment is very high, and complicated calibration procedures make it difficult to be used in engineering applications.

At present, most of the residual stress measurements on steel sections are obtained from the hold-drilling method and the sectioning method as these two methods are relatively simple in operation. Experimental results of residual stresses on steel sections with the hole-drilling method were presented by several researchers (Lee *et al*., 2012; Tong *et al*., 2012; Liu and Chung, 2018). This method was also incorporated into ASTM (2001) as the standard procedure for residual stress measurements. However, for structural hollow sections such as RHS and CHS with small cross-sectional dimensions or curved corners, the method may be applied with some difficulty. Only limited test results are available in the literature.

2.2.2 Residual stress measurement of CHS

The sectioning method is widely adopted for residual stress measurements of CHS. The methodology of this method is detailed in Tebedge *et al*. (1973) and Rossini *et al*. (2012). Figure 2.2 illustrates a typical instrumentation for residual stress measurement using this method. This method requires the measurement of relative deformations due to a release of residual stresses upon removal of part of the material through wire-cutting. The deformations released during the cutting process can either be measured with strain gauges, Whittemore gauges or curvature dials, as shown in Figure 2.3. In general, both axial deformation and curvature may occur in the strips after cutting, which correspond to two different residual stress components, i.e. membrane residual stress, σ_m, and bending residual stress, σ_b, as illustrated in Figure 2.4. Membrane residual stresses are found to dominate in hot-rolled and welded sections, while bending residual stresses are dominant in cold-formed sections (Rossini *et al*. 2012). It should be noted that through thickness distribution of residual stresses of the sections cannot be measured with strain gauges as they are mounted onto the surfaces of the specimen only. Therefore, the residual stress patterns obtained with this method is based on an assumption that bending residual stresses vary linearly through the thickness of the sections.

The sectioning method has been successfully applied to obtain residual stress distributions of normal strength steel and stainless steel sections in the past forty years (Chen and Ross, 1977; Cruise and Gardner, 2008, Ban *et al*., 2013, Ma *et al*., 2015, Somodi and Kövesdi, 2017; Zheng *et al*., 2019). The cross-sectional types include I-section, RHS and CHS.

For high strength steel CHS, many researchers conducted residual stress measurements in the past years. A summary of these tests are shown in Table 2.2.

Jiao and Zhao (2003) measured residual stresses of a CHS with a nominal yield strength at 1350 N/mm^2. The measured residual stresses were found to be about only 4% of the yield strength. Shi *et al*. (2013) conducted residual stress measurements on five high strength Q420 steel CHS with a nominal yield strength of 420 N/mm^2. The released strains were measured by Whittemore gauges with a gauge length of 254 mm. Experimental results of this study are shown in Figure 2.5. Residual stresses on both the inner surface and the outer surface are provided. However, the test results are found to have large scattering among themselves. Ma *et al*. (2015) measured both longitudinal and transverse residual stresses of a high strength CFCHS with a nominal yield strength at 1100 N/mm^2. The released strains after wire-cutting were measured by strain gauges. Figure 2.6 presents the measured residual stress distributions, where the magnitudes of the residual stresses were normalized with 0.2% proof strength obtained from respective coupon tests. Yang *et al*. (2016) presented experimental results of residual stresses on eight high strength Q690 cold-formed CHS. Both the sectioning method and the hole-drilling method were adopted to study relative accuracy of these two measurement methods. It was found that strain measurement using handheld Whittemore gauges may affect the precision of measurement, and cause the scattering of results.

2.2.3 Residual stress patterns for CHS

A number of residual stress patterns for normal strength steel CHS have been proposed based on experimental data reported in the literature since 1970s. Wagner *et al*. (1976) proposed a bilinear model to describe residual stress distributions in CHS, while Chen and Ross (1977) recommended a multi-linear residual stress distribution. Shi *et al*. (2013) proposed simplified models on both the outer and the inner surfaces for high strength Q420 steel CHS. Yang *et al*. (2016) proposed a bilinear model for high strength Q690 CHS. These residual stress models are illustrated in Figure 2.7.

It should be noted that the simplified models proposed by Wagner *et al*. (1976) and Yang *et al*. (2017) are able to fulfil cross-sectional force equilibrium while the model proposed by Chen and Ross (1977) does not fulfill force equilibrium.

2.2.4 Summary

It is found from the selected literature reported in previous sections that experimental results of residual stresses in high strength steel CHS are limited. Effects of various manufacturing processes, including cold-forming and welding onto the residual stress distributions in CHS have not been quantified. Moreover, it is difficult to define a single residual stress pattern for high strength steel CFCHS for use in all levels of inelastic analysis because both the magnitude and the distribution of these stresses are dependent on the manufacturing process and the cross-section geometry.

In general, existing residual stress patterns proposed by the researchers are based on their own test results. Their range of application remains questionable on steel sections with high strength steel or different cross-section dimensions. Hence, it is necessary to conduct experimental investigations to study these residual stresses in high strength CFCHS to enrich existing database and to develop a general finite element approach to predict residual stresses in CFCHS with different section dimensions.

2.3 NUMERICAL SIMULATION OF MANUFACTURING PROCESSES

Laboratory measurements of residual stresses in CFCHS are time-consuming, and only limited test results can be obtained by adopting the sectioning and the hole-drilling methods. With assistance of increasingly developed finite element programnes, many research studies have been conducted to simulate the manufacturing processes and to predict mechanical responses of CHS.

2.3.1 Modeling of cold-forming

Quach *et al*. (2004) established a two dimensional plane strain pure bending model to simulate the coiling and uncoiling process of a steel sheet, and an analytical solution was proposed to predict residual stresses of cold-formed steel sections. When dealing with strain hardening, a theoretical method was proposed that involved complicated differential equations. Residual stress distributions throughout the thickness of a cold-formed steel sheet were predicted. It was found that through-thickness variations of residual stresses were non-linear. The magnitude of residual stresses are also found to be sensitive to the coiling radius and the yield strength of the steel sheet. It should be noted that simple forms of analytical solutions of the residual stresses were difficult to be obtained. Spring back after bending was not considered.

Moen *et al*. (2008) presented a simplified analytical solution to predict both longitudinal and transverse residual stresses due to cold bending. It was assumed that the stress-strain curve of the steel sheet was elastic-perfectly plastic, and the bending radii were very small, i.e. r/t ranging from 2 to 8. The cold forming process consisted of two stages: i) plastic bending, and ii) elastic spring back. The simplified analytical solution is shown in Figure 2.8.

It should be noted that there are simple forms of residual stress distributions available in the literature, and the values were quantified as fractions of the yield strengths of the steel plates. These solutions did not consider any cold work strain hardening of the steel plates.

The residual stresses were, therefore, considered to be somehow underestimated for CFCHS with large *r*/*t* ratios.

2.3.2 Modeling of welding

Numerical investigations into welding process in steel structures were extensively studied in the past decades. Various heat source models, reduction factors for mechanical properties of steel as well as thermal properties of steel at elevated temperatures have been investigated.

Both two dimensional and three dimensional models have been developed for coupled thermomechanical analysis to obtain temperature history and residual stresses for welded steel sections. At present, there are still some factors that are difficult to be considered in numerical simulation of welding, including phase transformation of steel, microstructures of weld metal and heat affected zones. Hence, assumptions and some degree of simplification on these factors are adopted to reduce complexity of the numerical models as well as to obtain results with acceptable accuracy.

3D modeling

A double ellipsoidal model proposed by Goldak *et al*. (1984) has been widely employed to simulate a moving heat source during welding in three dimensional models (Sonti and Amateau, 1989; Wahab *et al*., 1998; Gery *et al*., 2005; De *et al*., 2013; Chukkan *et al*., 2015). A schematic view of this model is presented in Figure 2.9. Heat flux densities at specified positions are presented in Equations 2.1 and 2.2.

$$\begin{cases} q_f\left(x,y,z\right)=\dfrac{6\sqrt{3}f_fQ}{a_1bc\pi\sqrt{\pi}}\exp(-\dfrac{3x^2}{a_1^2})\exp(-\dfrac{3y^2}{b^2})\exp(-\dfrac{3z^2}{c^2}) \\ q_r\left(x,y,z\right)=\dfrac{6\sqrt{3}f_fQ}{a_2bc\pi\sqrt{\pi}}\exp(-\dfrac{3x^2}{a_2^2})\exp(-\dfrac{3y^2}{b^2})\exp(-\dfrac{3z^2}{c^2}) \end{cases} \tag{2.1}$$

where q_f and q_r are the volumetric heat flux in the front and the rear [W/m^3];

a_1, a_2, b and c are semi-axes of the double ellipsoid [m];

Q is the total heat energy input of welding [J];

x, y and z are the local coordinates; and

f_f and f_r are fractions illustrating energy distribution, and $f_f + f_r = 2$.

And the total heat energy Q is calculated according to

$$Q = \eta \cdot U \cdot I \tag{2.2}$$

where η denotes the welding efficiency;

U denotes the voltage of the welding arc [V]; and

I denotes the welding current [A].

The input of the heat source model can be achieved by defining the subroutine function *DFLUX in ABAQUS. Liu and Chung (2018) conducted parametric studies on various parameters of this heat source model. Recommended values for these parameters were provided for GMAW and SAW of high strength S690 steel. The numerical models were calibrated with measured temperature histories and residual stresses of high strength steel S690 welded H-sections.

It is shown that with careful calibration, three dimensional thermomechanical analyses are effective to predict residual stresses within high strength steel welded sections.

2D modeling

Coupled thermomechanical analysis using a 3D model is rather time consuming, especially for multi-pass welding of thick plates or sections. In order to reduce computational resources, Pilipenko (2001) introduced a method which simplified a 3D welding process into a 2D process. A ramp heat model is proposed by Shim *et al*. (1992) for such 2D analysis. The motion of heat source is simplified by applying the body heat flux to the elements, as shown in Figure 2.10. This model has been employed in various 2D analyses (Lindgren, 2001; Jiang *et al*., 2005; Liu *et al*., 2011).

2.3.3 Sequentially and fully coupled thermomechanical analysis

Sequentially coupled thermomechanical analysis

The differences between sequentially and fully coupled thermomechanical analyses have been introduced in Ellobody (2014). In a sequentially coupled thermomechanical analysis, the stress/deformation field is dependent on the temperature field, while the temperature field is not dependent on the stress/deformation field, which can be obtained separately.

The analysis is performed by firstly conducting an uncoupled heat transfer analysis to get the temperature results. Then a stress analysis is carried out with an input of nodal temperature results as predefined fields. The mesh scheming and step increments in these two models should be identical. It should be noted that any mechanical properties will be ignored in the heat transfer analysis. The material nonlinearity will be considered in a separate stress analysis. Also, different elements are employed in these two different processes. Linear heat transfer elements are adopted for heat transfer analysis while linear or nonlinear stress elements can be used for stress analysis.

Fully coupled thermomechanical analysis

A fully coupled thermomechanical analysis is usually conducted when the mechanical and thermal results strongly affect each other, and therefore, must be obtained simultaneously. In ABAQUS (Standard), it is computed by a coupled temperature-displacement analysis. Temperature-dependent material properties are considered. Coupled temperature-displacement elements are adopted, but pure heat transfer elements cannot be used in this analysis. Both temperature and stress results can be obtained from a single model, but the computational time of a fully coupled analysis is usually much longer than that of a sequentially coupled analysis.

2.3.4 Summary

Numerical modeling of various fabrication processes of CHS involves complex material models which require certain extents of simplification.

In the present study, two different stages, i.e. transverse cold-bending and longitudinal welding are considered for manufacturing of CHS. From the extensive review and the comparison among various modeling techniques discussed in previous sections, it is adopted that cold-bending of steel plates will be simulated by 2D plane strain analysis while welding of CHS will be modelled by 3D sequentially coupled thermomechanical analysis.

2.4 CURRENT DESIGN RULES

Structural behaviour of tubular joints between normal strength steel hollow sections have been extensively investigated in the past decades. The research findings have been developed into various design rules adopted by some international design specifications. Design recommendations for the design of tubular joints were firstly proposed by the International Institute of Welding (IIW) Subcommission XV-E in 1981(IIW, 1981). This document was then developed into the 2nd and the 3rd editions 1989 and 2009 respectively (Lan and Chan, 2018). Eurocode EN 1993-1-8 (CEN, 2005) adopted the design recommendations proposed by the 2nd edition of IIW recommendations (IIW, 1989). The latest version of CIDECT Design Guide 1 (Wardenier *et al.*, 2008) follows closely to the 3rd edition of IIW recommendations (IIW, 2009).

2.4.1 Design strength for CHS T-joints

The design formulae for T-joints between CHS given in both CIDECT Design Guide 1 and EN 1993-1-8 are compared in Table 2.3. It is found that the design formulae for chord plastification in both design codes have similar forms of expressions, and both consist of a strength function Q_u, and a chord stress function Q_f (or k_p).

It should be noted that in CIDECT, a reduction factor of 0.9 is adopted for calculating the design strengths of joints with S460 steels, but no guidance is provided for S690 steels. In general, lower ductility of high strength steel and larger deformations that may occur are considered. The design yield strength of steel, f_y, is also limited to be not larger than 0.8 f_u, which results in a total reduction of joint resistance at about 15%. Similarly, according to EN 1993-1-12 (CEN 2007), a reduction factor of 0.8 is applied for calculating joint resistances of T-joints between structural hollow sections with steel grade up to S700.

2.4.2 Deformation limits

The ductility requirements for T-joints between CHS are dependent on various cases (Havula 2018). In general, deformation limit proposed by Yura *et al*. (1981) and Lu *et al*. (1994) are widely adopted to determine ultimate loads of these sections. Yura et al. (1981) proposed a deformation limit of 60 $d_1 f_y$ / E, and a rotation limit of 80 f_y / E. Moreover, Lu *et al*. (1994) proposed a general out-of-plane deformation limit of 3% of the outer diameter of the chord (0.03d_0) to define the ultimate resistances of joints. Such deformation limit is also incorporated in CIDECT Design Guide 1 to determine the resistances of a joint between CHS. A deformation limit of 1% (0.01d_0) is adopted to control joint deformations at serviceability limit states.

2.5 PREVIOUS STUDIES ON T-JOINTS BETWEEN HIGH STRENGTH CHS

Current design rules for T-joints between high strength CHS were developed based on extensive numerical results and re-assessment of existing experimental results (Qian et al., 2008). However, it was generally considered that there were insufficient experimental results for these joints at that time. Therefore, strength reduction factors combined with limitations on the ratios of tensile to yield strengths, f_u / f_y, were adopted to provide conservative design rules for practical design.

In recent years, there has been an increasing number of research on joints between high strength steel structural hollow sections. Various joint types with various cross-section geometry were studied to enlarge the database for these joints, as well as to appraise applicability of the current design rules. Analyses on experimental results on X-joints between high strength CHS and RHS subjected to brace axial compression suggested that the current reduction factors from EN 1993-1-8 may be too conservative for high strength steel. (Becque and Wilkinson, 2017; Lee *et al*., 2017; Kim, 2018) Applicability of these reduction factors still remains controversial.

2.5.1 Behaviour of T-joints between high strength CHS

For T-joints between high strength CHS subjected to brace axial compression, the interaction between overall chord bending and local joint failure should be considered. It is difficult to investigate each of these two failure modes in tests. Therefore, it is more straightforward to conduct experiments on those X-joints because axial brace loads do not cause in-plane bending moments in chords.

Up till the presence, experimental investigation on T-joints between high strength CHS are found to be limited. Choi et al. (2012) conducted experiments on four T-joints between hot-finished CHS under axial compression. The nominal yield strength of the CHS was 480N/mm^2. All these four test specimens failed in chord plastification. Kim *et al*. (2012) reported experimental results of 12 T-joints between high strength CHS under cyclic in-plane bending. The measured yield strengths of the CHS are 464 and 584 N/mm^2. From these test results, it is found that joints between high strength CHS have desirable performance in joint resistance without any significant reduction in ductility, when compared with those of joints between normal strength CHS.

Moreover, numerical investigations have been widely carried out. Van der Vegte and Makino (2005) introduced a finite element approach to exclude effects of boundary conditions and chord lengths to the joint resistances by applying compensating in-plane bending moments at the ends of the chords, as shown in Figure 2.11. It was also pointed out that the chord length parameter, α (= 2 L_0 / d_0) , will influence the resistances of these T joints. And a chord length of 10 d_0 (α = 20) is sufficiently long to exclude any influence caused by chord end conditions. By adopting this approach, a function Q_f, which took accounts of the effect of chord stresses was further developed, and this function was incorporated into various design codes such as EN1993-1-8 (CEN, 2005) and CIDECT Design Guide 1 (Wardenier *et al*., 2008).

2.5.2 Summary

Existing experimental data on T-joints between high strength CHS are found to be limited in the literature. Current design rules for T-joints between high strength CHS are considered to be developed based on test results of normal strength steels and numerical analyses. Hence, it is necessary to carry out specific experimental investigations on T-joints between high strength CHS under various loading conditions to enlarge the existing database.

It is also highly desirable to develop finite element models with high precision to assess accuracy of various reduction factors on axial resistances of these T-joints between high strength steel CHS in order to improve design efficiency. Effects of cold-forming, welding-induced residual stresses and strength reductions in the heat affected zones of these joints on their structural behaviour should also be investigated.

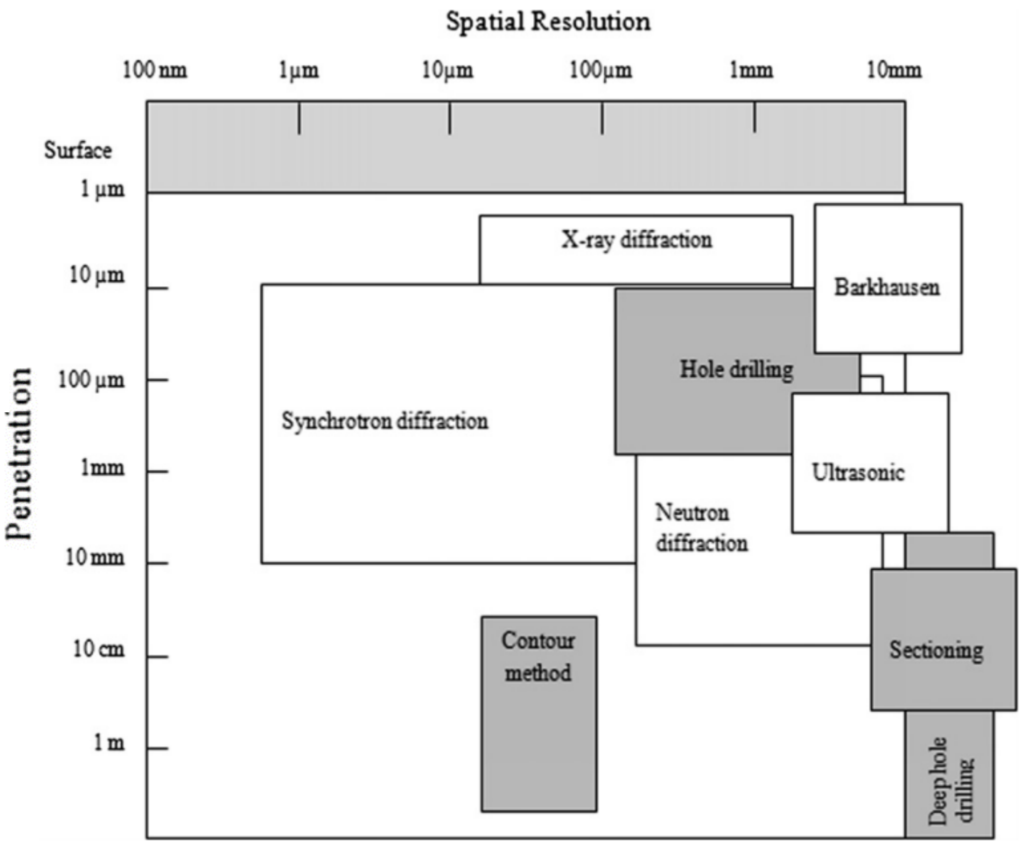

Figure 2.1 Penetration and spatial resolutions of various techniques (Rossini *et al*. 2012)

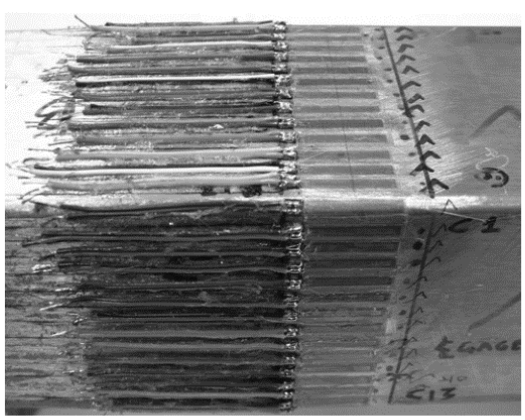

Figure 2.2 Typical instrumentation for residual stress measurement (Cruise and Gardner 2008)

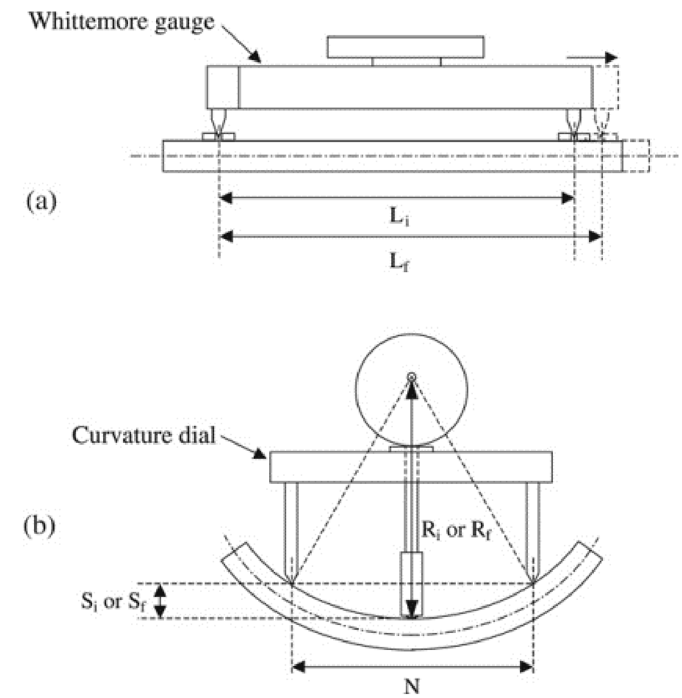

Figure 2.3 Deformation measured by Whittemore gauge and curvature dial (Cruise and Gardner, 2008)

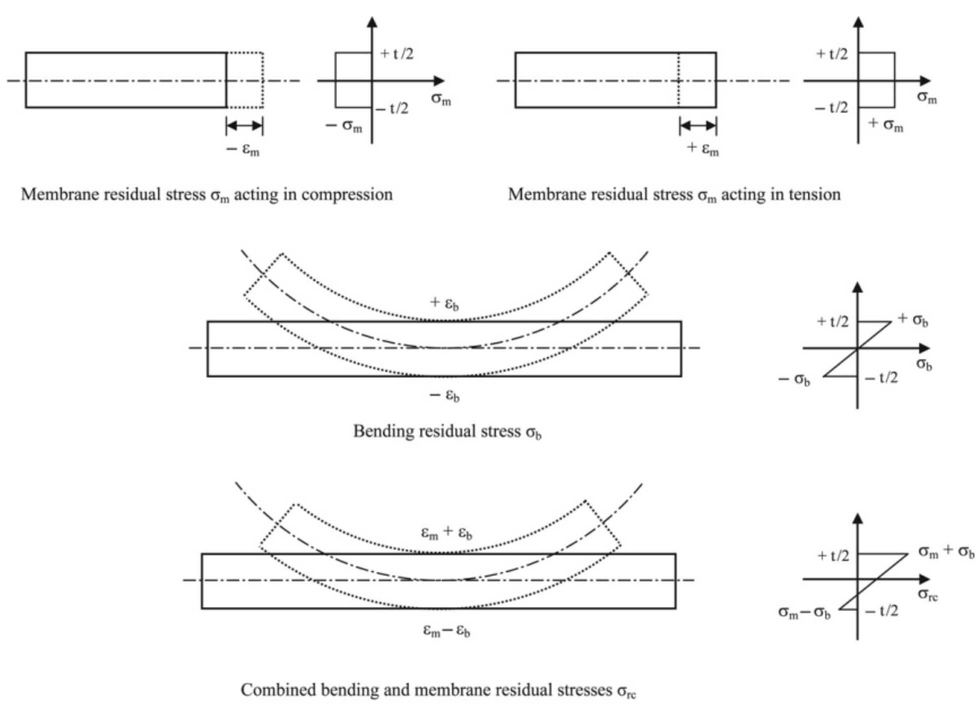

Figure 2.4 Modeling of residual stresses with membrane and bending stress components (Cruise and Gardner, 2008)

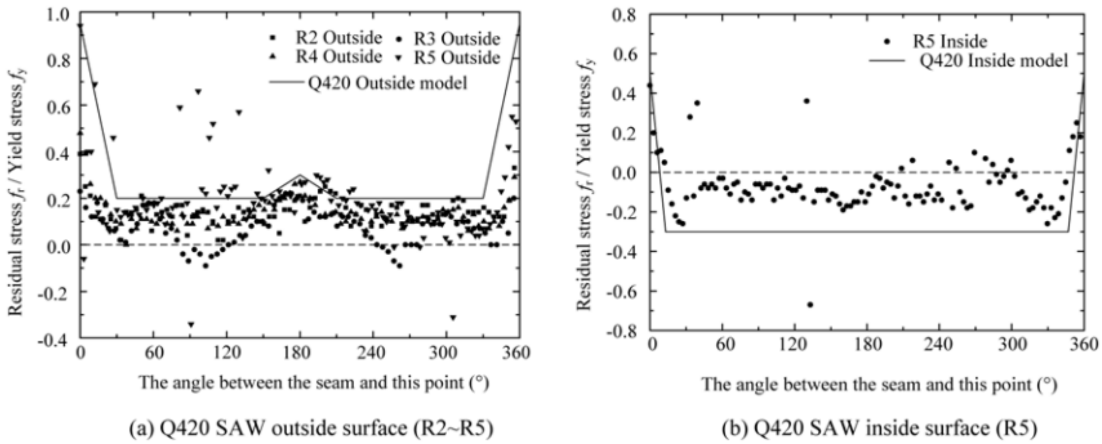

Figure 2.5 Experimental results of residual stresses of Q420 CHS (Shi *et al*., 2013)

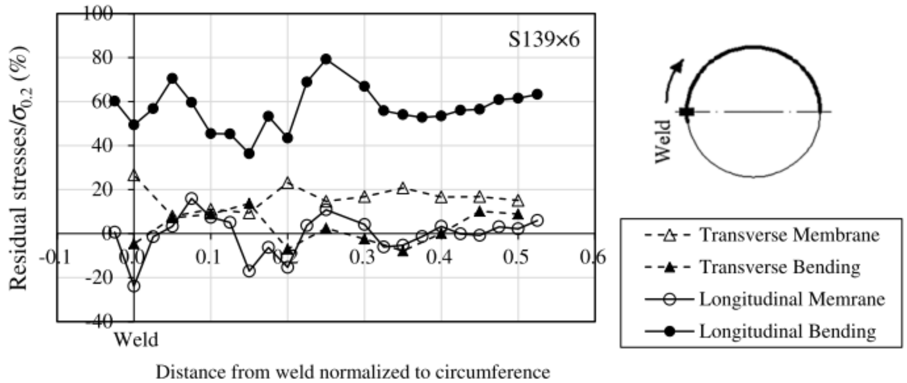

Figure 2.6 Experimental results of residual stresses of CHS (Ma *et al*., 2015)

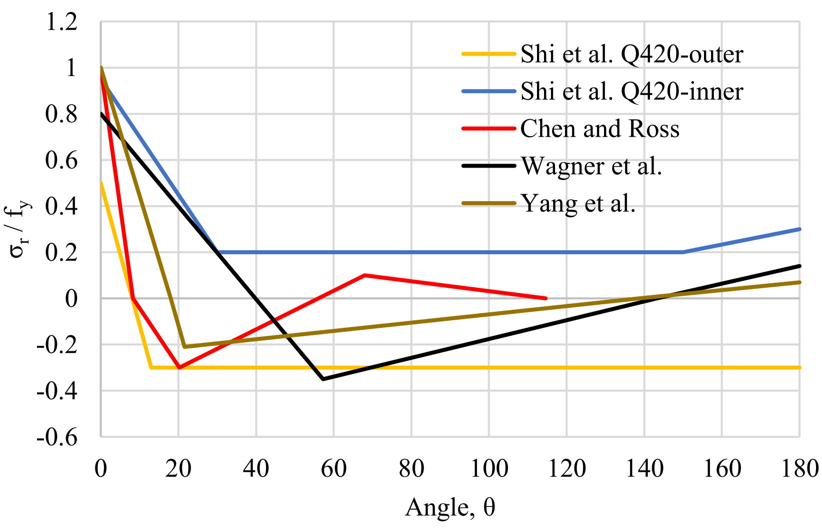

Figure 2.7 Comparison of existing residual stress patterns for CFCHS

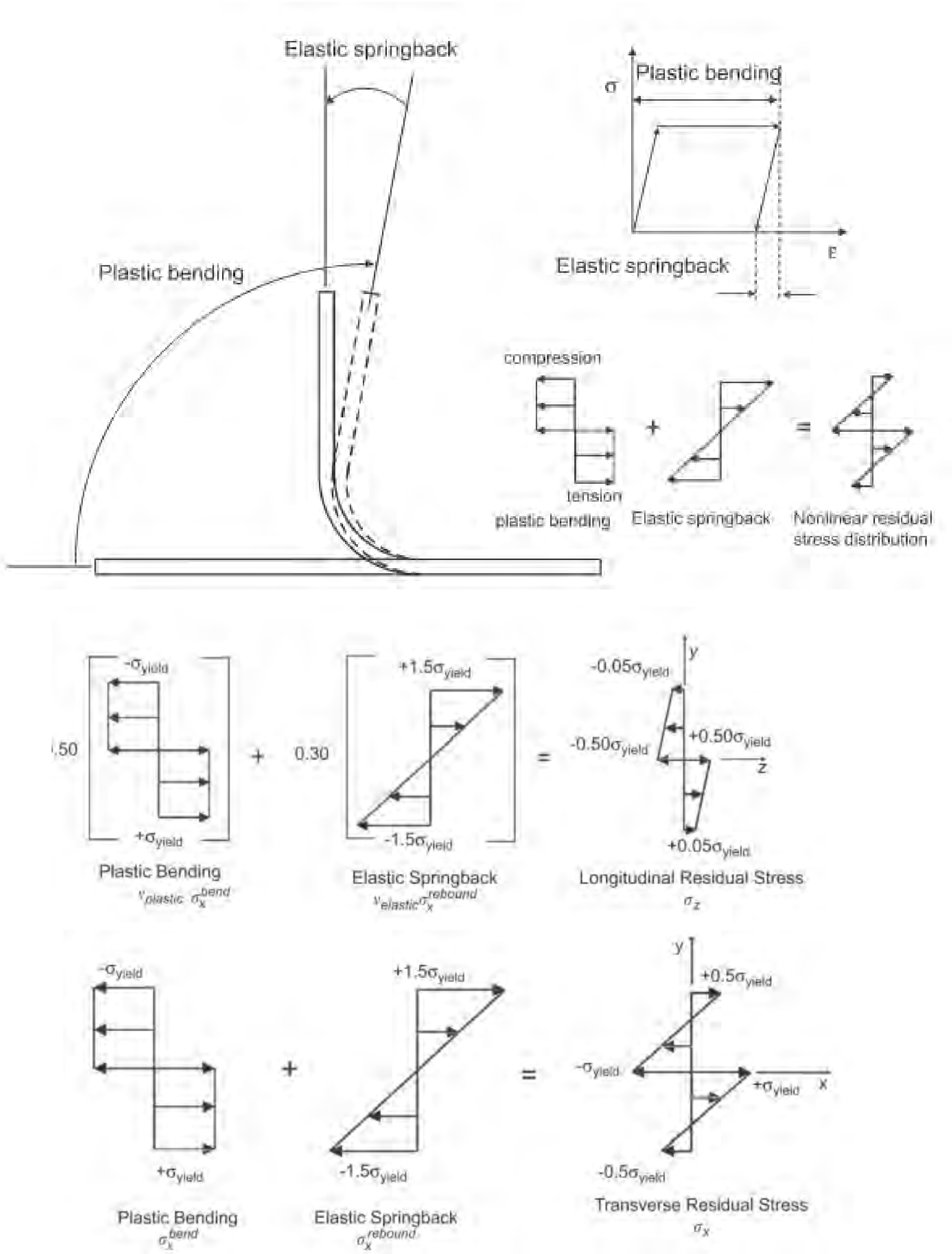

Figure 2.8 Analytical solutions of longitudinal and transverse residual stress (Moen *et al.*, 2008)

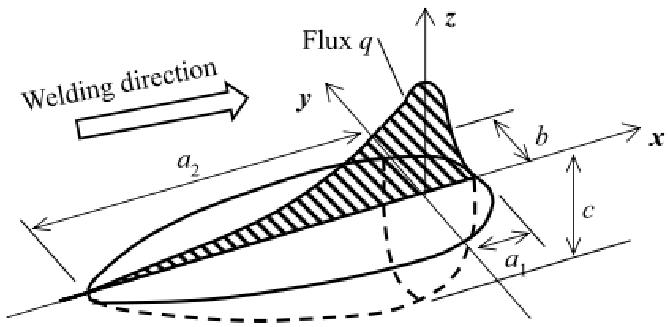

Figure 2.9 Double ellipsoidal heat source model (Goldak *et al*., 1984)

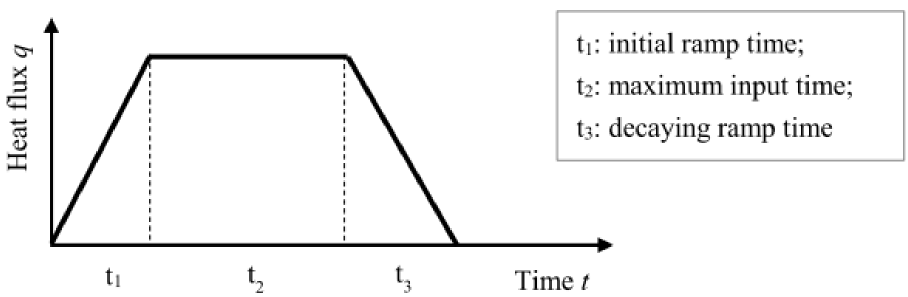

Figure 2.10 Ramp heat source model for 2D analysis (Shim *et al*., 1992)

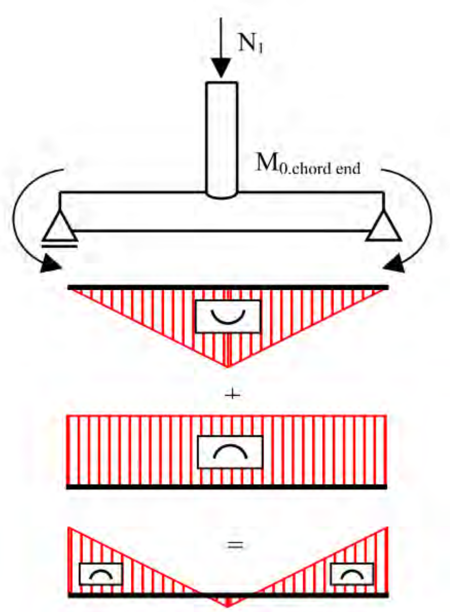

Figure 2.11 Loading scheme and moment distribution of T-joints (van der Vegte and Makino, 2005)

Table 2.1 Comparison of residual stress measurement techniques (Rossini *et al*., 2012)

Technique	Advantage	Disadvantage
X-ray diffraction	Ductile, Generally available, Wide range of materials, Hand-held systems, Macro and Micro RS	Lab-based systems, Small components, Only basic measurements
Hole Drilling	Fast, Easy use, Generally available, Hand-held, Wide range of materials	Interpretation of data, Semi destructive, Limited strain sensitivity and resolution
Neutron Diffraction	Macro and Micro RS, Optimal penetration and resolution, 3D maps	Only specialist facility, Lab-based system
Barkhausen Noise	Very quick, Wide sensitive to Microstructure effects especially in welds, Hand-held	Only ferromagnetic materials, Need to divide the microstructure signal from that due to stress
Ultrasonic	Generally available, Very quick, Low cost, Hand-held	Limited resolution, Bulk measurements over whole volume
Sectioning	Wide range of material, Economy and speed, Hand-held	Destructive, Interpretation of data, Limited strain resolution
Contour	High-resolution maps of the stress normal to the cut surface, Hand-held, Wide range of material, Larger components	Destructive, Interpretation of data, Impossible to make successive slices close together
Deep hole drilling	Deep interior stresses measurement, Thick section components, Wide range of material	Interpretation of data, Semi destructive, Limited strain sensitivity and resolution
Synchrotron	Improved penetration and resolution of X-rays, Depth profiling, Fast, Macro and micro RS	Only specialist facility, Lab-based systems

Table 2.2 Summary of residual stress measurement of high strength steel CFCHS

Author	**Fabrication method**	**Method of measurement**	**Yield strength of steel (N/mm^2)**	**D (mm)**	**t (mm)**	**D/t ratio**
Jiao and Zhao (2003)	Cold-forming and welding	Sectioning	1350	38 to 75	1.6	24 to 46
Shi *et al*. (2013)	Cold-forming and welding	Sectioning	381 to 506	168 to 377	5 to 8	31 to 47
Ma *et al*. (2015)	Cold-forming and welding	Sectioning	937 to 1160	139	6	23
Yang *et al*. (2017)	Cold-forming and welding	Sectioning	690	250 to 350	8	31 to 44

Table 2.3 Comparison of design formula from CIDECT Design Guide 1 and Eurocode EN 1993-1-8

	CIDECT Design Guide 1 (2008)	EN 1993-1-8 (2005) EN 1993-1-12 (2007)
Brace axial compression	$N_1 = Q_u Q_f \dfrac{f_{y0} t_0^2}{\sin\theta}$ $Q_u = (2.6 + 17.7\beta^2)\gamma^{0.2}$ $Q_f = (1-\lvert n\rvert)^{C_1}$ $n = \dfrac{N_0}{N_{pl,0}} + \dfrac{M_0}{M_{pl,0}}$ $C_1 = 0.45 - 0.25\beta$ for chord compressive stress $C_1 = 0.20$ for chord tension stress	$N_1 = Q_u k_p \dfrac{f_{y0} t_0^2}{\sin\theta}$ $Q_u = (2.8 + 14.2\beta^2)\gamma^{0.2}$ For $n_p > 0, k_p = 1 - 0.3n_p(1+n_p)$ For $n_p \le 0, k_p = 1$ $n_p = \dfrac{\sigma_{p,Ed}}{f_{y0}}$
Brace in-plane bending	$M_1 = Q_u Q_f \dfrac{f_{y0} t_0^2}{\sin\theta_1} d_1$ $Q_u = 4.3\beta\gamma^{0.5}$, $Q_f = (1-\lvert n\rvert)^{C_1}$ $n = \dfrac{N_0}{N_{pl,0}} + \dfrac{M_0}{M_{pl,0}}$, $C_1 = 0.45 - 0.25\beta$ for chord compressive stress $C_1 = 0.20$ for chord tension stress ($n \ge 0$)	$M_1 = Q_u k_p \dfrac{f_{y0} t_0^2}{\sin\theta_1} d_1$ $Q_u = 4.85\beta\gamma^{0.5}$ For $n_p > 0, k_p = 1 - 0.3n_p(1+n_p)$ For $n_p \le 0, k_p = 1$ $n_p = \dfrac{\sigma_{p,Ed}}{f_{y0}}$
Material limit	$f_y \le 460$ N/mm^2 and $f_y \le 0.8\ f_u$	$f_u / f_y \ge 1.05$ for 460 N/mm^2 $\le f_y \le$ 700 N/mm^2
Strength reduction factor	1.0 for S355 0.9 for S355 to S460	1.0 for S355 0.9 for S355 to S460 0.8 for S460 up to S700

CHAPTER THREE

INVESTIGATIONS INTO RESIDUAL STRESSES IN COLD-FORMED CHS

3.1 INTRODUCTION

In this chapter, a comprehensive experimental and numerical investigation into residual stresses of S690 cold-formed circular hollow sections (CFCHS) was presented in order to examine the effects of various fabrication processes on residual stresses of CFCHS.

The key activities of the investigation are:

Task A Experimental investigation

- To fabricate eight CFCHS of different cross-sectional dimensions.
- To measure surface temperature history at specific locations using thermocouples during welding.
- To measure residual stresses in these CFCHS using the sectioning method, and to obtain the residual stress distributions.

Task B Numerical investigation

- To establish finite element models to simulate (i) transverse cold-forming, and (ii) longitudinal welding of CHS, and to predict mechanical responses after welding.
- To compare measured and predicted surface residual stresses of these CHS.
- To propose simplified residual stress pattern for subsequent analyses.

In order to obtain basic mechanical properties of S690 high strength steel and S355 normal strength steel, standard tensile tests were carried out on standard coupons made from steel plates with various thicknesses.

It should be noted that a total of eight CFCHS with different geometric dimensions were manufactured, and they were classified into two series for comparison, namely, (i) cold-formed circular hollow sections without welding, and (ii) cold-formed welded circular hollow sections. Steel plates were formed into circular tubes using a three-roller bending machine. Then, longitudinal welding was performed by a qualified welder while welding parameters during the entire welding process were recorded for subsequent numerical analyses. Surface temperature history at selected positions were measured with thermocouples. Surface residual stresses of both cold-formed and welded sections were measured with the sectioning method.

Numerical models were established to simulate both the transverse cold-forming and the longitudinal welding operations. The residual stresses predicted with various manufacturing processes were compared with measured residual stresses obtained in this study as well as test results reported by other researchers. Moreover, a simplified residual stress pattern for high strength S690 steel was proposed for subsequent analyses.

3.2 EXPERIMENTAL INVESTIGATION

3.2.1 Material tests

In order to obtain the basic mechanical properties of both normal strength S355 steel and high strength S690 steel plates with various thicknesses, a series of standard tensile tests were carried out according to BS EN ISO-6892-1 (CEN, 2009).

Test programme

A total of 16 standard tensile coupons were tested, among which 10 were rectangular coupons and 6 were circular coupons. The test programme for the material tests is listed in Table 3.1 while the geometric dimensions of these standard tensile coupons are shown in Figure 3.1.

The gauge lengths of the standard tensile coupons are determined according to Equation 3.1 from BS EN ISO-6892-1.

$$L_0 = 5.65\sqrt{A_0} \tag{3.1}$$

where A_0 is the original cross-sectional area along the parallel portion of the coupon.

Test setup

The tensile coupon tests were conducted with Instron 8803 Servo Hydraulic Fatigue Testing System. It is a multi-function material testing system which can be used for both monotonic and cyclic tests. The tension/compression capacity of the testing system is 500kN. An extensometer with a gauge length of 25mm is mounted onto test specimens to measure their strains throughout testing.

A photographic deformation analysis (PDA) method is adopted to measure longitudinal deformations and instantaneous diameters of the test coupons. A digital camera is used to take high resolution images of these test coupons during tests at a regular time interval of

30 seconds. The camera is properly held in position throughout testing so that the deformations and the instantaneous diameters of the test coupons can be obtained by calculating changes in number of pixels of corresponding images. The test setup is demonstrated in Figure 3.2.

Test results

A total of 16 coupons were tested successfully. The measured material properties of S355 and S690 steel plates are summarized in Table 3.2. The stress-strain curves of all the coupons are plotted in Figure 3.3.

It should be noted that in EN 1993-1-12, requirements for high strength steel materials up to grade S700 have been specified as follows:

i) $f_u / f_y \geq 1.05$, ii) $\varepsilon_u \geq 15 f_y / E$, and iii) $\varepsilon_f \geq 10\%$

where f_u and f_y are the tensile strength and the yield strength of steel

ε_u is the elongation at tensile strength

ε_f is the elongation at fracture

Based on the test results, it is found that the test results of S690 steels are highly consistent. The average yield strength of 6 mm and 10 mm thick S690 steel plates are found to be 731 N/mm^2 and 783 N/mm^2 respectively, and the elongation at fracture of each of the S690 coupons exceeds 15%. Hence, all high strength S690 steel materials in this study are shown to satisfy these requirements.

3.2.2 Manufacturing process of welded CHS

In general, steel plates were first cut from the parent steel plates through the use of plasma cutting technique. Then, the edges of these plates were bent locally using a press-brake machine. After that, these plates with pre-bent edges were bent transversely to form circular sections by a three-roller bending machine. Finally, longitudinal welding was performed by a qualified welder using a gas metal arc welding (GMAW) method. The fabrication processes are shown in Figure 3.4.

3.2.3 Temperature measurement

Test programme

A total of four S690 CFCHS with different cross-sectional dimensions were prepared, namely, Sections C1 to C4. The test programme of these sections is summarized in Table 3.3. Measured geometric dimensions of Sections C1 to C4 are presented in Table 3.4. All these sections are welded using a GMAW method.

Test setup and instrumentations

Type-K thermocouples were used in the present study, and they were attached at specified locations on the outside surface of the sections. The accuracy of these thermocouples is ± 1.5 ℃, and their working temperature can reach up to 1200℃. A schematic arrangement of the thermocouples is illustrated in Figure 3.5.

A total of 6 thermocouples were attached onto the outside surface of each specimen, and they were 100 mm apart in the longitudinal direction, while the spacing between the two thermocouples on the transverse direction was 10 mm. HT putty was employed to isolate exposed surfaces of these thermocouples from the air so that temperature measurement was not interfered by heat convection nor radiation. Hence, their temperatures were measured only through direct heat conduction in this study. An Avio R500 high resolution infrared thermal imaging camera was also employed to obtain the temperature field during welding. It should be noted that the camera is able to capture high resolution images with a measurement range from -40℃ to 2000℃. Figure 3.6 shows the test setup for temperature measurement on a test specimen.

Welding procedures

Before welding, single-V weld grooves at the edges of the steel plates were prepared, and ceramic backings were attached at the underside of the weld seams. The cross-sectional dimensions and the weld groove details are illustrated in Figure 3.7. Figure 3.8 shows the GMAW welding method employed, and the welding electrode ER110S-G (with a diameter of 1.2 mm) according to AWS A5.28 is employed. It should be noted that the nominal yield strength of the welding electrode is 720 N/mm^2 while the measured yield strengths of S690 steel plates with thicknesses of 6 mm and 10 mm are 731 N/mm^{2}and 787 N/mm^2 respectively. Therefore, an under-matched welding is achieved although an over-matched welding is designed. The mechanical properties of the welding electrode are summarized in Table 3.5.

A multi-pass weld method was adopted to control the heat energy input. For Sections C1 and C2, a two-pass welding procedure was employed while for Sections C3 and C4, a three-pass welding procedure was employed. Key welding parameters, including current, voltage and welding speed have been carefully recorded during welding, as summarized in Table 3.6.

Test results

Temperature history of Sections C1, C2, C3 and C4 obtained from thermocouples are plotted in Figures 3.9 to 3.12. The measured maximum temperatures are listed in Tables 3.8 to 3.11. The first group of thermocouples, T1, T3 and T5, were found to increase rapidly when the heat source approached. After reaching peak values, the temperatures of these thermocouples dropped approximately to 200℃ in about 250s. The other group, namely, T2, T4 and T6 which were further away from the weld seam, were found to record lower temperatures during welding.

3.2.4 Residual stress measurements

Residual stresses of CFCHS were measured using a sectioning method. This method is based on the elastic theory, and the principles of this method are described in the previous chapter. The objectives of residual stress measurements are:

- To provide measured residual stress distributions in both S690 CFCHS and CFCHS-NW (no welding).

- To study effects of the transverse cold-forming onto the residual stress distributions in S690 CFCHS.
- To propose a simplified residual stress model for high strength S690 CFCHS based on experimental results.

Two CFCHS, namely, Sections C1 and C2, and two CFCHS without welding, namely, Sections C1-NW and C2-NW were prepared for residual stress measurements. Each CHS was cut with the use of cold-sawing into three parts with different lengths, i.e. 150 mm, 260 mm and 250 mm. Sectioning of the CHS was performed in the middle part with a length of 260 mm. The test programme is summarized in Table 3.11.

Test setup and instrumentation

It is widely considered that longitudinal residual stresses have the most significant influence on the structural behaviour of CHS. Therefore, in this study, only longitudinal residual stresses are measured.

Arrangements of measurement points of each CHS are shown in Figures 3.13 and 3.14. The distribution of residual stresses are assumed to be symmetrical along the weld seams of the CHS. Hence, only half of each of the CHS is prepared for strain measurement.

During preparation of the tests, strain gauges were attached to both outer and inner surfaces at the mid-length of each section. The width of each longitudinal strip was 10 mm, and waterproof glue was applied to protect all the strain gauges. Wire-cutting was then performed to give a total of 24 strips from Sections C1-NW and C1, and a total of 32 strips from Sections C2-NW and C2. Coolant was applied during the cutting process in order to minimize any heat generated, as shown in Figures 3.15 and 3.16.

Test results

Strain readings prior to and after the wire-cutting were recorded. Residual strains on both the outer and the inner surfaces, ε_o and ε_i respectively, were calculated by subtracting the final measured strains from the initial measured strains. Residual stresses were calculated according to the Hook's Law, as shown in Equations 3.2 and 3.3, where E is the measured elastic modulus of the steel material.

$$\sigma_o = -\varepsilon_o \cdot E \tag{3.2}$$

$$\sigma_i = -\varepsilon_i \cdot E \tag{3.3}$$

By assuming a linear distribution of residual stresses within the thickness of a strip, the residual stresses can be divided into two components, namely, i) membrane residual stress σ_m, and ii) bending residual stress σ_b according to Equations 3.4 and 3.5 as follows:

$$\sigma_m = \frac{\sigma_o + \sigma_i}{2} \tag{3.4}$$

$$\sigma_b = \frac{\sigma_o - \sigma_i}{2} \tag{3.5}$$

Residual stresses of all the strips before and after wire cutting are listed in Table 3.12 a) to d), where a positive value indicates a tensile residual stress and a negative value indicates a compressive residual stress. The residual stresses are normalized with the measured yield strengths of the steel plates.

The measured residual stress distributions on the outer and the inner surfaces of each CHS are presented in Figure 3.17 while the calculated membrane and bending residual stresses are illustrated in Figure 3.18. It should be noted that

- For cold-formed CHS without welding, i.e. CFCHS-NW

  a) Tensile residual stresses are found on the outer surface of the cold-formed CHS while compressive residual stresses are found on the inner surface.

  b) Bending residual stresses with an average magnitude of 0.28 f_y are measured, except that very low values were obtained from the strips on the edge.

- For cold-formed CHS, i.e. CFCHS,

c) Residual stresses are shown to be very high in adjacent to the weld seams, where a maximum value is obtained on the outer surface of the CHS. This should be attributed to the differential cooling between the weld metal and the parent metal nearby after welding. This will cause quick contraction and formation of high locked-in tensile stresses adjacent to the weld seam. As the distance from the weld seam increases, the membrane residual stresses decrease significantly. Moreover, a magnitude of about 0.3 f_y of bending residual stress also indicates the effect of cold-forming to the welded CHS. The deformed shape of strips cut from the test specimens are illustrated in Figure 3.19.

3.3 NUMERICAL MODELING

In order to predict residual stresses due to both transverse cold bending and longitudinal welding, 2D and 3D numerical models have been established with a widely employed finite element package, namely, ABAQUS (2009). An overview of the numerical analysis is presented in Figure 3.20. A 2D model is adopted to simulate the transverse cold-bending process to predict residual stresses due to cold bending. A sequentially coupled thermomechanical analysis is then performed to simulate the longitudinal welding process. Heat transfer analysis is carried out to obtain the temperature field during welding and cooling. The predicted temperature history at specified points are compared with the measured temperature history in order to calibrate the heat transfer model.

Then, the time-dependent temperature field is incorporated into another 3D model with different elements for thermomechanical analysis. The predicted residual stresses due to welding on both the inner and the outer surfaces of the CHS are compared with the measured residual stresses as presented in previous sections. A simplified residual stress pattern is proposed based on both the experimental and the numerical results.

3.3.1 Transverse cold bending

Cold bending is simulated using a 2D finite element model. A steel plate with a length of the mid-surface perimeter of the CHS is bent numerically into a circle. Both the mesh and the boundary conditions of the 2D model are shown in Figure 3.21. Twelve layers of 2D plane strain elements CPE4R with reduced integration and hourglass control are employed. It should be noted that one end of the steel plate is fixed while the other end is free. Both geometrical and material nonlinearities are incorporated into the model. All the nodes at the free end of the steel plate is set to be coupled to the reference node. A unit rotation is applied to the reference node to simulate the bending process. Von Mises criterion is applied to capture yielding of the steel plates. Simplified true stress-strain curves obtained from standard tensile tests are adopted in the numerical model, as illustrated in Figure 3.22.

Through a number of parametric studies, it is found that for those CHS with radius to thickness ratios, r/t, ranging from 10 to 25, the normalized residual stresses are very close to one another, and they may be considered to be the same. The predicted residual stress distributions in S355 and S690 CHS after cold-forming are plotted in Figure 3.23. It is found that both longitudinal and transverse residual stresses in S690 CHS are smaller than those in S355 CHS having the same bending radii. The longitudinal surface residual stresses in S690 and S355 CHS are very close to one another. Figure 3.24 plots the proposed simplified residual stress patterns for S690 CHS with a r/t ratio at 12.5. It is shown that the residual stress patterns are similar to the simplified analytical solutions from Moen *et al*. (2008), although the predicted longitudinal residual stress is found to be $0.2f_y$. It should be noted that $0.05f_y$ is given in an analytical solution which is calculated according to an elastic-perfect plastic stress-strain relationship.

3.3.2 Longitudinal welding

Sequentially-coupled thermomechanical analysis

A sequentially-coupled thermomechanical analysis is conducted to simulate longitudinal welding of CFCHS. A two-stage analysis including (i) heat transfer analysis, and (ii) stress analysis are carried out sequentially in this study. Three dimensional heat transfer element DC3D8 is adopted in the heat transfer analysis while stress element C3D8R is employed for the stress analysis. An overall view of the numerical model of Section C1 is shown in Figure 3.25. Four layers of solid elements are adopted throughout the thickness of the steel plate. Local mesh refinement is adopted in the model for computational efficiency.

Relevant temperature-dependent material properties including thermal conductivity, specific heat and thermal expansion coefficient given by EN 1993-1-2(CEN, 2005) are adopted in the present study, as shown in Figure 3.26. Mechanical properties of S690 steel plates at ambient temperature are provided in Figure 3.22. A double-ellipsoidal model is used to simulate a moving welding heat source. The welding parameters discussed in Section 3.2.3 are also employed in the model. Longitudinal residual stresses obtained from the 2D model in Section 3.3.1 are fully incorporated into the model as the initial stresses at various integration points of the solid elements. These initial residual stresses within the plate thickness are shown in Figure 3.27.

Mesh convergence study

A mesh convergence study is carried out to determine the optimum mesh sizes of the proposed numerical model. Three different mesh schemes are adopted for comparsion. The programme for the mesh convergence study is shown in Table 3.13. The global mesh sizes vary from 5 mm to 10 mm, and the local mesh sizes at the weld seam vary from 1mm to 3mm. The detailed finite element meshes of these three models are presented in Figure 3.28.

Figure 3.29 illustrates a comparison of the residual stresses on the outer surfaces at the mid-section of these three models. A convergence trend can be found among these three models from a coarser mesh to a finer mesh. The difference in the maximum surface residual stress on the outer surfaces between “fine” and “very fine” meshes is only 0.4%, which is considered to be satisfactory. Therefore, a global mesh size of 5 mm and a local mesh size of 2 mm the weld seam are adopted for subsequent numerical analyses in order to achieve both numerical accuracy and computational efficiency.

3.3.3 Finite element results

Temperature history

Figure 3.30 illustrates the transient temperature distributions of each weld run during welding of Section C1. The regions in grey colour represents the filler metal for welding, where the temperatures are higher than 1500 °C. In Figures 3.31 and 3.32, the measured surface temperature history at the locations of thermocouples are compared with those predicted by numerical models. It is found that the predicted temperature history agree very well with the measured data.

Residual stress distributions

Both the measured and the predicted surface residual stresses at the mid-sections of Section C1 and C2 are plotted in Figures 3.33 and 3.34, where θ represents the angle from the weld seam, as shown in Figure 3.35. In general, the predicted residual stresses are found to agree well with the measured data. However, the predicted residual stresses at the weld seam have a large variation from the measured values. The measured residual stresses on both the inner and the outer surfaces at the weld seam are significantly smaller than the predicted values. This is because the weld metal at this location has already been yielded after welding. Therefore, the sectioning method is considered to be not accurate enough to measure the residual stresses at this location as this method is only applicable to measure elastic strains.

3.3.4 Proposed residual stress distributions

Proposed residual stress pattern

Based on the experimental and numerical results, a simplified multilinear model is proposed to describe the residual stress distributions in S690 CFCHS. The mathematical equations are presented as follows

For outer surfaces $$\frac{\sigma_r}{f_y} = \begin{cases} -10.8\bar{\theta}+1 & 0 \le \bar{\theta} \le 0.083 \\ 0.53\bar{\theta}+0.055 & 0.083 < \bar{\theta} \le 0.55 \\ -0.11\bar{\theta}+0.41 & 0.55 < \bar{\theta} \le 1 \end{cases} \quad (3.6)$$

For inner surfaces $$\frac{\sigma_r}{f_y} = \begin{cases} -18.1\bar{\theta}+1 & 0 \le \bar{\theta} \le 0.083 \\ 0.53\bar{\theta}-0.54 & 0.083 < \bar{\theta} \le 0.55 \\ -0.11\bar{\theta}-0.19 & 0.55 < \bar{\theta} \le 1 \end{cases} \quad (3.7)$$

where σ_r denotes the residual stresses, f_y denotes the yield strength of the steel material, and $\bar{\theta} = \theta/\pi$. In Figures 3.36 and 3.37, the proposed residual stress model on both the outer and the inner surfaces are compared with the measured and the predicted residual stresses of Sections C1 and C2. The proposed model is demonstrated to be able to predict the measured residual stress distributions of S690 CFCHS covered in this study.

In addition to the above equations, an averaged through-thickness residual stress model is also provided. It should be noted that the bending residual stresses are not considered, and only the membrane residual stresses are shown in this model. The equations are presented as follows:

Average residual stresses $$\frac{\sigma_r}{f_y} = \begin{cases} -14.40\bar{\theta}+1 & 0 \le \bar{\theta} \le 0.083 \\ 0.53\bar{\theta}-0.24 & 0.083 < \bar{\theta} \le 0.55 \\ -0.11\bar{\theta}+0.11 & 0.55 < \bar{\theta} \le 1 \end{cases} \quad (3.8)$$

Check of self-equilibrium of residual stresses

It is acknowledged that residual stresses are self-equilibrant stress systems within a cross section. Therefore, self-equilibrium is examined for the proposed average residual stress model to ensure there is no out-of-balance force.

Integration of residual stresses within a CFCHS is carried out as follows:

$$\int_{0}^{0.083}\left(-14.40\overline{\theta}+1\right)\mathrm{d}\overline{\theta}+\int_{0.083}^{0.55}\left(0.53\overline{\theta}-0.24\right)\mathrm{d}\overline{\theta}+\int_{0.55}^{1}\left(-0.11\mathrm{x}+0.11\right)\mathrm{d}\overline{\theta}=0.009\approx 0 \qquad (3.9)$$

Consequently, the proposed residual stress model is proved to be in self-equilibrium.

Comparison with existing residual stress models

A residual stress model for CFCHS for normal strength steel was first proposed by Wagner *et al*. (1976) while Chen and Ross (1977) suggested a bilinear model based on experimental results obtained from the sectioning method. Yang *et al*. (2017) carried out residual stress measurements on the high strength S690 steel CFCHS, and a modified bilinear model was proposed. They pointed out that the area of tensile residual stresses, which was attributed to the effect of welding, was smaller in the high strength steel CHS than that in the normal strength steel CHS. Moreover, the maximum compressive residual stresses in the high strength steel CHS was smaller than that in the normal strength steel CHS, which is only $0.2f_y$.

A comparison between the proposed residual stress model and the existing models is presented in Figure 3.38. It is shown that the general distribution pattern of the proposed model is similar to the model proposed by Yang *et al*. (2017). The maximum tensile residual stress is $0.2f_y$, which is equal to that of the Yang's model, but significantly smaller than $0.3f_y$ and $0.35f_y$, as proposed for the normal strength steel. The area under tensile residual stresses is even smaller than that of the Yang's model. Hence, it is demonstrated that the effect of welding is less significant.

3.4 CONCLUSIONS

In order to examine the effects of various fabrication processes on residual stresses of the S690 cold-formed circular hollow sections (CFCHS), a systematic experimental and numerical investigation into thermal and mechanical responses in S690 CFCHS with different cross-sectional dimensions was carried out in this study.

The following conclusions are drawn:

a) Surface temperature history in S690 CFCHS were measured with thermocouples during welding and cooling, and they have been employed to calibrate successfully against advanced numerical models for heat transfer analyses in sequentially thermomechanical coupled analyses.

b) Residual strains on both the inner and the outer surfaces of S690 CFCHS were measured with strain gauges, and corresponding residual stresses were obtained with sectioning method. These residual stresses were successfully employed to calibrate the proposed 2D and 3D numerical models through comparison of measured and predicted surface residual stresses.

c) Based on both experimental and numerical results, residual stress distributions on both the inner and the outer surfaces of high strength S690 CFCHS were proposed. A simplified average residual stress model was also proposed after comparison with existing residual stress models available in literature. The proposed residual stress model is readily employed for numerical investigation into structural behaviour of various structural members made of S690 CFCHS.

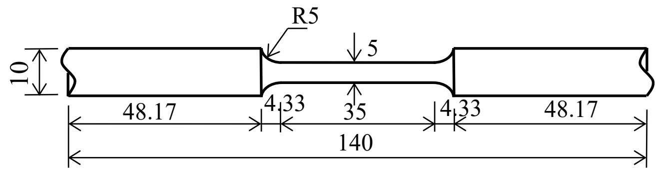

(a) Standard coupon for 10 mm thick steel plates

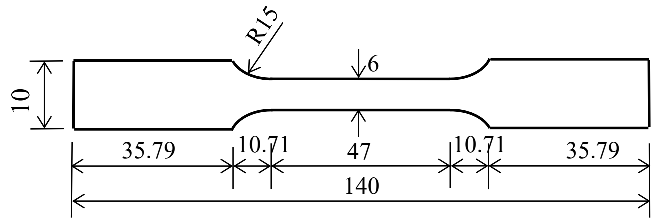

(b) Standard coupon for 6 mm thick steel plates

Figure 3.1 Geometric properties of standard tensile coupons

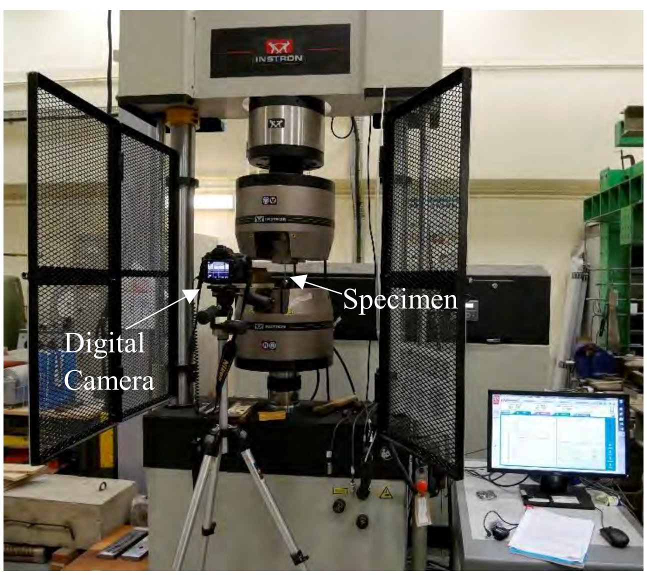

a) Test setup

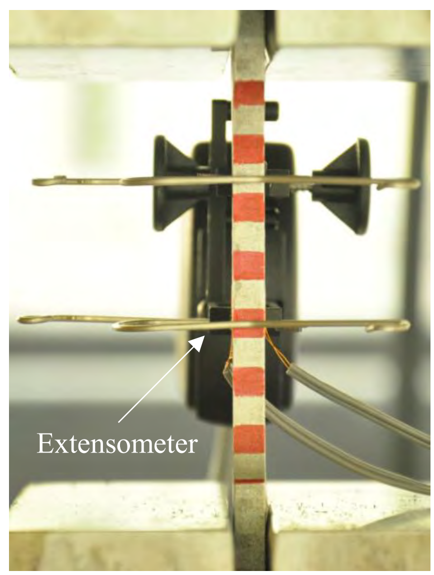

b) A rectangular coupon

Figure 3.2 Test setup for standard tensile tests

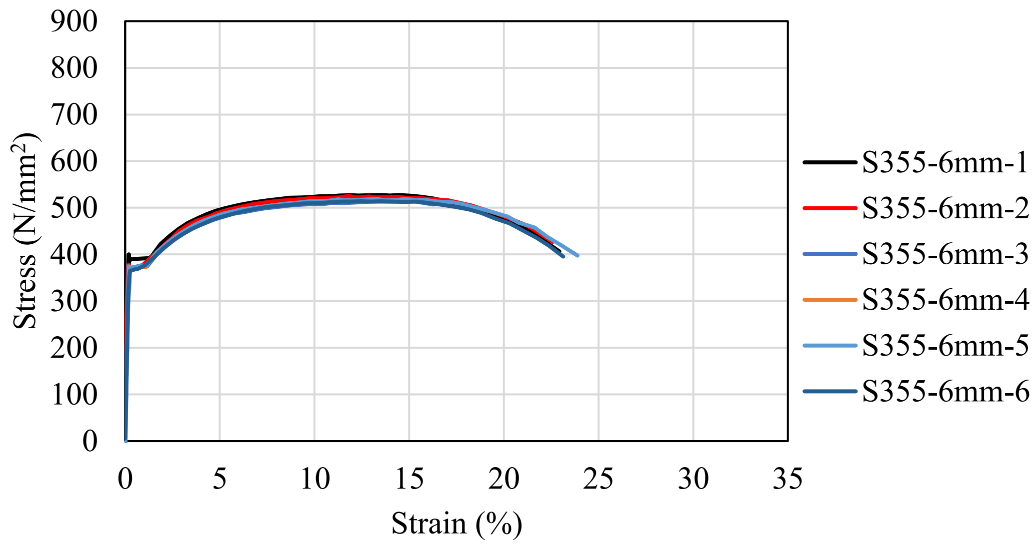

Figure 3.3 a) Stress-strain curves of coupons from 6 mm thick S355 steel plate

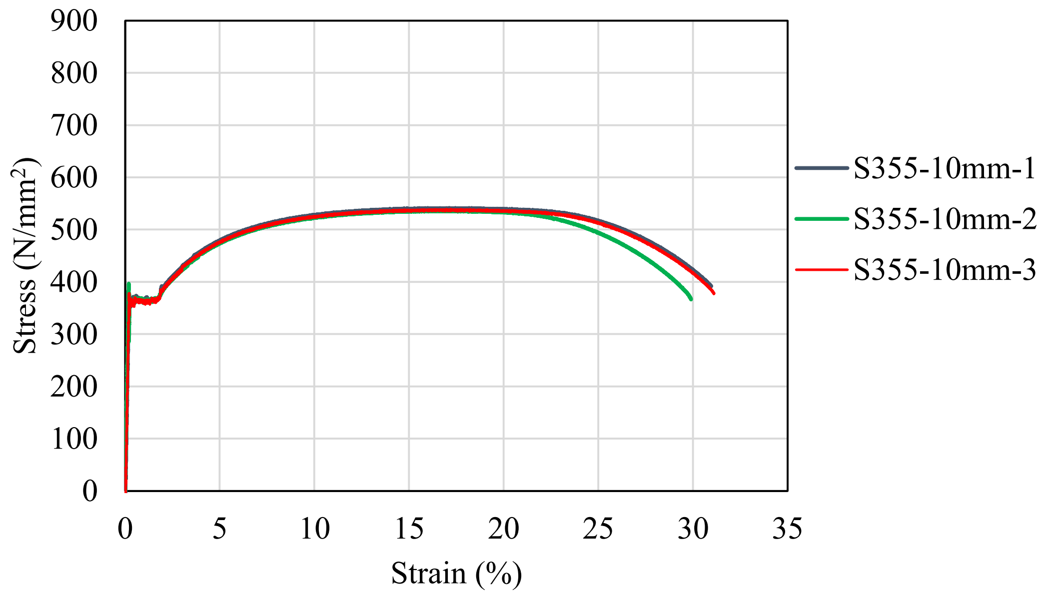

Figure 3.3 b) Stress-strain curves of coupons from 10 mm thick S355 steel plate

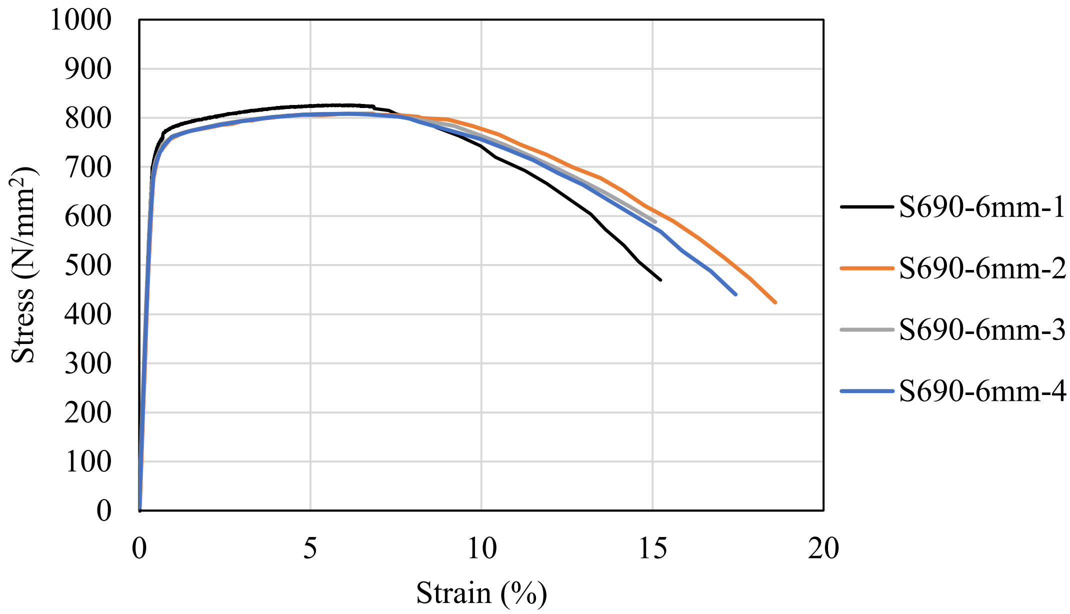

Figure 3.3 c) Stress-strain curves of coupons from 6 mm thick S690 steel plate

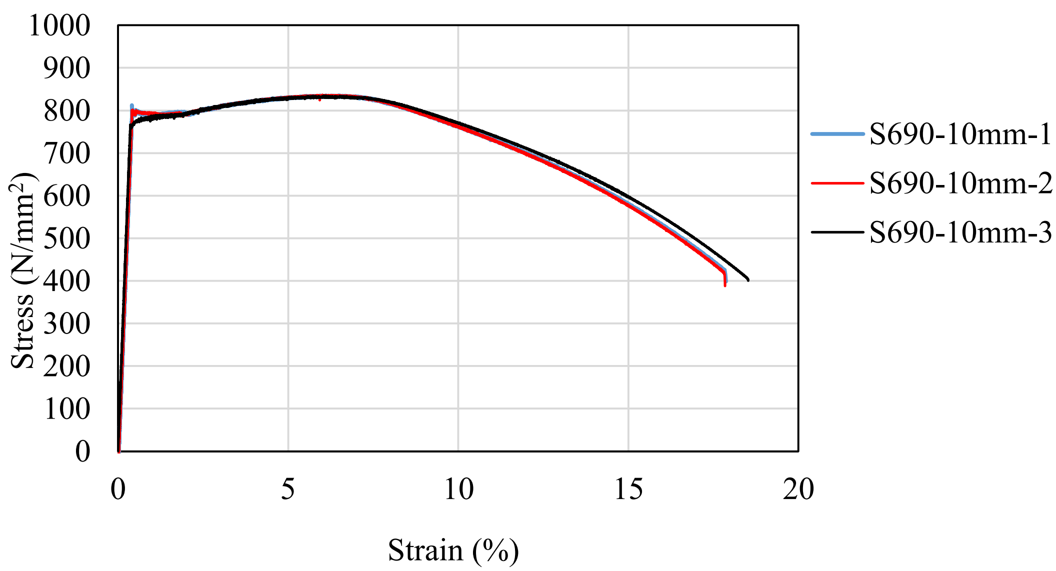

Figure 3.3 d) Stress-strain curves of coupons from 10 mm thick S690 steel plate

a) A press-brake machine

b) A steel plate with pre-bent edge on one side

c) Three-roller bending machine

d) CFCHS after welding

Figure 3.4 Fabrication process of welded CFCHS

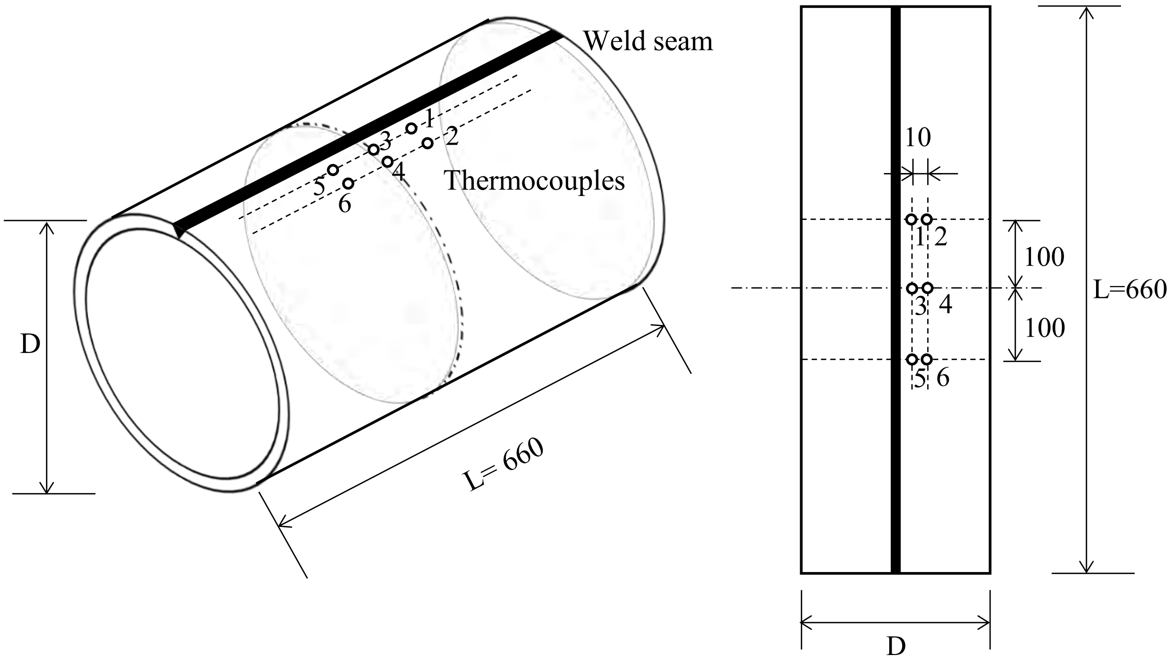

Figure 3.5 Arrangement for measurement points

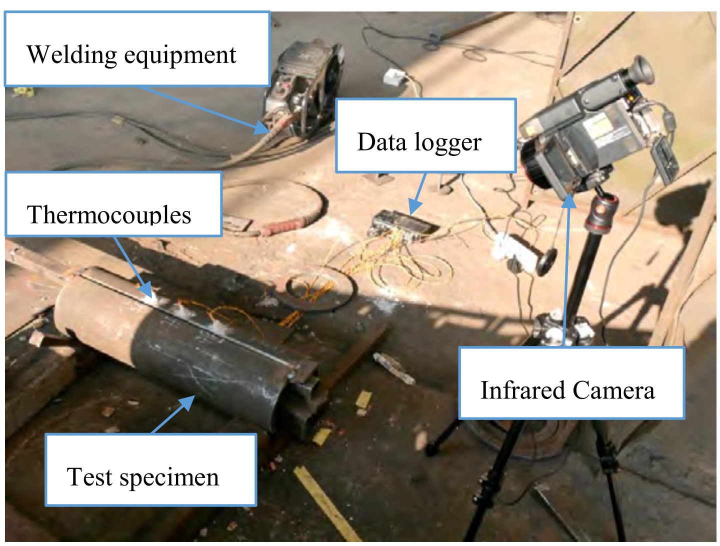

Figure 3.6 Test setup

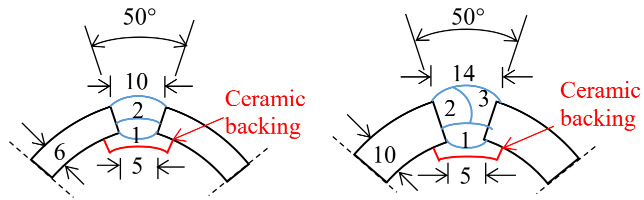

Weld groove for Sections C1 and C2

Weld groove for Sections C3 and C4

Figure 3.7 Detail of weld grooves

a) Gas metal arc welding (GMAW)

b) Section C2 after 1st weld pass

c) Section C2 after 2nd weld pass

Figure 3.8 Welding procedures

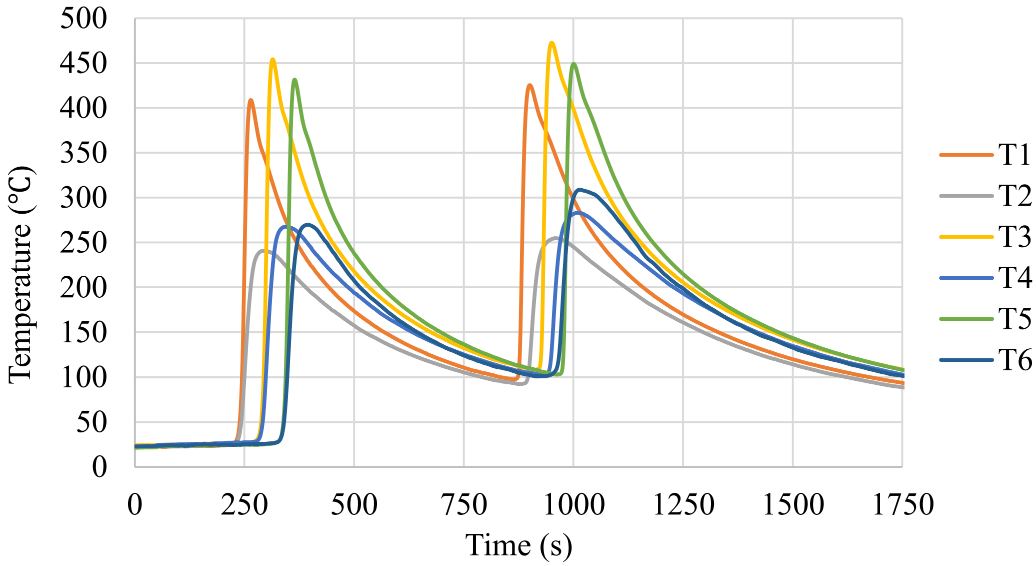

Figure 3.9 Temperature history of Section C1

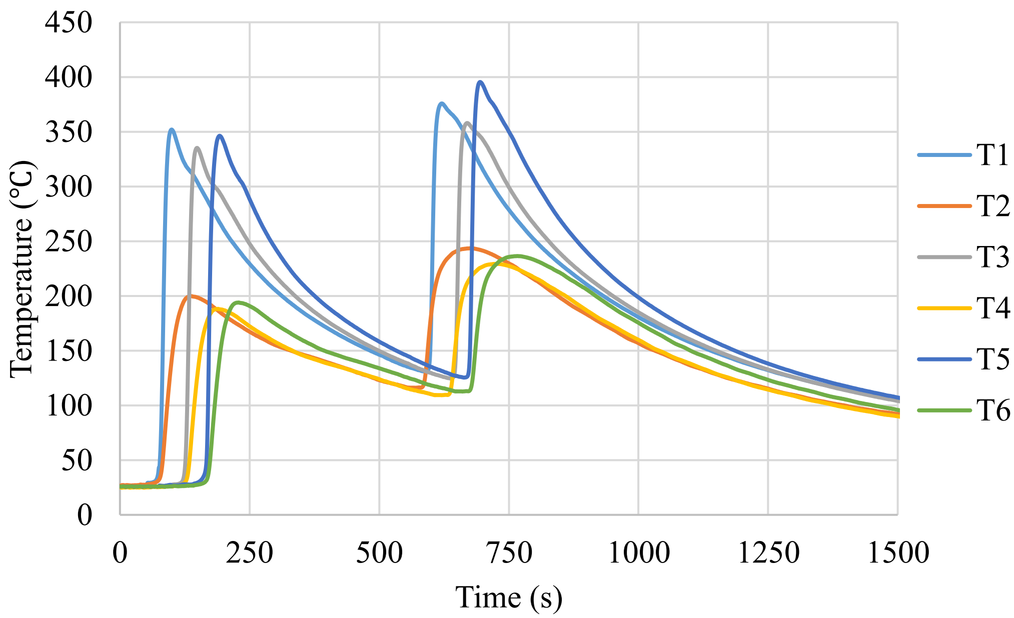

Figure 3.10 Temperature history of Section C2

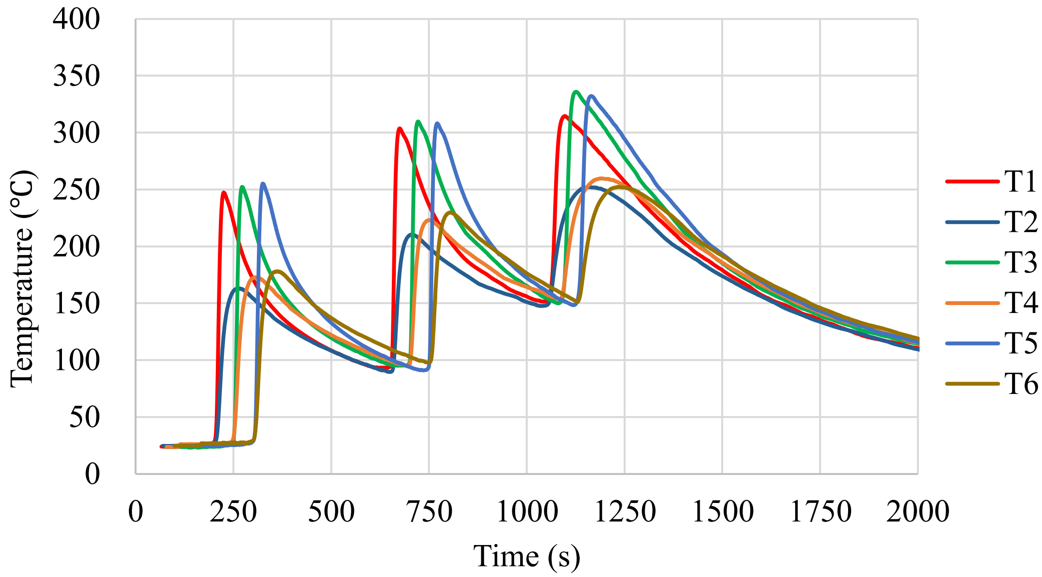

Figure 3.11 Temperature history of Section C3

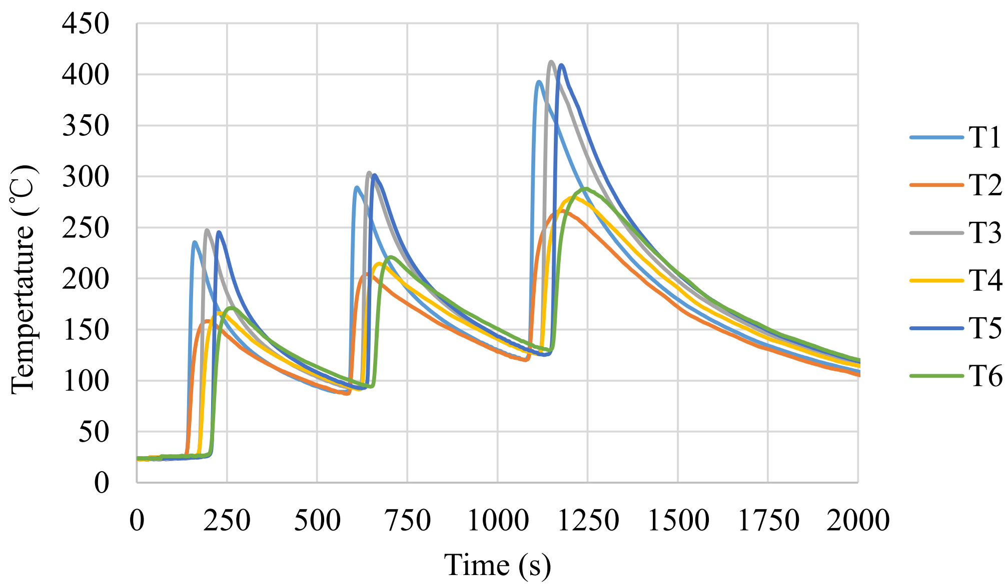

Figure 3.12 Temperature history of Section C4

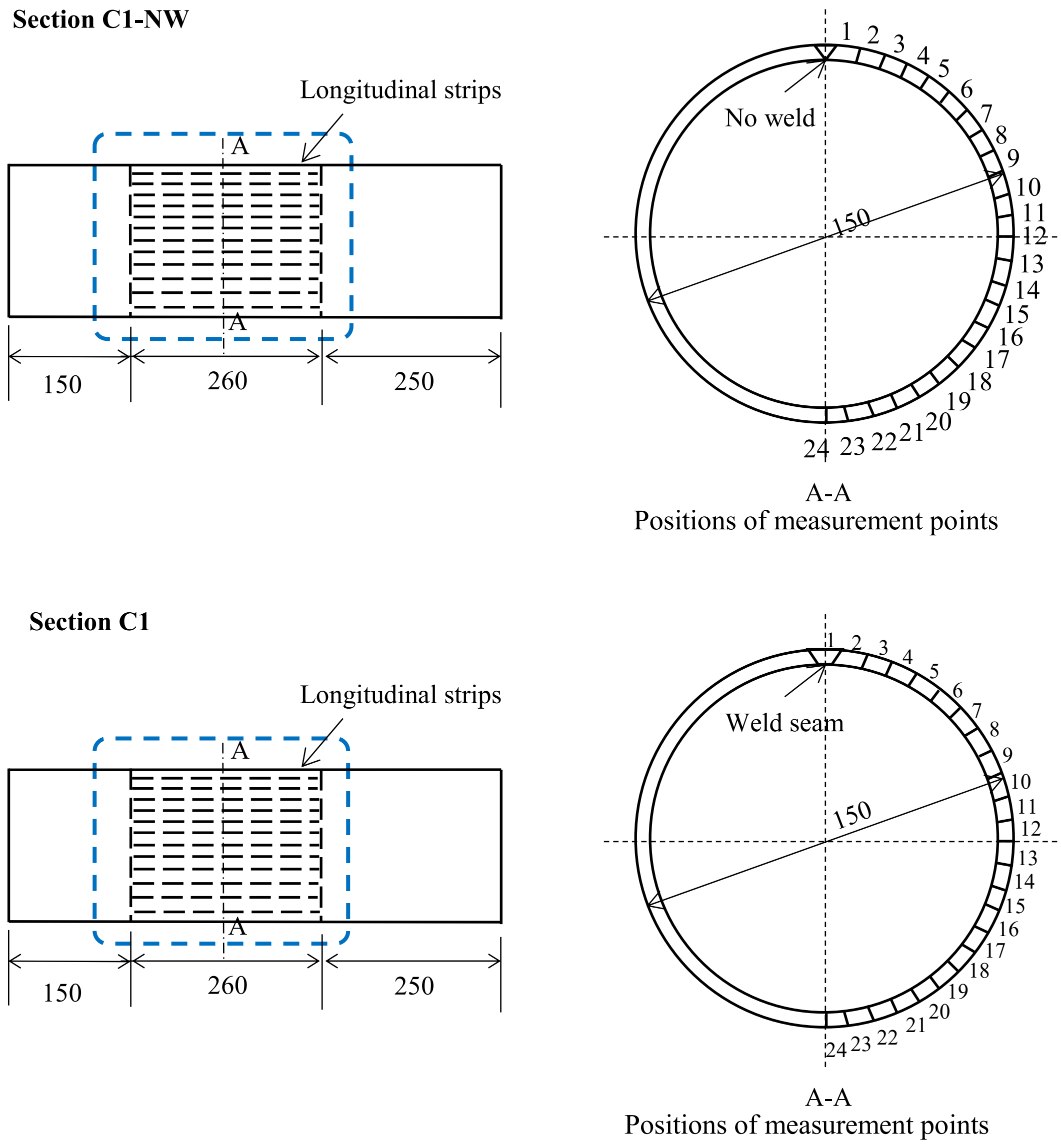

Figure 3.13 Arrangement of measurement points of Sections C1-NW and C1

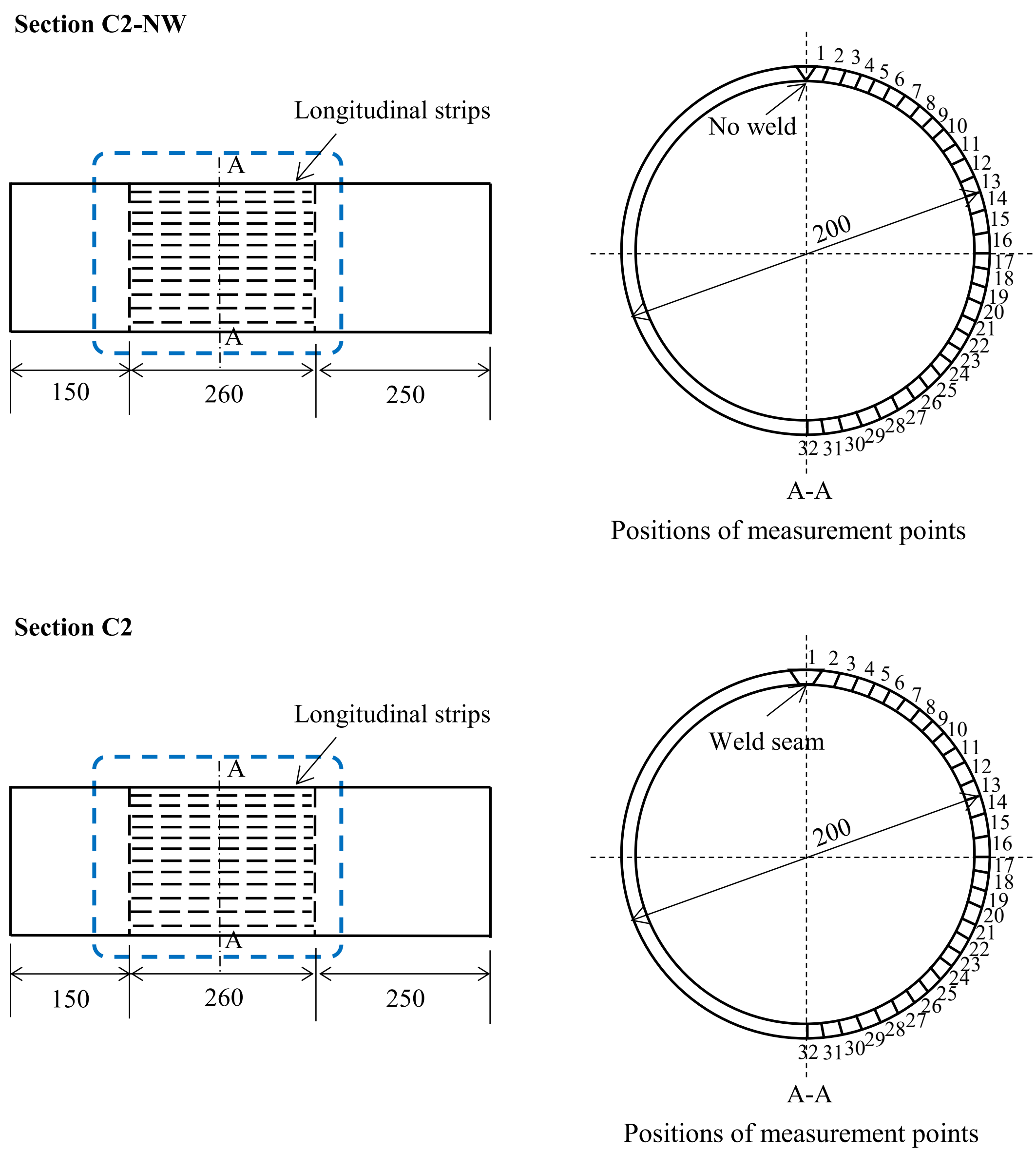

Figure 3.14 Arrangement of measurement points of Sections C2-NW and C2

Section C1-NW | Section C1 | Section C2-NW | Section C2

Figure 3.15 Test specimens with strain gauges and waterproof glue

Figure 3.16 Wire cutting of Section C1

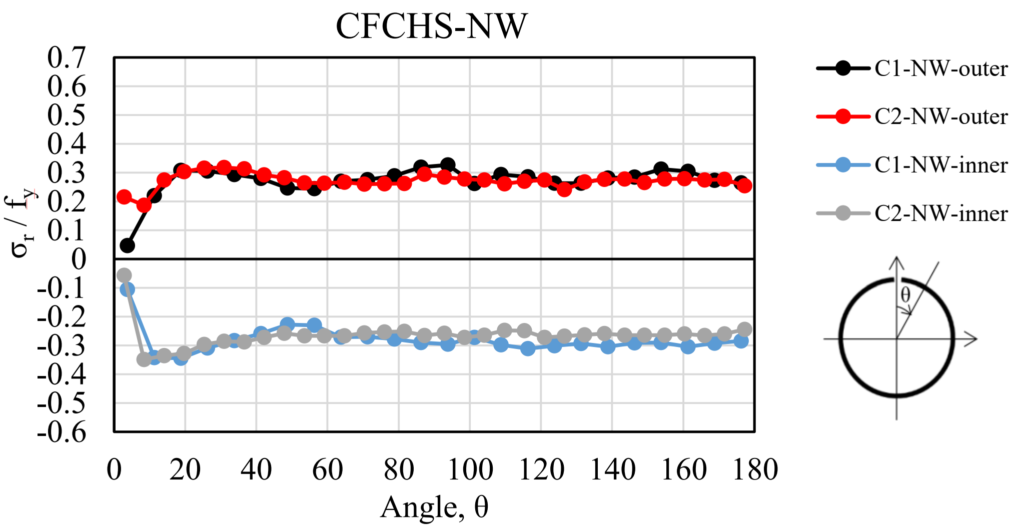

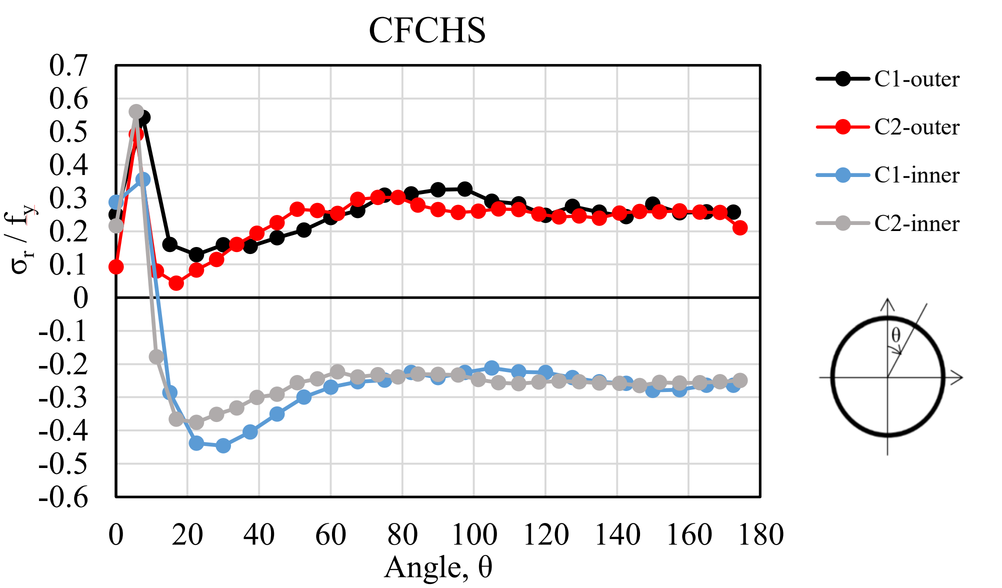

Figure 3.17 Measured surface residual stresses of CFCHS

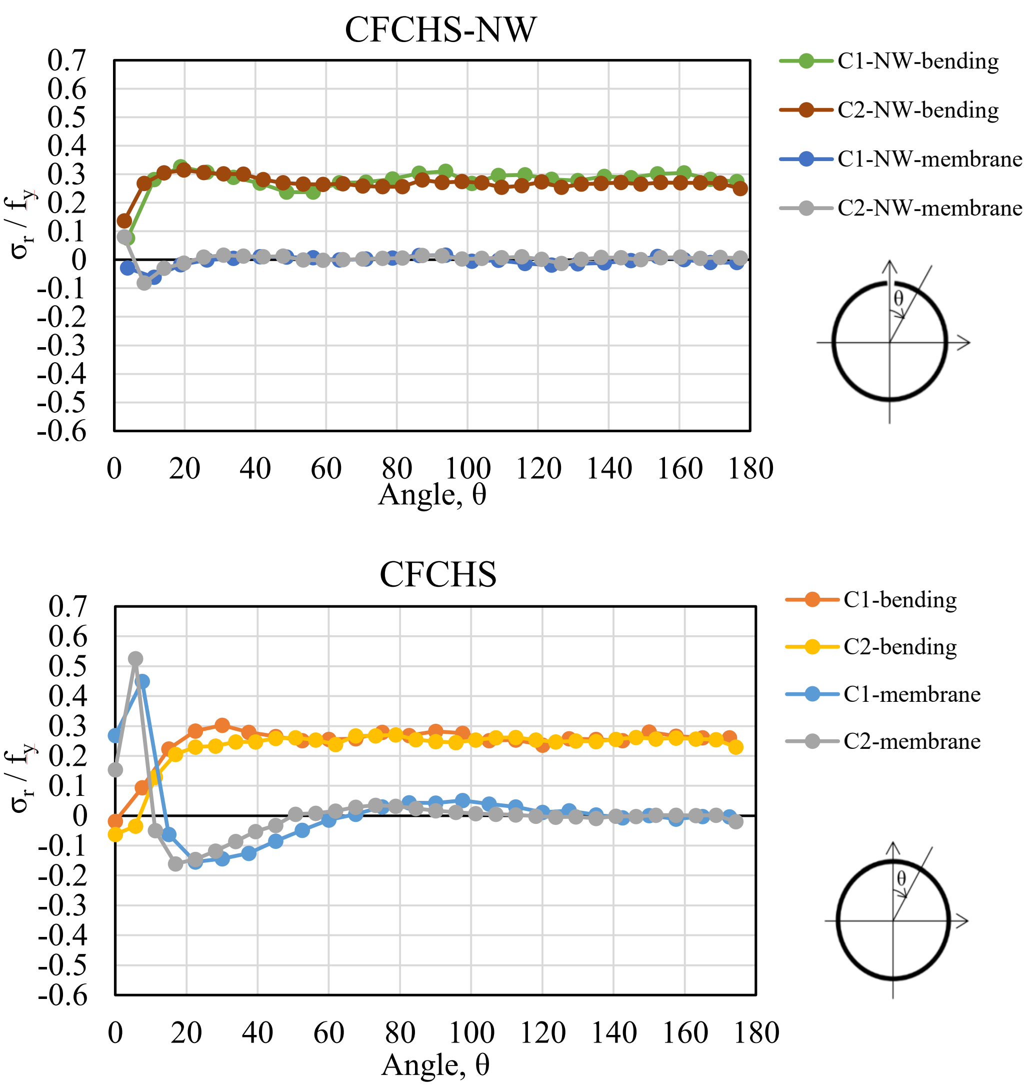

Figure 3.18 Membrane and bending residual stresses of CFCHS

a) Deformed strips cut from Section C1-NW

b) Deformed strips cut from Section C1

c) Deformed strips cut from Section C2-NW

d) Deformed strips cut from Section C2

Figure 3.19 Deformed strips cut from CFCHS

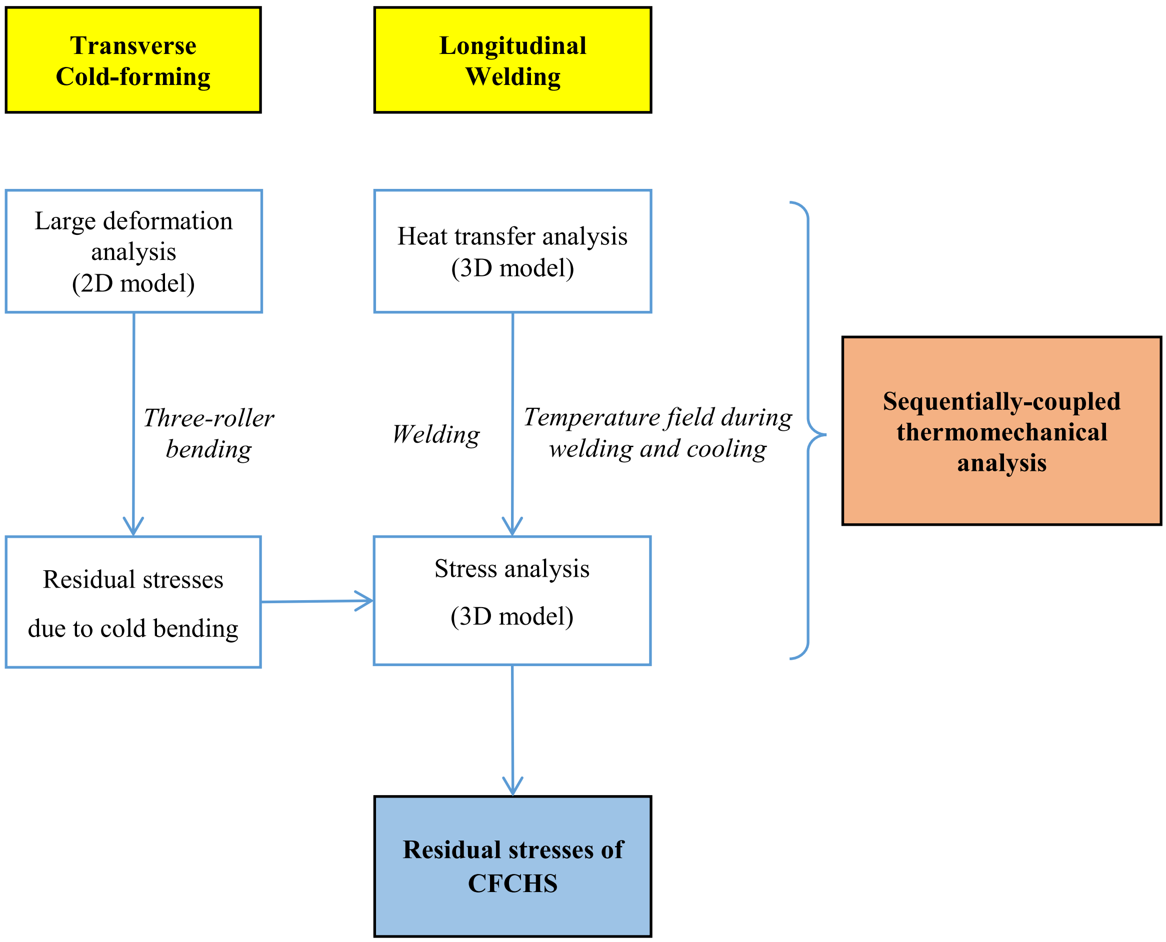

Figure 3.20 Flowchart of numerical prediction for residual stresses

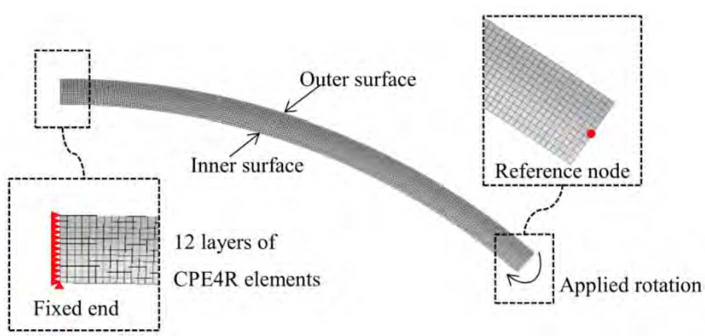

Figure 3.21 2D model of transverse bending

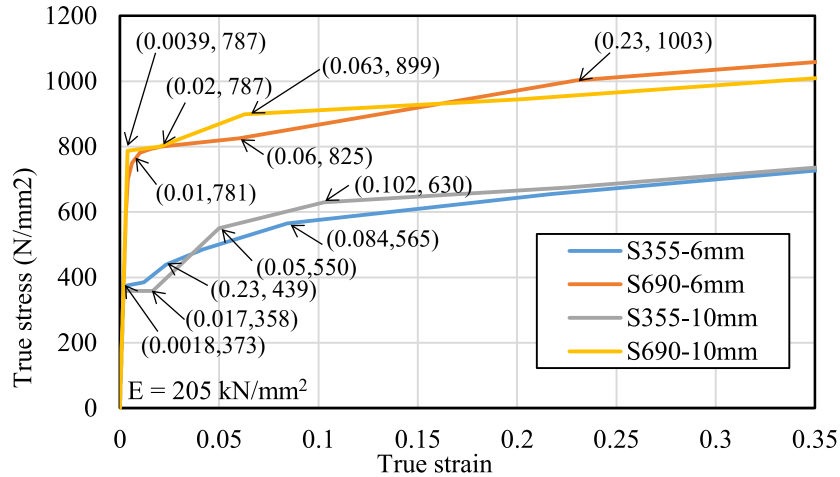

Figure 3.22 True stress-strain curves for finite element modeling

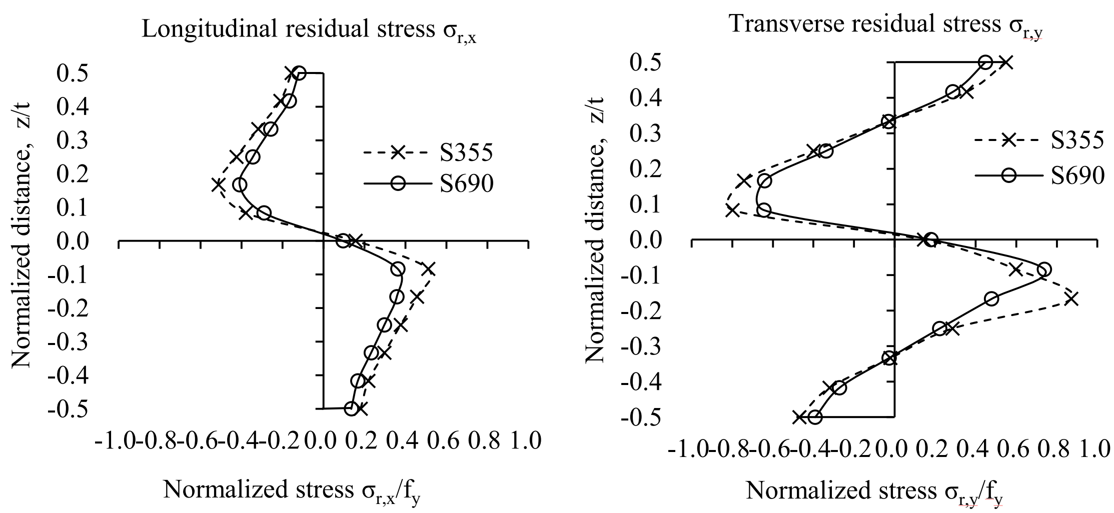

Figure 3.23 Predicted residual stresses in S355 and S690 CFCHS-NW after cold-bending and elastic spring back (r/t = 12.5)

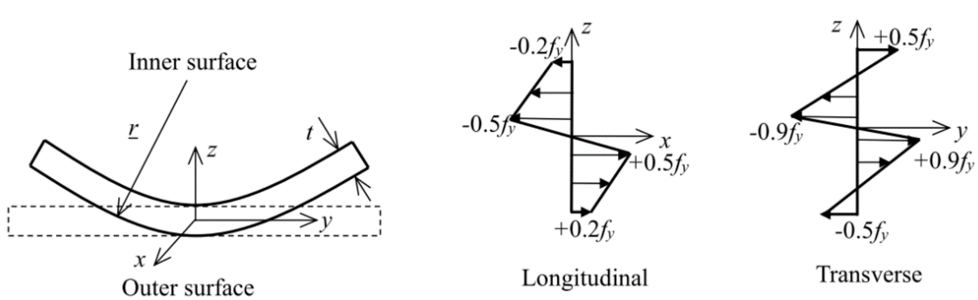

Figure 3.24 Simplified residual stresses in S690 CFCHS-NW after cold-bending and elastic spring back

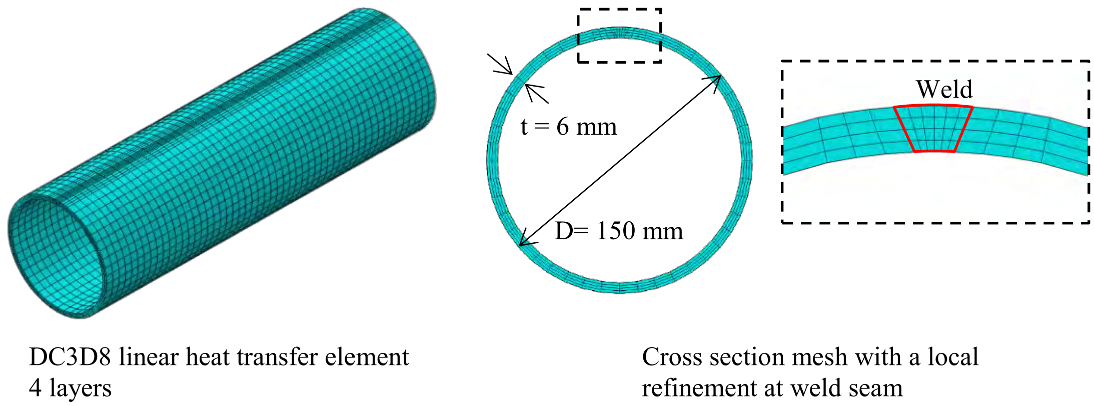

Figure 3.25 3D numerical model of Section C1 for welding

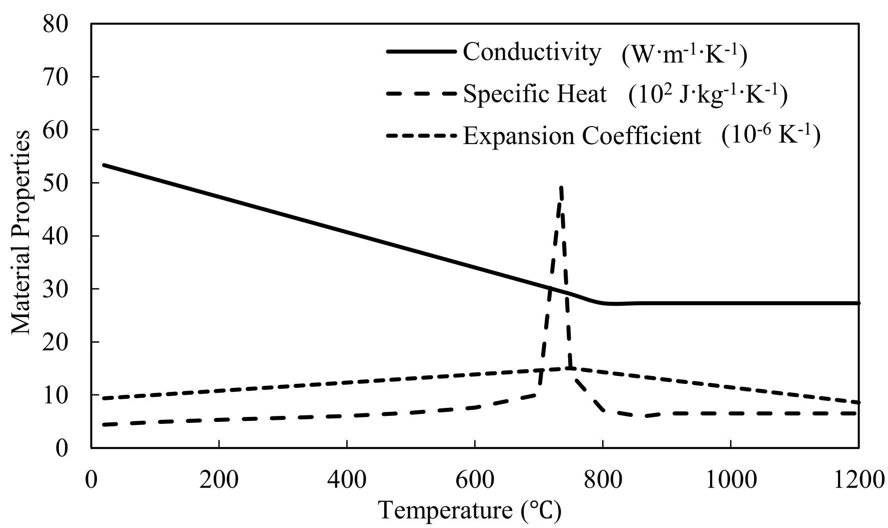

Figure 3.26 Thermal properties for S690 CFCHS at elevated temperatures

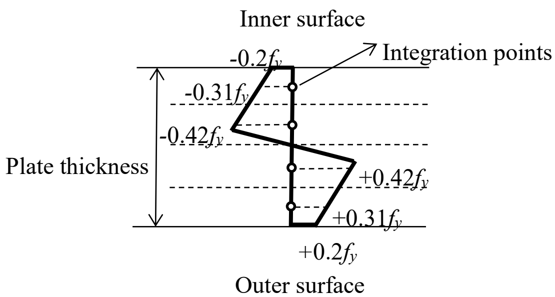

Figure 3.27 Initial longitudinal residual stress pattern in 3D model for S690 CFCHS

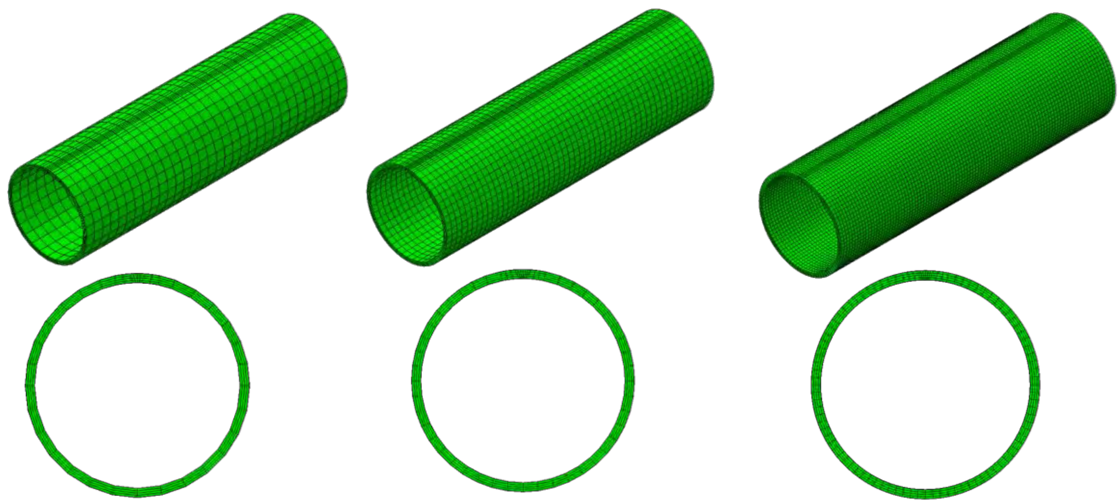

a) Coarse mesh	b) Fine mesh	c) Very fine mesh
Global mesh size: 15mm	Global mesh size: 10mm	Global mesh size: 5mm
Local mesh size: 3mm	Local mesh size: 2mm	Local mesh size: 1mm

Figure 3.28 Mesh convergence study

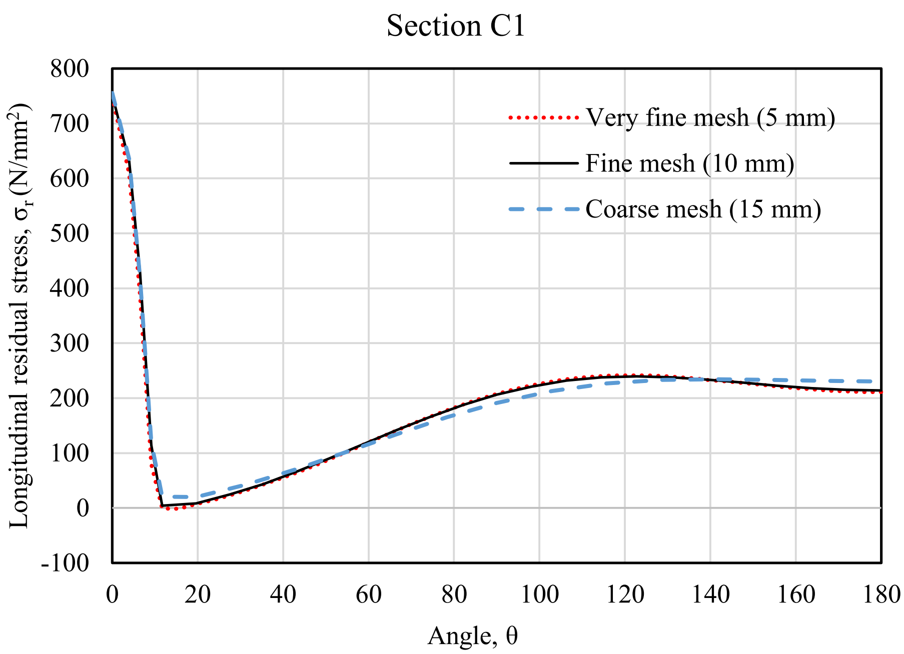

Figure 3.29 Comparison of residual stresses on the outer surface of Section C1

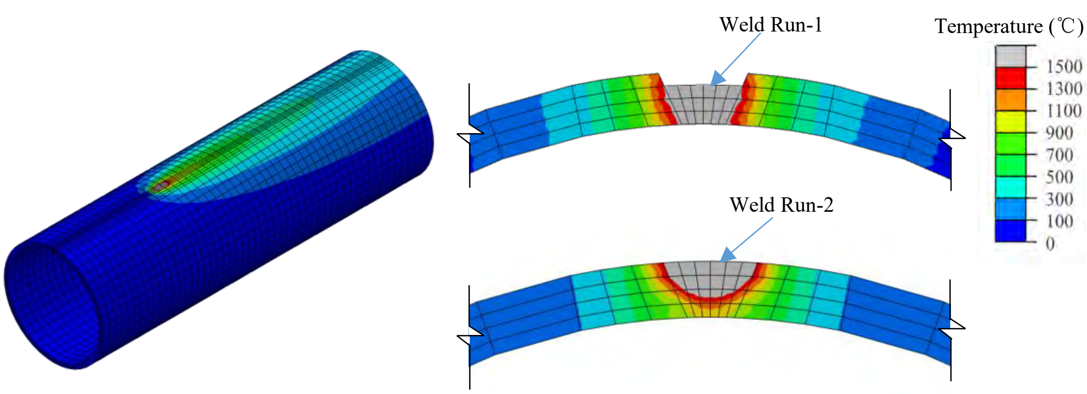

Figure 3.30 Transient temperature distributions in S690 CFCHS – Section C1

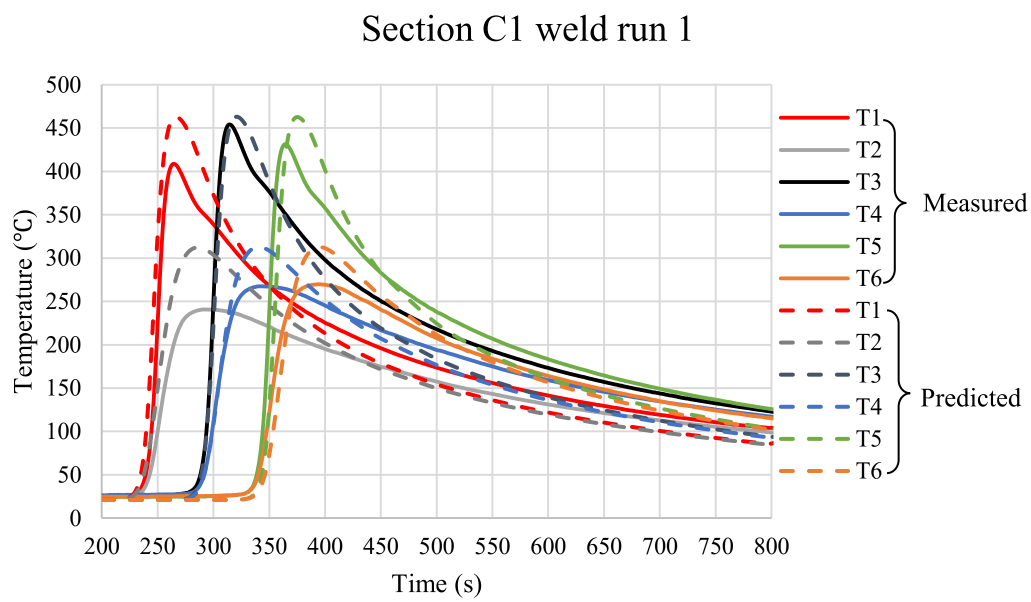

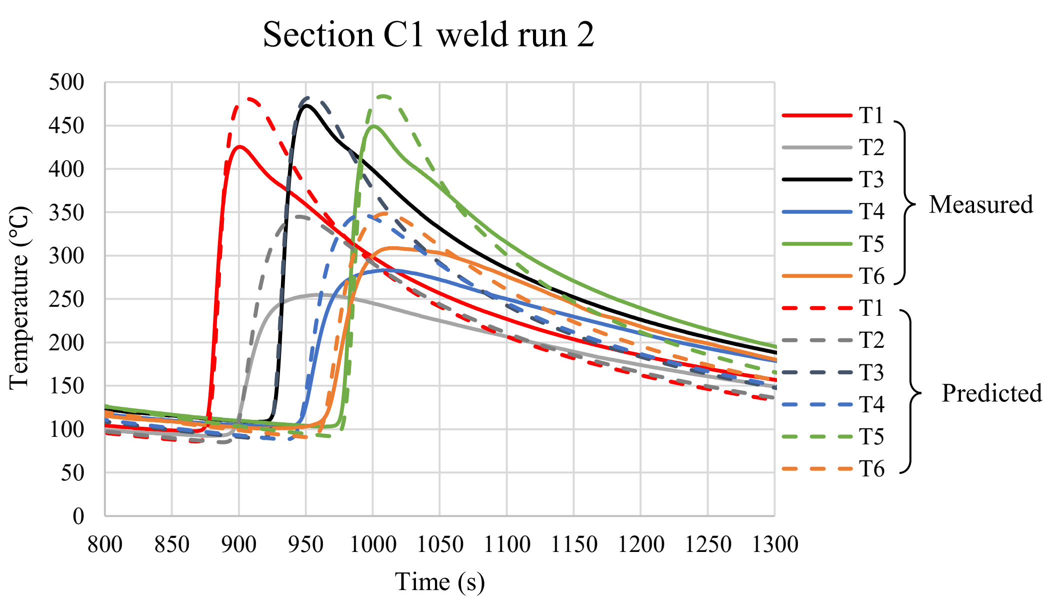

Figure 3.31 Comparison of measured and predicted temperature history in S690 CFCHS – Section C1

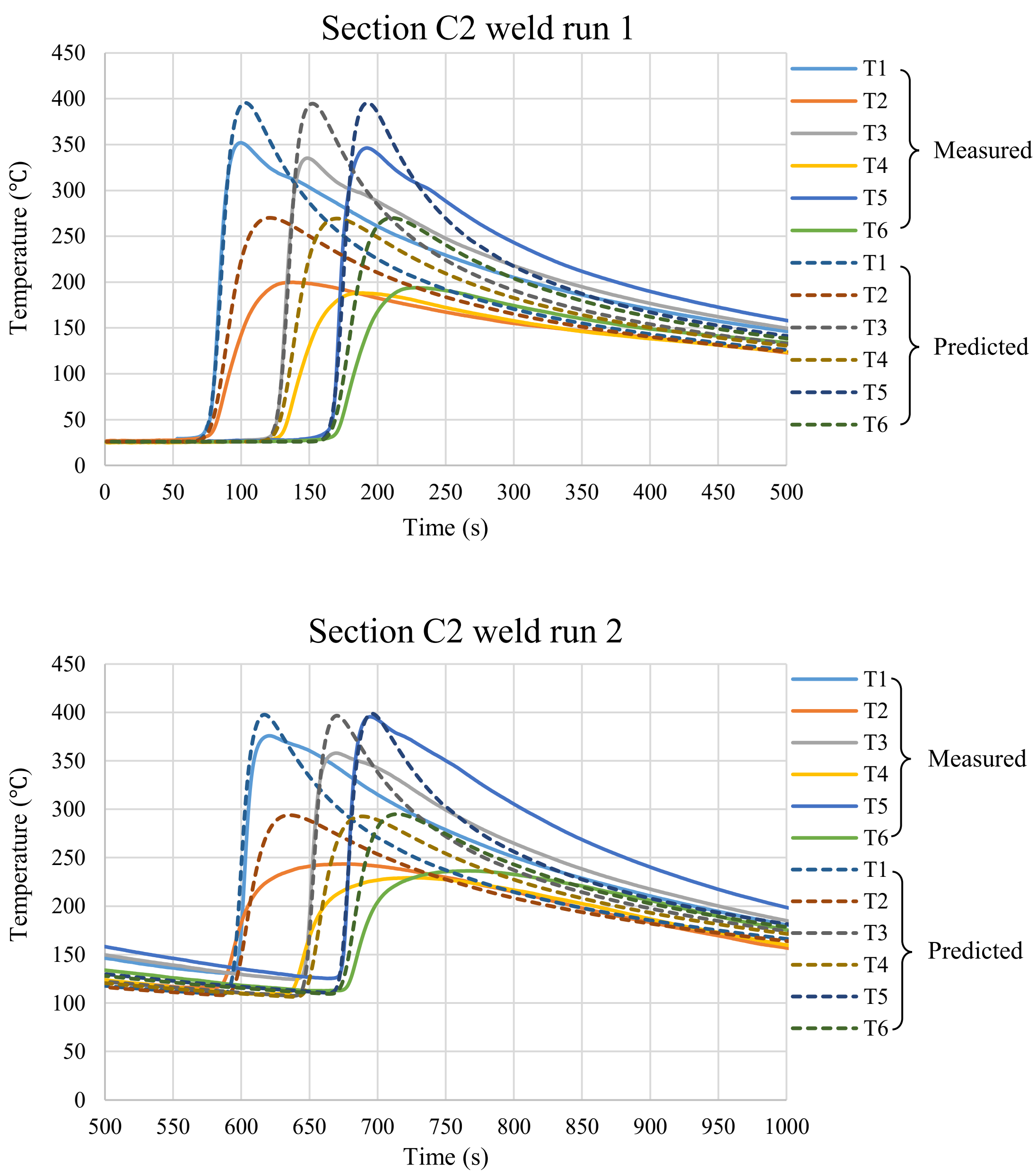

Figure 3.32 Comparison of measured and predicted temperature history in S690 CFCHS – Section C2

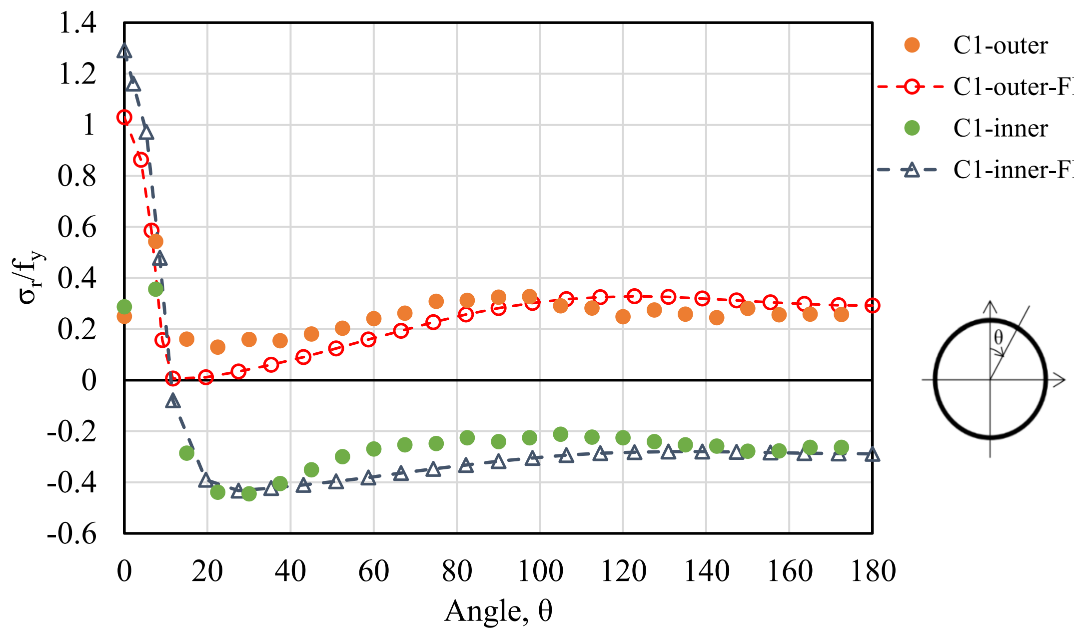

Figure 3.33 Comparison of measured and predicted surface residual stresses in S690 CFCHS – Section C1

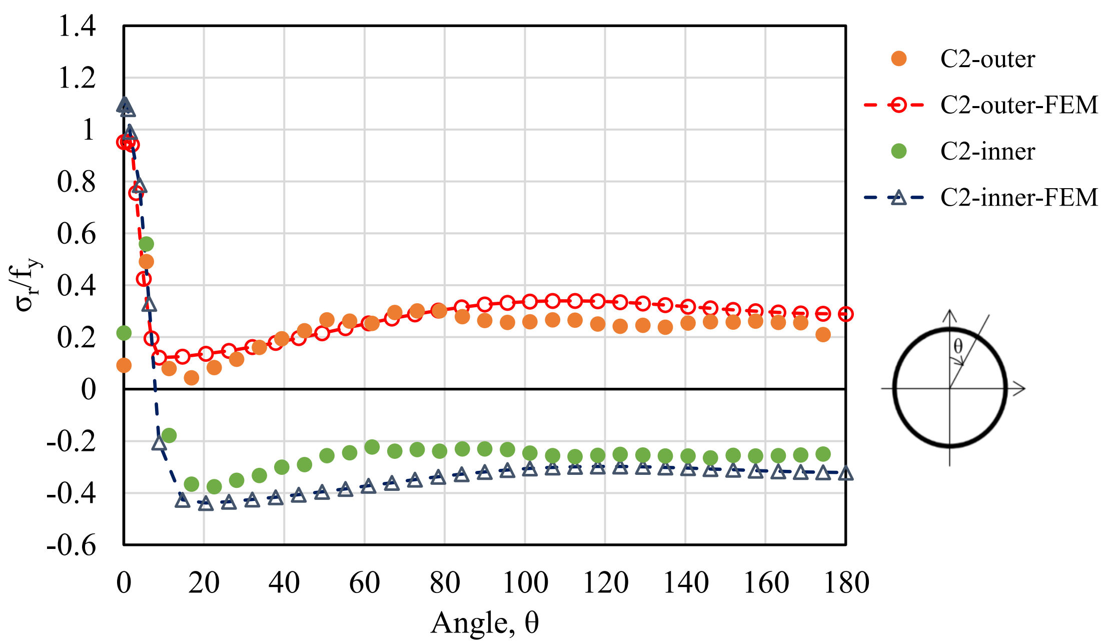

Figure 3.34 Comparison of measured and predicted surface residual stresses in S690 CFCHS – Section C2

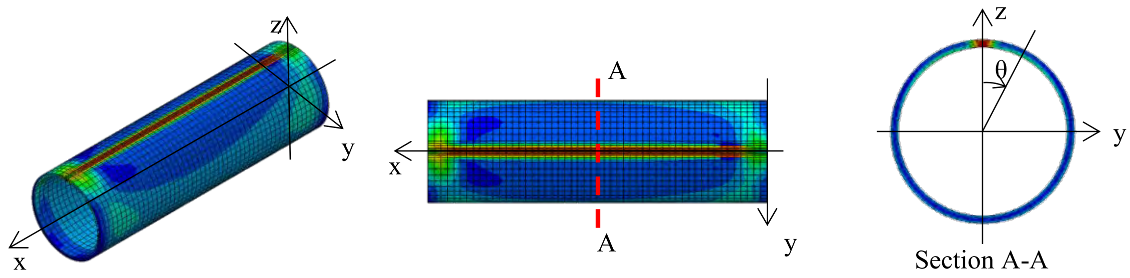

Figure 3.35 Residual stresses at mid-section of S690 CFCHS – Section C1

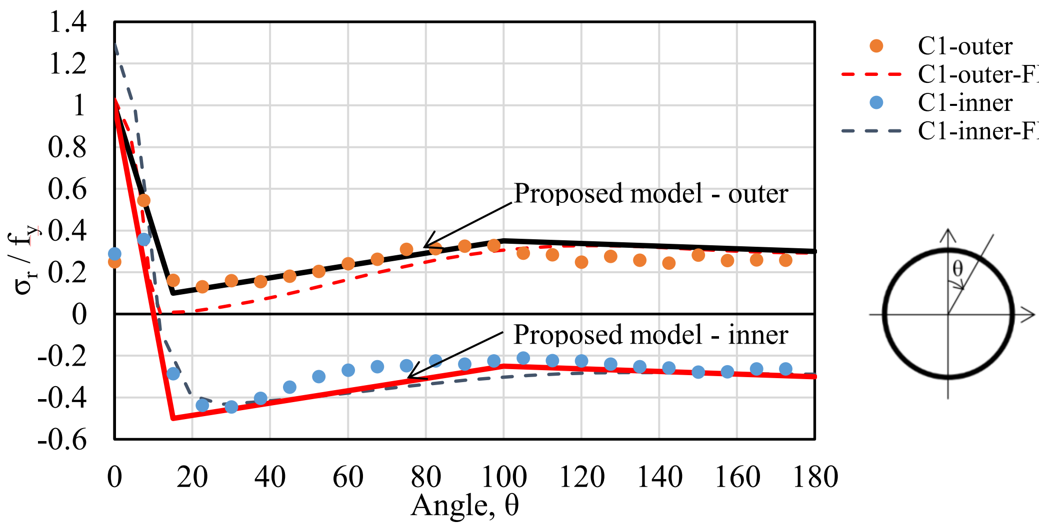

Figure 3.36 Comparison of surface residual stresses of S690 CFCHS – Section C1

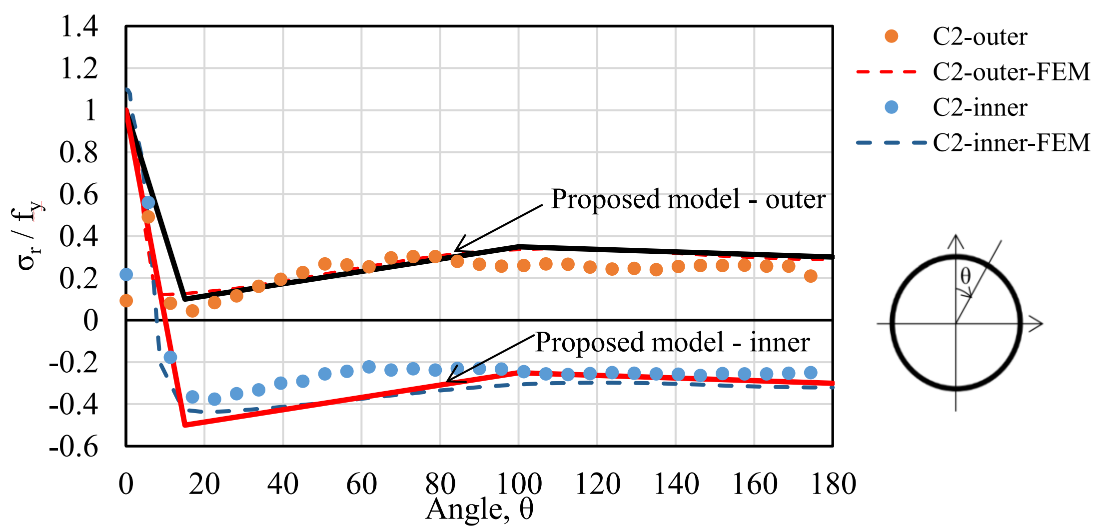

Figure 3.37 Comparison of surface residual stresses of S690 CFCHS – Section C2

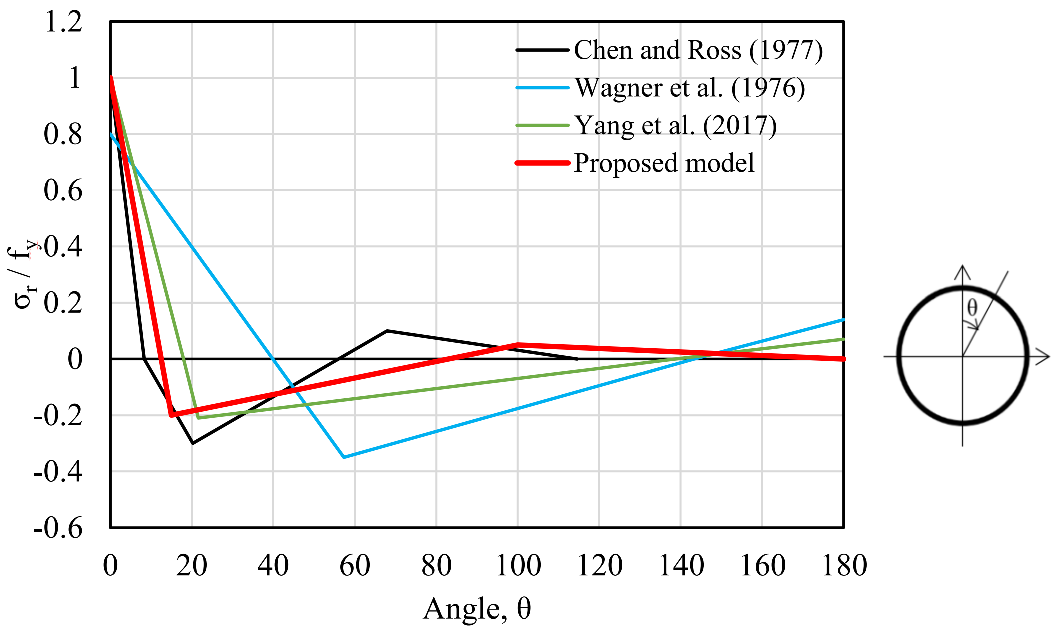

Figure 3.38 Comparison of existing and proposed residual stress patterns

Table 3.1 Test programme of standard tensile tests for S355 and S690 steel materials

Steel grade	Plate thickness (mm)	Cross-sectional shape	Cross-sectional dimension (mm)	Gauge length (mm)	No. of tests
S355	6	Rectangular	6×6	33	6
S355	10	Circular	Φ=6	30	3
S690	6	Rectangular	6×6	33	4
S690	10	Circular	Φ=6	30	3

Table 3.2 Summary of measured material properties

Steel grade	Plate thickness (mm)	No.	Young's modulus E (kN/mm^2)	Yield strength f_y (N/mm^2)	Tensile strength f_u (N/mm^2)	Ratio of tensile strength to yield strength f_u / f_y	Strain at tensile strength ε_u (%)	Elongation at fracture ε_f (%)
S355	6	1	205	391	527	1.35	14.5	24.7
		2	205	370	525	1.42	11.8	22.6
		3	204	369	515	1.40	15.1	22.6
		4	204	370	516	1.39	13.7	24.0
		5	203	371	519	1.40	14.7	23.9
		6	202	367	514	1.40	13.5	23.1
	10	1	207	360	541	1.50	16.0	31.2
		2	204	357	536	1.50	16.8	30.0
		3	206	357	539	1.51	17.0	31.1
S690	6	1	201	745	826	1.11	6.2	15.9
		2	202	729	809	1.11	6.8	18.6
		3	201	728	808	1.11	5.8	15.1
		4	204	722	808	1.12	6.1	17.4
	10	1	203	788	835	1.06	6.5	17.8
		2	205	786	837	1.06	6.7	17.8
		3	210	775	834	1.08	6.7	18.5

Table 3.3 Test programme of temperature measurements

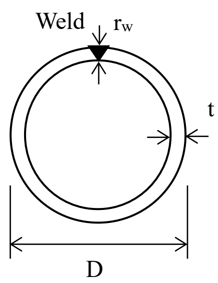

Section	D (mm)	t (mm)	L (mm)	Welding method
C1	150	6	660	GMAW
C2	200	6	660	
C3	200	10	660	
C4	250	10	660	

Table 3.4 Measured geometric properties

Specimen	D (mm)	t (mm)	L (mm)
C1	150.0	6.0	660.0
	151.0	5.9	661.0
	150.0	5.9	658.0
C2	201.0	6.0	661.0
	201.0	5.9	658.0
	200.0	6.0	659.0
C3	202.0	10.0	661.0
	201.0	10.0	659.0
	200.0	9.9	661.0
C4	251.0	10.0	660.0
	249.0	10.0	659.0
	249.0	10.1	659.0

Table 3.5 Material properties of welding electrode

Standard	Electrode	Supplier	Weld method	Diameter (mm)	Yield strength (N/mm^2)	Tensile strength (N/mm^2)	Elongation (%)
AWS A5.28	ER110S-G	Bohler	GMAW	1.2	720	880	15

Table 3.6 Welding parameters for CFCHS

Section	Weld run No.	Current I (A)	Voltage U (V)	Welding speed v (mm/s)	Welding efficiency η	Heat input energy Q (kJ/mm)
C1	1	135-150	18.2	1.84	0.85	1.14~1.26
	2	175-185	21.2	2.81	0.85	1.12~1.19
C2	1	165-180	19.5	2.40	0.85	1.14~1.24
	2	166-185	21.1	3.25	0.85	0.92~1.02
C3	1	175-180	19.7	2.32	0.85	1.26~1.30
	2	200-210	23.6	3.67	0.85	1.09~1.15
	3	200-210	24.2	3.04	0.85	1.35~1.42
C4	1	160-175	19.7	2.92	0.85	0.92~1.00
	2	200-210	24.2	4.13	0.85	1.00~1.05
	3	215-230	25.2	3.04	0.85	1.53~1.62

Table 3.7 Measured maximum temperatures of Section C1

Welding run	Maximum temperature at measurement points (°C)					
	T1	T2	T3	T4	T5	T6
1	409	241	454	268	454	270
2	425	255	473	283	473	309

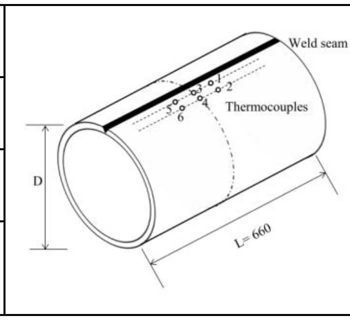

Table 3.8 Measured maximum temperatures of Section C2

Welding run	Maximum temperature at measurement points (°C)					
	T1	T2	T3	T4	T5	T6
1	352	200	335	188	364	194
2	376	244	358	229	395	236

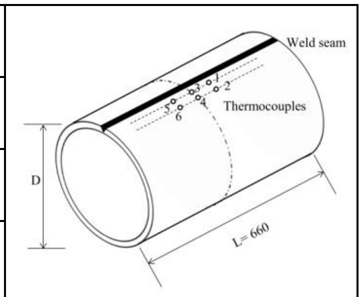

Table 3.9 Measured maximum temperatures of Section C3

Welding run	Maximum temperature at measurement points (°C)						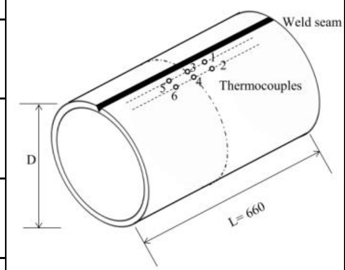
	T1	T2	T3	T4	T5	T6	
1	247	163	252	173	255	178	
2	304	210	310	223	308	230	
3	315	252	336	260	332	230	

Table 3.10 Measured maximum temperatures of Section C4

Welding run	Maximum temperature at measurement points (°C)						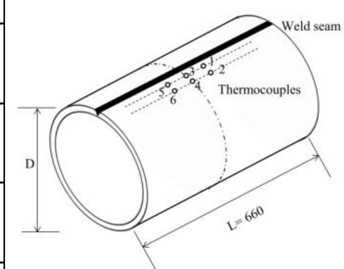
	T1	T2	T3	T4	T5	T6	
1	236	158	247	166	245	171	
2	289	204	304	215	301	221	
3	393	266	412	280	409	288	

Table 3.11 Test programme of sectioning method

Section	Outer diameter D (mm)	Plate thickness t (mm)	Length L (mm)	Welding method
C1-NW	150	6	260	—
C1	150	6	260	GMAW
C2-NW	200	6	260	—
C2	200	6	260	GMAW

Table 3.12 a) Longitudinal residual stresses of Section C1-NW

Point	Inner $\sigma_{rl,i}$(N/mm^2)	$\sigma_{rl,i}/f_y$	Outer $\sigma_{rl,o}$(N/mm^2)	$\sigma_{rl,o}/f_y$	Membrane σ_m(N/mm^2)	σ_m/f_y	Bending σ_b(N/mm^2)	σ_b/f_y
1	-78	-0.11	35	0.05	-21	-0.03	56	0.08
2	-252	-0.34	162	0.22	-45	-0.06	207	0.28
3	-253	-0.34	227	0.31	-13	-0.02	240	0.33
4	-227	-0.31	226	0.31	-1	0.00	227	0.31
5	-209	-0.28	217	0.29	4	0.01	213	0.29
6	-191	-0.26	206	0.28	8	0.01	199	0.27
7	-168	-0.23	182	0.25	7	0.01	175	0.24
8	-170	-0.23	180	0.24	5	0.01	175	0.24
9	-200	-0.27	199	0.27	0	0.00	199	0.27
10	-199	-0.27	203	0.28	2	0.00	201	0.27
11	-205	-0.28	213	0.29	4	0.01	209	0.28
12	-213	-0.29	235	0.32	11	0.01	224	0.30
13	-217	-0.29	241	0.33	12	0.02	229	0.31
14	-201	-0.27	194	0.26	-3	0.00	197	0.27
15	-219	-0.30	216	0.29	-1	0.00	218	0.30
16	-229	-0.31	210	0.29	-9	-0.01	220	0.30
17	-222	-0.30	194	0.26	-14	-0.02	208	0.28
18	-216	-0.29	194	0.26	-11	-0.01	205	0.28
19	-224	-0.30	207	0.28	-8	-0.01	216	0.29
20	-215	-0.29	210	0.29	-2	0.00	212	0.29
21	-214	-0.29	230	0.31	8	0.01	222	0.30
22	-224	-0.30	225	0.30	0	0.00	225	0.30
23	-216	-0.29	201	0.27	-7	-0.01	208	0.28
24	-210	-0.28	195	0.26	-7	-0.01	202	0.27

Table 3.12 b) Longitudinal residual stresses of Section C1

Point	Inner $\sigma_{rl,i}$(N/mm^2)	$\sigma_{rl,i}/f_y$	Outer $\sigma_{rl,o}$(N/mm^2)	$\sigma_{rl,o}/f_y$	Membrane σ_m(N/mm^2)	σ_m/f_y	Bending σ_b(N/mm^2)	σ_b/f_y
1	212	0.29	184	0.25	198	0.27	-14	-0.02
2	262	0.36	400	0.54	331	0.45	69	0.09
3	-211	-0.29	118	0.16	-46	-0.06	165	0.22
4	-323	-0.44	95	0.13	-114	-0.15	209	0.28
5	-328	-0.45	117	0.16	-106	-0.14	223	0.30
6	-298	-0.40	114	0.15	-92	-0.13	206	0.28
7	-259	-0.35	133	0.18	-63	-0.09	196	0.27
8	-221	-0.30	150	0.20	-35	-0.05	186	0.25
9	-199	-0.27	177	0.24	-11	-0.01	188	0.26
10	-186	-0.25	193	0.26	3	0.00	190	0.26
11	-183	-0.25	227	0.31	22	0.03	205	0.28
12	-166	-0.23	230	0.31	32	0.04	198	0.27
13	-177	-0.24	240	0.33	31	0.04	208	0.28
14	-166	-0.23	241	0.33	38	0.05	204	0.28
15	-156	-0.21	214	0.29	29	0.04	185	0.25
16	-165	-0.22	208	0.28	22	0.03	187	0.25
17	-166	-0.23	183	0.25	8	0.01	174	0.24
18	-177	-0.24	203	0.27	13	0.02	190	0.26
19	-187	-0.25	190	0.26	2	0.00	188	0.26
20	-190	-0.26	180	0.24	-5	-0.01	185	0.25
21	-206	-0.28	207	0.28	1	0.00	207	0.28
22	-204	-0.28	189	0.26	-8	-0.01	197	0.27
23	-194	-0.26	190	0.26	-2	0.00	192	0.26
24	-194	-0.26	190	0.26	-2	0.00	192	0.26

Table 3.12 c) Longitudinal residual stresses of Section C2-NW

Point	Inner	$\sigma_{rl,i}/f_y$	Outer	$\sigma_{rl,o}/f_y$	Membrane	σ_m/f_y	Bending	σ_b/f_y
	$\sigma_{rl,i}$(N/mm^2)		$\sigma_{rl,o}$(N/mm^2)		σ_m(N/mm^2)		σ_b(N/mm^2)	
1	-41	-0.06	159	0.22	59	0.08	100	0.14
2	-257	-0.35	138	0.19	-60	-0.08	197	0.27
3	-247	-0.34	203	0.28	-22	-0.03	225	0.31
4	-241	-0.33	224	0.30	-9	-0.01	233	0.32
5	-218	-0.30	233	0.32	7	0.01	225	0.31
6	-211	-0.29	234	0.32	12	0.02	222	0.30
7	-212	-0.29	231	0.31	9	0.01	222	0.30
8	-200	-0.27	215	0.29	8	0.01	208	0.28
9	-190	-0.26	209	0.28	9	0.01	199	0.27
10	-197	-0.27	195	0.26	-1	0.00	196	0.27
11	-196	-0.27	194	0.26	-1	0.00	195	0.26
12	-196	-0.27	196	0.27	0	0.00	196	0.27
13	-189	-0.26	192	0.26	2	0.00	190	0.26
14	-186	-0.25	193	0.26	3	0.00	189	0.26
15	-185	-0.25	194	0.26	4	0.01	189	0.26
16	-196	-0.27	217	0.29	11	0.01	206	0.28
17	-190	-0.26	210	0.29	10	0.01	200	0.27
18	-200	-0.27	205	0.28	2	0.00	203	0.27
19	-195	-0.26	203	0.27	4	0.01	199	0.27
20	-182	-0.25	192	0.26	5	0.01	187	0.25
21	-183	-0.25	200	0.27	8	0.01	191	0.26
22	-201	-0.27	202	0.27	1	0.00	201	0.27
23	-197	-0.27	178	0.24	-9	-0.01	187	0.25
24	-194	-0.26	197	0.27	2	0.00	196	0.27
25	-191	-0.26	204	0.28	7	0.01	198	0.27
26	-195	-0.26	205	0.28	5	0.01	200	0.27
27	-195	-0.26	196	0.27	1	0.00	196	0.27
28	-195	-0.26	205	0.28	5	0.01	200	0.27
29	-191	-0.26	206	0.28	7	0.01	199	0.27
30	-195	-0.27	203	0.27	4	0.00	199	0.27
31	-192	-0.26	204	0.28	6	0.01	198	0.27
32	-180	-0.24	188	0.26	4	0.01	184	0.25

Table 3.12 d) Longitudinal residual stresses of Section C2

Point	Inner	$\sigma_{rl,i}/f_y$	Outer	$\sigma_{rl,o}/f_y$	Membrane	σ_m/f_y	Bending	σ_b/f_y
	$\sigma_{rl,i}$(N/mm^2)		$\sigma_{rl,o}$(N/mm^2)		σ_m(N/mm^2)		σ_b(N/mm^2)	
1	159	0.22	68	0.09	114	0.15	-46	-0.06
2	413	0.56	362	0.49	387	0.53	-25	-0.03
3	-131	-0.18	59	0.08	-36	-0.05	95	0.13
4	-270	-0.37	32	0.04	-119	-0.16	151	0.21
5	-277	-0.38	61	0.08	-108	-0.15	169	0.23
6	-259	-0.35	85	0.11	-87	-0.12	172	0.23
7	-245	-0.33	118	0.16	-63	-0.09	182	0.25
8	-221	-0.30	143	0.19	-39	-0.05	182	0.25
9	-214	-0.29	166	0.23	-24	-0.03	190	0.26
10	-189	-0.26	197	0.27	4	0.01	193	0.26
11	-181	-0.25	193	0.26	6	0.01	187	0.25
12	-164	-0.22	187	0.25	11	0.02	176	0.24
13	-176	-0.24	218	0.30	21	0.03	197	0.27
14	-171	-0.23	222	0.30	26	0.03	197	0.27
15	-176	-0.24	222	0.30	23	0.03	199	0.27
16	-170	-0.23	206	0.28	18	0.02	188	0.25
17	-170	-0.23	195	0.26	13	0.02	183	0.25
18	-172	-0.23	189	0.26	9	0.01	181	0.24
19	-182	-0.25	192	0.26	5	0.01	187	0.25
20	-189	-0.26	197	0.27	4	0.01	193	0.26
21	-191	-0.26	196	0.27	2	0.00	193	0.26
22	-188	-0.25	185	0.25	-1	0.00	186	0.25
23	-185	-0.25	179	0.24	-3	0.00	182	0.25
24	-187	-0.25	181	0.25	-3	0.00	184	0.25
25	-190	-0.26	176	0.24	-7	-0.01	183	0.25
26	-190	-0.26	187	0.25	-1	0.00	189	0.26
27	-195	-0.26	191	0.26	-2	0.00	193	0.26
28	-188	-0.26	191	0.26	1	0.00	189	0.26
29	-189	-0.26	193	0.26	2	0.00	191	0.26
30	-189	-0.26	190	0.26	0	0.00	189	0.26
31	-186	-0.25	189	0.26	1	0.00	188	0.25
32	-184	-0.25	155	0.21	-15	-0.02	169	0.23

Table 3.13 Mesh convergence study

Model	Global mesh size (mm)	Local mesh size (mm)	Number of elements	Runtime (hrs)	Maximum residual stress on the outer surface (kN/mm^2)	Difference in axial resistance (%)
Coarse mesh	15	3	5,120	3.0	756	0.9%
Fine mesh	10	2	17,820	9.0	752	0.4%
Very fine mesh	5	1	38,800	33.0	749	0

CHAPTER FOUR

STRUCTRUAL BEHAVIOUR OF STOCKY COLUMNS UNDER AXIAL COMPRESSION

4.1 INTRODUCTION

This chapter presents an experimental and numerical investigation into local buckling behaviour of stocky columns of high strength S690 cold-formed circular hollow sections (CFCHS). A total of eight stocky columns with four different cross-sections have been tested successfully. Measured cross-section resistances of these S690 CFCHS are compared with those predicted resistances according to design rules provided in EN1993-1-1. It is shown that the existing design rules are applicable to predict compressive resistances of these S690 CFCHS.

Numerical models of these stocky columns of S690 CFCHS are established. Initial residual stresses due to transverse bending and longitudinal welding have been incorporated into these numerical models. Geometrical and material non-linear analyses of these models have been successfully completed. It is shown that numerical compressive resistances of these sections are compared well with these measured compressive resistances.

Then, the validated numerical models are adopted to carry out a series of parametric studies in order to investigate effects of various welding procedures and structural parameters onto the compressive resistances of these stocky columns of S690 CFCHS. After a comprehensive data analyses on the numerical results of the parametric studies, the existing rules on section classification given in EN1993-1-1 are shown to be highly applicable to high strength S690 CFCHS.

4.2 EXPERIMENTAL INVESTIGATION

4.2.1 Test specimens and material properties

A total of eight stocky columns of high strength S690 CFCHS were proposed to be tested under axial compression. Fabrication processes of those CFCHS are described in Chapter 3 in detail. Steel plates with a thickness of 20 mm were welded onto both ends of each stocky column to ensure that axial loadings are uniformly distributed onto the sections during the compression tests. The cross-sectional dimensions of Sections C1, C2, C3 and C4 are illustrated in Figure 4.1. For each section, two identical test specimens are prepared as repeated tests. For example, for Section C1, the two stocky columns are labeled as Columns C1-A and C1-B. Measured geometric properties of all test specimens are listed in Table 4.1, where L denotes the height of columns, D denotes the outer diameter, t denotes the wall thickness of the sections, and r_w denotes the weld size.

Standard coupon tests were carried out to obtain basic mechanical properties of these S690 steel plates with thicknesses of 6 mm and 10 mm. Details of test procedures and test results are described in Chapter 3. The key parameters including Young's moduli, yield strengths, and tensile strengths are taken as the average values of the results from the coupon tests, and they are summarized in Table 4.2.

4.2.2 Test setup and test procedures

Two different testing systems were employed to apply axial compression forces according to the expected ultimate test loads of these stocky columns, as shown in Figure 4.2 a) and b).

A MTS testing system with a compressive loading capacity of 3,500 kN was employed for compression tests of Sections C1 and C2 while Sections C3 and C4 were tested with a hydraulic servo control testing system with a compressive loading capacity of 10,000 kN. Instrumentation of the stocky column tests is illustrated in Figure 4.2 c). Four strain gauges are mounted at the mid-height of the test specimens in order to measure their axial strains while four displacement transducers are installed to measure their axial shortenings.

It should be noted that, in the beginning of the test, a preloading process was performed. All specimens were loaded to 30% of the design resistances, $N_{c,Rd}$, and unloaded back to zero at a loading rate of 300 kN/min. Such a preloading process was performed for three times, so that unintended eccentricities were minimized through careful re-alignment of the test specimens. Then, a compression force up to 70% of the design resistance, $N_{c,Rd}$ was applied at a loading rate of 200 kN/min. The loading was then continued through a displacement control at a rate of 0.5 mm/min. The testing procedure was terminated when the applied load was reduced more than 20% of the peak value.

4.2.3 Test results

Failure mode

As both ends of each stocky column of CFCHS were welded with end plates, they were effectively restrained from rotation, and hence, it was regarded as a fixed end condition. It should be noted that these test specimens fail in local buckling, and no weld fracture is observed. As illustrated in Figure 4.3, an outward buckle in the circumferential direction, which is often called an 'elephant's foot' buckle, is observed. For Sections C1, C2 and C3, buckling failure occurs at approximately $D/4$ away from the section end. For Section C4, local buckling is found at about $D/2$ away from the section end. Local buckling is also observed at the mid-height of specimen C4-A. The difference in the failure positions may be attributed to different initial imperfections among these sections.

Section resistances

A summary of key experimental results, including the ultimate test loads, $N_{c,Test}$, the corresponding axial shortenings, Δ_u, the predicted compressive resistance $N_{c,Rd}$, and ratio of $N_{c,Test}$ / $N_{c,Rd}$ are presented in Table 4.4. The axial resistance, $N_{c,Rd}$, is calculated according to Equation 4.1.

$$N_{c,Rd} = A \cdot f_y \tag{4.1}$$

where f_y is the yield strength of the steel plate, and A is the cross-sectional area of the section. It is found that the measured compressive resistances of Sections C1, C2, C3 and

C4 are all higher than the predicted values according to the design rules provided in EN 1993-1-1(CEN 2006). It should be noted that the strength enhancement of Sections C1 are over 10% of predicted compressive resistance. For Sections C3, the measured compressive resistances are about 8% higher than the predicted values. For sections C2 and C4, the measured compressive resistances are about 5% higher than the predicted values.

Load-shortening behaviour

The applied load versus axial shortening curves of all these stocky columns are illustrated in Figure 4.4. The axial shortening, Δ, is taken as the average readings from the four displacement transducers. The applied load increases linearly up to about 70% of the expected section resistances of these stocky columns. Then, the slopes of the load-shortening curves begin to reduce gradually, when the applied loads continue to increase. This is considered to be attributed to the presence of residual stresses which are induced during fabrication, which cause early yielding in parts of the sections.

Section classifications

Cross-section classification rules for steels with yield strengths up to 460 N/mm^2 are described in EN 1993-1-1 (CEN 2005) and EN 1993-1-6 (CEN 2007). The geometrical limits for Class 1 to 3 are given by:

$$\text{Class 1: } D/\left(t\cdot\frac{235}{f_y}\right)\leq 50 \tag{4.2}$$

$$\text{Class 2: } D/\left(t\cdot\frac{235}{f_y}\right)\leq 70 \tag{4.3}$$

$$\text{Class 3: } D/\left(t\cdot\frac{235}{f_y}\right)\leq 90 \tag{4.4}$$

where D denotes the outer diameter, t denotes the wall thickness of the section, and f_y denotes the yield strength of the steel material.

For Classes 1 to 3 sections, the compressive resistances of those cross sections are calculated by Equation 4.1 while for Class 4 sections, the compressive resistances are calculated according to Equation 4.5.

$$N_{c,Rd} = \chi \cdot A \cdot f_y \tag{4.5}$$

where χ is a reduction factor for local buckling determined as a function of the relative slenderness of the section.

In the present study, only Section C2 is classified as a Class 4 section, which implies that premature local buckling may occur, and the section may not reach the plastic section resistance. However, the test results of C2 show that there is no reduction in the axial resistance. The current geometrical limits provided by EN1993-1-1 is therefore considered to be too conservative for S690 CFCHS in this study.

4.3 VALIDATION OF NUMERICAL MODELS

4.3.1 Proposed FE model

A finite element package ABAQUS 6.12 is adopted for nonlinear numerical analyses of these stocky columns. An overall view of an established finite element model for Section C1 is illustrated in Figure 4.5. It should be noted that four layers of solid elements C3D8R are employed in the numerical model to capture plate buckling behaviour in these sections. An optimal mesh size of the finite element models are determined through a mesh convergence study. After a series of mesh convergence study, a general mesh size of 5 mm is adopted with an additional local mesh refinement for the weld seam. A local mesh size of 2 mm is adopted for weld elements.

4.3.2 Boundary conditions

It should be noted that two 20 mm thick S355 steel plates are welded at both ends of each stocky column, and axial compression forces are applied onto these columns without any eccentricity. Therefore, two reference points are set, and they are coupled with all nodes on the two ends of each stocky column with all six degrees of freedom in order to simulate the boundary conditions during the tests. Hence, axial load is imposed onto the top reference point while a fixed end condition is set for the bottom reference point to receive the reaction force. The boundary conditions of the model are shown in Figure 4.6.

4.3.3 Material properties

Two typical input stress-strain curves of these S690 steel plates are shown in Figure 4.7. They are simplified from the measured true stress-strain curves obtained from the standard tensile tests, which have been reported in the previous chapter. Isotropic hardening rule and Von Mises criteria are adopted for material plasticity of the steel material. The Poisson's ratio of the steel plates is taken as 0.3.

4.3.4 Initial imperfections

Residual stresses

Numerical models for predicting residual stresses due to both the transverse cold-forming process and the longitudinal welding process in these CFCHS are described in Chapter 3 in detail. It has been verified that the proposed numerical models are able to predict residual stress distributions in Sections C1 to C4 satisfactorily. The predicted residual stresses on both the inner and outer surfaces at the mid-section of Sections C1 to C4 from sequentially coupled thermomechanical analyses are shown in Figure 4.8. Hence, these residual stress fields obtained through sequentially coupled thermomechanical analyses are directly incorporated into the proposed models as initial stress states through the use of *initial conditions command in ABAQUS. The effects of residual stresses induced during both the cold-forming process and the longitudinal welding process are fully incorporated into the proposed model.

Initial geometrical imperfections

Global imperfection is not considered in the models of these stocky columns in this study while local imperfection is taken as the lowest buckling mode of the model after an eigenvalue analysis. It is widely known that the amplitude of local imperfection, w, has an important influence on the structural behaviour of these stocky columns. However, measurements of these local imperfections are extremely time-consuming to be conducted. In order to determine an appropriate amplitude of local imperfections, a parametric study on four different local imperfection amplitudes, namely, $w = 0.01t$, $0.1t$, $0.2t$ and $0.5t$ are adopted for assessment.

Tables 4.3 summarizes the parametric study of Sections C1 and C2. The applied load versus axial shortening curves of these numerical models and the corresponding test curves are plotted in Figure 4.9. It is shown that differences between the curves with $w = 0.01t$ and $w = 0.1t$ are so small that these two curves are almost the same. It should be noted that an imperfection amplitude of $0.2t$ gives the most accurate predictions in terms of both the ultimate loads and the corresponding axial shortenings. Therefore, $w = 0.2t$ is taken as the amplitude of the local imperfection for subsequent numerical analyses of all the stocky columns.

4.3.5 Numerical results

Failure modes and load-deformation behaviour

Figure 4.9 illustrates a comparison between the observed and the predicted failure modes of Sections C1 and C2. It should be noted that both the failure mode and the location of the occurrence of local buckling are shown to be well predicted by the proposed numerical model.

The predicted applied load versus axial shortening curves of Sections C1 to C4 are plotted in Figures 4.10 together with the corresponding test curves. The design resistances of these sections, $N_{c,Rd}$, are provided in these figures for comparison. The numerical models are shown to be able to capture the load-deformation behaviour of these sections very well, and the predicted compressive resistances of all these sections are higher than the design values.

Comparison of section resistances

The predicted and the measured section resistances of these stocky columns are summarized in Table 4.4 for direct comparison. The ratios of the measured to the predicted resistances of all these stocky columns are found to range from 0.94 to 1.02 with an average ratio of 0.98 and a standard deviation of 0.03. Hence, the section resistances of these stocky columns of S690 CFCHS are considered to be accurately predicted with the proposed numerical models.

4.4 PARAMETRIC STUDY ON STOCKY COLUMNS OF CFCHS

4.4.1 Introduction

In order to generate a wide range of data on the structural behaviour of stocky columns of CFCHS, a series of parametric studies are conducted. The following parameters are selected:

- Yield strengths of steel, i.e. S355 and S690
- Residual stress patterns
- Cross-sectional slenderness

4.4.2 Effect of yield strengths of steel

In order to study effect of yield strengths of steel on the structural behaviour of the stocky columns, residual stress patterns for CFCHS with S355 and S690 steels need to be determined. These residual stresses of CFCHS with S690 steel are obtained from sequentially coupled thermomechanical analyses, and the numerical results have been validated with experimental results from the sectioning method in Chapter 3. This finite element approach has been proved to be able to predict residual stresses in CFCHS provided that the following key information are available: material properties of steel, and welding parameters. In the present study, material properties of S355 and S690 steel plates with 6 mm and 10 mm thicknesses have been obtained from standard tensile coupon tests. As shown in Figure 4.11, simplified true stress-strain curves are adopted in the numerical models. Moreover, the welding parameters are assumed to be the same for these two steel materials. Table 4.5 summarizes the welding parameters for each section adopted for numerical simulation.

The predicted surface residual stresses at the mid-sections of Sections C1 to C4 of CFCHS with S355 steel are shown in Figure 4.12. The predicted residual stresses are normalized with the yield strengths of the steel plates. A comparison on the predicted surface residual stresses of Section C1 with S355 and S690 steel are illustrated in Figure 4.13. The normalized residual stresses in Section C1 with S355 steel are found to be higher than those in Section C1 with S690 steel. The effect of welding onto both tensile and compressive residual stresses in S690 sections are less significant than that in S355 sections. For Section C1 with S690 steel, the averaged maximum normalized tensile and compressive residual stresses are found to be 1.16 f_y and -0.20 f_y respectively. They are found to be lower than those of S355 section by more than 19 % and 47 %. Similar findings are identified for the other sections, and they are summarized in Table 4.6. In general, the residual stresses of S690 sections are much lower than that of S355 sections.

Based on the numerical results of Sections C1 to C4 with S355 steel, a simplified longitudinal residual stress pattern for CFCHS with S355 steel is proposed as follows:

Average residual stresses
$$\frac{\sigma_r}{f_y} = \begin{cases} -12.27\overline{\theta}+1 & 0 \le \overline{\theta} \le 0.11 \\ 1.01\overline{\theta}-0.46 & 0.11 < \overline{\theta} \le 0.55 \\ -0.22\overline{\theta}+0.22 & 0.55 < \overline{\theta} \le 1 \end{cases} \tag{4.6}$$

where σ_r denotes the residual stresses, f_y denotes the yield strength of the steel material, and $\overline{\theta} = \theta/\pi$, θ denotes the angle measured from the weld seam.

Integration of the residual stresses along the perimeter of half of a CFCHS with S355 steel is carried out as follows:

$$\int_0^{0.11}\left(-12.27\overline{\theta}+1\right)d\overline{\theta} + \int_{0.11}^{0.55}\left(1.01\overline{\theta}-0.46\right)d\overline{\theta} + \int_{0.55}^{1}\left(-0.22\overline{\theta}+0.22\right)d\overline{\theta} = 0.003 \approx 0 \tag{4.7}$$

Consequently, the proposed residual stress model is shown to be in self-equilibrium.

By adopting the proposed residual stress fields as initial conditions, the structural behaviour of stocky columns of CFCHS with S355 and S690 steels under axial compression are analyzed numerically. It should be noted that for CFCHS with S355 steel, the same magnitudes of initial geometrical imperfections as those of CFCHS with S690 steel are employed in the numerical models. Table 4.7 presents the finite element results for compressive resistances of Sections C1 to C4 with S355 and S690 steels, and they are compared with the design resistances determined to EN 1993-1-1.

It is found that the predicted resistances for CFCHS with S355 steel are generally larger than the design resistances by more than 18% while the predicted resistances for CFCHS with S690 steel are larger than the design resistances by 3% to 8%.

Although the residual stresses in CFHCS with S690 steel are smaller than those in CFCHS with S355 steel, they follow a self-equilibrant system within the cross-section, and they have almost no influence on the compressive resistances of these stocky columns. Hence, the design rules for CFCHS with S355 steel are generally applicable for CFCHS with S690 steel.

4.4.3 Effect of residual stresses

In order to study the influence of residual stresses on the structural behaviour of stocky columns of CFCHS with S690 steel, three different cases are incorporated in numerical models of Sections C1, C2, C3 and C4 for comparison as follows:

- No initial residual stresses
- Residual stress fields predicted with sequentially coupled thermomechanical analyses
- Simplified longitudinal residual stress patterns

Residual stress fields for Sections C1 to C4 of CFCHS with S690 steel are presented in section 4.4.1. In order to provide simplified residual stress patterns for comparison. The surface longitudinal residual stresses at mid-height of each section are averaged to give the through thickness residual stresses.

Figure 4.14 shows the simplified longitudinal residual stress pattern which is employed in the numerical models for Sections C1 to C4 of CFCHS with S690 steel. They are incorporated into three dimensional finite element models.

Figures 4.15 shows a comparison of each section with different cases of residual stress distributions. The predicted compressive resistances of each section are compared in Table

4.8. The residual stress patterns are found to have almost no effect on the section resistances of these stocky columns of CFCHS with S690 steel, but they have slightly affected the initial extensional rigidity of these stocky columns. The relative errors of the predicted compressive resistances among these three conditions are within 1%. Hence, accuracy of these numerical analyses by adopting the proposed simplified residual stress pattern is considered to be acceptable.

4.4.4 Effect of cross-sectional slenderness

In order to study the effect of the cross-sectional slenderness on the structural behaviour of these stocky columns of CFCHS with S690 steel, a total of 16 CHS with different cross-sectional dimensions are adopted in a parametric study, as listed in Table 4.9.

A slenderness parameter, $D/[t(235/f_y)]$, ranging from 59 to 318, is adopted to define the slenderness of each section. It should be noted that these CFCHS with S690 steel are classified as Class 2 to 4 according to EN 1993-1-1.

An elastic-perfectly plastic stress-strain model of the S690 steel is adopted, and the nominal engineering stress-strain curve is transformed to give the true stress-strain curve according to Equations 4.8 and 4.9 as follows:

$$\sigma_{true} = \sigma\,(1+\varepsilon) \tag{4.8}$$

$$\varepsilon^{pl}_{true} = \ln(1+\varepsilon) - \sigma_{true} / E \tag{4.9}$$

where E denotes the initial Young's modulus, σ and ε are the nominal stress and the nominal strain respectively. The proposed true stress-strain curve of S690 steel is shown in Figure 4.16. The lowest eigenmode is adopted as the initial geometrical imperfection while the amplitude of initial geometrical imperfection w, is assigned to be 0.2 times of the plate thickness. The Riks method is used for application of load increment in ABAQUS to capture local buckling behaviour of these stocky columns. Moreover, the effect of longitudinal residual stresses is incorporated through the use of a simplified residual stress pattern.

The numerical results of all the 16 sections are presented in Table 4.9. The resistance ratio, $N_{c,FE}/N_{c,Rd}$ of each section is plotted against the slenderness parameter, $D/[t(235/f_y)]$ in Figure 4.17. The predicted resistances of these sections are compared with the design resistances. It is found that the predicted resistances have almost no reduction until the slenderness ratio exceeds 130. When the slenderness ratio exceeds 160, the reduction to the compressive resistance of these sections is 5%. It should be noted the existing slenderness limit for class 4 sections is 90, and it is confirmed to be rather conservative. Consequently, a revised value for the slenderness limit is highly desirable for improved structural efficiency.

4.5 DESIGN IMPLICATIONS

Both EN 1993-1-1 and CIDECT Design Guide 1 provide section classification rules for CFCHS with a steel grade not higher than S460. EN 1993-1-12 expands the scope of these rules to steel grade up to S700 with no further modification. The formulae are presented in Section 4.2.3.

Chan et al. (2015) carried out a systematic numerical investigation on high strength stocky columns of CFCHS under axial compression to examine applicability of existing section classification rules provided in EN 1993-1-1. Finite element models with shell elements without residual stresses were used for parametric studies. It was suggested that current slenderness limits for high strength CFCHS with a steel grade up to S700 may be relaxed from 90 to 185.

From the results of the current parametric studies, the slenderness limit of 90 is confirmed to be generally applicable for CFCHS with S690 steel while the slenderness limit of 185 is considered to be unconservative. A new slenderness limit of 130 is proposed in the present study. It should be noted that the proposed numerical models have not considered any strain hardening of the steel materials, therefore the predicted resistances represent values of a lower bound condition with a certain safety margin. The new slenderness limit will allow effective use of stocky columns of S690 CFCHS steel corresponding to the proven structural behaviour as demonstrated in both the experimental and the numerical investigations conducted in the present study.

4.6 CONCLUSIONS

This chapter presents a systematic experimental and numerical investigation into stocky columns of S690 CFCHS under axial compression.

A summary of the findings are concluded as follows:

a) Eight stocky columns with four cross-sectional dimensions of CFCHS with S690 steel have been tested successfully under axial compression. The measured compressive resistances of these sections are larger than the design values according to EN 1993-1-1. Full section resistances of these CFCHS with S690 steel have been successfully mobilized.

b) Residual stresses of S355 and S690 CFCHS with four different cross-sectional dimension have been studied with validated finite element models through sequentially coupled thermomechanical analyses. Simplified residual stress patterns have been provided, and they are readily applied to structural models for practical design.

c) Parametric studies on various parameters such as yield strengths of steel, residual stress patterns and cross-sectional slenderness have been conducted. The numerical results has shown that with the same cross-sectional dimensions, compressive resistances of stocky columns of CFCHS with S690 steel are larger than those of CFCHS with S355 steel by more than 60%. Residual stresses have almost no effect on the compressive resistances of these stocky columns of CFCHS with S690 steel.

d) Current section classification rules are found to be very conservative for CFCHS with S690 steel. A new slenderness limit of 130 is recommended to replace the existing slenderness limit of 90 in EN 1993-1-1 to improve design efficiency.

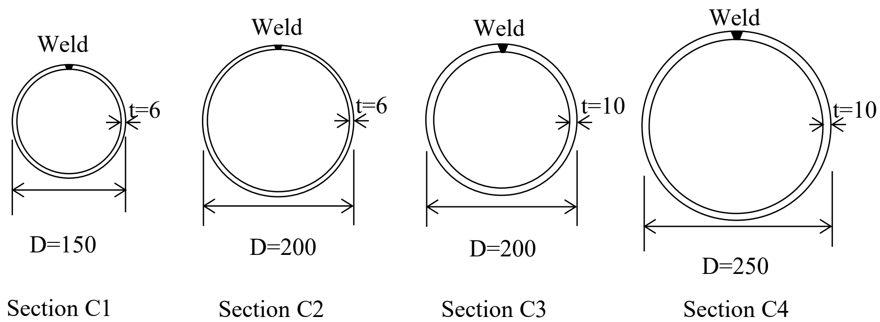

Figure 4.1 Geometrical dimensions of CFCHS covered in the study

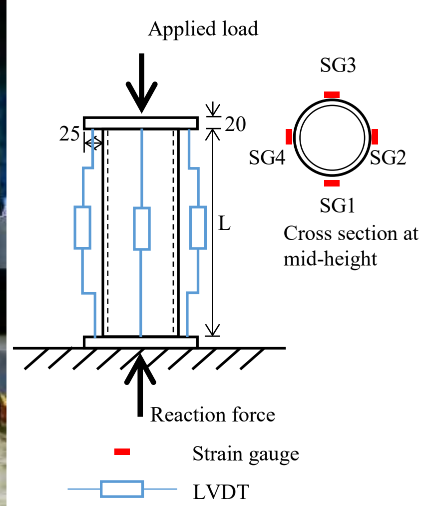

a) 300 tons MTS testing system

b) 1000 tons hydraulic servo control testing system

c) Instrumentation

Figure 4.2 Test setup and instrumentation

Section C1-A Section C1-B

a) Section C1

Section C2-A Section C2-B

b) Section C2

Section C3-A Section C3-B

c) Section C3

Section C4-A Section C4-B

d) Section C4

Figure 4.3 Deformed shapes of stocky columns of S690 CFCHS after test

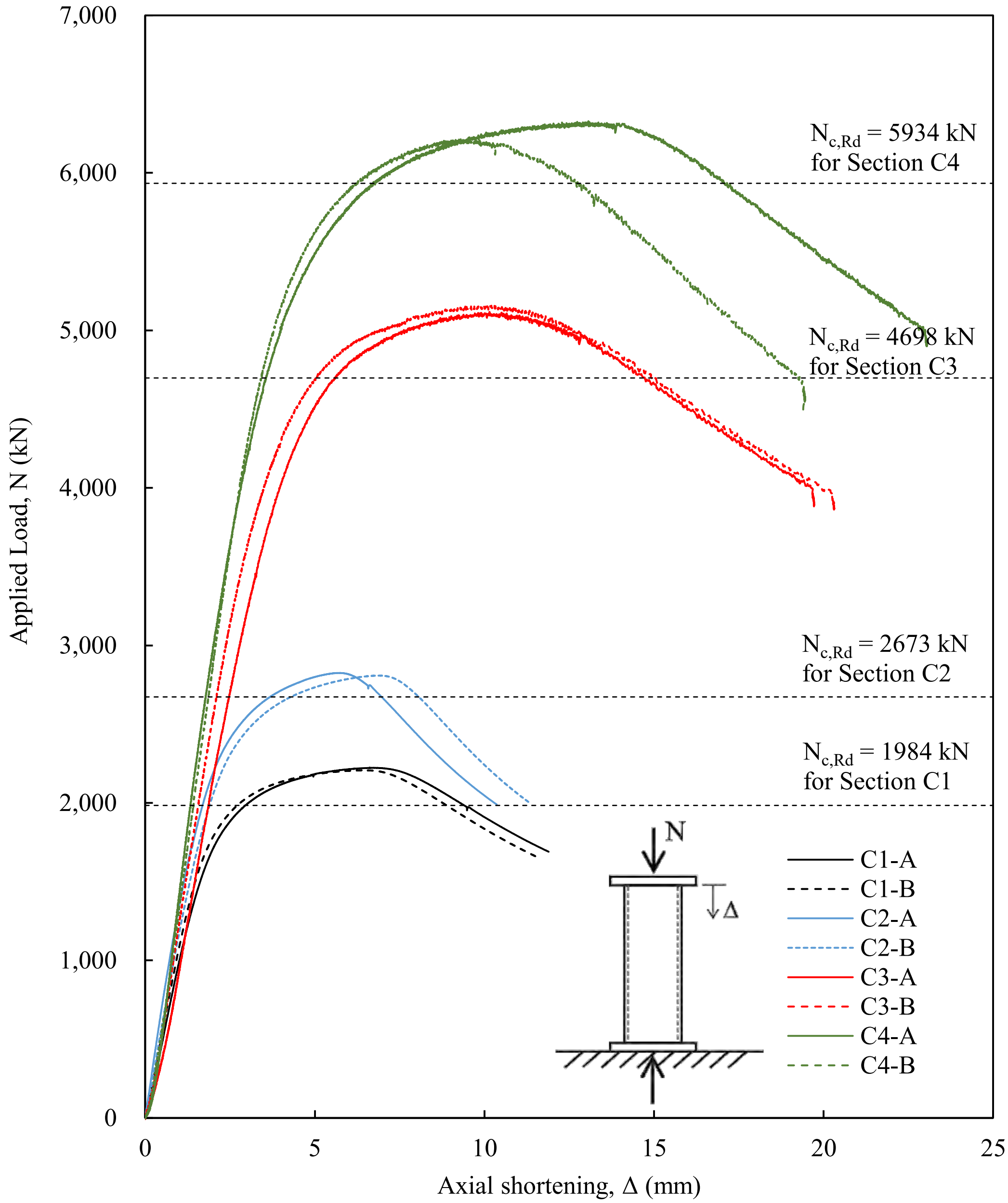

Figure 4.4 Measured load-axial shortening curves of stocky columns of S690 CFCHS

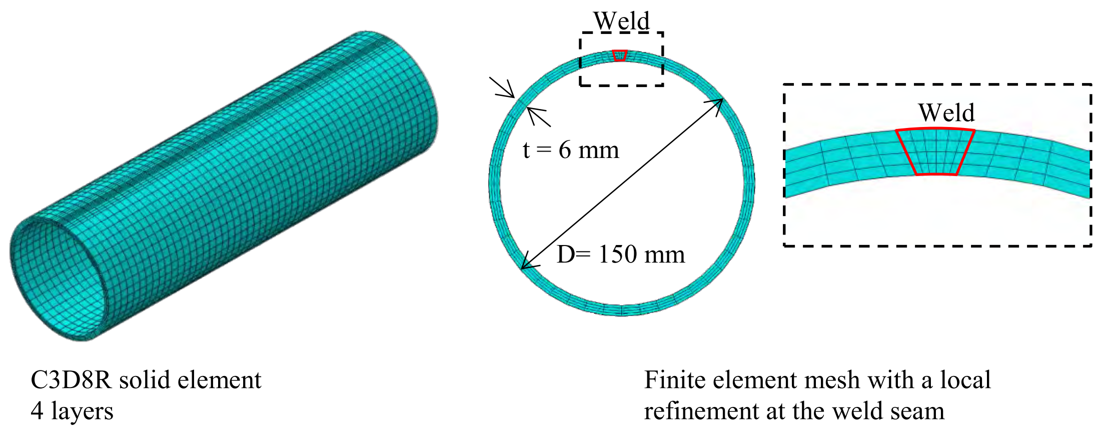

Figure 4.5 Finite element model for Section C1

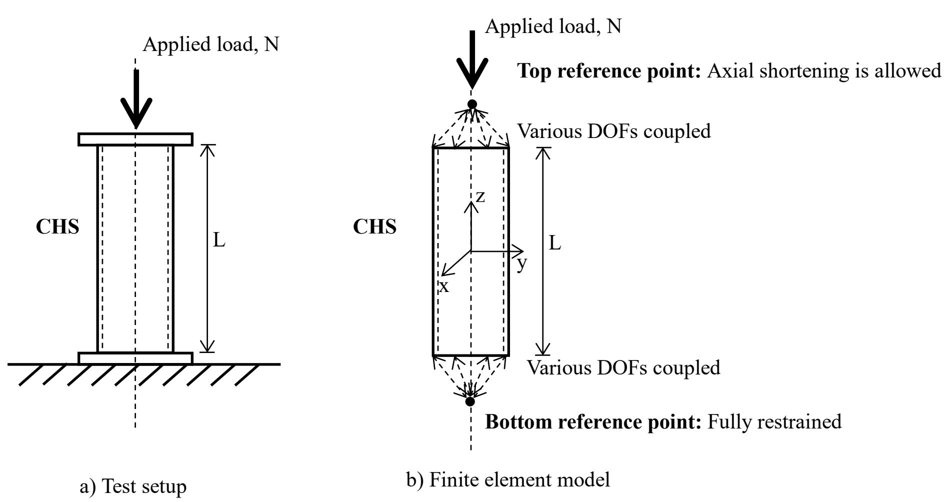

Figure 4.6 Boundary conditions for stocky columns under axial compression

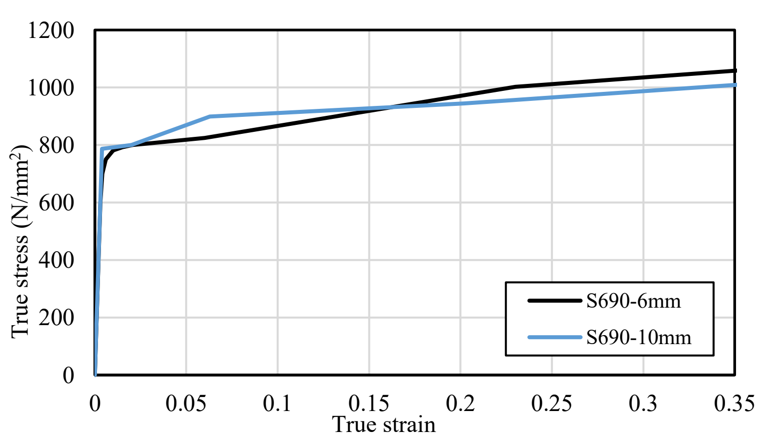

Figure 4.7 True stress-strain curves of S690 steel plates

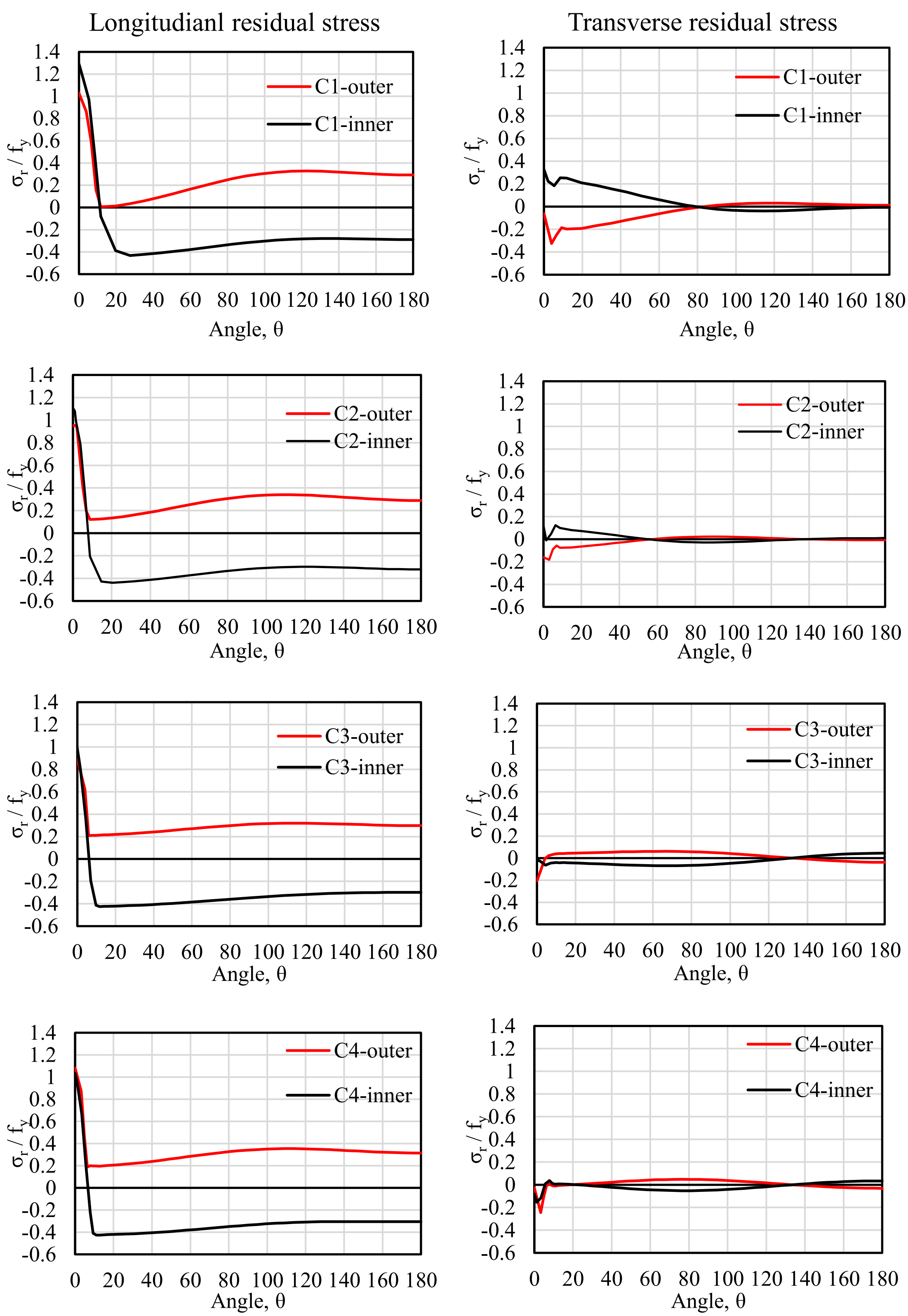

Figure 4.8 Predicted surface residual stresses

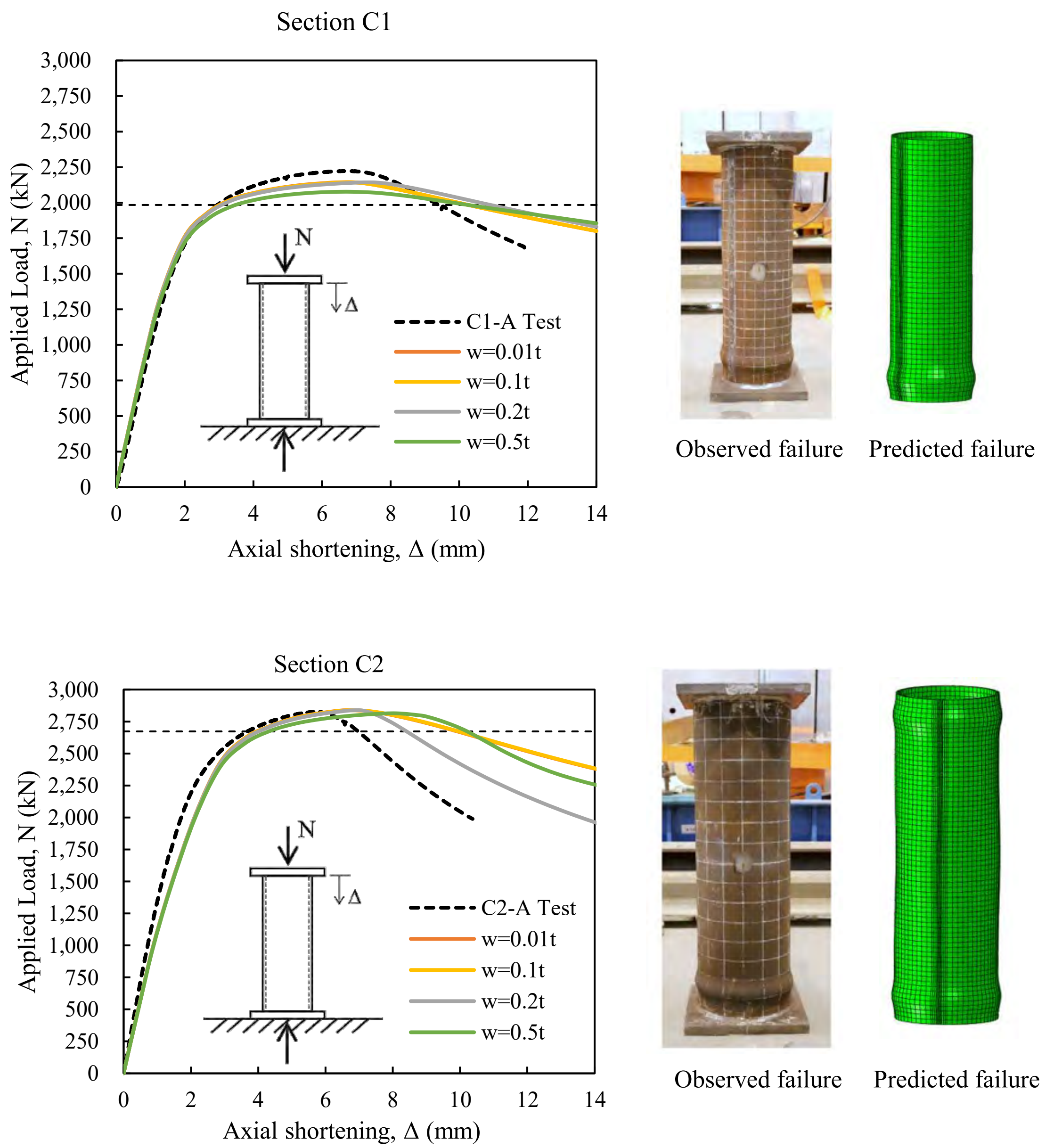

Figure 4.9 Predicted load-axial shortening curves for Sections C1 and C2 with different initial geometrical imperfections

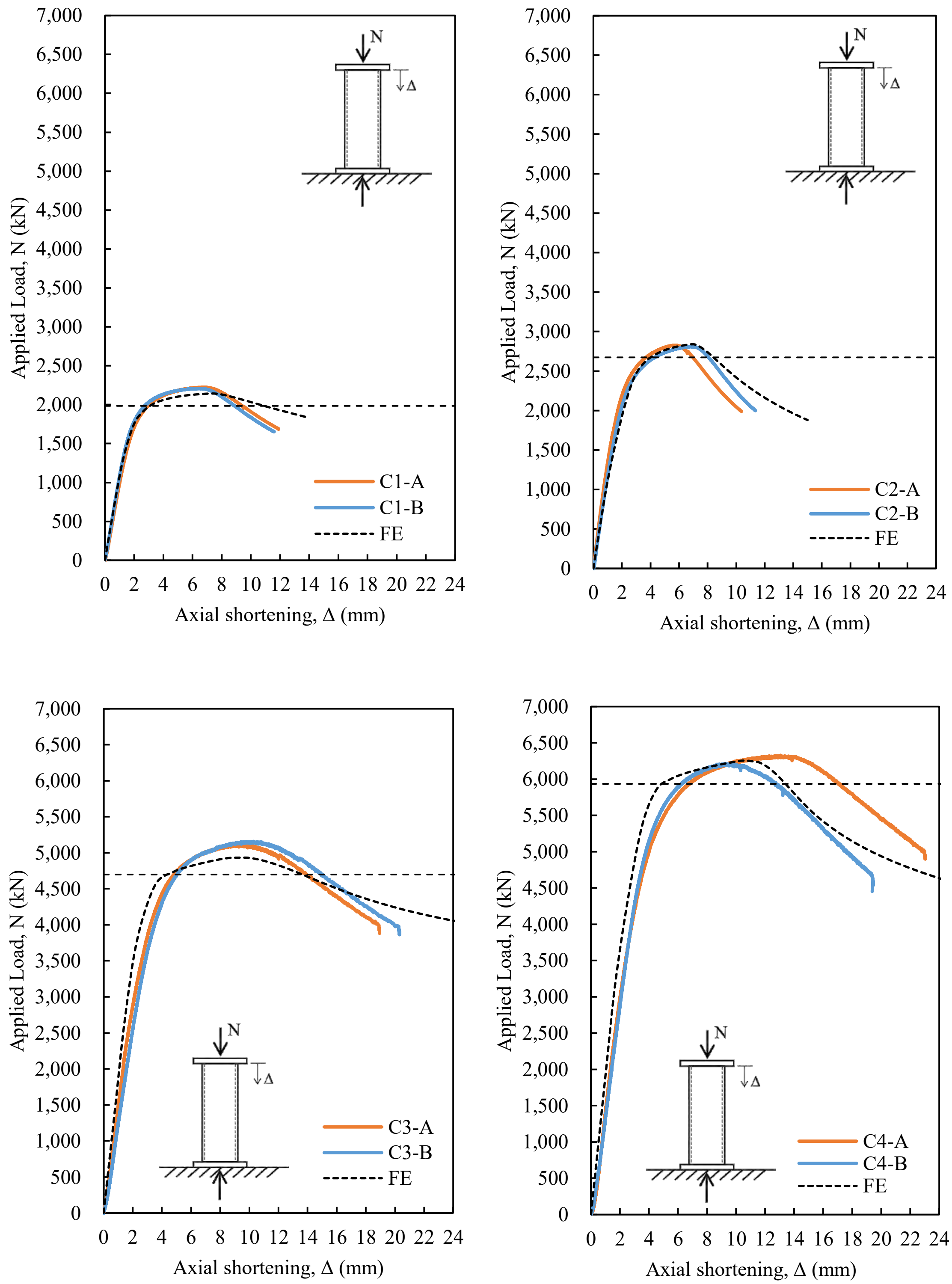

Figure 4.10 Comparison of measured and predicted load-shortening curves of stocky columns of CFCHS

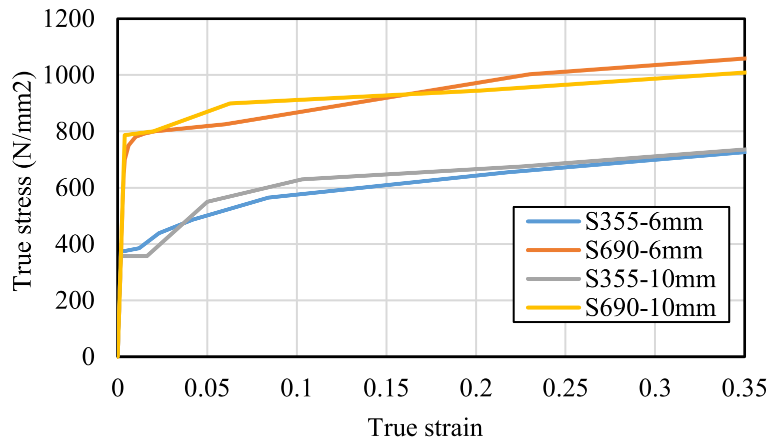

Figure 4.11 True stress-strain curves for parametric studies

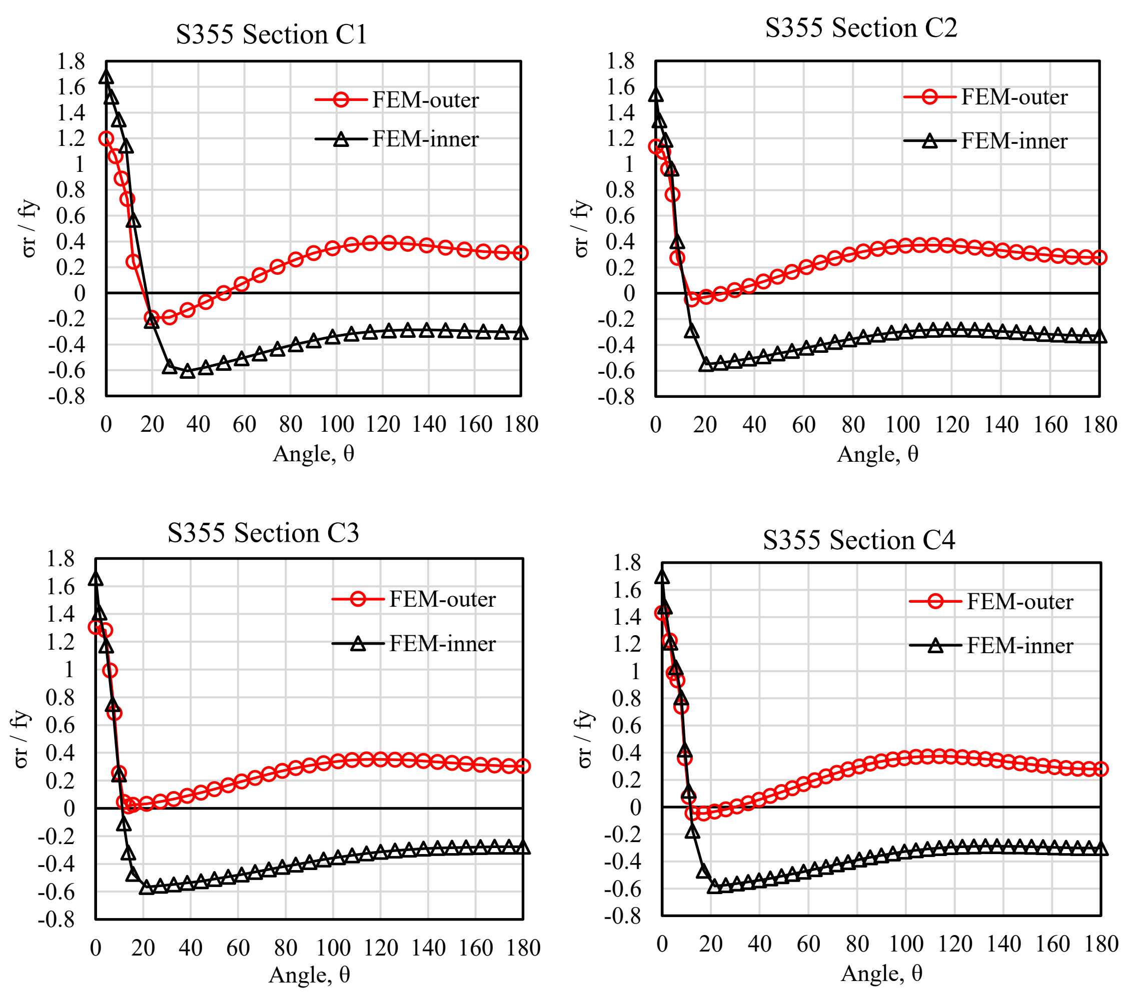

Figure 4.12 Predicted surface residual stresses of S355 CFCHS

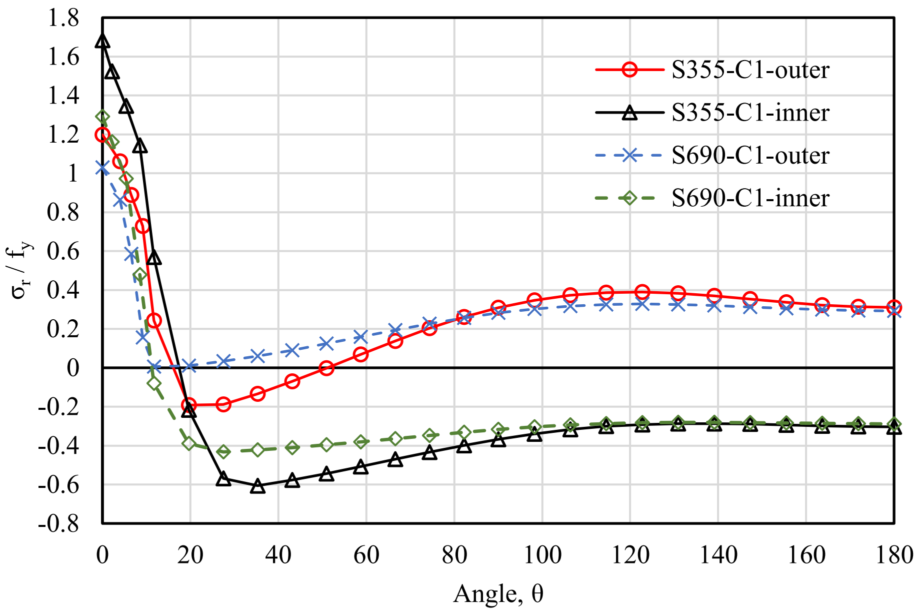

Figure 4.13 Comparison of surface residual stresses of S355 and S690 CFCHS – Section C1

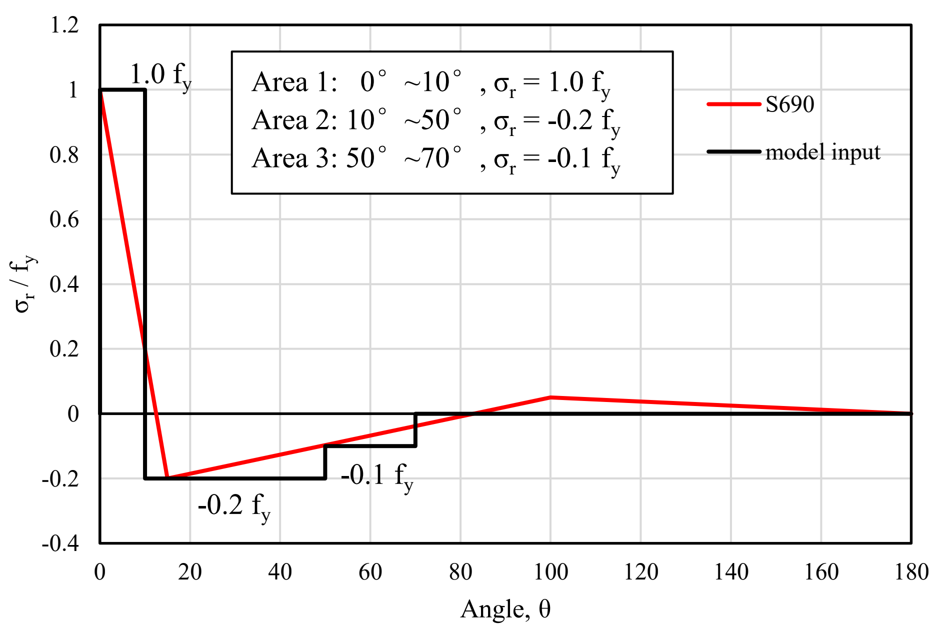

Figure 4.14 Simplified longitudinal residual stress patterns of S690 CFCHS

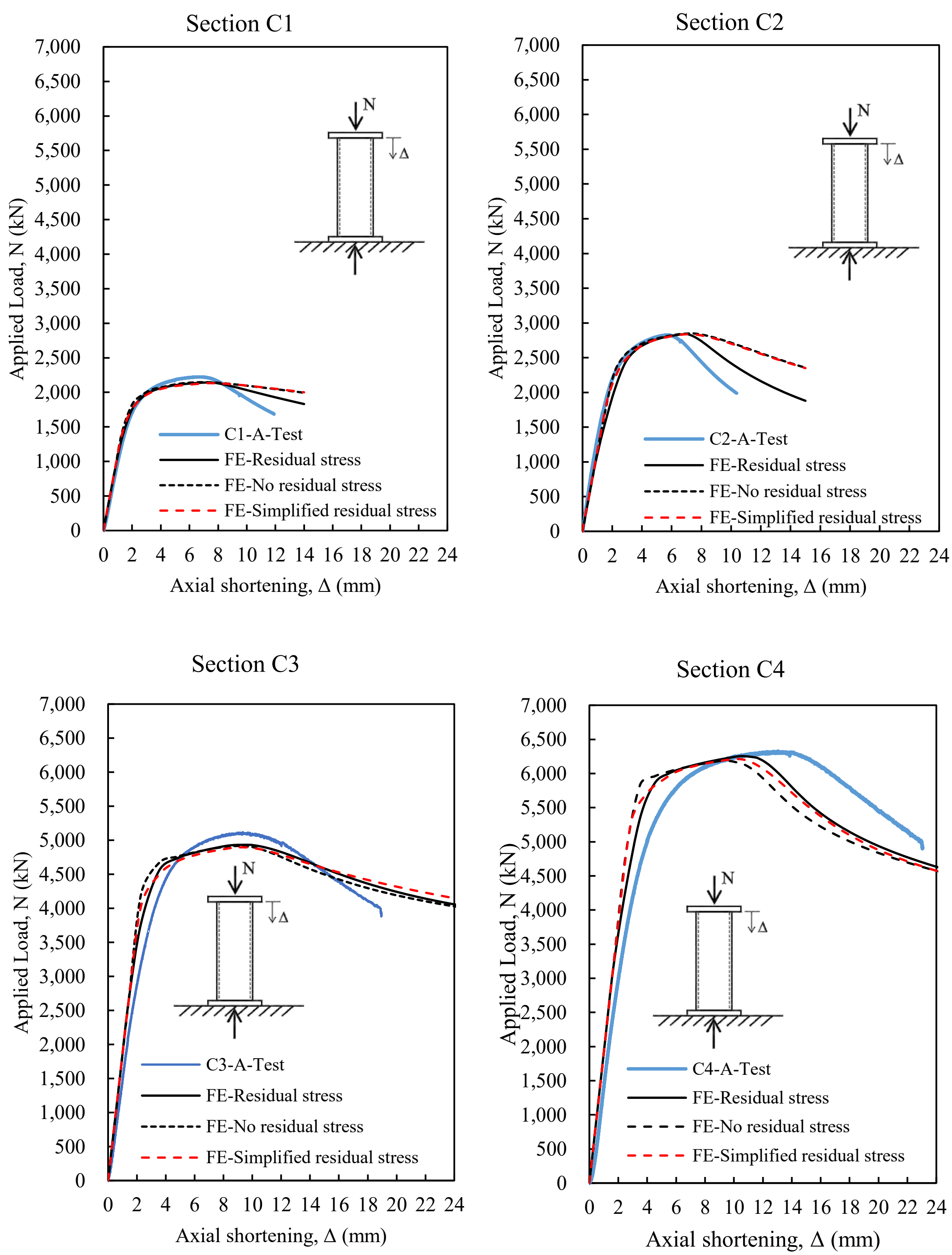

Figure 4.15 Effects of residual stresses on stocky columns of CFCHS

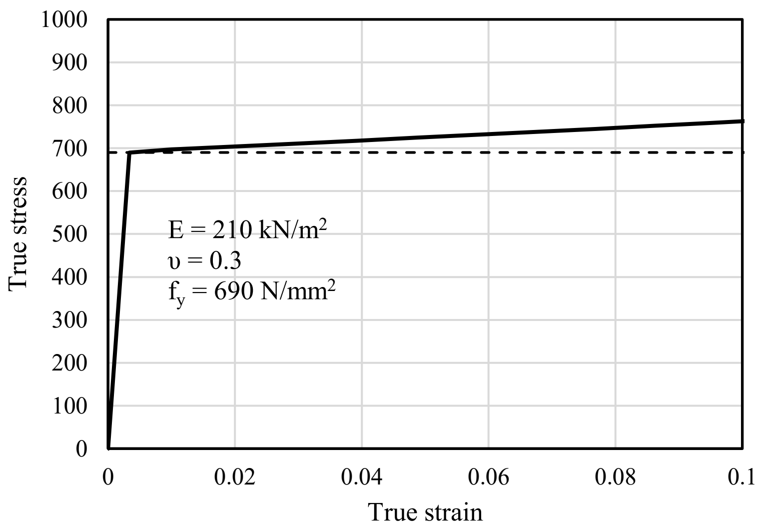

Figure 4.16 Stress-strain relationship for S690 steels

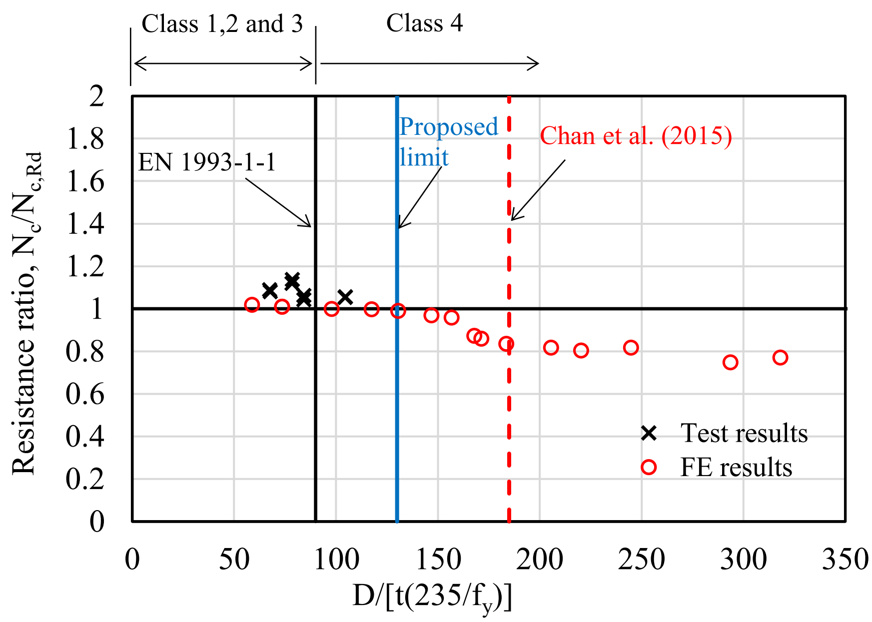

Figure 4.17 Parametric study on cross-sectional slenderness of S690 CFCHS

Table 4.1 Measured geometric dimensions of S690 CFCHS

Section	Length, L (mm)	Outer diameter, D (mm)	Plate thickness, t (mm)	Section Classification	D/t	Weld size, r_w (mm)	Area A (mm^2)
C1-A	501.0	149.5	5.9	Class 3	25.2	9.7	2672.4
C1-B	499.5	150.0	6.0		25.2	9.8	2694.1
C2-A	650.6	200.7	6.0	Class 4	33.6	9.8	3653.6
C2-B	649.5	200.3	6.0		33.6	9.8	3645.3
C3-A	649.5	201.8	10.0	Class 2	20.2	15.4	6013.1
C3-B	650.2	201.2	10.0		20.1	15.4	6017.3
C4-A	799.7	251.0	10.0	Class 3	25.1	13.0	7566.4
C4-B	799.7	251.0	10.0		25.1	13.0	7566.4

Table 4.2. Test results of tensile coupon tests

Steel plate	Young's modulus E (kN/mm^2)	Yield strength f_y (N/mm^2)	Tensile strength f_u (N/mm^2)	f_u/f_y	Strain at tensile strength ε_u (%)	Elongation at fracture ε_f (%)
S690-6 mm	202	731	813	1.11	6.23	16.8
S690-10mm	204	787	836	1.06	6.51	17.0

Table 4.3 Parametric study on initial geometrical imperfections of Sections C1 and C2

Section	Local imperfection amplitude, *w*	Predicted ultimate load $N_{c,FE}$ (kN)	Measured ultimate load $N_{c,Test}$ (kN)	$\frac{N_{c,FE}}{N_{c,Test}}$	Predicted axial shortening under $N_{c,FE}$ $\Delta_{u,FE}$ (mm)	Measured axial shortening under $N_{c,Test}$ $\Delta_{u,Test}$ (mm)	$\frac{\Delta_{u,FE}}{\Delta_{u,Test}}$
C1	0.01t	2144	2223	0.968	6.71	6.64	0.99
	0.1t	2143		0.967	6.62		1.00
	0.2t	2143		0.967	7.23		0.92
	0.5t	2077		0.938	6.77		0.98
C2	0.01t	2839	2824	1.005	6.62	6.97	0.95
	0.1t	2838		1.005	6.62		0.95
	0.2t	2838		1.005	6.81		0.98
	0.5t	2814		0.996	8.12		1.16

Table 4.4 Summary of test results of stocky columns of S690 CFCHS

Section	Section Classification	Measured axial resistance $N_{c,Test}$ (kN)	Predicted axial resistance $N_{c,FE}$ (kN)	Measured axial shortening at $N_{c,Test}$ $\Delta_{u,Test}$ (mm)	Predicted axial shortening at $N_{c,FE}$ $\Delta_{u,FE}$ (mm)	Resistance ratio $\frac{N_{c,FE}}{N_{c,Test}}$
C1-A	Class 3	2223	2143	6.64	7.23	0.96
C1-B		2206		6.43		0.97
C2-A	Class 4	2824	2838	5.75	6.81	1.00
C2-B		2808		6.90		1.01
C3-A	Class 2	5117	4852	10.15	9.78	0.96
C3-B		5158		10.30		0.96
C4-A	Class 3	6329	6255	13.06	10.51	0.99
C4-B		6214		9.27		1.01
Mean						0.98
Standard deviation, σ						0.03

Table 4.5 Welding parameters for numerical modeling

Section	Weld run No.	Current I (A)	Voltage U (V)	Welding speed v (mm/s)	Welding efficiency η	Heat input energy Q (kJ/mm)
C1	1	150	18.2	1.84	0.85	1.26
	2	185	21.2	2.81	0.85	1.19
C2	1	180	19.5	2.40	0.85	1.24
	2	185	21.1	3.25	0.85	1.02
C3	1	175	19.7	2.32	0.85	1.26
	2	210	23.6	3.67	0.85	1.15
	3	200	24.2	3.04	0.85	1.35
C4	1	175	19.7	2.92	0.85	1.00
	2	210	24.2	4.13	0.85	1.05
	3	215	25.2	3.04	0.85	1.53

Table 4.6 Comparison of numerical results of average longitudinal residual stresses in S355 and S690 CFCHS

Section	Tensile residual stress σ_{rt} / f_y		Maximum residual stress ratio of S690/S355	Compressive residual stress σ_{rc} / f_y		Maximum residual stress ratio of S690/S355
	S355	S690		S355	S690	
C1	1.44	1.16	0.81	-0.38	-0.2	0.53
C2	1.34	1.03	0.77	-0.29	1.03	0.77
C3	1.48	0.94	0.64	-0.27	-0.11	0.41
C4	1.56	1.06	0.70	-0.31	-0.12	0.39

Table 4.7 Parametric study on material yield strengths of stocky columns of CFCHS

Section	S355			S690		
	$N_{c,FE}$ (kN)	$N_{c,Rd}$ (kN)	$\frac{N_{c,FE}}{N_{c,Rd}}$	$N_{c,FE}$ (kN)	$N_{c,Rd}$ (kN)	$\frac{N_{c,FE}}{N_{c,Rd}}$
C1	1319	1012	1.30	2143	1984	1.08
C2	1634	1364	1.20	2838	2673	1.06
C3	2774	2137	1.30	4852	4698	1.03
C4	3179	2699	1.18	6255	5934	1.05

Table 4.8 Parametric study on residual stresses of stocky columns of CFCHS

Section	Case 1 Residual stress field $N_{c,FE,1}$ (kN)	Case 2 No residual stress $N_{c,FE,2}$ (kN)	Resistance ratio $\frac{N_{c,FE,2}}{N_{c,FE,1}}$	Simplified residual stress $N_{c,FE,3}$ (kN)	Resistance ratio $\frac{N_{c,FE,3}}{N_{c,FE,1}}$
C1	2143	2148	1.00	2132	0.99
C2	2838	2849	1.00	2837	1.00
C3	4932	4914	1.00	4895	0.99
C4	6188	6255	1.01	6211	1.00

Table 4.9 Parametric study on cross-sectional slenderness of S690 CFCHS

Section	D (mm)	t (mm)	Class	Slenderness parameter $D/[t(235/f_y)]$	Design resistance $N_{c,Rd}$ (kN)	FE result $N_{c,FE}$ (kN)	Resistance ratio $\frac{N_{c,FE}}{N_{c,Rd}}$
C1	150	6	2	73	1873	1893	1.01
C2	200	6	4	98	2523	2523	1.00
C3	200	10	2	59	4119	4200	1.02
C4	250	10	3	73	5202	5257	1.01
C5	150	2	4	220	642	516	0.80
C6	200	2	4	294	858	643	0.75
C7	250	3	4	245	1606	1313	0.82
C8	250	4	4	184	2133	1781	0.83
C9	650	6	4	318	8376	6459	0.77
C10	700	10	4	206	14957	12222	0.82
C11	700	12	4	171	17897	15391	0.86
C12	800	14	4	168	23853	20836	0.87
C13	800	15	4	157	25525	24482	0.96
C14	800	16	4	147	27192	26342	0.97
C15	800	18	4	130	30513	30213	0.99
C16	800	20	4	117	33816	33735	1.00

CHAPTER FIVE

STRUCTRUAL BEHAVIOUR OF T-JOINTS BETWEEN CFCHS UNDER AXIAL COMPRESSION

5.1 INTRODUCTION

In order to investigate the structural behaviour of high strength S690 welded steel T-joints, a series of T-joints between cold-formed circular hollow sections (CFCHS) were fabricated and tested under axial compression in brace members.

A total of six T-joints between CFCHS with two different steel grades were tested. A typical failure mode was observed that all joints failed in an interaction between the local plastification of the chords and overall plastic bending of the chords.

Three dimensional finite element models with geometrical and material non-linearity have been established and verified after calibration against test results. Both measured geometrical dimensions and material properties of these CFCHS are also incorporated into the proposed models. The verified finite element models are employed for parametric studies on effects of various geometric parameters and material strengths.

Both the experimental and the numerical results are compared with design resistances obtained from existing design codes, including EN 1993-1-8 and CIDECT Design Guide 1. Applicability of these design methods for design of high strength S690 welded steel T-joints between CFCHS were examined.

5.2 EXPERIMENTAL INVESTIGATION

5.2.1 Test programme

A total of six T-joints between S690 CFCHS were fabricated. Figure 5.1 shows a schematic view of a typical T-joint specimen for testing. The test programme is presented in Table 5.1 while Figure 5.2 presents detailed configuration of a T-joint. The lengths of both the chords and the braces of the joints are L_0 = 1200 mm and L_1 = 600 mm respectively. The span between two pinned supports are L = 1500 mm. To study the effect of different steel grades on the structural behaviour of these T-joints, both the normal strength steel S355 and the high strength steel S690 are used for fabrication of T-joints. Specimens T1-C and T3-C are made from S355 steels while the other four were made from S690 steels. The following geometrical parameters are covered: i) the brace to chord diameter ratio ($\beta = d_1 / d_0$) is assigned to range from 0.6 to 0.8, ii) the ratio of brace wall thickness to chord wall thickness ($\tau = t_1 / t_0$) is assigned to range from 0.8 to 1.0. The diameter of the chord is assigned to be 250 mm, and its thickness is assigned to be 10 mm. The measured geometric dimensions of the six T-joint specimens are summarized in Table 5.2.

Standard tensile tests were conducted to obtain the basic material properties of both the S355 and the S690 steel plates. The test method and the procedures are detailed in Chapter 3. Figures 5.3 and 5.4 present the geometric dimensions of the tensile coupons and the typical stress-strain curves of the S355 and the S690 steel plates. A summary of key results of the standard tensile tests are shown in Table 5.3.

All of these T-joints were welded between CFCHS. The fabrication processes of theses CFCHS are described in detail in Chapter 3. Edge preparation was performed for the ends of braces in order to make profiled connecting surfaces for joint welding. The chords and the braces were then connected together through a combination of partial penetration butt welds and fillet welds. Welding of all these T-joints between CFCHS were performed by a highly skilled welder in a well-equipped fabricator. The welding electrode ER110S-G (with a diameter of 1.2 mm) according to AWS A5.28 (AWS, 2005) was employed for GMAW of high strength S690 steels. It should be noted that the nominal yield strength of the welding electrode is 720 N/mm^2, while the measured yield strengths of S690 steel plates are 731 N/mm^{2}and 787 N/mm^2. Therefore, an under-matched welding was achieved dispite an over-matched welding was designed. For welding of S355 steels, the welding wire E71T-1 (with a diameter of 1.2 mm) in accordance with AWS A5.20 (AWS, 1995) was adopted. Both chemical compositions and mechanical properties of these welding electrodes are summarized in Tables 5.4 and 5.5. The measured weld sizes at crown points and saddle points of each joint were shown in Table 5.6.

5.2.2 Test setup and test procedures

Figure 5.5 illustrates typical test setup and instrumentation for the joint tests. All these tests were carried out at the Structural Engineering Research Laboratory of the Hong Kong Polytechnic University. A hydraulic servo control testing system with a compressive loading capacity of 10,000 kN was employed for the compression tests. Both ends of the chord of each T-joint were attached to two vertical supports through two steel pins. Only in-plane rotations were allowed at both ends of the chord. Two laser levels were installed in front of and at the left of the T-joint during testing to ensure the centre of the brace was carefully aligned with the centre of the loading attachment.

For each T-joint, four strain gauges with a 5 mm gauge length were mounted onto the brace to monitor axial strains of the brace during testing. Twelve displacement transducers were used to measure horizontal and vertical deformations of the T-joints at various specified locations during tests, including deformations at crown points and possible support slippages.

Compression force was applied onto the loading plate on the top plates of the braces of the T-joints through a vertical loading actuator. Before each test, a preloading process was first conducted for three times. An axial load of 30% of the predicted axial resistances of the T-joints, $N_{c,Rd}$, was applied, and then unloaded at a loading rate of 150 kN/mm to minimize initial bending.

In each test, the loading rate was firstly set to be about 50 kN/min. When the axial load reached up to 80% of the predicted resistance of the T-joint, an axial displacement rate of

0.3 mm/min was set to control the axial load. After reaching the peak load, a displacement rate of 0.5 mm/min was set until the applied load dropped below 80% of the peak load.

5.2.3 Test results

Failure modes

All the T-joints were tested successfully and they all failed in an interaction between a global failure mode and a local failure mode as follows:

- Overall plastic bending of the chord
- Local plastification of the chord at the joint panel zone

This is because the axial compression force acting on the brace will induce bending moment and shear force in the chord. The chord section at the joint panel zone is therefore under compressive stresses (Figure 5.8). Such compressive chord stresses will reduce the joint resistance. The deformed shapes and the typical failure modes of these T-joints are illustrated in Figures 5.6 and 5.7. No weld cracking was observed among all these tests.

Load-displacement curves

The vertical displacement at the mid-span of the chord of each T-joint is calculated as follows

$$\delta = \frac{D_6 + D_7}{2} \tag{5.1}$$

Applied load versus chord mid-span vertical displacement curves of these T-joints are shown in Figure 5.9.

Load-chord indentation curves

In the present study, the maximum indentation, or distortion, is found to occur at the crown point of the chord. Hence, this deformation, namely, chord indentation Δ, is taken as the maximum relative deformation at the crown points and the center of the chord, which is calculated according to Equation 5.1.

$$\text{Chord indentation, } \Delta = \max(D_4 - \delta, D_5 - \delta) \tag{5.2}$$

The applied load versus chord indentation curves of all the T-joints are shown in Figure 5.10.

5.2.4 Data analyses

Joint resistances

In the present study, the maximum load resistance of each T-joint is defined by the lower value of: i) the applied ultimate load of the joint, and ii) the applied load corresponding to an ultimate deformation limit, where the deformation limit is proposed by Lu *et al.* (1993). This out-of-plane deformation limit is defined as 3% of the outer diameter of the chord, i.e. $0.03d_0$, according to CIDECT Design Guide 1.

It is observed from the applied load versus chord indentation curves of all the tests that all tested joints reached the ultimate loads prior to the deformation limit, i.e. $0.03d_0$ or 7.5 mm. Hence, the applied ultimate load of each joint is determined as its axial compressive resistance.

The axial resistances of these T-joints are calculated according to various equations given in the following design specifications:

a) CIDECT Design Guide 1

In CIDECT Design Guide 1, the design resistances of T-joints between CHS for chord plastification is calculated according to Equations 5.3 to 5.6 as follows.

$$N_{\mathrm{CIDECT}} = Q_u Q_f \frac{f_{y0} t_0^2}{\sin\theta} \quad (5.3)$$

$$Q_u = 2.6(1+6.8\beta^2)\gamma^{0.2} \quad (5.4)$$

$$Q_f = (1-|n|)^{C_1} \quad (5.5)$$

$$n = \frac{N_0}{N_{pl,0}} + \frac{M_0}{M_{pl,0}} \text{ in connecting face} \quad (5.6)$$

where N_{CIDECT} is the ultimate resistance predicted by CIDECT, f_{y0} is the yield strength of the chord, t_0 is the thickness of the chord, θ is the angle between the centerlines of the chord and the brace, β is the ratio of brace diameter to chord diameter ($\beta = d_1/d_0$), γ is $d_0/2t_0$, N_0 and M_0 are the axial force and the bending moment applied to the chord, $N_{pl,0}$ is the axial resistance of the chord, $M_{pl,0}$ is the plastic moment resistance of the chord, $C_1 = 0.45-0.25\beta$ for chord compression stress ($n<0$), and $C_1 = 0.20$ for chord tension stress ($n\geq 0$).

It should be noted that the mean strength function $Q_{u,\mathrm{Mean}}$ in CIDECT are derived from a regression analysis based on numerical database of normal strength steel T-joints, (van der Vegte *et al*. 2009) as follows

$$Q_{\mathrm{u,Mean}} = 1.19 \times 2.6\left(1+6.8\beta^2\right)\gamma^{0.2} \tag{5.7}$$

A safety factor of 1.19 was adopted for design.

b) EN 1993-1-8

In EN 1993-1-8, the design resistances of T-joints between CHS for chord plastification is calculated according to Equations 5.8 to 5.10 as follows:

$$N_{\mathrm{EC3}} = Q_u k_p \frac{f_{y0} t_0^2}{\sin\theta} \tag{5.8}$$

$$Q_u = (2.8 + 14.2\beta^2)\gamma^{0.2} \tag{5.9}$$

$$n_p = \frac{\sigma_{p,Ed}}{f_{y0}} \text{ in connecting face} \tag{5.10}$$

where N_{EC3} is the axial resistance predicted by EN 1993-1-8, $k_p = 1-0.3n_p(1+n_p)$ for $n_p > 0$ (compression) and $k_p = 0$ when $n_p \leq 0$ (tension), $\sigma_{p,Ed}$ is the maximum compressive stress in the chord excluding the stress due to components parallel to the chord axis.

It should be noted that in both design codes, there is a function which considers the effect of chord stress on the joint resistance. For these T-joints under brace compression, the applied axial load always causes large bending moment in the chord. Therefore, the chord stress function is lower than 1.0, which will result in a reduction in the joint resistance. For long chords, such a reduction will be significant.

The design resistances of all the T-joints are summarized in Table 5.7. For Joints T1-C, T3-C, T4 and T5, the calculated maximum bending moments in the chords all exceed the plastic moment resistances of the chord. Hence, an overall failure mode of chord bending is considered to be dominant in these joints. However, a local failure mode of chord plastification is considered to be dominant in Joints T2A and T2B through a back analysis on the maximum bending moments in the chords.

It is found that with the same geometric dimensions, the measured resistances of S690 Joints T2A and T2B are higher than those of the S355 Joint T1-C by 58% and 69% respectively. Similarly, the measured resistance of S690 Joint T4A is higher than that of the S355 Joint T3-C by 80%. By comparing results of Joints T4 and T5, it is shown that the resistance of a T-joint does not always increase by increasing the wall thickness of the brace.

Both CIDECT Design Guide 1 and EN1993-1-8 are considered to be structurally adequate for prediction of the axial resistances of T-joints between S690 CFCHS without the need of applying the reduction factors of 0.9 or 0.8. Even without these reduction factors, both formulae give an under-prediction of about 12% to 35%. The safety margin is considered to be quite large. Therefore, the strength reduction factor of 0.8 defined by EN 1993-1-12 is considered to be very conservative for these S690 T-joints in the present study, as it will give an even larger under-prediction of the joint resistances.

5.3 NUMERICAL INVESTIGATION

5.3.1 Proposed FE model

Nonlinear finite element models of these six T-joints between S355 and S690 CFCHS with brace axial compression are established and analyzed using the commercial finite element programme ABAQUS (2009). A large number of numerical investigations on T-joints between CHS have been conducted with shell elements in which the weld between the brace and the chord is simplified with shell elements so that their effects on strengths and stiffness of T-joints are considered. (van der Vegte and Makino, 2010)

In the present study, solid elements C3D8R are employed for modeling the T-joints. Three layers of solid elements are employed through the thickness of the CFCHS in order to capture local bending behaviour. A general mesh size of 6mm is determined through a mesh sensitivity study, after considering both computational efficiency and accuracy of the numerical results. An overall view of the finite element mesh of a typical T-joint is shown in Figure 5.11. Partial penetration butt-welds are simplified as deep penetration fillet welds in accordance with EN 1993-1-8 (2005). The weld size between the chord and the brace of each joint is determined as the average measured weld sizes obtained from the experiments.

The stress-strain curves of the S690 steel plates of 6 and 10 mm thick obtained from standard tensile tests are converted to true stress-strain curves, as illustrated in Figure 5.12. Stress-strain curves of S355 and S690 welds are simplified using an elastic-perfect plastic model. The initial elastic moduli of both S355 and S690 welds are taken as 210 kN/mm^2, according to EN 1993-1-1. The input true stress-strain curves of the welds are shown in Figure 5.13. The Poisson's ratio is taken as 0.3. Isotropic hardening rule and von Mises yield criterion are adopted.

5.3.2 Mesh convergence study

A convergence study on mesh configurations of the proposed model of Joint T2A is conducted to determine the optimum mesh size for the numerical simulation. Three different mesh sizes are adopted for comparison, i.e. 3 mm, 5 mm and 10 mm, as shown in Table 5.8. The detailed finite element meshes of these three models are presented in Figure 5.14.

Figure 5.15 illustrates a comparison of the results of these three models under axial compression in terms of applied load versus chord indentation curves. A convergence trend can be found among these three models from a coarser mesh to a finer mesh. The difference in axial resistances between "fine" and "very fine" meshes is only 0.35%, which is considered to be satisfactory. Therefore, a general mesh size of 5mm is adopted for subsequent numerical analyses in order to achieve both numerical accuracy and computational efficiency.

5.3.3 Boundary conditions

The boundary conditions of the proposed FE models are shown in Figure 5.16. Three reference points are set, and they are coupled with the nodes on both surfaces of the chord ends and the top surface of the brace with all six degrees of freedom. An axial load is applied onto Reference Point A through the static Riks method given in ABAQUS/Standard.

5.3.4 Validation of numerical models

Figures 5.17 to 5.22 illustrate both the observed and the predicted deformed shapes of the T-joints at failure. The measured and predicted axial load versus chord mid-span vertical displacement curves and the axial load versus chord indentation curves of each T-joint and compared in Figure 5.23 and Figure 5.24 respectively.

The axial resistances from the numerical results are also compared with the test results in Table 5.9. The differences between the measured and the predicted axial resistances of these T-joints are lower than 6%, with a mean value of the axial resistance ratio $N_{c,FE}$ / $N_{c,Test}$ of 1.00. Therefore, the proposed numerical models are found to be able to predict structural behaviour of these T-joints under brace axial compression well, and they are readily employed for subsequent parametric studies.

5.3.5 Parametric studies

In order to generate a comprehensive set of numerical data, a total of 186 numerical models are constructed to investigate effects of various parameters on the structural behaviour of T-joints between S690 CFCHS under brace axial compression. These parameters include yield strength of steel materials, various geometric parameters such as β, 2γ, and chord stress ratio, n. The numerical parametric study programme is shown in Table 5.10. It should be noted that β varies from 0.2 to 1.0, 2γ varies from 25 to 40, and n varies from -0.8 to +0.8. The thicknesses of the brace and the chord are 6 and 10 mm respectively. The geometrical dimensions of the FE models for the parametric studies are presented in Table 5.11. True stress-strain curves of S690 steel plates and the welds are input in the FE models, as described in the previous section. The weld size of each joint is set to satisfy the requirement by Clause 4.5.2 in EN 1993-1-8 (CEN, 2005) and Clause 3.9 in CIDECT Design Guide 1 (Wardenier *et al*. 2008). The minimum throat thickness a is assigned to be $1.48t_1$, where t_1 is the thickness of the brace.

A method to eliminate chord bending moments

It should be noted that the failure mode of these T-joints under brace axial compression is found to be an interaction between chord overall bending and chord local plastification. Separate failure modes are difficult to be obtained through experiments. However, effects of chord bending moment can be compensated by applying negative bending moments at the chord ends in numerical analyses (van der Vegte and Makino, 2005) and the magnitudes of these chord end moment are calculated according to Equation 5.11 as follows:

$$M_{0,end} = 0.25N(L - d_1) \tag{5.11}$$

where L is the span of the chord, N is the applied axial force and d_1 is the outer diameter of the brace.

By adopting this method, the failure mode for each T-joint with compensating chord end moments will be chord plasitfication only. After bending moments due to brace compression are eliminated, the numerical results are ready for direct comparison with predictions from various design specifications.

Figure 5.25 shows a comparison of the applied load versus chord indentation curves of Joint T2A with and without chord end compensation moments. The predicted axial resistance of Joint T2A with chord end compensation moments is 1140 kN, which is found to be higher than the regular corresponding resistance without compensation moments at

864 kN, by 32%. The difference between these two values indicates the significant effect of chord bending moment due to a brace axial load.

Therefore, in the subsequent parametric studies, all FE models are analyzed with chord end compensation moments so that the numerical results will not be influenced by chord bending moments due to brace axial loads.

Effect of chord length parameter, α (= 2 L_0 / d_0)

Previous studies from van der Vegte and Makino (2010) have shown that a chord length of 6d_0 (α = 12) is considered to be sufficient to exclude the influence of the chord length on the axial resistance of T-joints between CHS, especially when γ and β are relatively small (2γ = 25.4 or β = 0.25). For all the T-joints in the present study, α is 9.6, which is smaller than the suggested value proposed by van der Vegte and Makino (2010). Therefore, a parametric study on α is carried out.

6 FE models of these T-joints with three different values of the chord length parameter α at 9.6, 15.0 and 20.0 and two different values of the brace to chord diameter ratio, β at 0.6 and 0.8 are established.

The load versus chord indentation curves of these T-joints with different values of α when β = 0.6 are shown in Figure 5.26. Figure 5.27 illustrates the normalized axial resistances of the S690 T-joints with different values of α and β.

It is shown that the chord length parameter α has almost no influence on the axial resistances of these S690 T-joints with chord end compensation moments when $\alpha \geq 9.6$. Therefore, α = 9.6 is considered to be sufficient in this study to exclude any effect of chord end conditions and of bending moments due to brace axial loads.

Effect of brace to chord diameter ratio, β (= d_1 / d_0)

Figure 5.28 illustrates the effect of β on the axial resistances of T-joints with different values of 2γ at 25, 30, 35 and 40. The axial resistances of these T-joints are normalized with f_{y0} t_0^2, and they are compared with those predicted resistances according to i) CIDECT mean strength equations, Equation 5.7 and design equations, Equations 5.3 to 5.6 , and ii) EN 1993-1-8 equations, Equations 5.8 to 5.10. In general, the axial resistances of these T-joints are found to increase with an increase of β.

The numerical results are found to be larger than the design resistances according to both design codes, but smaller than the predictions according to CIDECT mean strength equations, except when β=1.0. Among these three equations, CIDECT design equations give the most accurate predictions for the axial resistances of these T-joints.

Effect of chord diameter to thickness ratio, 2γ (= d_0 / t_0)

Figure 5.29 illustrates the effect of γ on the axial resistances of these T-joints with different values of β at 0.2, 0.4, 0.6, 0.8 and 1.0. Similarly, it is found that the axial resistances increase with an increase of γ. The dotted line in the figure shows the predicted resistances from the CIDECT design equation. When β is small, CIDECT is found to be able to give accurate predictions. However, as β is increases, CIDECT design resistances are found to be increasingly conservative.

Effect of chord stress ratio, n

EN1993-1-8 defines a chord stress function, k_p , to consider a reduction to the axial resistances of these T-joints due to different levels of chord stresses. Similarly, a function of Q_f is also defined in CIDECT Design Guide 1. The detail formulae have been described in Section 5.2.3. It should be noted that in EN 1993-1-8, no reduction is considered when the chord is in tension. This is subsequently modified in CIDECT in order to provide more accurate predictions for the axial resistances of these T-joints.

Figure 5.30 illustrates the numerical reduction factors with different chord stress ratios when 2γ = 25. It is found that the numerical results are larger than the predicted results obtained from either CIDECT Deisgn Guide 1 or EN 1993-1-8. When the chords are in compressive stresses, the predictions of both design specifications are very close to each other while when the chords are in tensile stresses, the predictions to CIDECT provide more conservative results.

It should also be noted that when β is small ($\beta \leq 0.4$) and the chords are under moderate tensile stresses, there is a strength enhancement to the axial resistances of these T-joints.

Hence, it is considered that the chord stress function proposed in CIDECT Design Guide 1 is sufficiently accurate to predict any reduction in the axial resistances of these T-joints in the presence of both compressive and tensile chord stresses.

5.3.6 Summary of parametric study results

A series of parametric studies have been carried out to study effects of various parameters on the axial resistances of T-joints under brace axial compression. According to the numerical results, CIDECT Design Guide 1 is generally considered to be applicable for the design of T-joints between high strength S690 CFCHS as it provides more accurate predictions than those design equations given in EN 1993-1-8.

The current reduction factors of 0.8 in EN 1993-1-12 and 0.9 in CIDECT Design Guide 1 are both considered to lead to very conservative design resistances of these T-joints between S690 CFCHS under axial compression. It is suggested that these reduction factors should be removed to improve structural efficiency.

5.4 CONCLUSIONS

In this chapter, an experimental and numerical investigation into structural behaviour of T-joints between S690 CFCHS is presented.

It should be noted that:

a) A total of six T-joints between S355 and S690 CFCHS have been successfully tested under brace axial compression. All test specimens are found to have sufficient strength and ductility.

b) With the same geometric dimensions, the measured resistances of those S690 joints are higher than those of the S355 joints by 58% to 80%. Hence, the axial resistances of these T-joints do not increase in a linear manner with an increase in the wall thickness of the brace or steel grade.

c) Current design rules provided in CIDECT Design Guide 1 and EN1993-1-8 are considered to be structurally adequate for prediction of the axial resistances of these T-joints between S690 CFCHS with a large safety margin.

d) Through a series of parametric studies on these T-joint between CFCHS, CIDECT Design Guide 1 is shown to provide more accurate prediction in the axial resistances of the T-joints than those design equations provided in EN 1993-1-8. Current reduction factors of 0.8 in EN 1993-1-12 and 0.9 in CIDECT Design Guide 1 are suggested to be removed to improve structural efficiency while maintaining a sufficient safety margin.

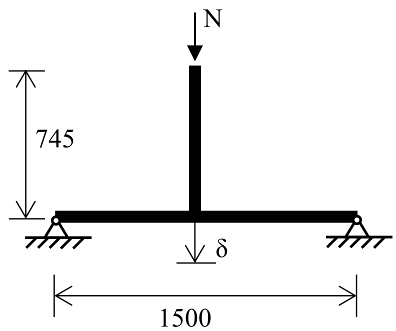

Figure 5.1 Schematic view of a T-joint test under brace axial compression

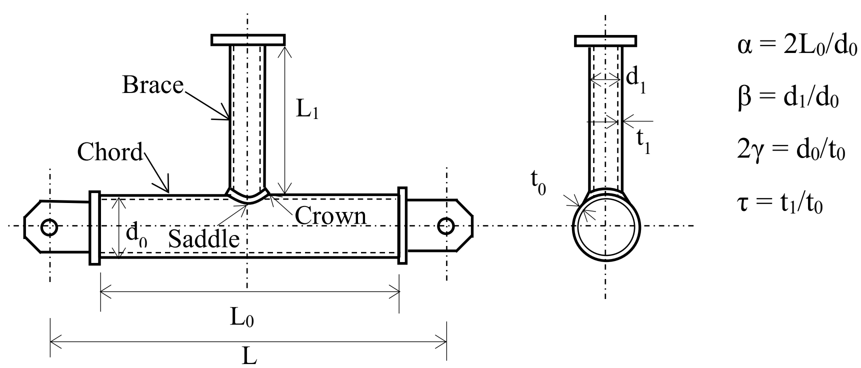

Figure 5.2 Configuration of a typical T-joint

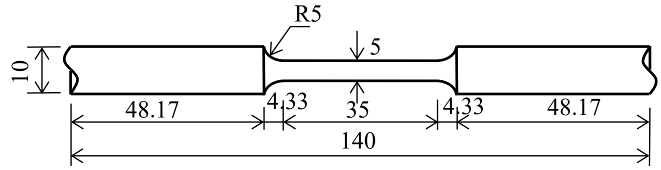

(a) Standard coupon for 10 mm thick steel plates

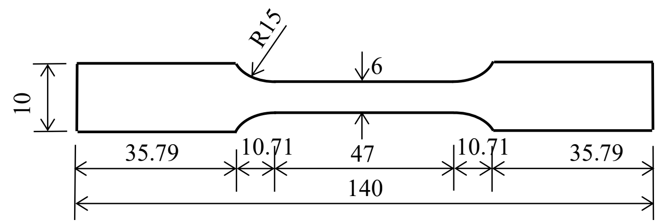

(b) Standard coupon for 6 mm thick steel plates

Figure 5.3 Geometric properties of standard tensile coupons

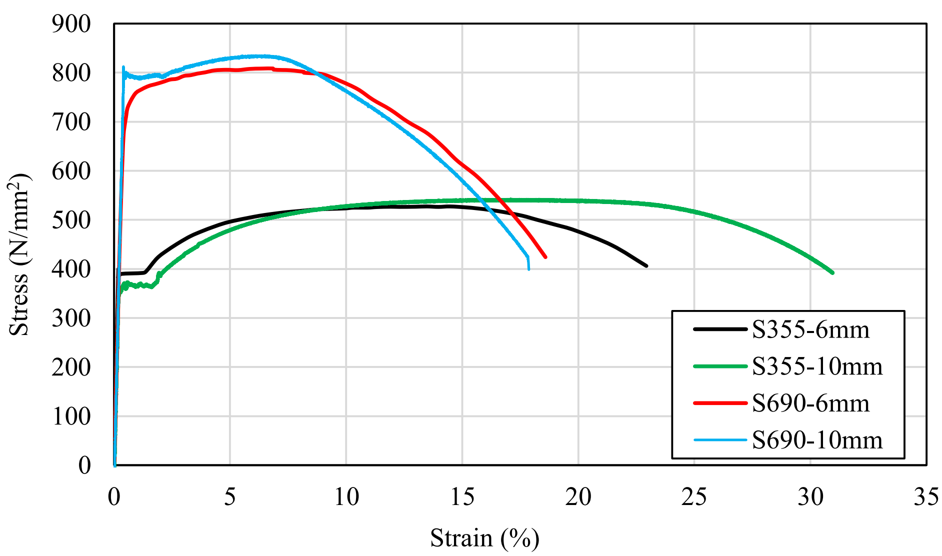

Figure 5.4 Measured stress-strain curves of S355 and S690 steel plates

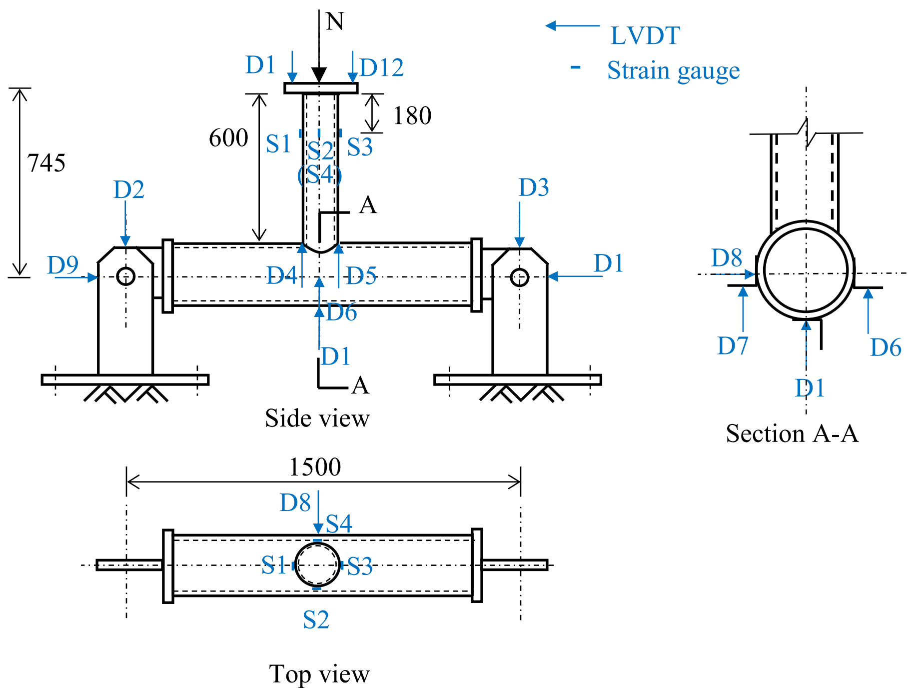

Figure 5.5 Test setup and instrumentation

Joint T1-C

Joint T2A

Joint T2B

Joint T3-C

Joint T4

Joint T5

Figure 5.6 Deformed T-joints under brace axial compression after test

Local plastic deformation of the chord

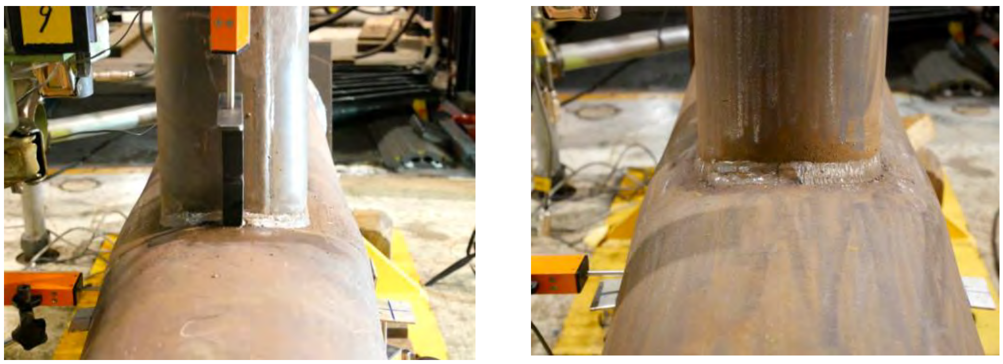

Out-of-plane ovalization of the chord

Figure 5.7 Typical local failure of Joint T2A

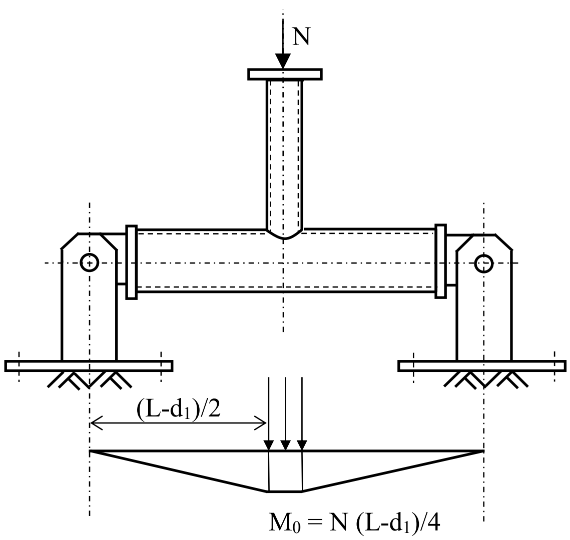

Figure 5.8 Bending moment of the chord in a typical T-joint test

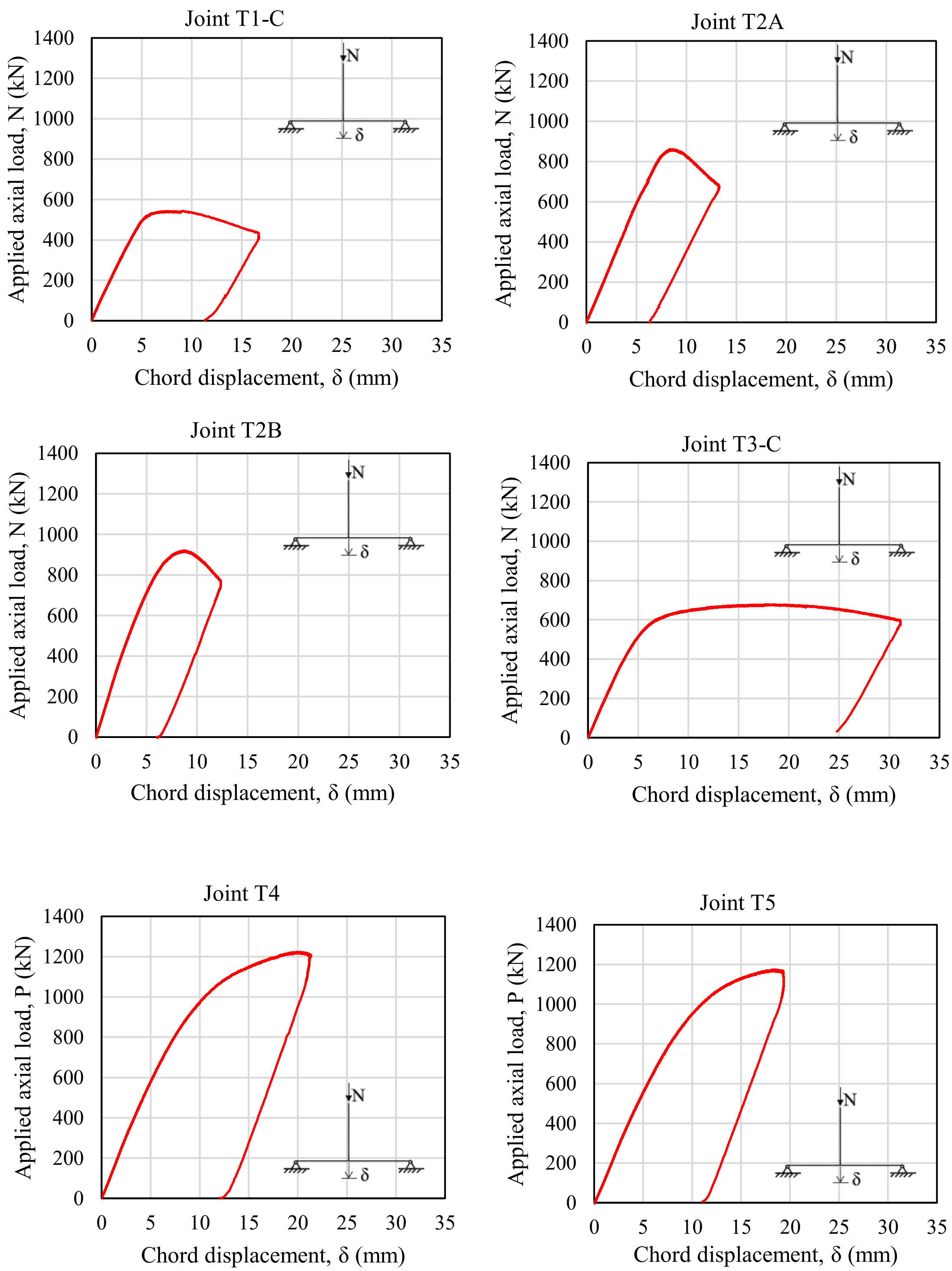

Figure 5.9 Applied load-chord mid-span vertical displacement curves of T-joints between CFCHS

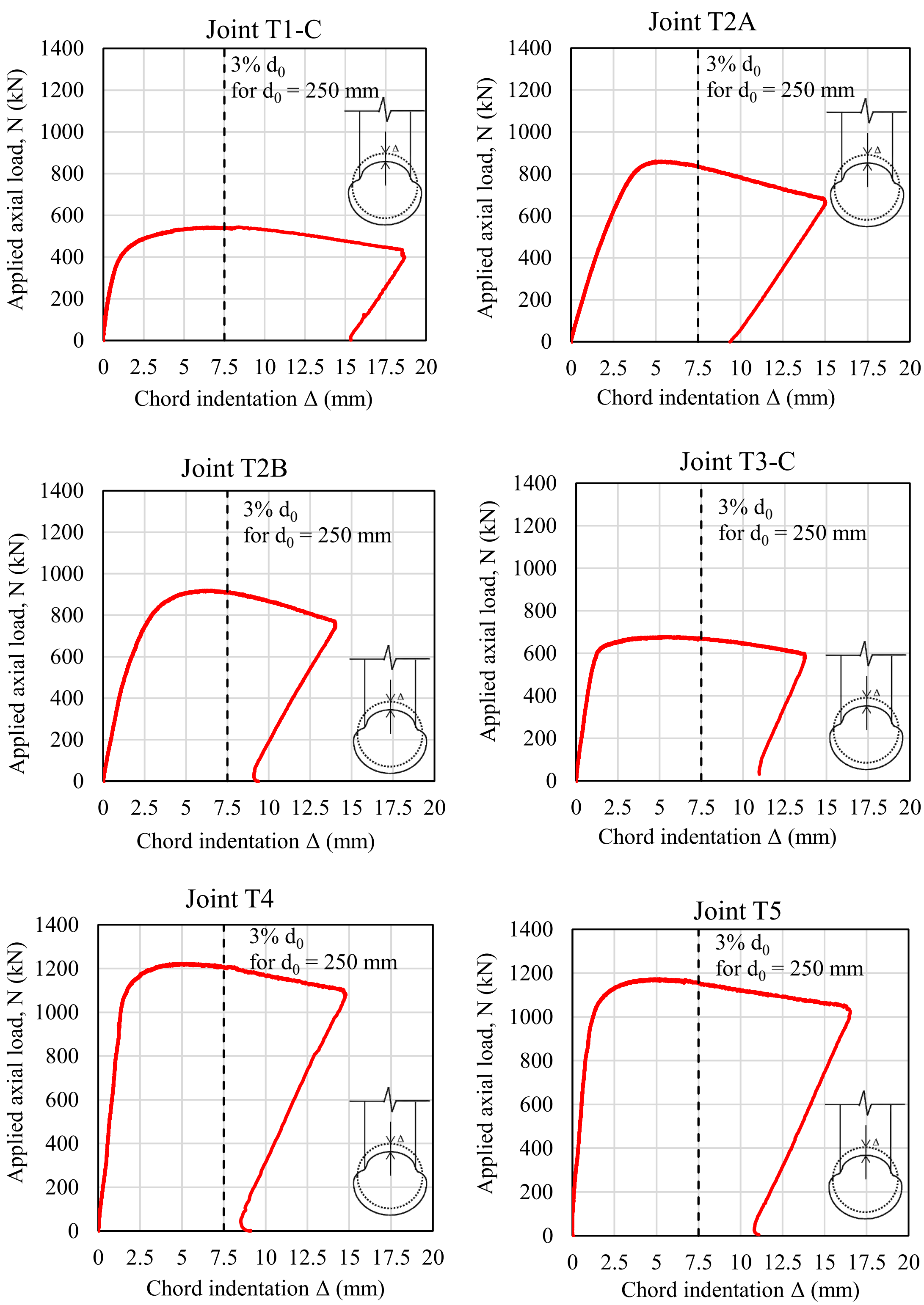

Figure 5.10 Applied load-chord indentation curve of T-joints between CFCHS

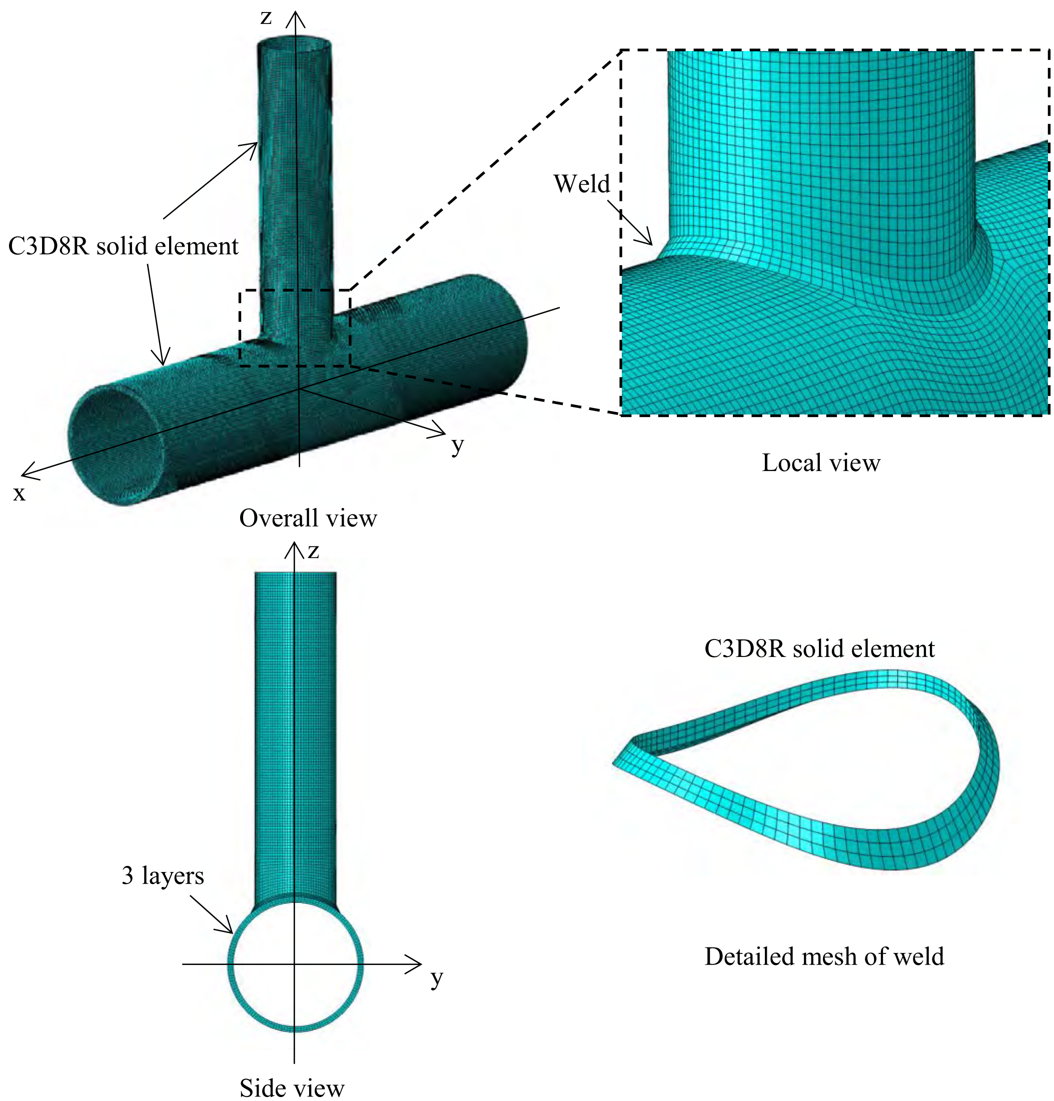

Figure 5.11 Finite element mesh of a typical T-joint

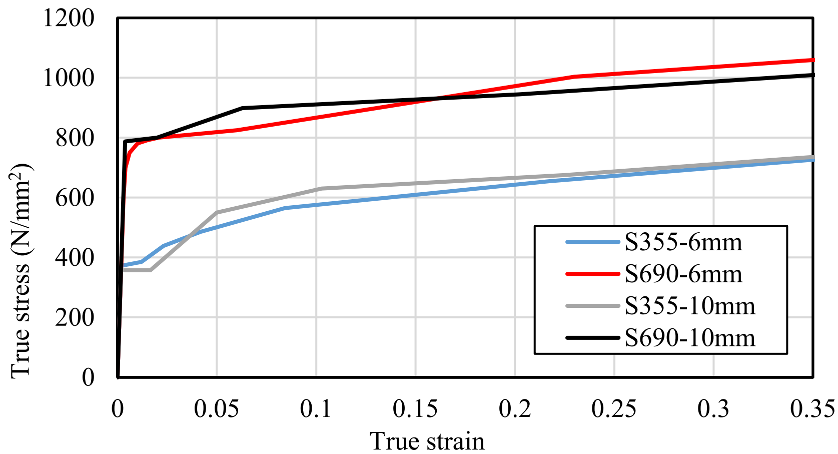

Figure 5.12 True stress-strain curves for numerical study

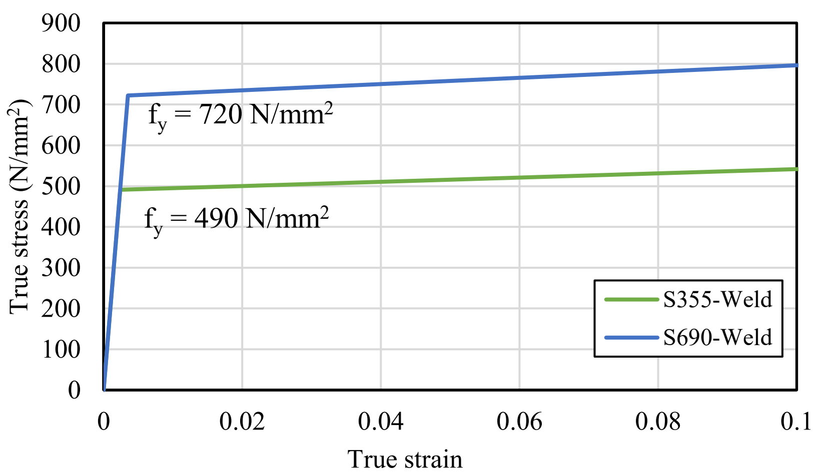

Figure 5.13 True stress-strain curves for the welds

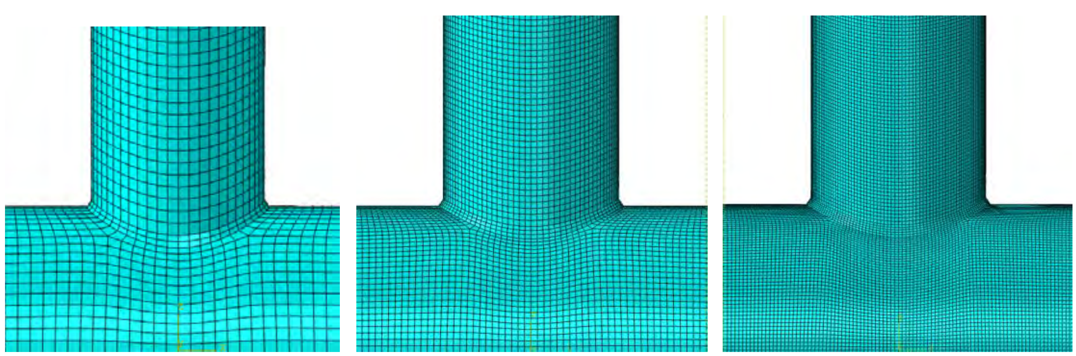

a) Coarse mesh　　b) Fine mesh　　c) Very fine mesh

Figure 5.14 Detail of finite element mesh

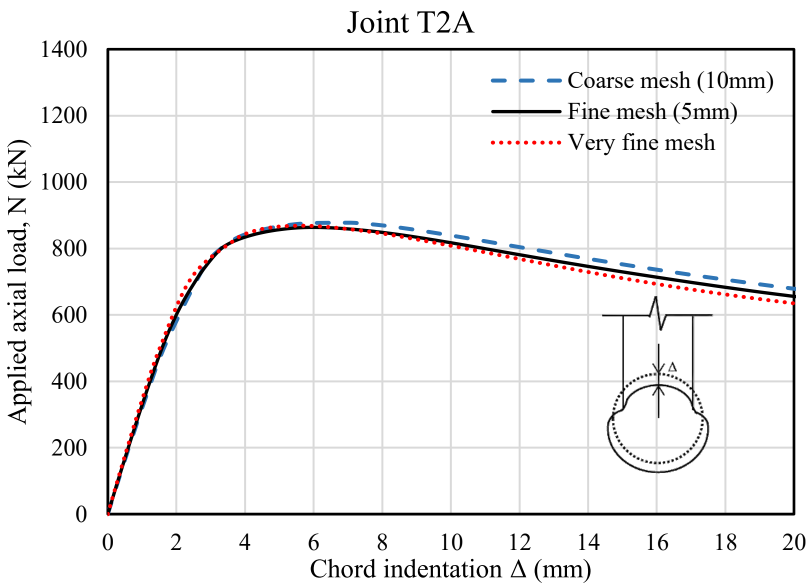

Figure 5.15 Results of mesh convergence study

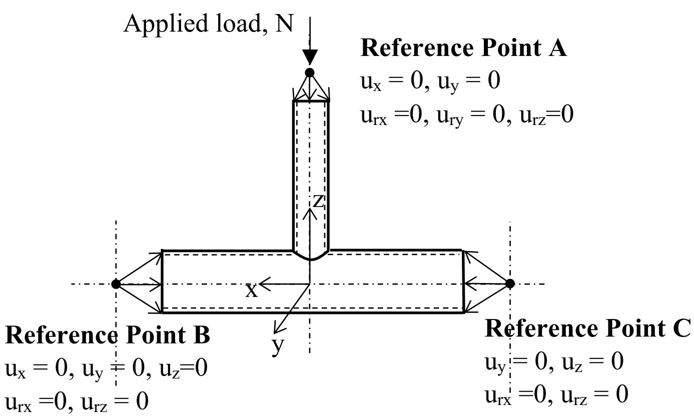

Figure 5.16 Boundary conditions for the FE models

Joint T1-C

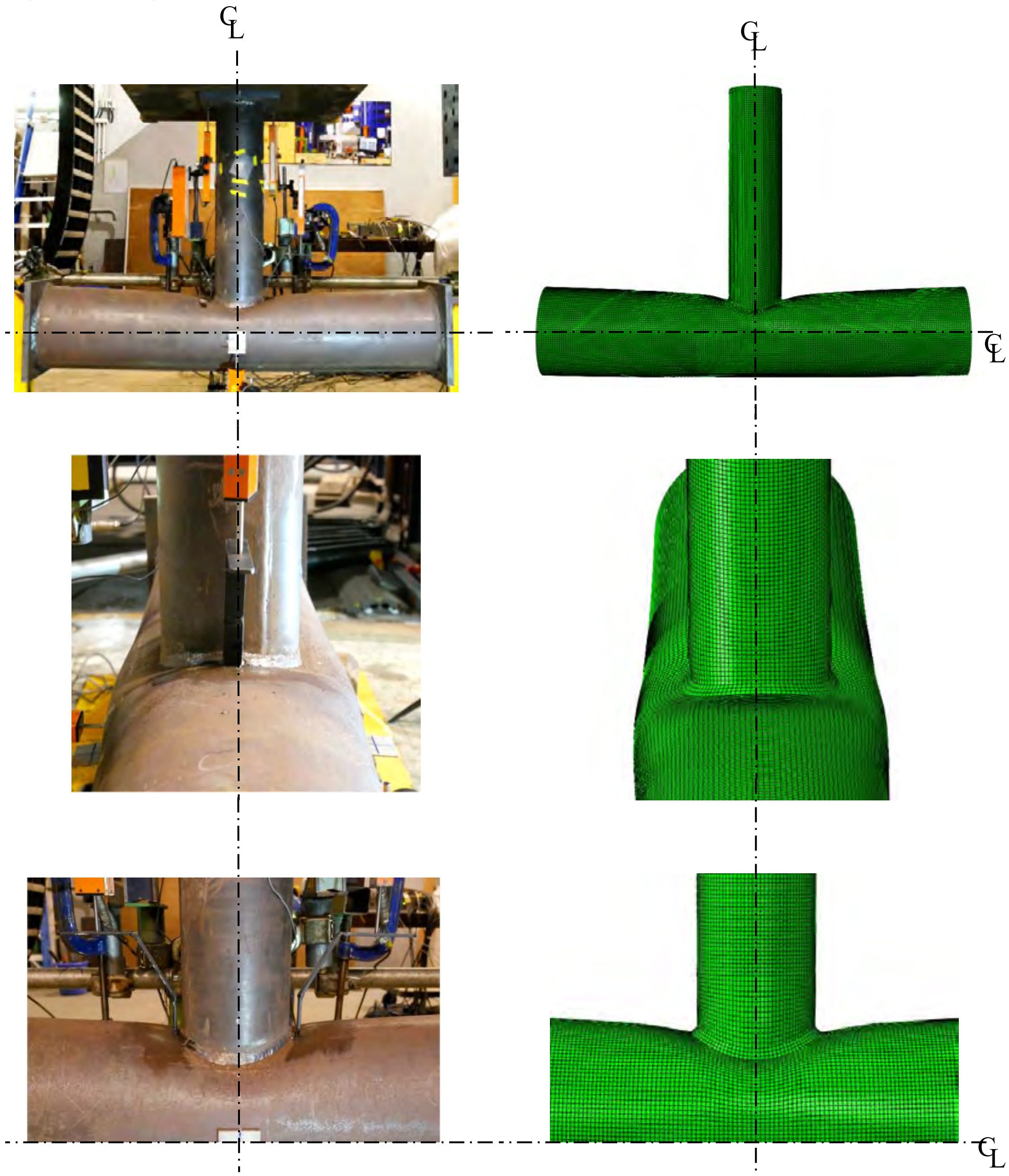

Figure 5.17 Observed and predicted deformed shapes of Joint T1-C

Joint T2A

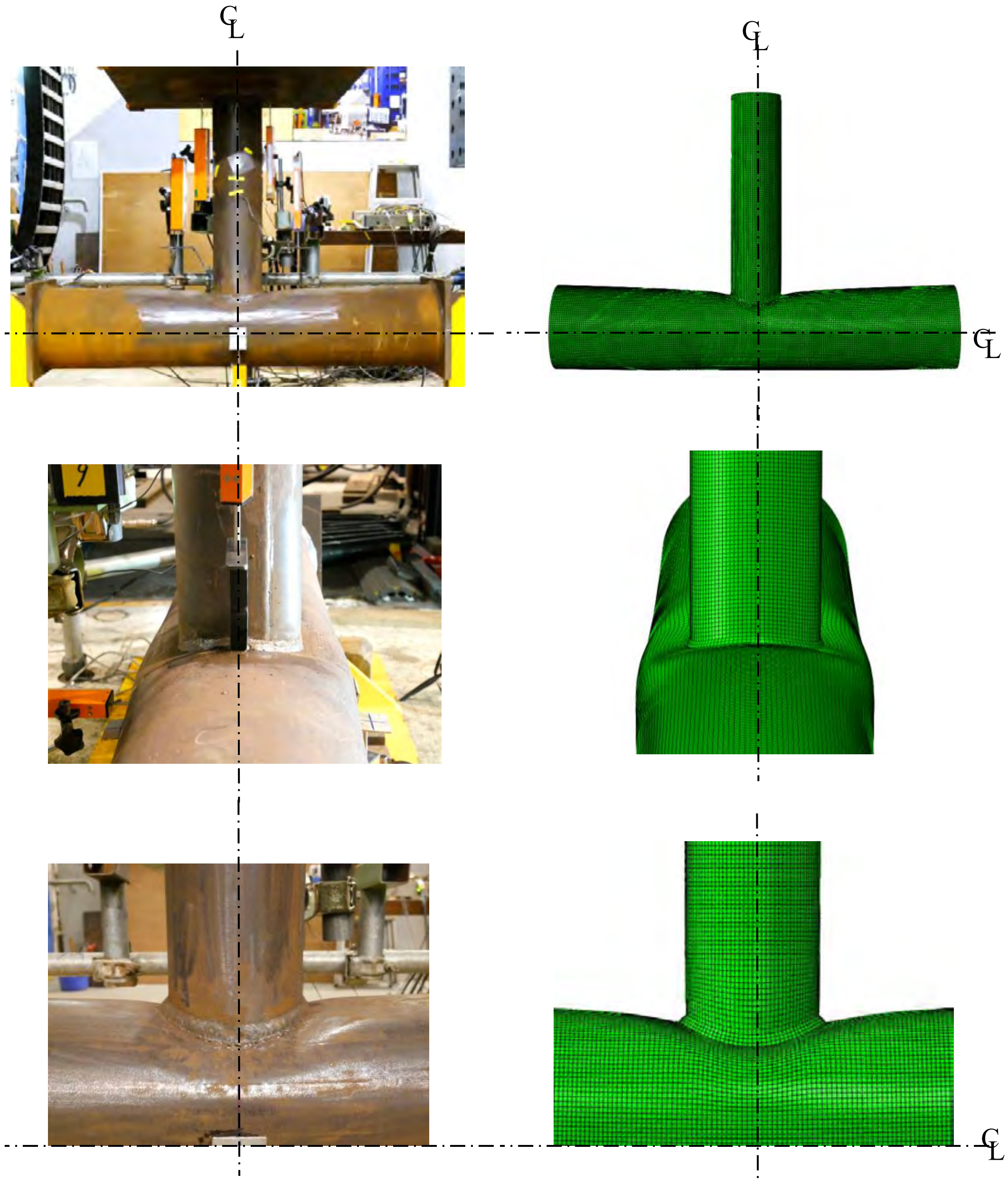

Figure 5.18 Observed and predicted deformed shapes of Joint T2A

Joint T2B

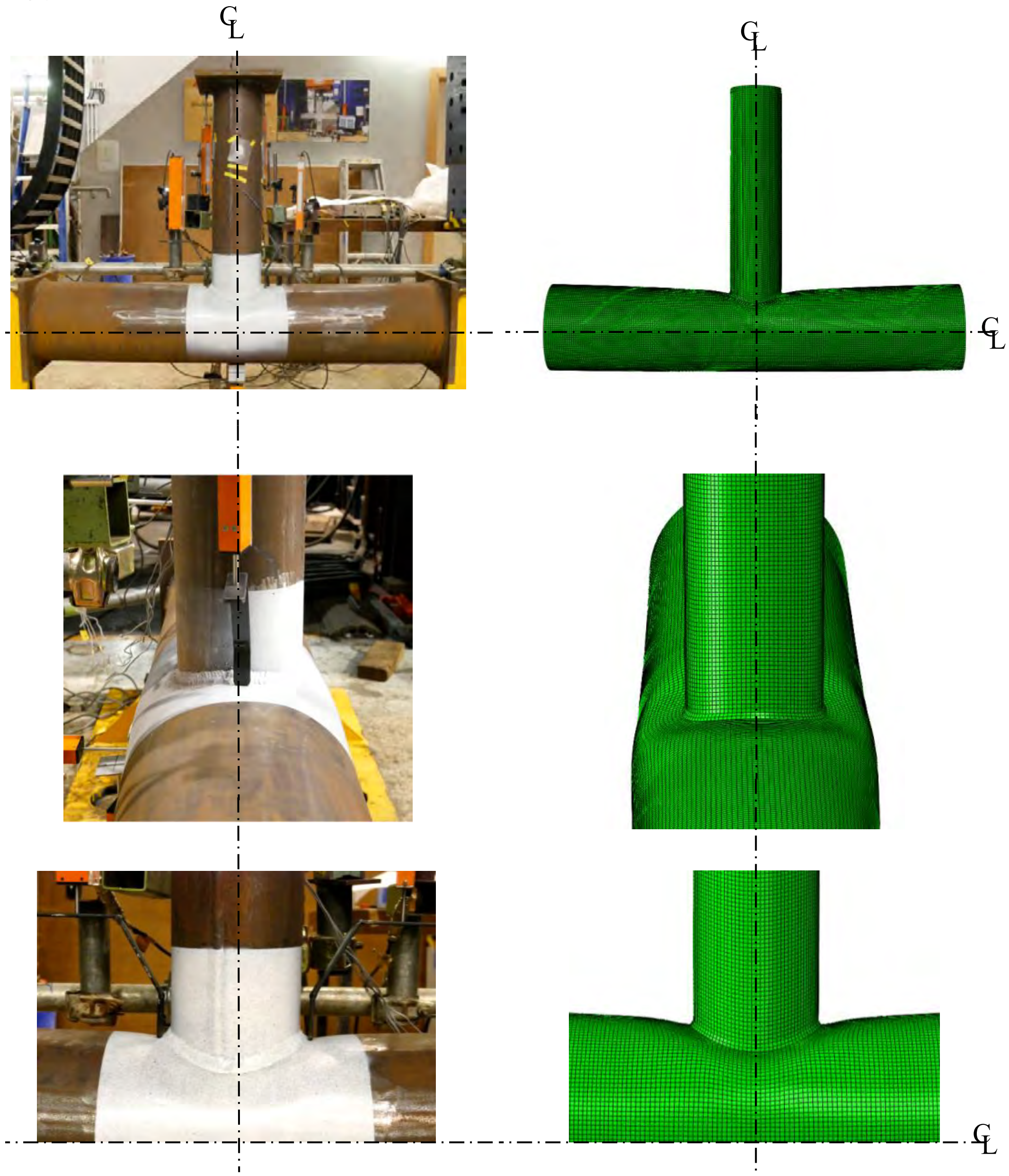

Figure 5.19 Observed and predicted deformed shapes of Joint T2B

Joint T3-C

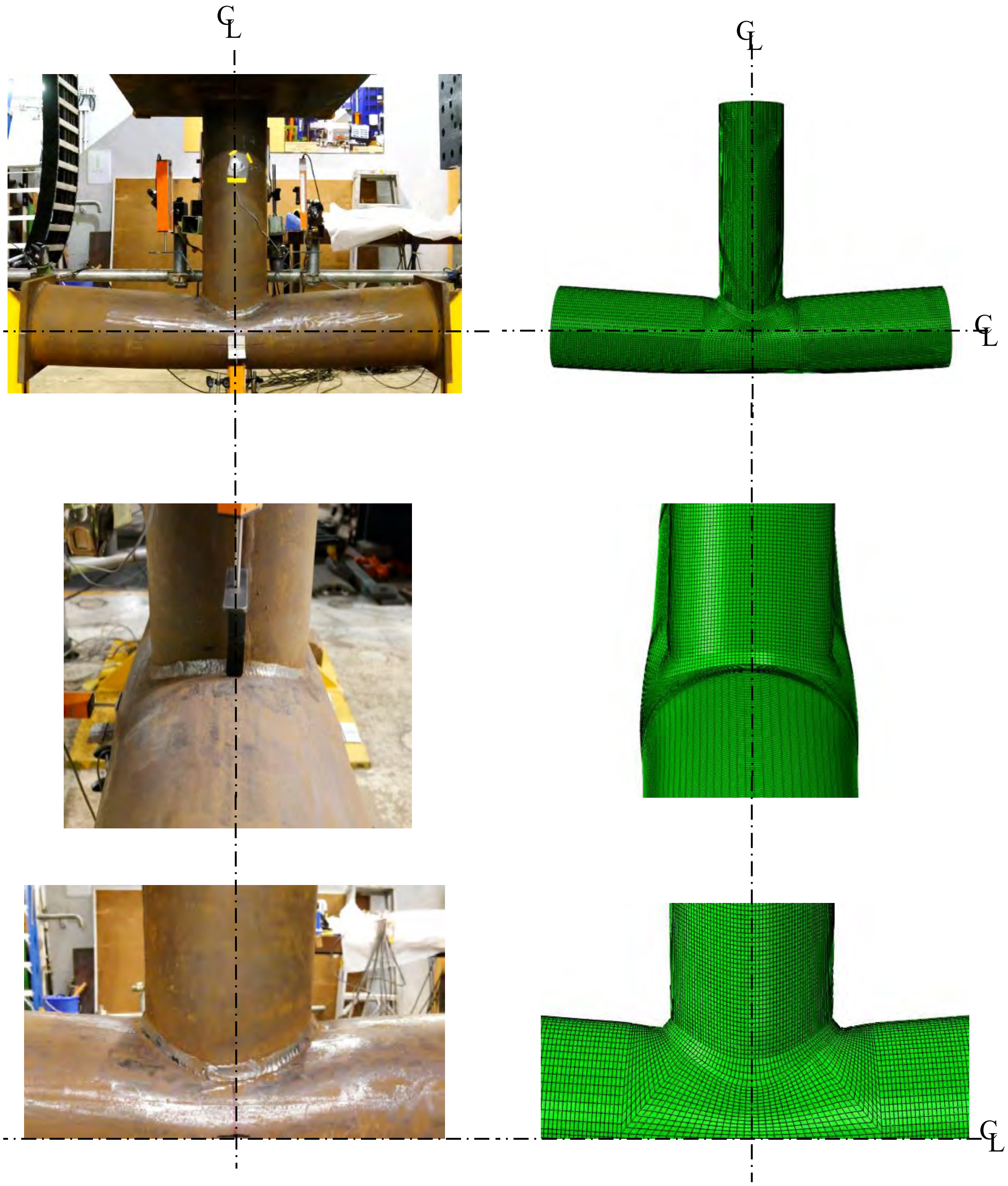

Figure 5.20 Observed and predicted deformed shapes of Joint T3-C

Joint T4

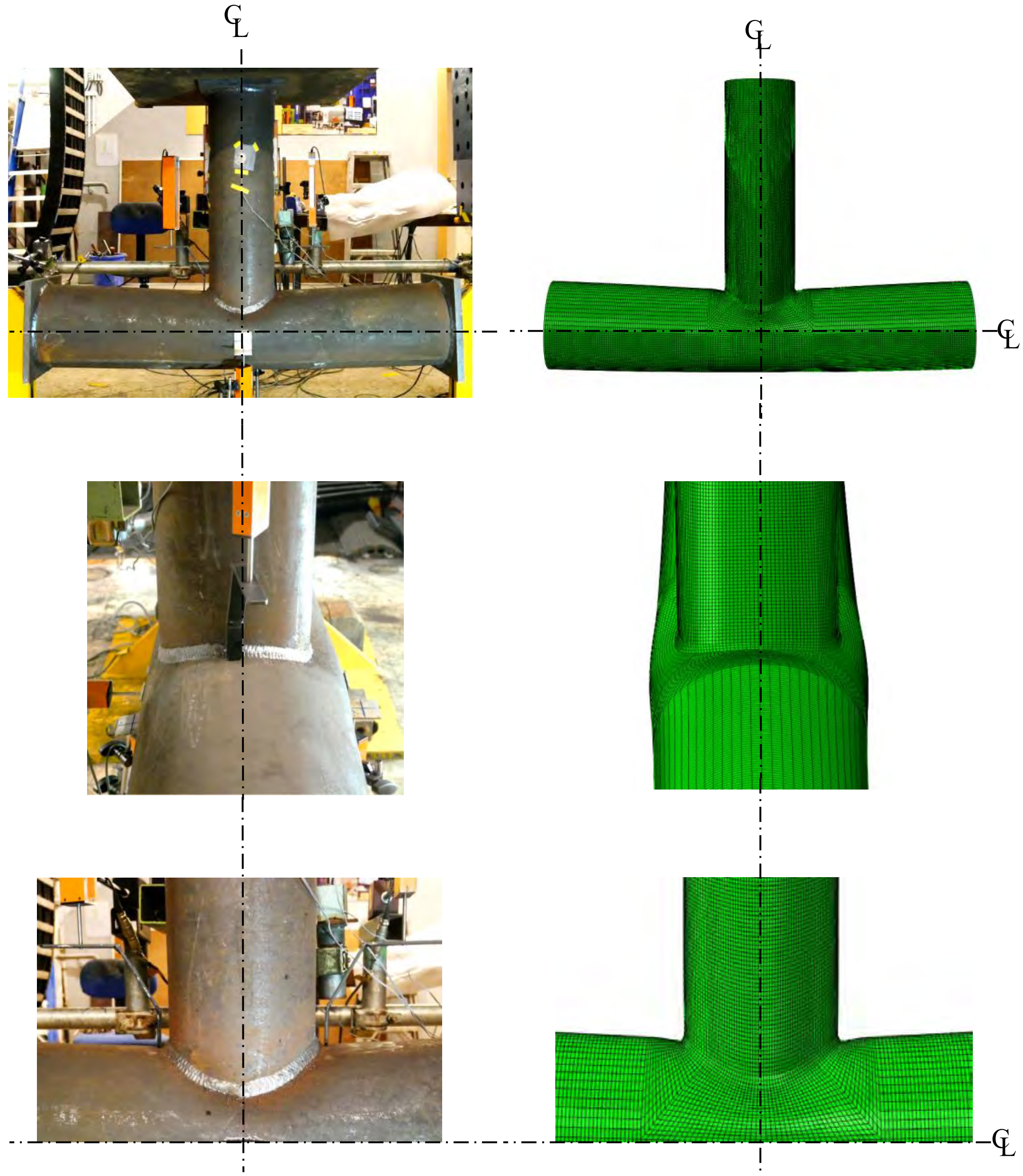

Figure 5.21 Observed and predicted deformed shapes of Joint T4

Joint T5

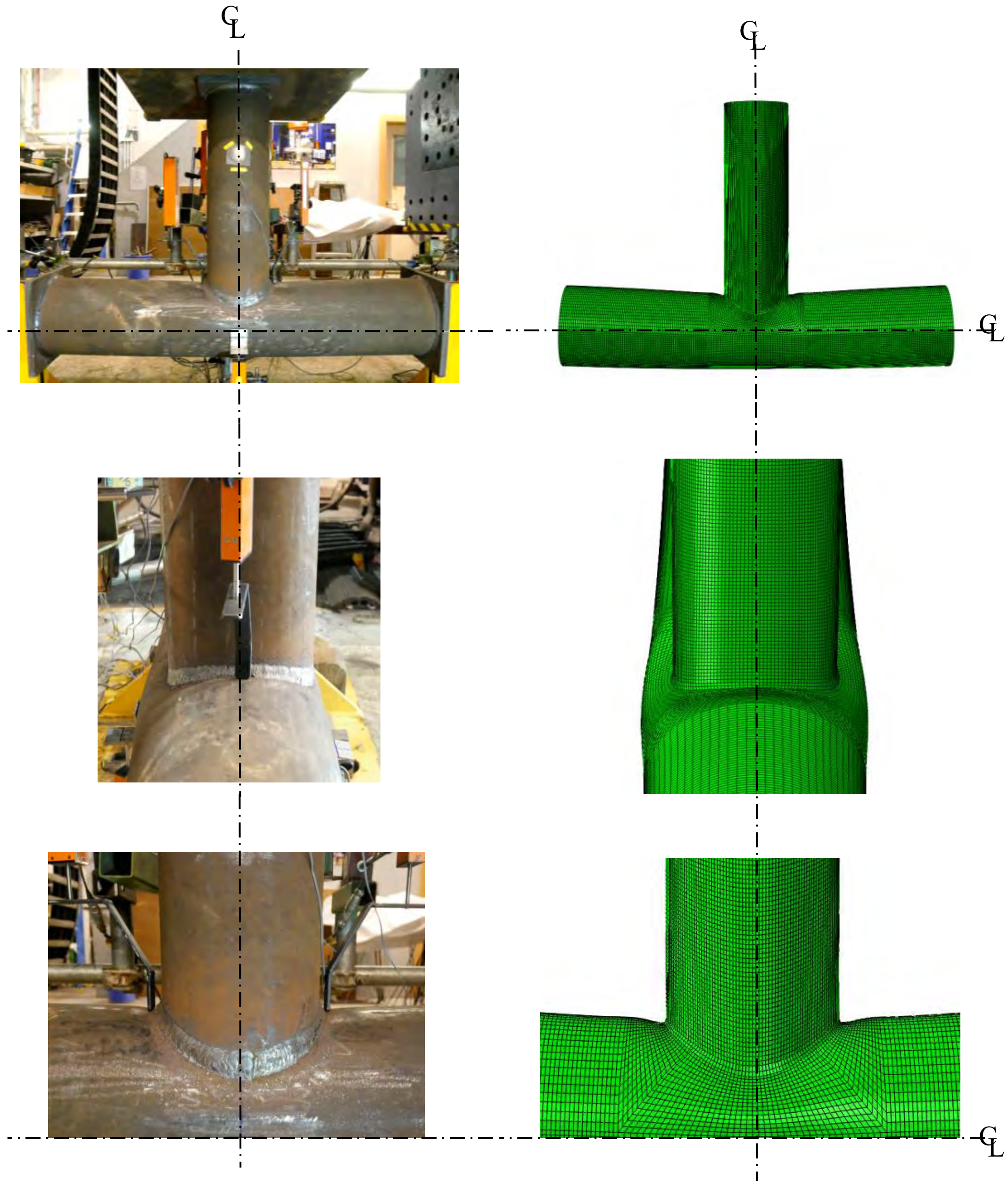

Figure 5.22 Observed and predicted deformed shapes of Joint T5

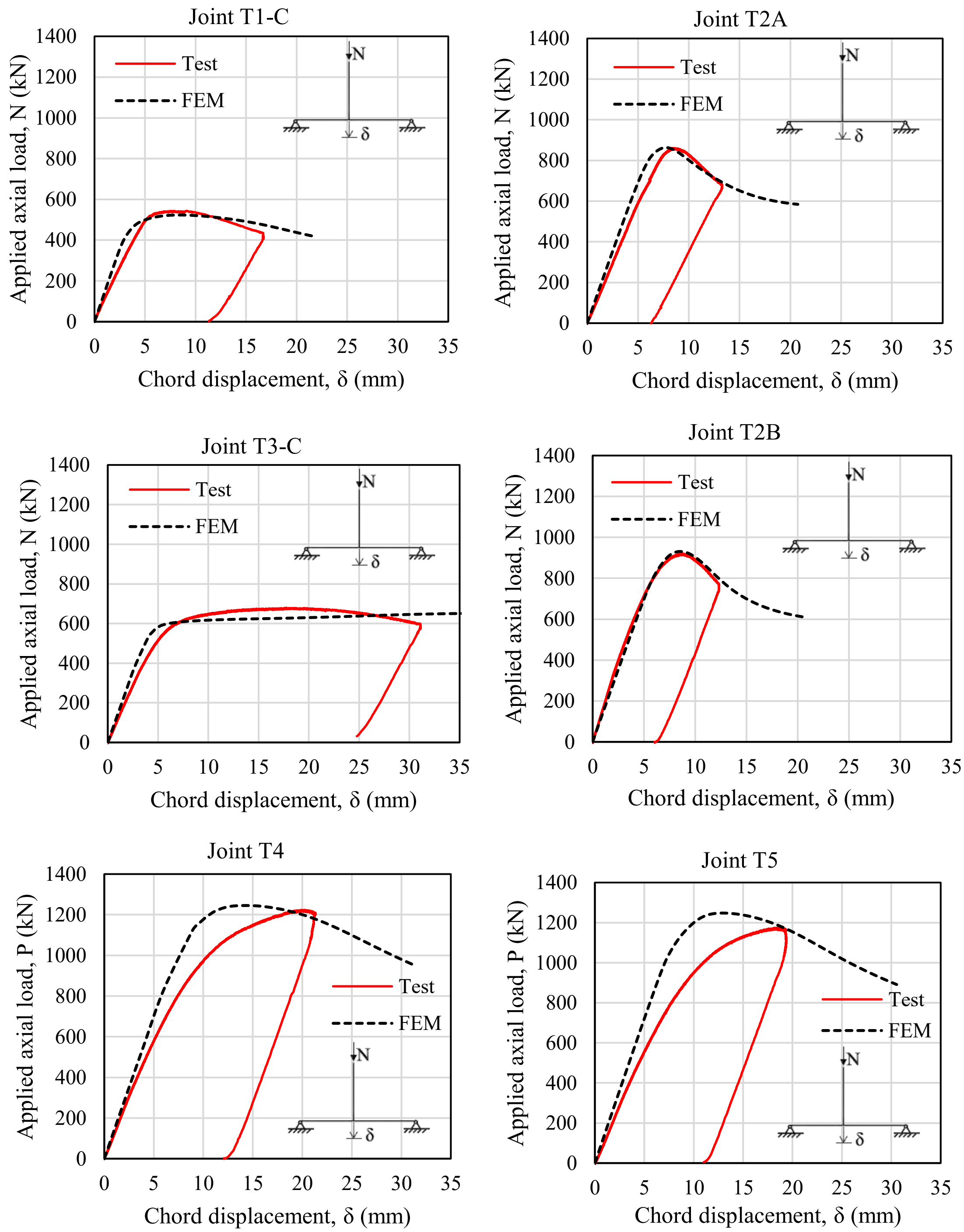

Figure 5.23 Applied load-chord mid-span vertical displacement curves of T-joints between CFCHS

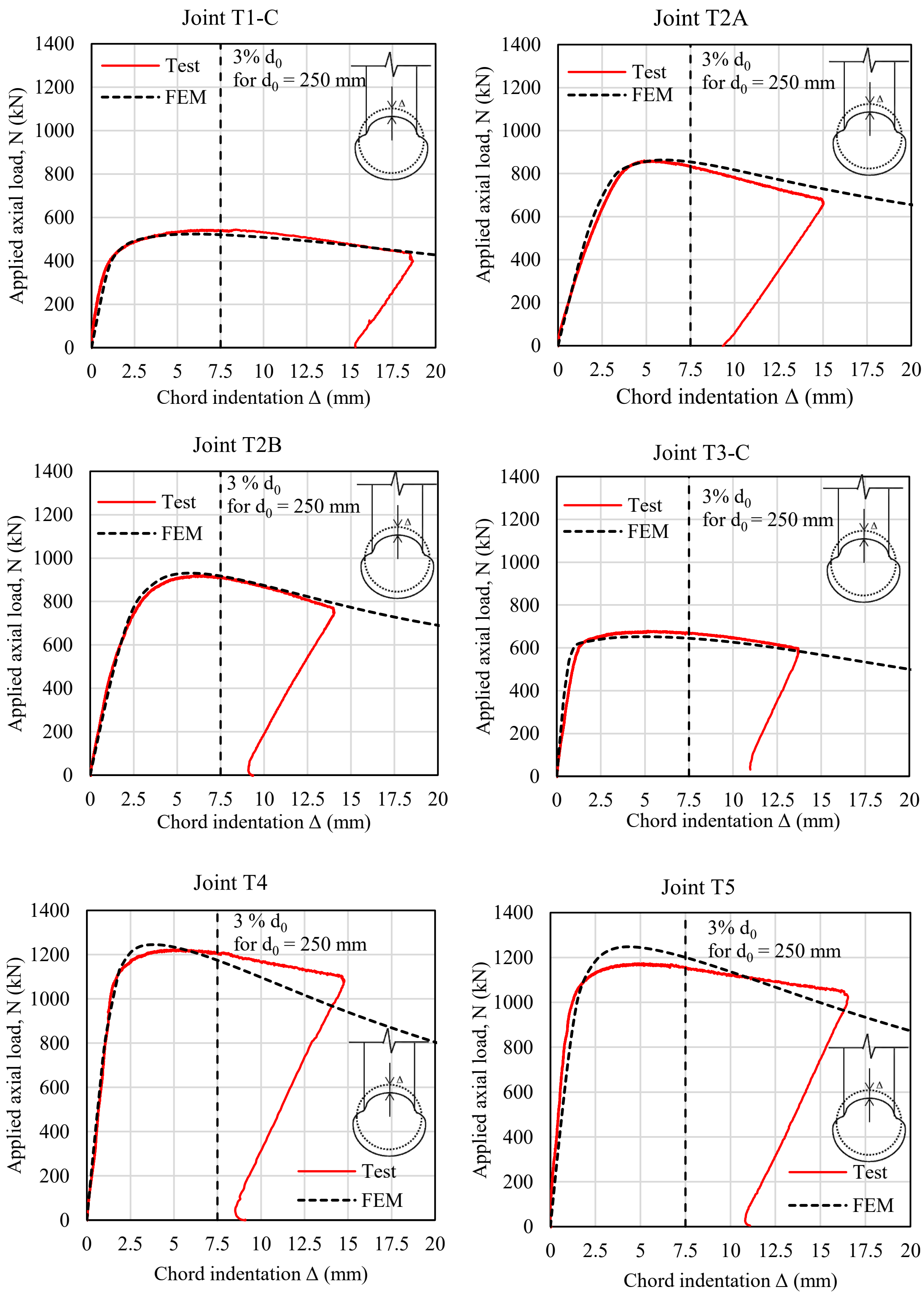

Figure 5.24 Load-chord indentation curves of T-joints between CFCHS

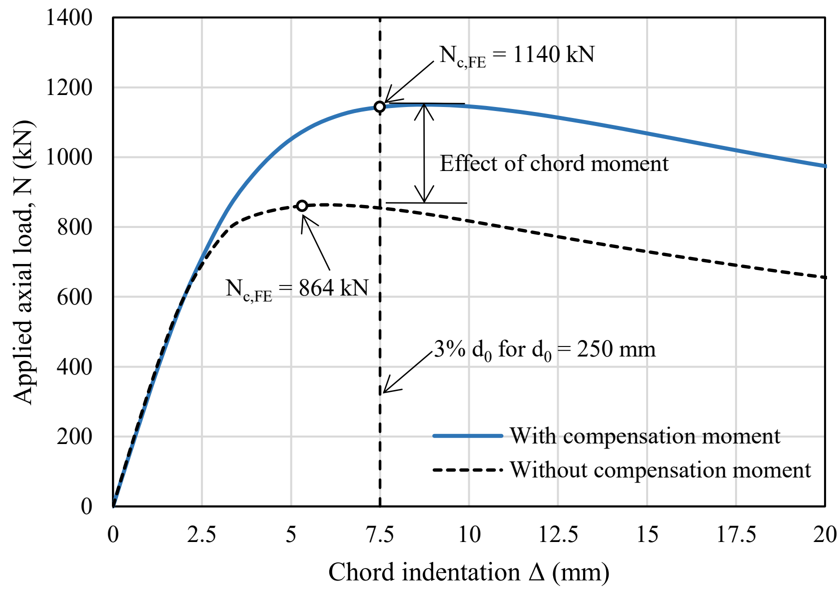

Figure 5.25 Load-chord indentation curves of Joint T2A with and without chord end compensation moments

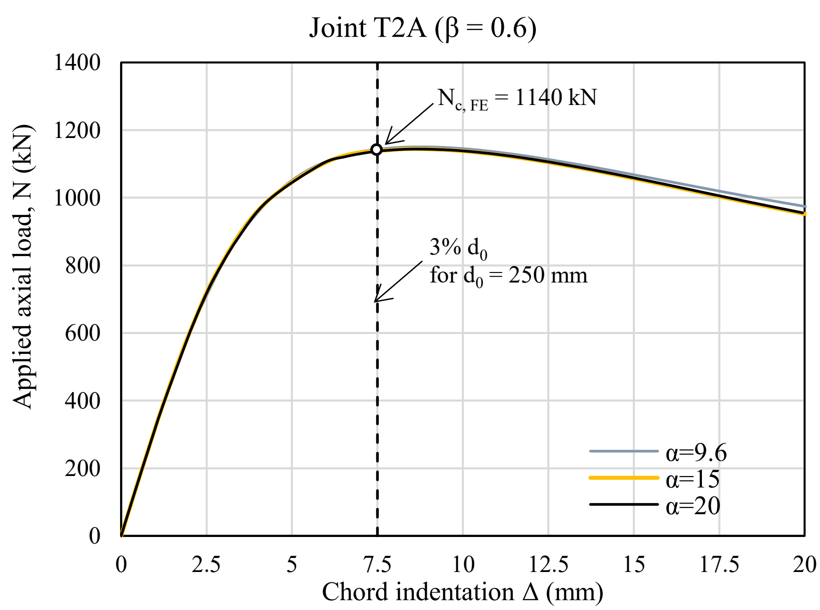

Figure 5.26 Effect of chord length parameter α on axial resistance of a typical T-joint between CFCHS

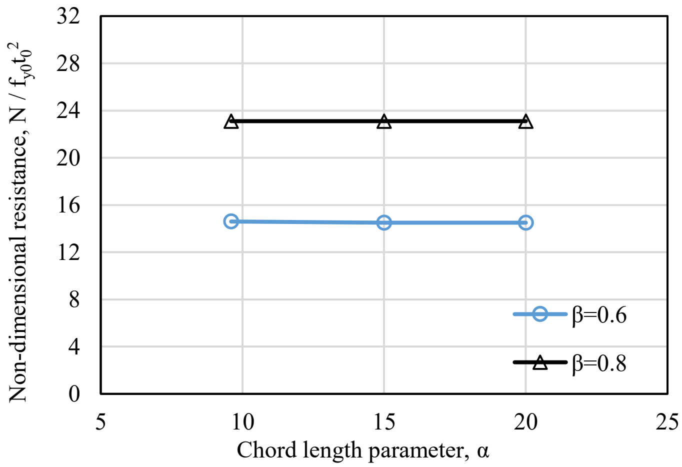

Figure 5.27 Effects of chord length parameter α on axial resistances of T-joints between CFCHS

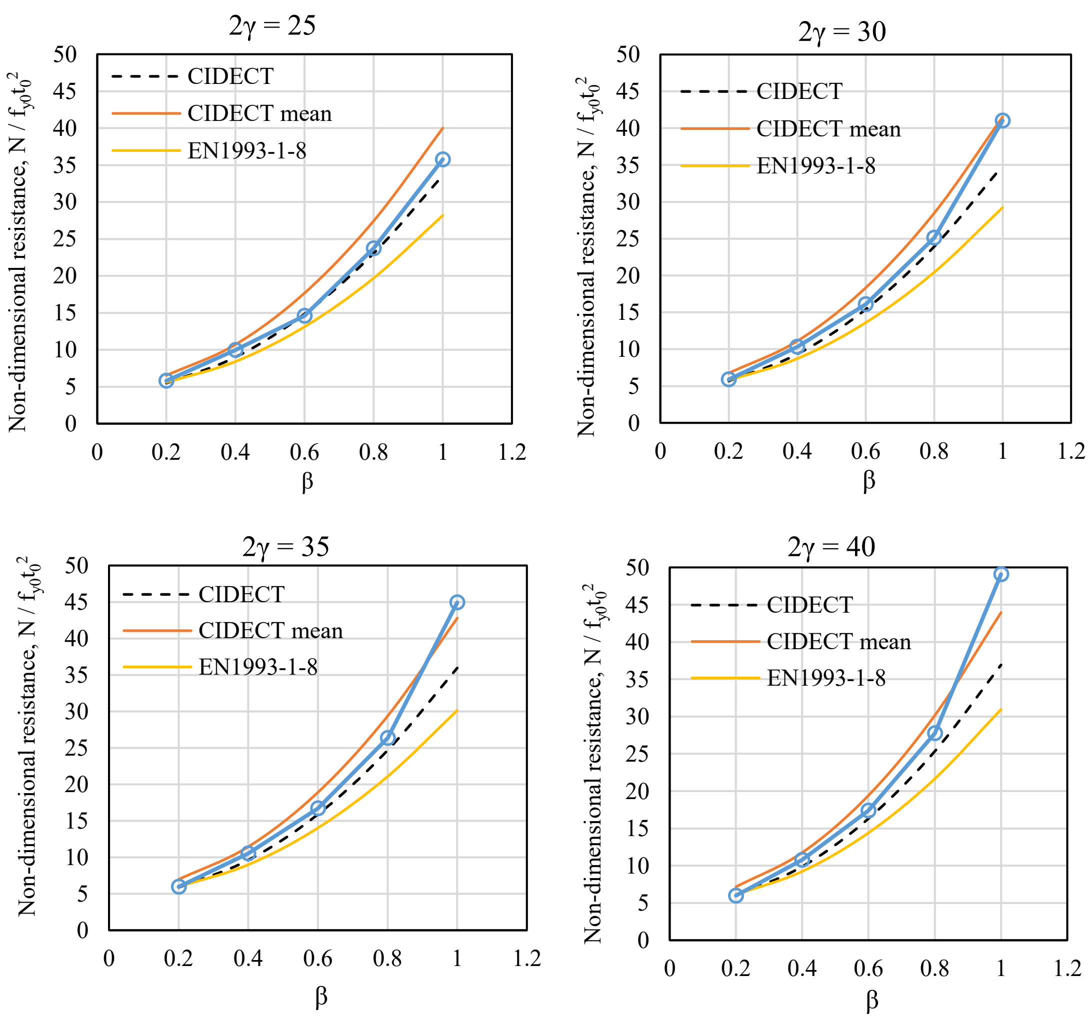

Figure 5.28 Effects of parameter β on axial resistances of T-joints between CFCHS

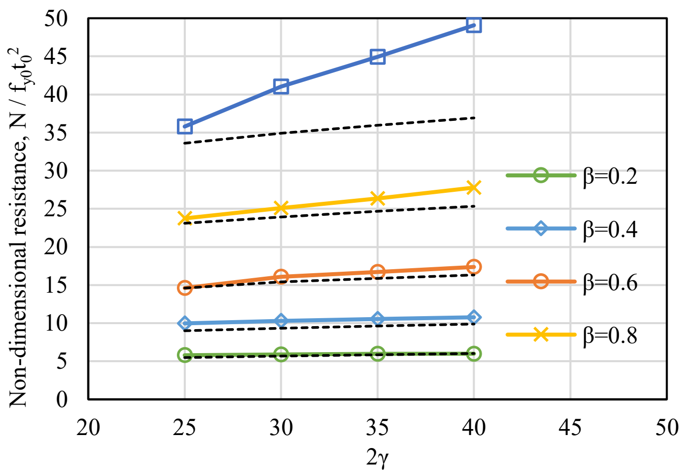

Figure 5.29 Effects of parameter 2γ on axial resistances of T-joints between CFCHS

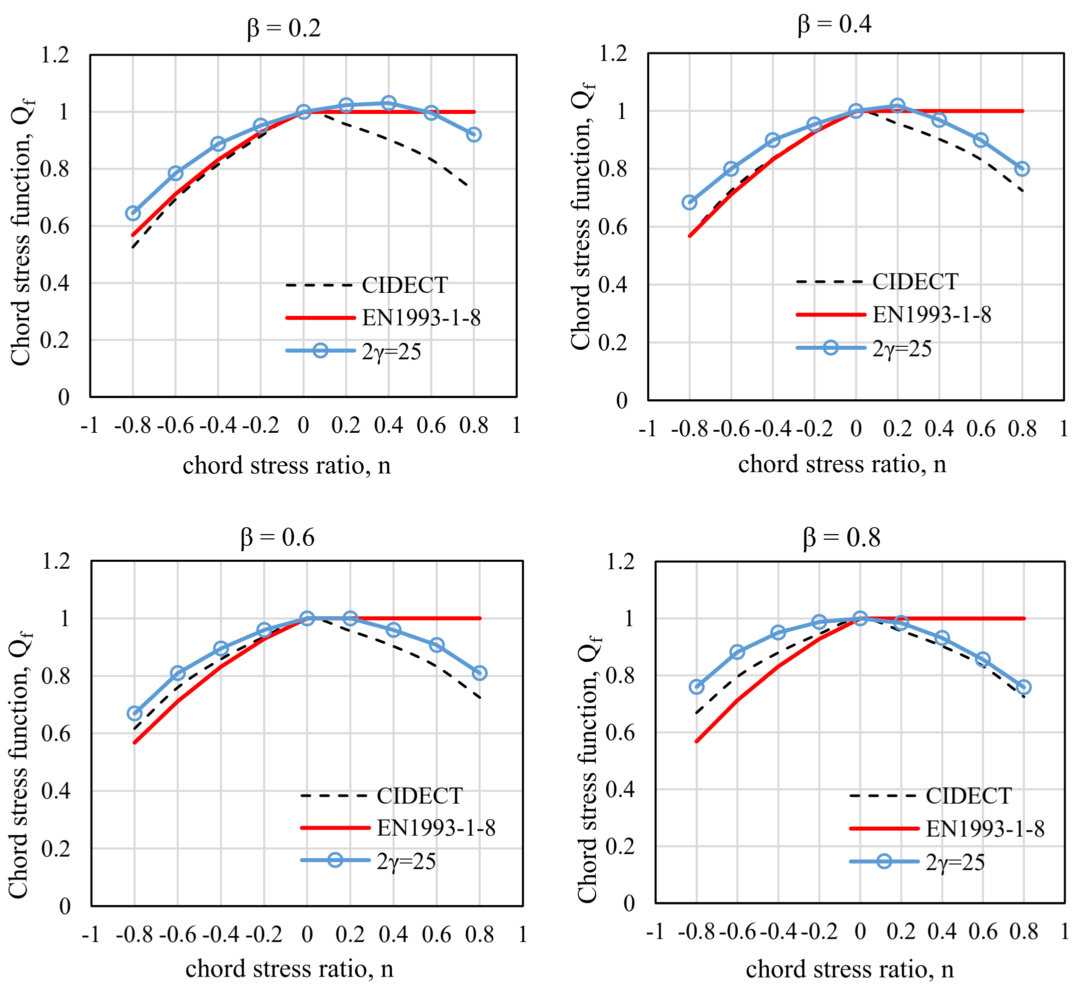

Figure 5.30 Effects of chord stress ratios on axial resistances of T-joints between CFCHS

Table 5.1 Test programme for T-joints between S690 CFCHS under brace axial compression

Test specimen	Steel grade	Chord member $d_0 \times t_0$ (mm×mm)	Brace member $d_1 \times t_1$ (mm×mm)	α	β	γ	τ
T1-C	S355	250×10	150×6	9.6	0.6	12.5	0.6
T2A	S690	250×10	150×6	9.6	0.6	12.5	0.6
T2B	S690	250×10	150×6	9.6	0.6	12.5	0.6
T3-C	S355	250×10	200×6	9.6	0.8	12.5	0.6
T4	S690	250×10	200×6	9.6	0.8	12.5	0.6
T5	S690	250×10	200×10	9.6	0.8	12.5	1.0

Table 5.2 Measured geometric dimensions of test specimens

Specimen	Steel grade	Chord length L_0 (mm)	Chord diameter D_0 (mm)	Brace length L_1 (mm)	Brace diameter D_1 (mm)
T1-C	S355	1199.9	251.6	599.3	152.3
T2A	S690	1198.8	251.6	599.4	152.6
T2B	S690	1198.8	251.5	599.4	152.0
T3-C	S355	1201.1	251.5	599.4	200.5
T4	S690	1199.0	251.8	599.2	200.9
T5	S690	1198.5	251.5	599.4	201.3

Table 5.3 Summary of results for tensile coupon tests

Tensile coupon	Young's modulus E (kN/mm^2)	Yield strength f_y (N/mm^2)	Tensile strength f_u (N/mm^2)	f_u/f_y	Strain at tensile strength ε_u (%)	Ductility requirement for S690 $15f_y/E$ (%)	Elongation at fracture ε_f (%)
S690-6 mm	202	731	813	1.11	6.23	5.43	16.8
S690-10mm	204	787	836	1.06	6.51	5.79	17.0
S355-6mm	204	373	519	1.39	13.9	-	23.5
S355-10mm	206	358	539	1.50	16.6	-	30.8

Table 5.4 Chemical composition of welding electrodes

Electrode	C	Si	Mn	P	S	Cr	Ni	Mo	Cu
ER110S-G	0.090	0.80	1.70	0.015	0.015	0.3	1.85	0.6	0.1
E71T-1	0.055	0.38	1.35	0.015	0.010	-	-	-	-

Table 5.5 Mechanical properties of welding electrodes

Standard	Electrode	Supplier	Weld method	Diameter (mm)	Yield strength (N/mm^2)	Tensile strength (N/mm^2)	Elongation (%)
AWS A5.28	ER110S-G	Bohler	GMAW	1.2	720	880	15
AWS A5.20	E71T-1	Lanyu	GMAW	1.2	490	580	27

Table 5.6 Measured weld sizes at crown and saddle points

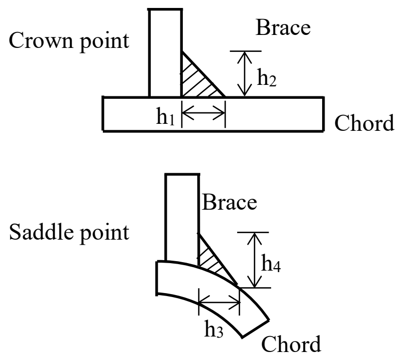

Joint	h_1 (mm)	h_2 (mm)	h_3 (mm)	h_4 (mm)
T1-C	9.0	11.2	4.3	3.3
T2A	10.1	11.5	3.5	3.7
T2B	11.0	12.5	2.9	4.0
T3-C	11.3	12.6	3.3	4.2
T4	11.1	12.9	5.5	4.5
T5	12.0	12.8	1.7	2.7

Table 5.7 Summary of test results of T-joints between S690 CFCHS

Joint	Steel grade	$N_{c,Test}$ (kN)	$M_{0,Test}$ (kNm)	$M_{pl,0}$ (kNm)	$M_{0,Test}$/ $M_{pl,0}$	N_{CIDECT} (kN)	$N_{c,Test}$/ N_{CIDECT}	$N_{CIDECT,Mean}$ (kN)	$N_{c,Test}$/ $N_{CIDECT, Mean}$	N_{EC3} (kN)	$N_{c,Test}$/ N_{EC3}	Failure mode
T1-C	S355	544	183.6	155.7	1.18	349	1.56	293	1.31	311	1.75	CB
T2A	S690	861	290.6	342.3	0.85	767	1.12	645	0.94	683	1.26	CP
T2B	S690	920	310.5	342.3	0.91	767	1.20	645	1.01	683	1.35	CP
T3-C	S355	679	220.7	155.7	1.42	439	1.55	369	1.30	391	1.74	CB
T4	S690	1223	397.5	342.4	1.16	968	1.26	813	1.06	860	1.42	CB
T5	S690	1175	381.8	342.4	1.12	968	1.21	813	1.02	860	1.42	CB

$N_{c,\ Test}$ denotes the measured strength of T-joints

$M_{0,Test}$ denotes the calculated maximum bending moment in the chord

$M_{pl,0}$ denotes the plastic moment resistance of the chord

N_{CIDECT} denotes the ultimate resistance predicted by CIDECT design guide 1 without reduction factor

$N_{CIDECT,\ Mean}$ denotes the ultimate resistance predicted by mean strength equation by CIDECT design guide 1

N_{EC3} denotes the ultimate strength predicted by according to EN 1993-1-8 without reduction factor

CB denotes an overall failure mode of chord bending

CP denotes a local failure mode of chord plastification

Table 5.8 Mesh convergence study

Model	Mesh size (mm)	Number of elements	Runtime (hrs)	Axial resistance (kN)	Difference in axial resistance (%)
Coarse mesh	10	36,960	0.1	878	1.27
Fine mesh	5	138,864	1.0	864	-0.35
Very fine mesh	3	355,932	4.0	867	0

Table 5.9 Comparison of measured and predicted axial resistances for T-joints

Joint	Steel grade	$N_{c,Test}$ (kN)	$N_{c,FE}$ (kN)	Resistance ratio $N_{c,FE}/N_{c,Test}$
T1-C	S355	544	523	0.96
T2A	S690	861	864	1.00
T2B	S690	920	931	1.01
T3-C	S355	679	652	0.96
T4	S690	1223	1244	1.02
T5	S690	1175	1248	1.06
			Mean	1.00

Table 5.10 Parametric studies on T-joints between CFCHS under brace axial compression

Parameter	Range of parameter
β	0.2, 0.4, 0.6, 0.8, 1.0
2γ	25, 30, 40, 50
n	-0.8, -0.6, -0.4, -0.2, 0, +0.2, +0.4, +0.6, +0.8

Table 5.11 Geometrical dimensions of FE models for parametric studies

	FE model	Steel grade	d_1 (mm)	d_0 (mm)	β	t_1 (mm)	t_0 (mm)	τ	n
2γ=25	T1	S690	50	250	0.2	6	10	0.6	-0.8, -0.6, -0.4, -0.2, 0, +0.2, +0.4, +0.6,+0.8
	T2		100	250	0.4	6	10	0.6	
	T3		150	250	0.6	6	10	0.6	
	T4		200	250	0.8	6	10	0.6	
	T5		250	250	1.0	6	10	0.6	
2γ=30	T6		60	300	0.2	6	10	0.6	
	T7		120	300	0.4	6	10	0.6	
	T8		180	300	0.6	6	10	0.6	
	T9		240	300	0.8	6	10	0.6	
	T10		300	300	1.0	6	10	0.6	
2γ=35	T11		70	350	0.2	6	10	0.6	
	T12		140	350	0.4	6	10	0.6	
	T13		210	350	0.6	6	10	0.6	
	T14		280	350	0.8	6	10	0.6	
	T15		350	350	1.0	6	10	0.6	
2γ=40	T16		80	400	0.2	6	10	0.6	
	T17		160	400	0.4	6	10	0.6	
	T18		240	400	0.6	6	10	0.6	
	T19		320	400	0.8	6	10	0.6	
	T20		400	400	1.0	6	10	0.6	

CHAPTER SIX

STRUCTRUAL BEHAVIOUR OF T-JOINTS BETWEEN CFCHS UNDER IN-PLANE BENDING

6.1 INTRODUCTION

This chapter presents an experimental and numerical investigation into structural behaviour of high strength S690 welded T-joints between cold-formed circular hollow sections (CFCHS) subjected to in-plane bending. A total of ten specimens were tested. Six of them were tested under monotonic in-plane bending in the braces while the other four specimens were tested under cyclic in-plane bending. For those T-joints tested under monotonic in-plane bending, four of them were made from high strength S690 steels while the other two were made from normal strength S355 steels. Failure modes, load carrying capacities and deformation capacities of all the test specimens were reported. An innovative Digital Image Correlation (DIC) technique was employed to measure surface strain contours of specified areas of the T-joints. Surface strain developments at specified locations of the T-joints were monitored, and facture failure at heat affected zones were identified.

For those T-joints tested under cyclic in-plane bending, four specimens with identical geometrical dimensions were tested with two different loading protocols. The moment resistances of these T-joints were compared with those measured resistances obtained from the monotonic tests. Strength reduction to moment resistances due to cyclic loads was quantified, while energy dissipation characteristics of these T-joints were also identified.

Numerical investigation is conducted to simulate the structural behaviour of these T-joints under both monotonic and cyclic in-plane bending. Finite element models are established and calibrated against experimental results. The validated finite element models are adopted for subsequent parametric analyses to study various effects onto the structural behaviour of these T-joints between CFCHS. Both the measured and the predicted moment resistances are compared with design moment resistances obtained from EN 1993-1-8 and CIDECT Design Guide 1, and applicability of these two existing design rules are examined.

6.2 EXPERIMENTAL INVESTIGATION

6.2.1 Test programme

A total of ten T-joints between S690 CFCHS were fabricated for structural testing. Figure 6.1 illustrates a schematic view of a typical joint under investigation. The overall test programme is shown in Table 6.1.

Figure 6.2 presents a detailed configuration of a T-joint between CFCHS. The lengths of the chords and the braces are L_0 = 1200 mm and L_1 = 600 mm respectively, and the span between two pinned supports are L = 1500 mm. Joints T1-C and T3-C are made with S355 steels, and they are regarded as reference joints while the others are made with S690 steels. The following geometrical parameters are covered in the present test programme: i) the brace to chord diameter ratio ($\beta = d_1 / d_0$) is assigned to range from 0.6 to 0.8, ii) the ratio of brace wall thickness to chord wall thickness ($\tau = t_1 / t_0$) is assigned to range from 0.8 to 1.0. The diameter of the chord is assigned to be 250 mm, and its thickness is assigned to be 10 mm. The measured geometric properties of these T-joints are summarized in Table 6.2.

Standard tensile tests were conducted to obtain basic material properties of both S355 and S690 steel plates. The test methods and the procedures are described in Chapter 3. Figure 6.3 presents the geometric dimensions of the tensile coupons and Figure 6.4 presents the typical stress-strain curves of S355 and S690 steel plates. A summary of results of the standard tensile tests are presented in Table 6.3.

All these T-joints are welded between CFCHS by experienced welders. The manufacturing process of these T-joints is described in Chapter 5. Both the chemical compositions and the mechanical properties of the welding electrodes are summarized in Tables 6.4 and 6.5. The measured weld sizes at crown points and saddle points of each joint are shown in Table 6.6.

It should be noted that three T-stub supports with two 20 mm thick S355 steel plates were welded to both ends of the chord and the top of the brace in order to connect with the loading attachments and the end supports through steel pins.

6.2.2 Test setup and test procedures

T-joints under monotonic in-plane bending

Figure 6.5a) presents an overall view of the test setup for these T-joints under monotonic in-plane bending, where these T-joints were attached to two supports and a lateral loading attachment through three steel pins. The lateral loading attachment was connected to a load cell, and strain gauges were mounted onto the brace to capture strain distributions during the entire test. Transducers were used to measure the displacements at selected locations. Displacements from LVDTs, i.e. Δ7 and Δ8 were used to calculate the rotation of the chord, θ_g.

$$\theta_g = \frac{\Delta 7 - \Delta 8}{200} \text{(rad)} \tag{6.1}$$

Δ1 and Δ2 were used to calculate the rotation of the brace, which is given by

$$\theta_{b1} = \frac{\Delta 1}{760}, \ \theta_{b2} = \frac{\Delta 2}{420} \ \text{(rad)} \tag{6.2}$$

It was found that these two rotations were very close to each other, hence, the brace can be regarded to act rigidly during tests. The joint rotation of the T-joint is given by

$$\theta = \frac{\theta_{b1} + \theta_{b2}}{2} - \theta_g \ \text{(rad)} \tag{6.3}$$

An in-plane bending moment was applied to the T-joint by pulling the end of the brace laterally through a hydraulic jack. The applied load was measured with a load cell, and it was applied at a controlled loading rate at about 0.3 kN/s in the elastic range. After attaining 0.8 times of nominal moment resistances of the brace, a displacement control at a rate of 1 mm/min was employed. In general, all the tests were terminated only after fracture failure occurred in all the roots of the braces of these T-joints except that Joints T1-C and T3-C were terminated when the lateral displacements exceeded the predicted deformation limits.

T-joints under cyclic in-plane bending

Joints T6 to T9 were tested with a hydraulic servo control testing system with a lateral loading capacity of 1000 kN. The test setup is shown in Figure 6.5b). The instrumentation of these T-joints are identical with Joints T1 to T5 under monotonic loads, as mentioned in the previous section. Cyclic in-plane bending moments were applied to these T-joints by pulling and pushing the ends of the braces laterally through a horizontal actuator. The horizontal load was applied through a displacement control at a rate of 3 mm/min.

Loading protocols for T-joints under cyclic in-plane bending

Two different loading protocols are adopted for the present study to apply lateral loads to the brace end, namely a) SAC loading protocol (Clark *et al*. 1997), and b) ECCS loading protocol (1986).

SAC and ANSI/AISC 341-16 (AISC 2016) both recommend cyclic tests on beam-column moment joints to be conducted by controlling the story drift angle, θ, imposed on the test specimen. The loading protocol is shown in Figure 6.6, and the target drift angles in various loading steps are presented in Table 6.7.

ECCS (1986) suggests that two monotonic tests need to be conducted to determine the positive and the negative reference elastic loads, and the corresponding reference elastic displacements. The positive and the negative reference elastic load P_y, and the corresponding reference elastic displacement Δ_y, are obtained from the force–

displacement curve. The reference elastic load is defined as the intersection between the tangent modulus E, at the origin of the force–displacement curve and the tangent that has a slope of $E/10$ as indicated on Figure 6.7. And the cyclic test is conducted with increasing displacements as presented in Table 6.8. It should be noted that, P_y and Δ_y are determined to be 120 kN and 30 mm from the load-displacement curves of Joints T2A and T2B, as shown in Figure 6.8.

In the present study, Joints T6 and T7 were tested with SAC loading protocol and Joints T8 and T9 were tested with ECCS loading protocol. It should be noted that the interstory drift angles are converted to the lateral displacements and those calculated lateral displacements at each loading step of these two loading protocols are compared in Figure 6.9. It is found that T-joints tested with SAC loading protocol will perform more load cycles while plastic deformations will be achieved before those tested with ECCS loading protocol.

6.2.3 Test results

Failure modes

a) Monotonic tests

The deformed shapes of all these T-joints after tests are presented in Figure 6.10. A number of failure modes have been identified among the six monotonic tests, depending on the steel grades of the T-joints. For Joints T1-C and T3-C, both with S355 steels, apparent local buckling at the compression sides of the braces was observed. Significant out-of-plane plastic deformation of the chords was also observed. For Joints T2A, T2B and T4, all of S690 steels, cracks were observed to be initiated within heat affected zones of the braces when the measured lateral displacements of the brace ends reached 85, 88 and 75 mm respectively. For Joint T5, also of S690 steels, a crack was observed to be initiated within the heat affected zone of the chord when the lateral displacement of the brace end reached 86 mm. Then, the crack propagated along the weld toe, causing a significant drop in the applied load. Figures 6.11 and 6.13 illustrate various fracture within the heat affected zones in these T-joints after tests.

b) Cyclic tests

Fatigue cracks were found in the heat affected zones of the braces of all the joints tested under cyclic in-plane bending moments, as shown in Figure 6.15. For Joints T6 and T7, fatigue cracks were observed to be initiated at the 37th and the 35th load cycles. For Joints T8 and T9, fatigue cracks were observed to be initiated at the 6th and the 5th load cycles. The lateral load dropped significantly after initiation of fracture.

Load displacement curves

a) Monotonic tests

The measured lateral load versus lateral displacement curves of all the T-joints under monotonic in-plane bending are plotted in Figures 6.12 and 6.14 for comparison. For those joints made of S690 steels, and also Joint T3-C, the ultimate lateral load resistance is defined as the maximum applied load in the tests. For Joint T1-C, the applied load is shown to increase continuously even after yielding, and no drop in the applied load was ever recorded throughout the entire test. In this case, a deformation limit according to Yura *et al*. (1981) is adopted to define the ultimate resistance of the joint, and hence, the joint is considered to have failed when its end rotation has reached $80\, f_y / E$ or 0.139 rad. The corresponding applied lateral load and displacement are found to be 76.4 kN and 107 mm respectively.

b) Cyclic tests

The measured lateral load versus lateral displacement hysteretic curves of Joints T6 to T9 are shown in Figure 6.16. The load-displacement hysteretic loops of these Joints T6, T7 and T8 are smooth and they are almost symmetrical in the tensile and the compressive area while the hysteretic loops of Joint T9 are not symmetrical, as only 4 load cycles are completed before fracture takes place. The strength hardening effect is observed in all these T-joints with an increase of the load cycles.

Strain contours obtained from digital image correlation (DIC) system

A digital image correlation (DIC) technique has been reported to be successfully applied to measure true stress-strain curves of standard coupon tests by several researchers (Li *et al*., 2018, Ho *et al*., 2018). The idea of this method is to use correlation algorithm to track speckle patterns with small facets on the specimen surfaces to obtain displacement fields. Principal strains are then calculated according to the measured displacement fields.

In this study, a DIC system with two cameras was employed to monitor the surface strain development of Joitns T4 and T5. According to the focal length of the digital cameras, an area of 240 mm × 200 mm was able to be covered in this study. Hence, these two cameras were set to focus on the tension side of the conjunction part of the brace and the chord, so that the maximum surface strain at tension side of the T-joint could be obtained. A black and white speckled pattern was painted on the surface of the T-joint. The setup of the DIC system is shown in Figure 6.17 a) while Figure 6.17 b) illustrates a typical joint with the speckled pattern and its image in the DIC system. Before testing, an image was first taken as reference, then subsequent images were captured at an interval of 60 seconds under loading.

Figure 6.18 presents the surface principal strain contours of Joint T4 at various deformation stages. The corresponding lateral loads and lateral displacements at specific points are also illustrated. Stress concentration is found to be at present from the HAZ adjacent to the weld toe. The maximum principal strain is observed at the HAZ at the brace as Point A on load-displacement curve. Then, the principal strain continues to increase in value until a tensile fracture occurs. Similar analyses are conducted on Joint T5, and the strain contours obtained from the DIC system are shown in Figure 6.19. The maximum principal strain is observed at the HAZ adjacent to the weld toe at of the chord. Then, the principal strain continues to increase in value until a tensile fracture occurs in the chord.

Applied load-surface principal strain curves at specified locations of Joints T4 and T5 are also plotted in Figures 6.18 and 6.19. For each joint, three points are selected for comparison. Points 1 and 2 are located on the surface of the brace. The distance between these two points is 60 mm. Point 3 is located on the surface of the chord. It should be noted that with an increase of the applied load, the principal strain at Point 1 on Joint T4 is found to develop most significantly, while the principal strain at Point 3 on Joint T5 is the largest among these three points. The local principal strains exceed 19.2 % and 33.9 % when fracture is observed. The results also indicate that fracture failure occurs at different locations of these two T-joints.

6.2.4 Data analyses

Moment resistances of T-joints under monotonic loads

The measured moment resistances of all the T-joints under monotonic in-plane bending are calculated according to Equation 6.4.

$$M_{\text{Test}} = r \times P_{\text{Test}} \text{ (kNm)} \tag{6.4}$$

where r = 0.76 m and it is the lever arm measured from the point of application of the applied load to the crown point of the joint. The corresponding moment-rotation curves of these joints are plotted in Figure 6.20.

The design moment resistances of the T-joints are compared with i) the design plastic moment resistances of braces, ii) the design moment resistances according to CIDECT Design Guide 1, $M_{Rd,1}$, and iii) the design moment resistances according to EN 1993-1-8, $M_{Rd,2}$.

The design formulae recommended by CIDECT Design Guide 1 and EN 1993-1-8 are presented as follows:

a) CIDECT Design Guide 1

$$M_{\text{Rd},1} = Q_u Q_f \frac{f_{y0} t_0^2}{\sin\theta_1} d_1 \tag{6.5}$$

$$Q_u = 4.3\beta\gamma^{0.5} \tag{6.6}$$

$$Q_f = (1-|n|)^{C_1} \tag{6.7}$$

$$n = \frac{N_0}{N_{pl,0}} + \frac{M_0}{M_{pl,0}} \text{ in connecting face} \tag{6.8}$$

Where $M_{Rd,1}$ is the design moment resistance determined with CIDECT Design Guide 1, f_{y0} is the yield strength of the chord, t_0 is the thickness of the chord, θ is the angle between the centerlines of the chord and the brace, β is the ratio of the brace diameter to the chord diameter ($\beta = d_1/d_0$), γ is $d_0/2t_0$, N_0 and M_0 are the axial force and the bending moment applied to the chord, $N_{pl,0}$ is the axial resistance of the chord, $M_{pl,0}$ is the plastic moment resistance of the chord, C_1 = 0.45-0.25β for chord compression stress (n<0), and C_1 = 0.20 for chord tension stress ($n \geq 0$).

b) EN 1993-1-8 with additional reduction factors

$$M_{\text{Rd},2} = 4.85\frac{f_{y0}t_0^2}{\sin\theta_1}d_1\sqrt{\gamma}\beta k_p \tag{6.9}$$

$$n_p = \frac{\sigma_{p,Ed}}{f_{y0}} \text{ in connecting face} \tag{6.10}$$

where $M_{Rd,2}$ is the design moment resistance determined with EN 1993-1-8, k_p = 1-0.3n_p(1+n_p) for $n_p > 0$ (compression) and k_p = 0 when $n_p \leq 0$ (tension), $\sigma_{p,Ed}$ is the maximum compressive stress in the chord excluding the stress due to components parallel to the chord axis.

Table 6.9 summarizes the comparison between the measured and design moment resistances of these T-joints. It is shown that EN 1993-1-8 generally provides an over-prediction of about 13% in the design moment resistance of the T-joints with normal strength steels, when compared with those determined with CIDECT. However, it should be noted that in CIDECT, a reduction factor of 0.9 is adopted for S460 steels, but no guidance is provided for S690 steels. Nevertheless, the reduction factor of 0.9 is also adopted in the present study. Similarly, a reduction factor of 0.8 is adopted in determining the design moment resistances of these S690 T-joints according to EN1993-1-12.

With the same joint geometry, there is generally an increase of 69 to 77% in the moment resistances of these S690 T-joints, when compared to those of T-joints with S355 steels. For those T-joints with S355 steels, the measured moment resistances are found to be higher than the design moment resistances approximately by 20% according to CIDECT while EN 1993-1-8 gives an overestimation of about 5%, which is considered to be more accurate in this study.

For those T-joints with S690 steels, both design specifications give very close moment resistances when different reduction factors are adopted. For T-joints with S690 steels, the measured moment resistances are found to be higher than those predicted values by 4% to 7%. A reduction factor of 0.9 adopted in CIDECT and a reduction factor of 0.8 adopted in EN 1993-1-8 are, therefore, shown to be structurally efficient for practical design.

Rotational capacity of T-joints under monotonic loads

The ductility requirements for S690 T-joints are dependent on various parameters (Havula, 2018). EN 1998-1(CEN, 2005) specifies a general rotation requirement of 0.035 rad for joints in seismic design. For tubular structures, deformation limits proposed by Yura *et al*. (1981) and Lu *et al*. (1994) are widely adopted for determination of their ultimate loads. Yura *et al*. (1981) proposed a rotation limit of $80\, f_y / E$. For S355 steels, it gives a nominal value of 0.139 rad. However, for S690 steels, the corresponding rotation calculated is 0.269 rad. It is shown from Figure 6.20 that fracture failure was observed in all joints with S690 steels before they reached a rotation of 0.15 rad, which is much lower than the proposed deformation limit by Yura.

Lu *et al*. (1994) proposed a general deformation limit of 3% to define the ultimate strength of the joints. For all the T-joints in the present study, the rotation limit is given by

$$\theta_{max} = \frac{0.03 d_0}{d_1/2} \text{ (rad)} \tag{6.11}$$

where d_0 and d_1 are the outer diameters of the chord and the brace respectively.

As shown in Figure 6.20, the rotation capacities of all the joints exceed the proposed deformation limit by Lu. It is shown that all the S690 CFCHS T-joints are able to demonstrate a certain level of ductility before fracture occurs.

Strength reduction of T-joints under cyclic loads

Table 6.10 summarizes the test results of Joints T6 to T9. Both the measured positive moment resistances and the negative moment resistances of these joints are compared with those measured from the monotonic tests reported above. It is found that the reduction in the moment resistances of Joints T6 and T7 are about 5% to 6%. While the reduction in the moment resistances of Joints T8 and T9 are smaller than 3%, the results indicate that the number of load cycles may affect the moment resistances of the T-joints. For those T-joints tested under more load cycles, it is evident that their moment resistances are reduced accordingly.

The backbone curves of Joints T6 to T9 are plotted in Figure 6.21 together with the measured load-displacement curve of Joint T2A. These backbone curves are found to be very close among themselves and they are very similar to the test curve of Joint T2A. Therefore, the cyclic behaviour is considered to provide accurate predictions for the monotonic behaviour of these joints in term of the back bone curve before fracture.

Rotational capacities of T-joints under cyclic loads

It should be noted that the maximum interstory drifts of all these T-joints exceed 0.07 rad, which is larger than the value of 0.035 rad required by EN 1998-1. Therefore these T-joints are considered to possess adequate rotational capacities, and they are applicable for seismic resistant structures.

Moreover, a reduction of about 33% to 42% are found in the ductility of those T-joints under cyclic loads, when compared with those tested under monotonic loads, and it is considered not to be influenced by the number of load cycles.

Energy dissipation characteristics of T-joints under cyclic loads

Energy dissipation characteristics of the T-joints under cyclic in-plane bending are evaluated by the energy dissipation ratio, η_a, which has been adopted in some research. (Soh *et al*., 2001, Wang and Chen, 2007)

For each T-joint, the dissipated energy, E_i of each load cycle is defined as the area enclosed by the load-displacement curve, and it is calculated as follows:

$$E_i = E_i^+ + E_i^- = S_{ABC} + S_{CDA} \tag{6.12}$$

where S_{ABC} and S_{CDA} are defined in Figure 6.22. E_i^+ and E_i^- are the energy dissipated in the tension and the compression half-cycle.

The energy dissipation ratio, $\eta_a = \sum_{i=1}^{n}\left(E_i^+ + E_i^-\right)/E_y$ (6.13)

$$E_y = P_y \Delta_y / 2 \tag{6.14}$$

It should be noted that P_y and Δ_y are determined to be 120 kN and 30 mm from the load-displacement curves of monotonic tests, as shown in Figure 6.8.

The dissipated energy of each cycle, the accumulative energy dissipation and the calculated energy dissipation ratios of Joints T6 to T9 are summarized in Table 6.11. It is found that the energy dissipation capacity of Joint T6 is the largest among these four T-joints. The energy dissipation ratios of Joints T6, T7 and T8 are all larger than a value of 4, which is required by API provision. (API 2002). Therefore, these T-joints are considered to have adequate energy dissipation capacities for application in seismic resistant structures.

6.3 NUMERICAL INVESTIGATION

6.3.1 Proposed FE models

Nonlinear finite element models are established using the finite element programme ABAQUS (2009). The modeling technique for T-joints between CFCHS under brace axial compression with solid elements are introduced in detail in Chapter 5, including the mesh scheming, and the material properties of both the steels and the welds.

For those T-joints under monotonic in-plane bending, these proposed finite element models are able to be adopted with only minor modifications in both the loading and the boundary conditions. Hence, for details of these models and input of the key parameters, please refer to Section 5.3.

For those T-joints under cyclic in-plane bending, material hardening of the steels is considered by adopting a kinematic hardening model. The true stress-strain curves obtained from standard coupon tests are adopted. It should be noted that fracture mechanism is outside the scope of the present study, and hence, it is not considered in the proposed models. Therefore these models are not able to predict initiation of cracks nor their propagation.

6.3.2 Boundary conditions

The boundary conditions of the proposed FE models are shown in Figure 6.23. Three reference points are set, and they are coupled with the nodes on both surfaces of the chord ends and the top surface of the brace with all six degrees of freedom. The lateral load is applied onto Reference Point A through a static general method in ABAQUS/Standard.

6.3.3 Validation of numerical models

Monotonic tests

Figure 6.24 illustrates a comparison of the measured and the predicted lateral load versus lateral displacement curves of the T-joints under monotonic in-plane bending. The proposed numerical models are shown to be able to predict the structural behaviour of these T-joints with a high accuracy. Local buckling behaviour of these T-joints, their initial stiffness, their load carrying capacities and the corresponding lateral displacements predicted with the numerical models are found to agree well with the experimental results.

As the proposed numerical models are not able to predict the initiation of fracture, the moment resistances of the numerical models are determined by adopting the proposed deformation limit by Lu. The predicted moment resistances of the T-joints are compared with those measured values in Table 6.12. Differences between the measured and the predicted moment resistances of these T-joints are found to be smaller than 8%, with a mean value of the moment resistance ratio M_{FE} / M_{Test} at 0.98.

Cyclic tests

The predicted hysteretic curves of Joints T6 to T9 are compared with those measured hysteretic curves from the tests in Figure 6.25.

It is found that the load-deformation behaviour of these joints within the elastic range agree very well with the test results. However, the numerical models give slightly higher stiffness in the plastic range than the measured values. Differences in the stiffness between the numerical and the test results may be attributed to the limitation of the material constitutive model which does not consider any accumulative damage in the steels. Therefore, degradation in the joint stiffness after repeated load cycles are not simulated accordingly.

Nevertheless, the maximum positive moments and the maximum negative moments obtained from the numerical models agree well with the measured values, as summarized in Table 6.13. Differences between the measured and the predicted positive moment resistances of these T-joints are found to be smaller than 3%, with a mean value of the moment resistance ratio at 1.01. Differences between the measured and the predicted negative moment resistances of these T-joints are found to be smaller than 3%, with a mean value of the moment resistance ratio at 1.02.

Hence, the proposed finite element models are generally considered to be applicable to simulate the structural behaviour of these T-joints under monotonic as well as cyclic in-plane bending moments.

6.3.4 Parametric studies

A total of 20 numerical models are established to investigate effects of various parameters on the structural behaviour of T-joints between S690 CFCHS under brace in-plane bending moments. Effects of various geometric parameters such as β and 2γ are studied. It should be noted that effect of chord stress ratio, n has been studied in Chapter 5. For T-joints between S690 CFCHS under brace in-plane bending, both design specifications uses the same formulae as those defined for T-joints under brace axial compression. Therefore, this parameter will not be studied repeatedly in the present study.

The numerical parametric study programme is shown in Table 6.14. It should be noted that β varies from 0.2 to 1.0, and 2γ varies from 25 to 40. The thicknesses of the brace and the chord are 6 mm and 10 mm respectively. The geometrical dimensions of the FE models for the parametric studies are presented in Table 6.15.

Effect of brace to chord diameter ratio, β (= d_1 / d_0)

Figure 6.26 illustrates the effect of β on the moment resistances of T-joints with different values of 2γ at 25, 30, 35 and 40.

The moment resistances of these T-joints are normalized with $d_1 f_{y0} t_0^2$, and they are compared with those predicted resistances according to i) CIDECT design equations, and ii) EN 1993-1-8 design equations. The moment resistances of these T-joints are found to increase with an increase of β almost linearly.

The numerical results are found to be smaller than the design moment resistances determined with both design codes when 2γ = 25, while they are closer to the design resistances according to CIDECT.

Effect of chord diameter to thickness ratio, 2γ (= d_0 / t_0)

Figure 6.27 illustrates the effect of γ on the axial resistances of these T-joints with different values of β at 0.2, 0.4, 0.6, 0.8 and 1.0. Similarly, it is found that the moment resistances increase with an increase of γ. The dotted line in the figure shows the predicted resistances from the CIDECT design equation. When β is small, CIDECT is found to be able to provide accurate predictions. However, when β is larger than 0.6, CIDECT design resistances are found to be increasingly conservative for $2\gamma > 30$, while they are found to be unconservative for $2\gamma < 30$.

6.4 CONCLUSIONS

This chapter presents a series of structural tests on welded T-joints between CFCHS subjected to in-plane bending moments. A total of 10 tests on T-joints between CFCHS have been conducted successfully. It is found that:

a) Compared with those T-joints with S355 steels, those T-joints with S690 steels generally achieve an increase of over 69% in term of moment resistances. The failure mode of fracture at HAZ was identified, which is found to be different from that of those T-joints with S355 steels.

b) Through the application of a DIC technique, the failure mechanism of those T-joints with S690 steels is identified from the surface principal strain contours. Both strain development and crack initiation at specified locations of the joints are also monitored systematically. The maximum principal strains in these joints are found to be 19.2% and 33.9% before fracture.

c) The measured moment resistances of these T-joints are compared with those predicted values obtained from CIDECT Design Guide 1, and EN 1993-1-8. It is shown that these modern design methods are generally applicable for prediction of the moment resistances of these T-joints with both S355 and S690 steels. It is necessary to apply the reduction factors proposed in various design specifications in the design of all these T-joints with S690, considering reduced ductility in these joints under in-plane bending moment.

d) The rotational capacities of all these T-joints are compared with the deformation limits proposed by Yura and Lu. The deformation limit proposed by Yura is found to overestimate the rotational capacities of the joints because it does not consider the occurrence of fracture and the reduced ductility of the high strength steels. However, all thes joints have succeeded in fulfilling the requirement of the proposed deformation limit by Lu. It is shown that all the T-joints between S690 CFCHS have adequate rotation capacities.

e) Hysteretic behaviour of the T-joints between S690 CFCHS are studied experimentally. The test results have shown that there is only a reduction of smaller than 6% in the moment resistances of the T-joints tested under cyclic loads when compared with those tested under monotonic loads. The measured maximum interstory drifts in these T-joints fully satisfy the requirements given in EN 1998-1-1. The energy dissipation capability of the T-joints tested with SAC loading protocol are larger than those tested with ECCS loading protocol. Hence, these T-joints between S690 CFCHS are generally considered to be applicable for seismic resistant structures.

f) Numerical investigations are carried out to simulate the structural behaviour of the T-joints between CFCHS under monotonic and cyclic in-plane bending. The proposed finite element models are shown to be effective to predict the load-deformation behaviour and the moment resistances of these T-joints.

g) Through a series of parametric studies on T-joints between CFCHS, CIDECT Design Guide 1 is shown to provide more accurate prediction in the moment resistances of the T-joints than those design equations provided in EN 1993-1-8. Current reduction factors of 0.8 in EN 1993-1-12 and 0.9 in CIDECT Design Guide 1 are considered to be necessary for design of T-joints between S690 CFCHS.

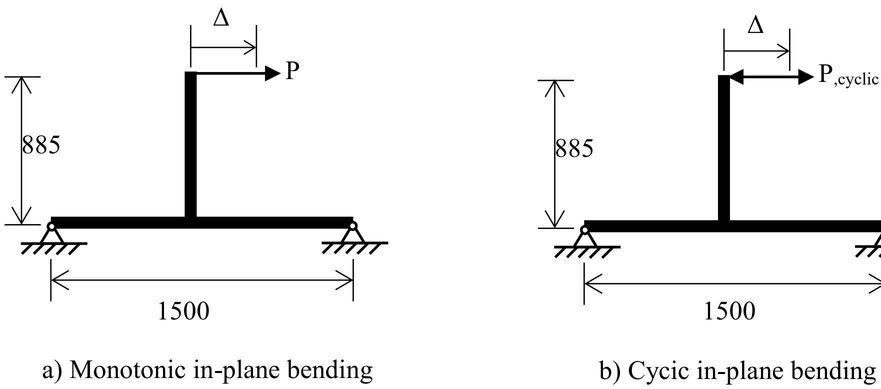

Figure 6.1 Schematic view of a T-joint test under brace monotonic and cyclic in-plane bending

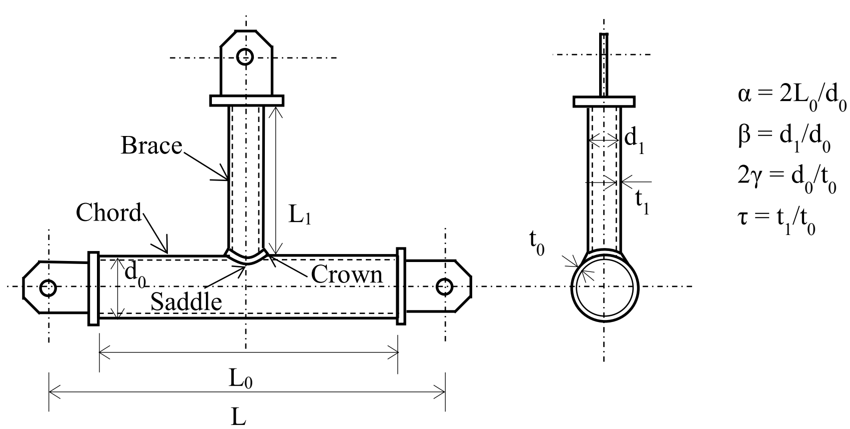

Figure 6.2 Configuration of a typical T-joint

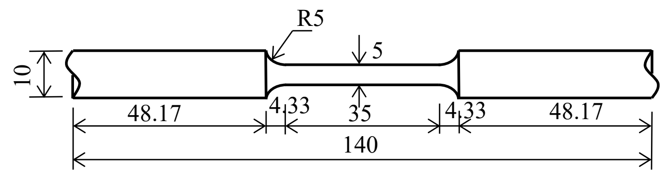

(a) Standard coupon for 10 mm thick steel plates

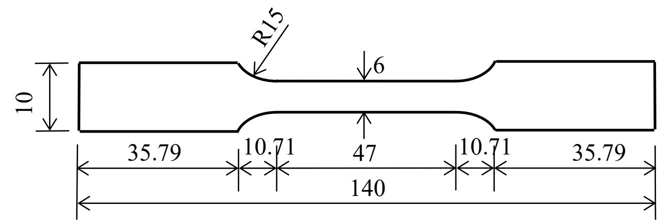

(b) Standard coupon for 6 mm thick steel plates

Figure 6.3 Geometric properties of standard tensile coupons

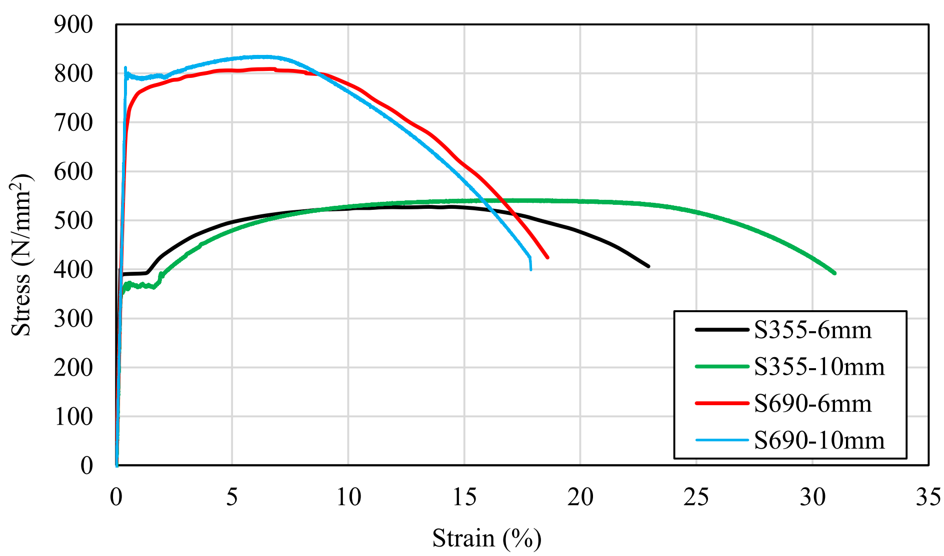

Figure 6.4 Measured stress-strain curves of S355 and S690 steel plates

a) A T-joint under brace monotonic in-plane bending

b) A T-joint under brace cyclic in-plane bending

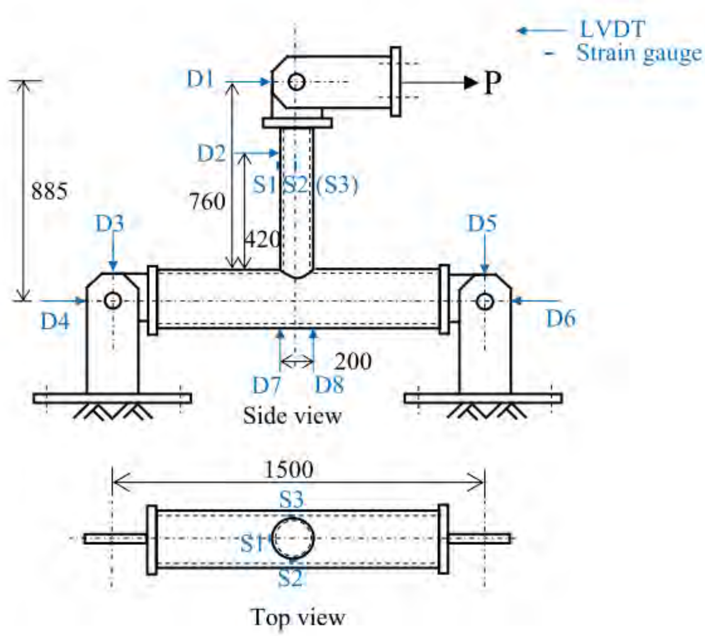

c) Instrumentation for T-joint tests

Figure 6.5 Test setup and instrumentation

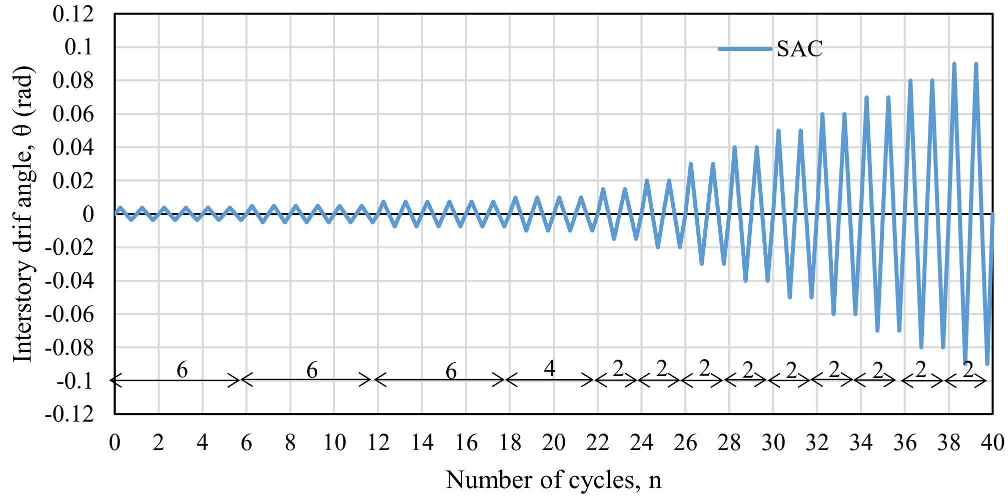

Figure 6.6 Loading steps defined by SAC loading protocol for cyclic tests

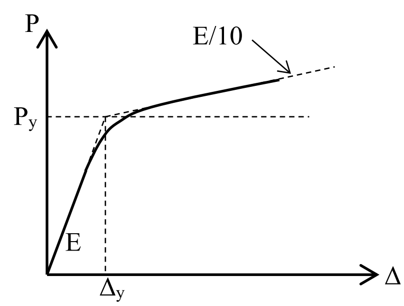

Figure 6.7 Definition of reference elastic force P_y and elastic displacement Δ_y (ECCS, 1976)

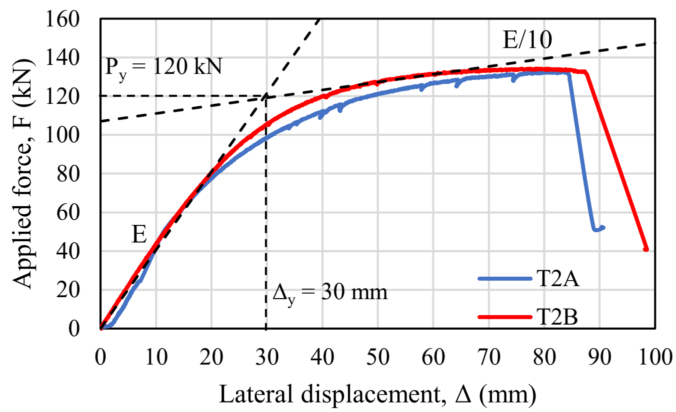

Figure 6.8 Determination of reference elastic force P_y and elastic displacement Δ_y

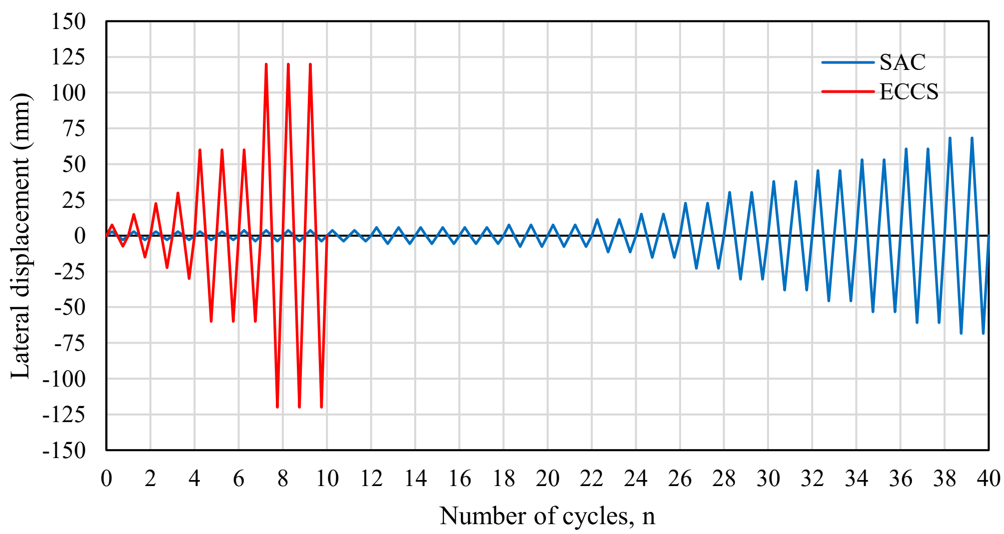

Figure 6.9 Comparison of SAC and ECCS loading protocols

Joint T1-C

Joint T2A

Joint T2B

Joint T3-C

Joint T4

Joint T5

Joint T6

Joint T7

Joint T8

Joint T9

Figure 6.10 Deformed T-joints under brace in-plane bending moments after tests

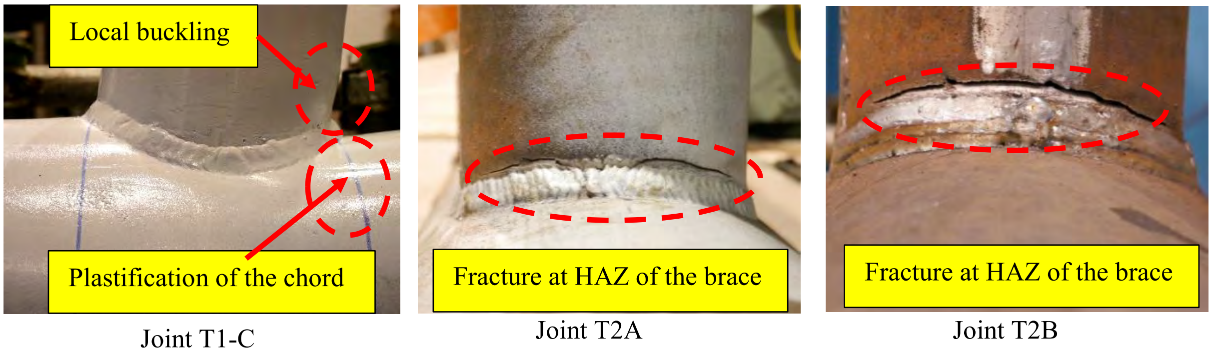

Figure 6.11 Failure modes in Joints T1-C, T2A and T2B after tests

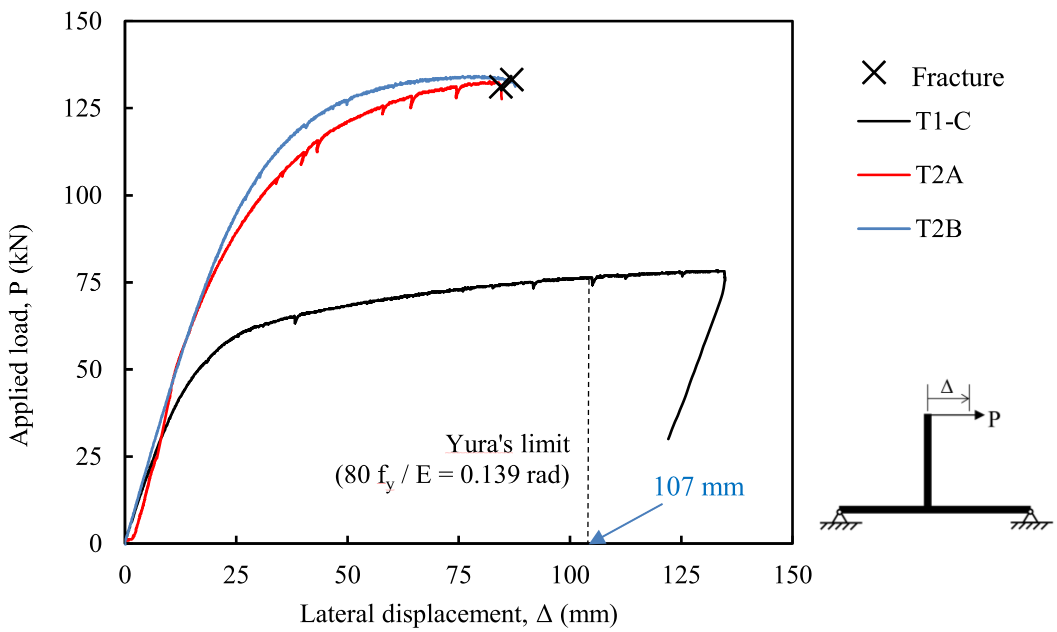

Figure 6.12 Lateral load-lateral displacement curves of JointsT1-C, T2A and T2B

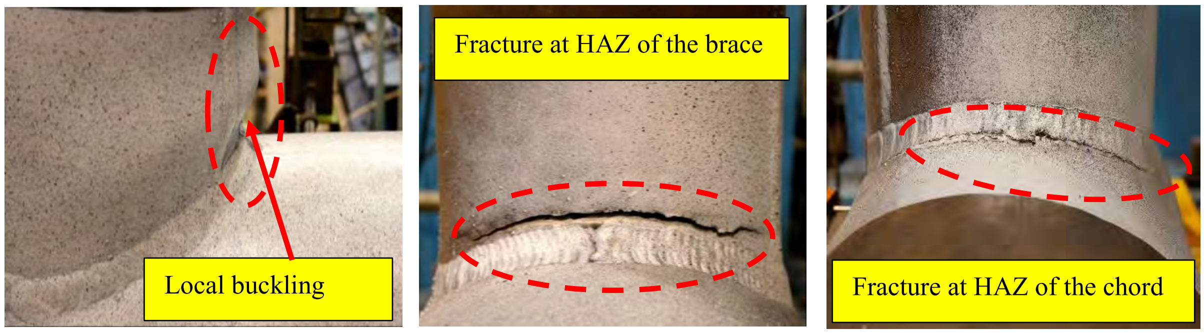

Joint T3-C Joint T4 Joint T5

Figure 6.13. Failure modes in Joints T3-C, T4 and T5 after tests

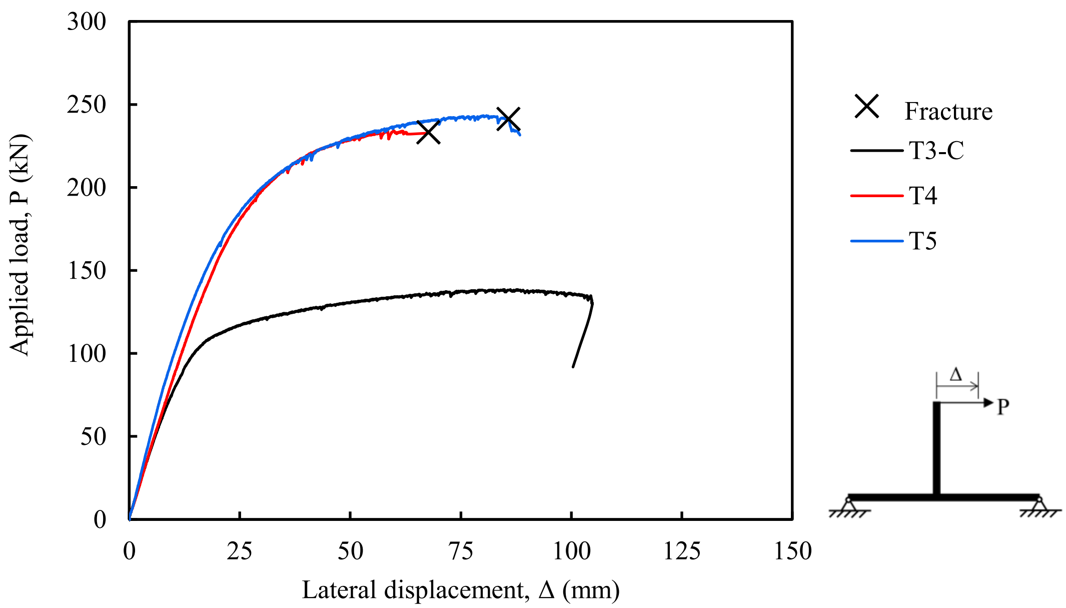

Figure 6.14 Lateral load-lateral displacement curves of Joints T3-C, T4 and T5

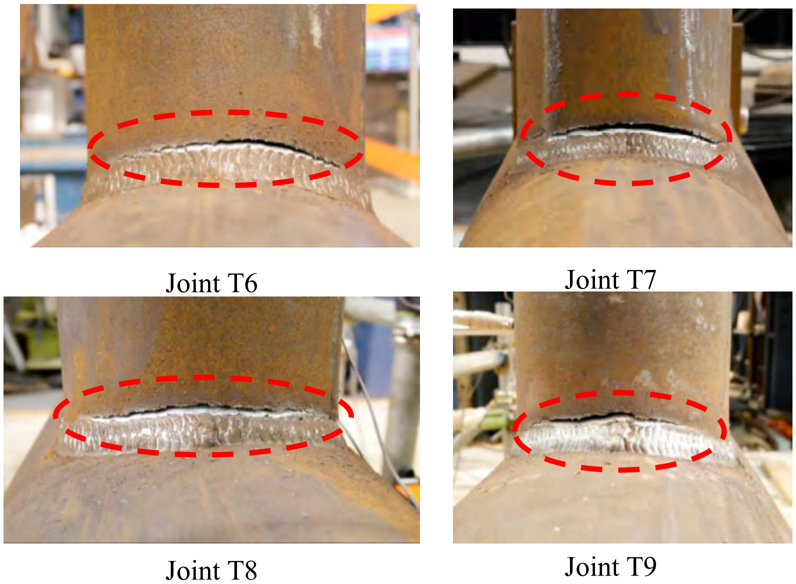

Figure 6.15. Failure modes in Joints T6 to T9 after tests

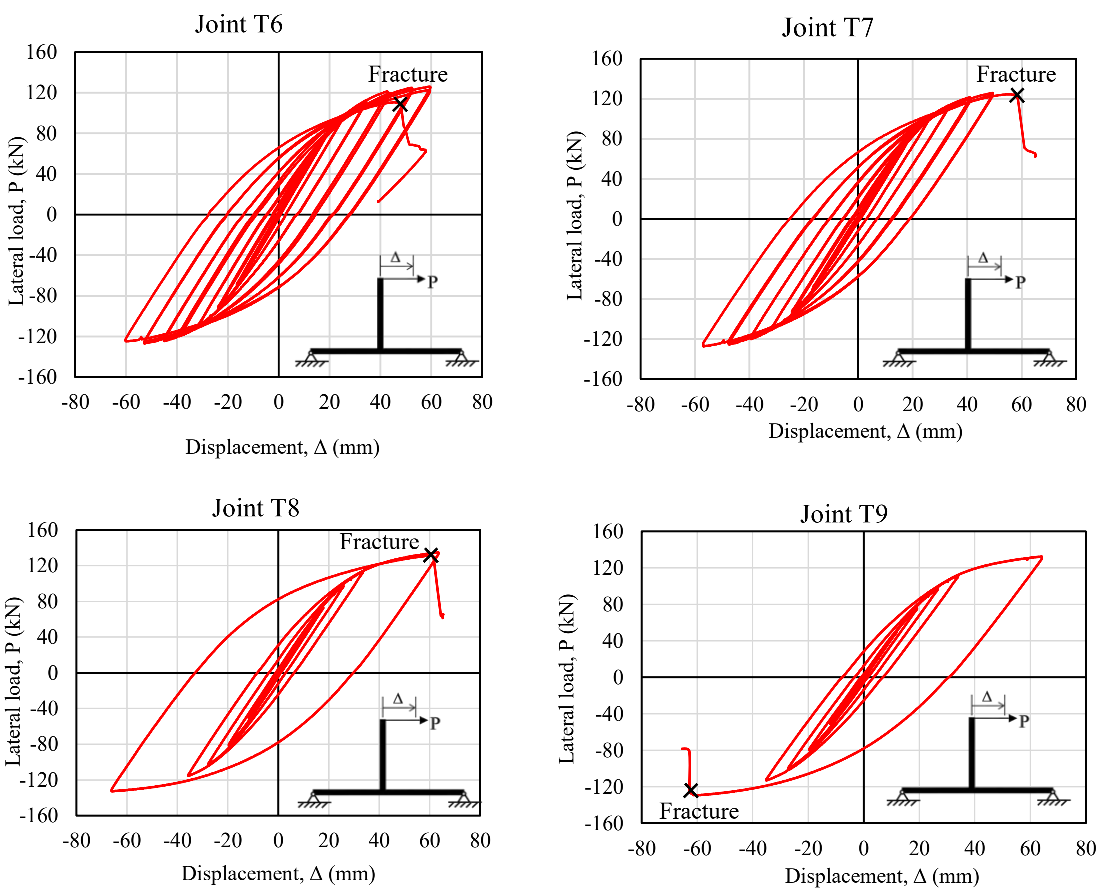

Figure 6.16 Lateral load-lateral displacement curves of Joints T6 to T9

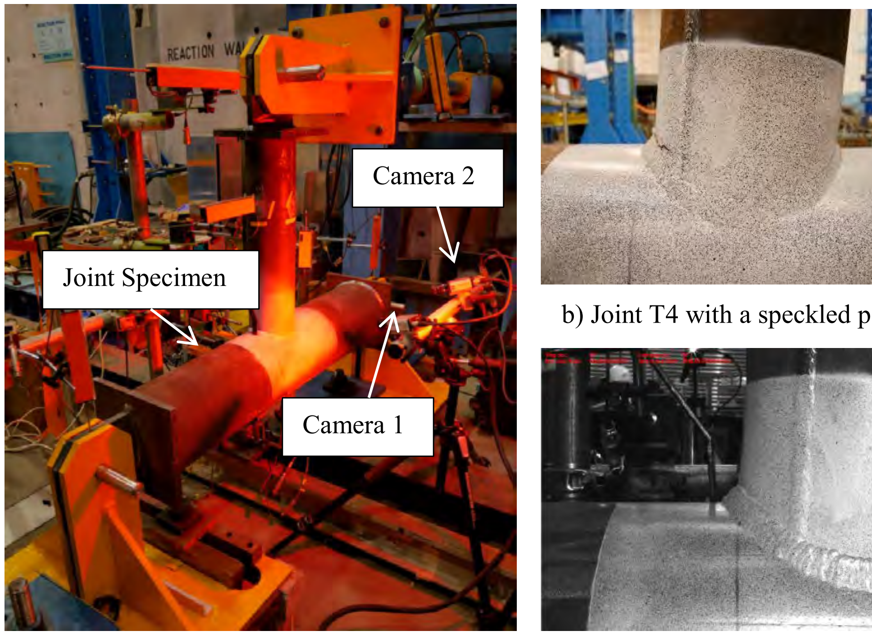

b) Joint T4 with a speckled pattern

a) Test setup

c) Image taken by a DIC system

Figure 6.17 Setup of DIC system for strain measurement

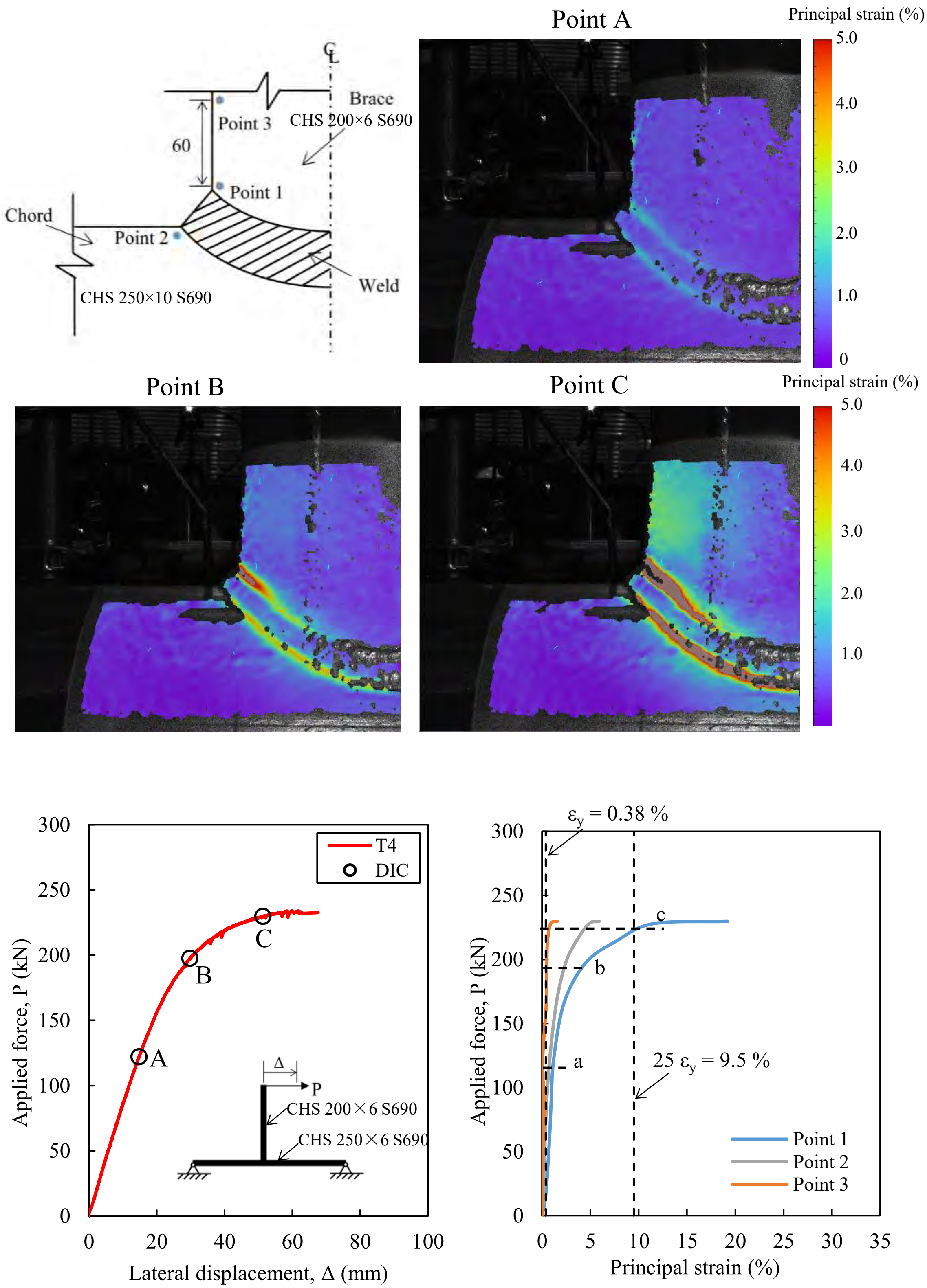

Figure 6.18 Strain contour and DIC measurement points of Joint T4

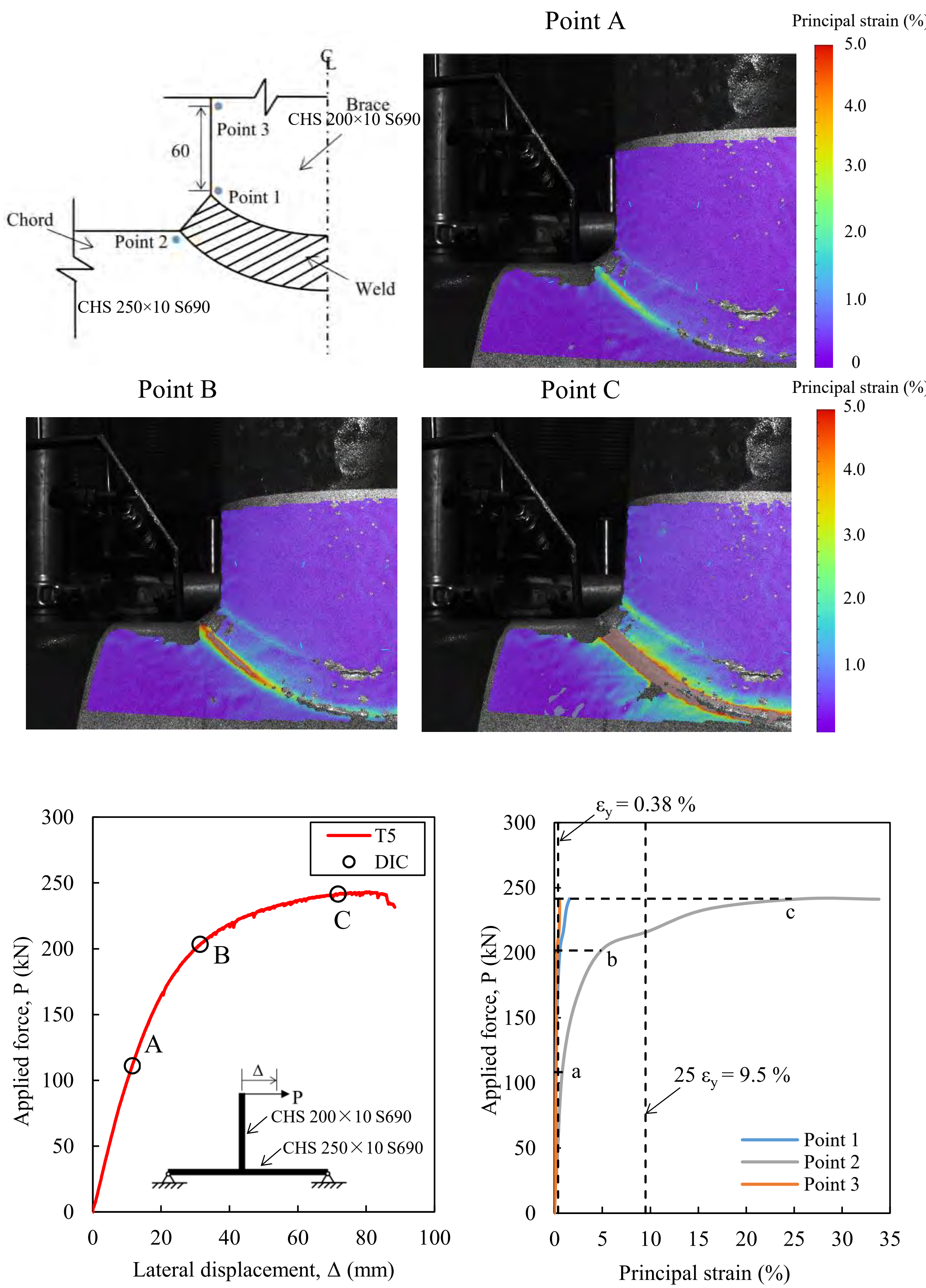

Figure 6.19 Strain contour and DIC measurement points of Joint T5

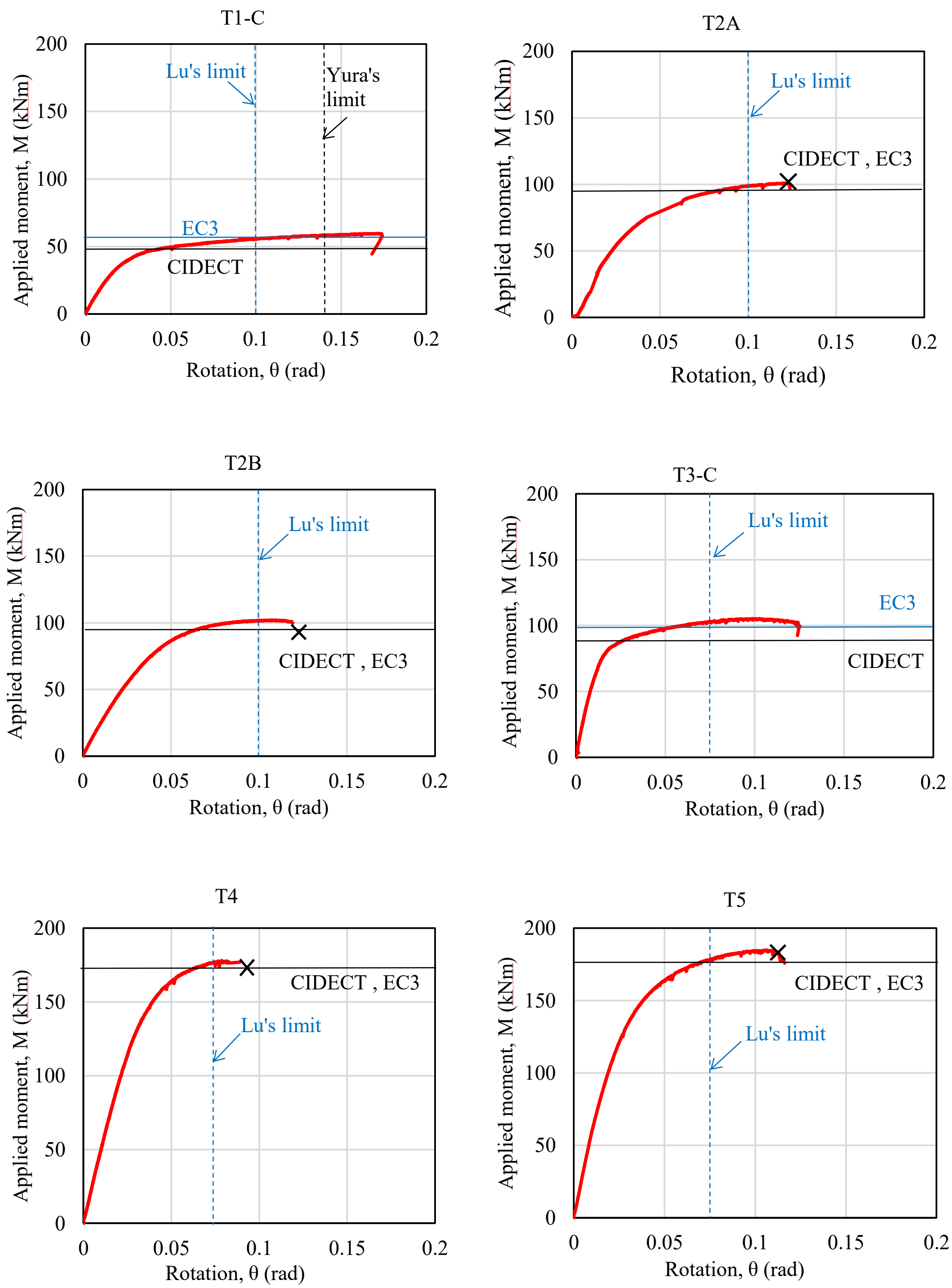

Figure 6.20 Moment-rotation curves of Joints T1-C to T5

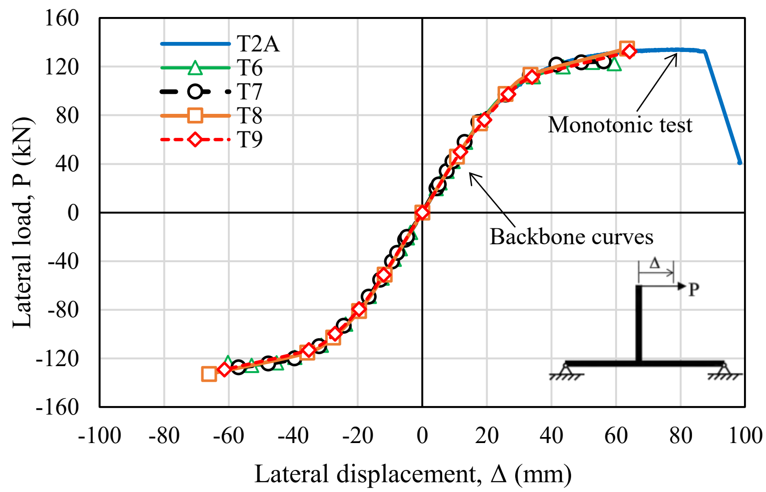

Figure 6.21 Comparison of test curve of Joint T2A and backbone curves of Joints T6 to T9

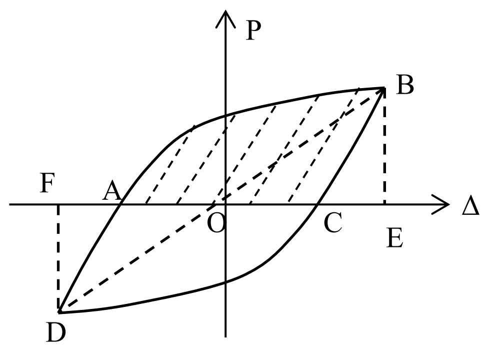

Figure 6.22 Definition of areas S_{ABC} and S_{CDA}

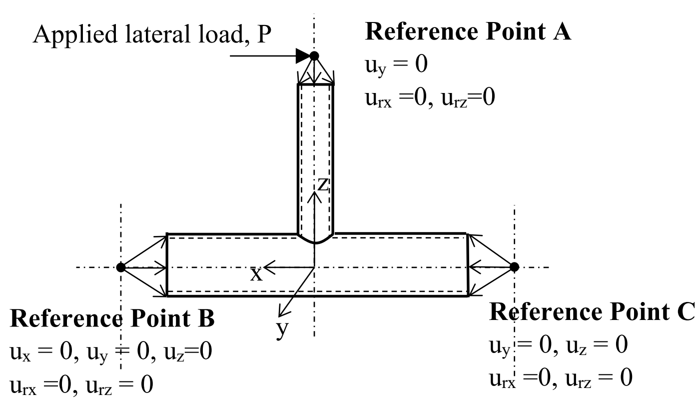

Figure 6.23 Boundary conditions for FE models

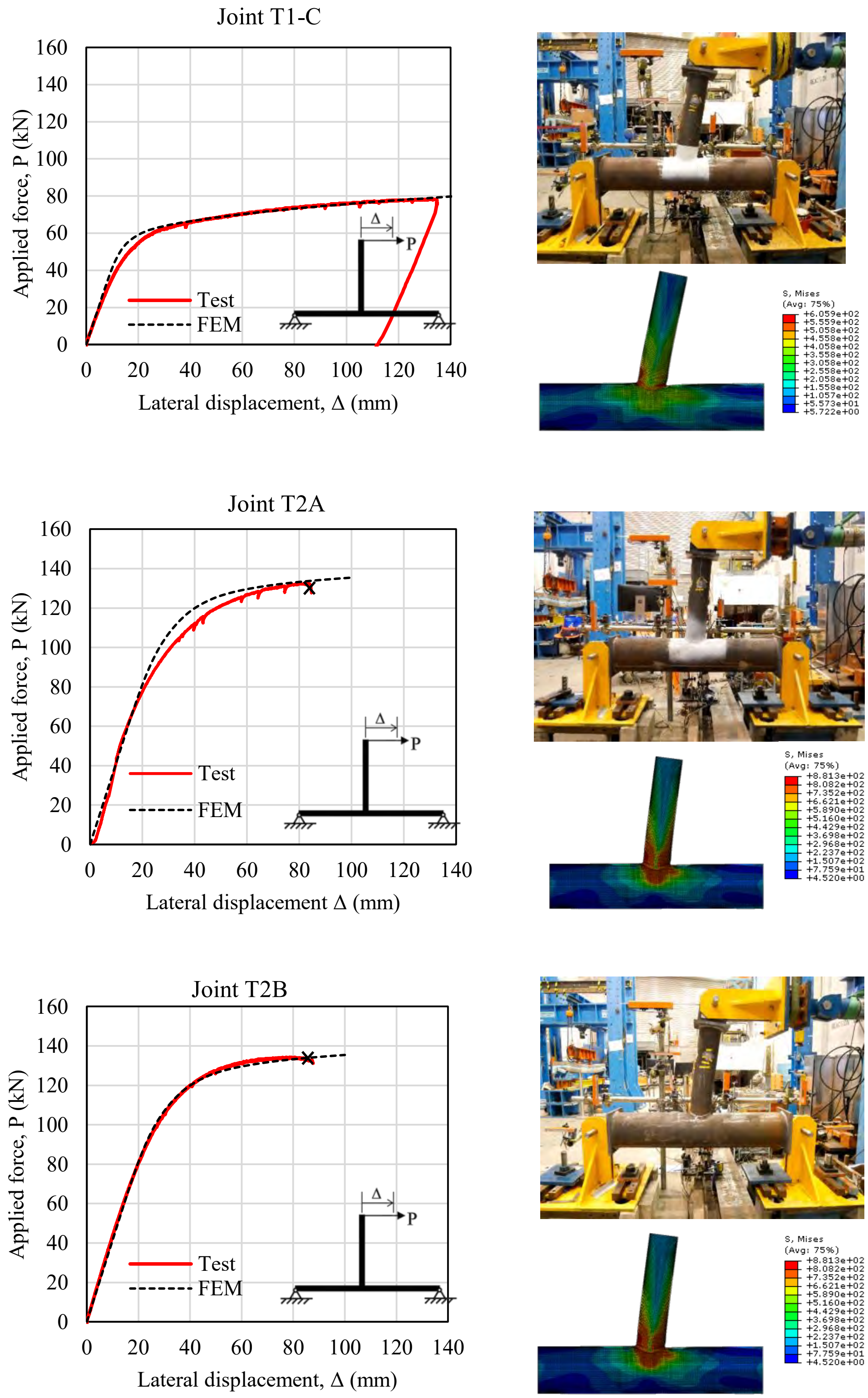

Figure 6.24 Comparison of experimental and numerical results of Joints

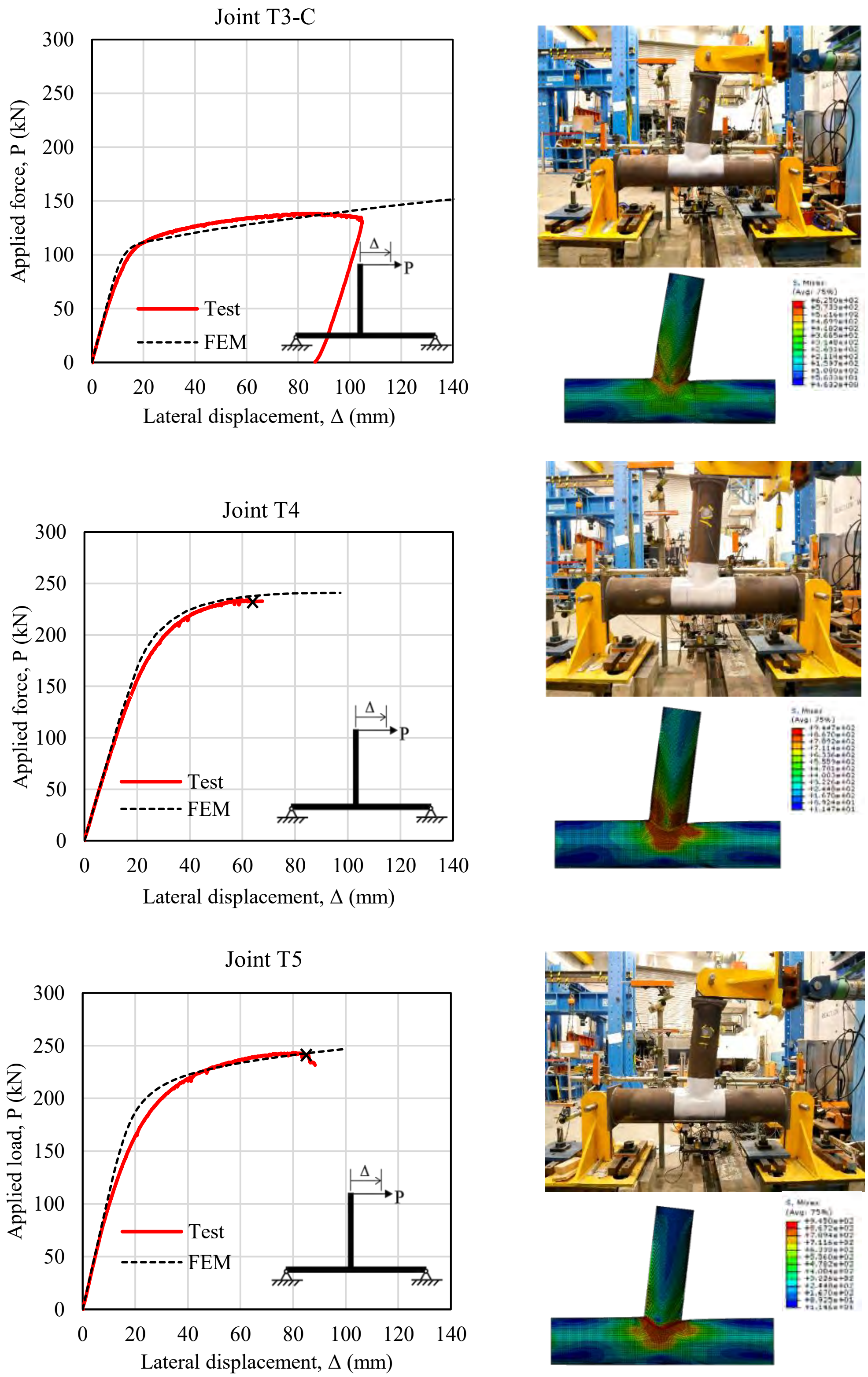

Figure 6.24 Comparison of experimental and numerical results (continued)

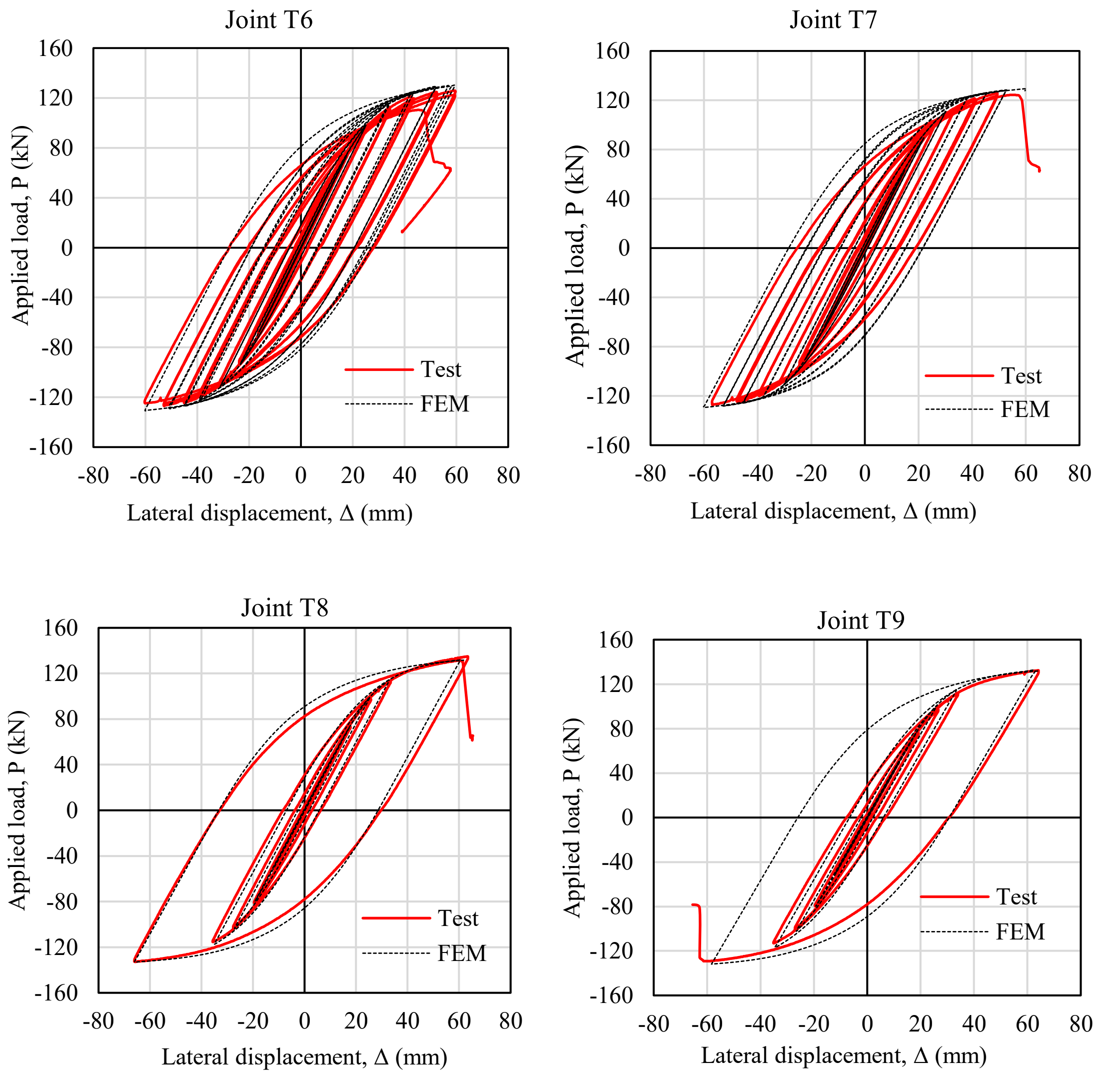

Figure 6.25 Measured and predicted hysteretic curves of T-joints under cyclic in-plane bending

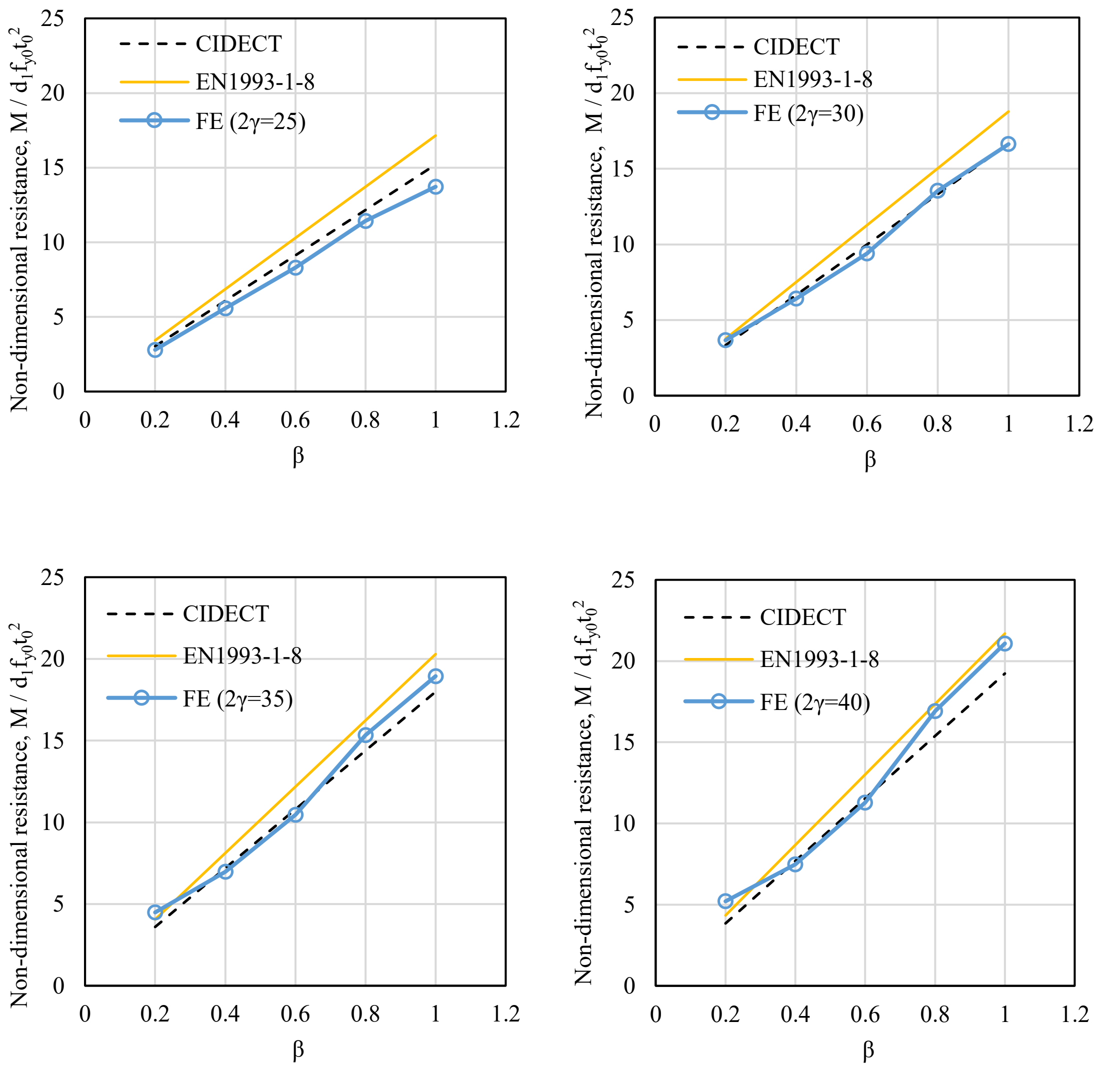

Figure 6.26 Effect of parameter β on moment resistances of T-joints between CFCHS

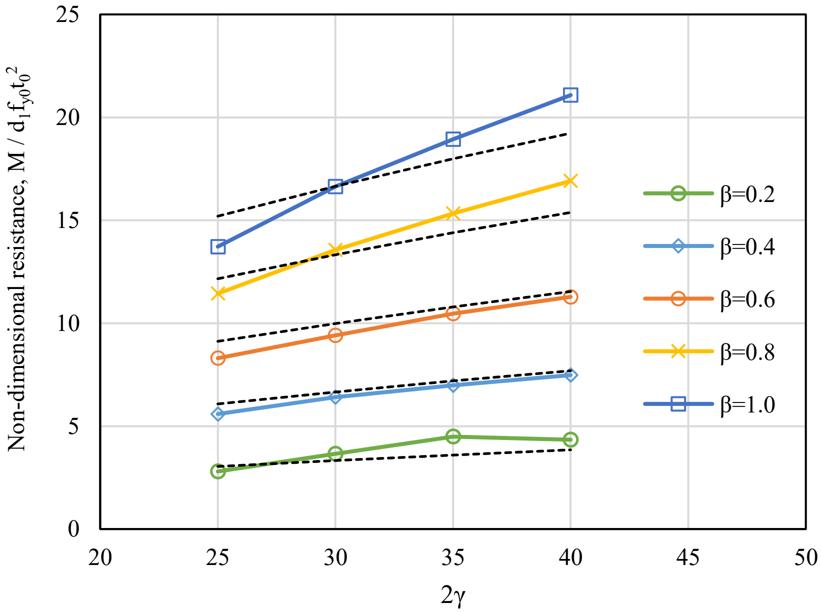

Figure 6.27 Effects of parameter 2γ on moment resistances of T-joints between CFCHS

Table 6.1 Geometric properties of T-joints

Loading type		Joints	Steel grade	Chord member $d_0 \times t_0$ (mm×mm)	Brace member $d_1 \times t_1$ (mm×mm)	α	β	γ	τ
Monotonic		T1-C	S355	250×10	150×6	9.6	0.6	12.5	0.6
		T2A	S690	250×10	150×6	9.6	0.6	12.5	0.6
		T2B	S690	250×10	150×6	9.6	0.6	12.5	0.6
		T3-C	S355	250×10	200×6	9.6	0.8	12.5	0.6
		T4	S690	250×10	200×6	9.6	0.8	12.5	0.6
		T5	S690	250×10	200×10	9.6	0.8	12.5	1.0
Cyclic	SAC	T6	S690	250×10	150×6	9.6	0.6	12.5	0.6
		T7	S690	250×10	150×6	9.6	0.6	12.5	0.6
	ECCS	T8	S690	250×10	150×6	9.6	0.6	12.5	0.6
		T9	S690	250×10	150×6	9.6	0.6	12.5	0.6

Table 6.2 Measured geometric properties of test specimens

Loading type		Joints	Steel grade	Chord length L_0 (mm)	Chord diameter d_0 (mm)	Brace length L_1 (mm)	Brace diameter d_1 (mm)
Monotonic		T1-C	S355	1199.3	251.6	599.3	151.4
		T2A	S690	1197.9	251.8	599.2	152.6
		T2B	S690	1199.3	251.9	599.3	152.2
		T3-C	S355	1200.7	251.5	599.4	201.5
		T4	S690	1199.6	251.9	599.2	201.5
		T5	S690	1198.6	251.8	599.2	201.5
Cyclic	SAC	T6	S690	1198.8	251.9	599.3	152.2
		T7	S690	1200.7	251.1	599.6	152.5
	ECCS	T8	S690	1202.5	252.1	599.0	152.0
		T9	S690	1199.0	251.8	599.3	151.5

Table 6.3 Summary of results for tensile coupon tests

Tensile coupon	Young's modulus E	Yield strength f_y	Tensile strength f_u	f_u/f_y	Strain at tensile strength ε_u	Ductility requirement for S690 $15f_y/E$	Elongation at fracture ε_f
	(kN/mm^2)	(N/mm^2)	(N/mm^2)		(%)	(%)	(%)
S690-6 mm	202	731	813	1.11	6.23	5.43	16.8
S690-10mm	204	787	836	1.06	6.51	5.79	17.0
S355-6mm	204	373	519	1.39	13.9	-	23.5
S355-10mm	206	358	539	1.50	16.6	-	30.8

Table 6.4 Chemical composition of welding electrodes

Electrode	C	Si	Mn	P	S	Cr	Ni	Mo	Cu
ER110S-G	0.090	0.80	1.70	0.015	0.015	0.3	1.85	0.6	0.1
E71T-1	0.055	0.38	1.35	0.015	0.010	-	-	-	-

Table 6.5 Mechanical properties of welding electrodes

Standard	Electrode	Supplier	Weld method	Diameter (mm)	Yield strength (N/mm^2)	Tensile strength (N/mm^2)	Elongation (%)
AWS A5.28	ER110S-G	Bohler	GMAW	1.2	720	880	15
AWS A5.20	E71T-1	Lanyu	GMAW	1.2	490	580	27

Table 6.6 Measured weld sizes at crown and saddle points

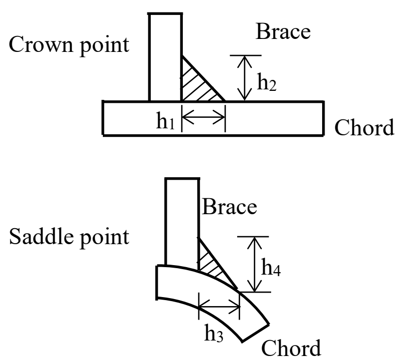

Joint	h_1 (mm)	h_2 (mm)	h_3 (mm)	h_4 (mm)
T1-C	9.5	11.5	6.9	6.0
T2A	9.5	10.8	5.0	4.0
T2B	9.9	12.5	4.5	3.5
T3-C	10.2	11.9	4.0	5.8
T4	12.5	13.0	4.9	4.8
T5	8.9	13.4	2.9	2.5
T6	8.4	11.9	4.8	4.9
T7	9.6	9.9	6.4	7.2
T8	9.5	12.4	4.3	4.2
T9	12.2	11.5	6.1	5.2

Table 6.7 Drift angles defined by SAC loading protocol

Load step	Drift angle, θ	Number of cycles, n
1	$\pm$ 0.00375	6
2	$\pm$ 0.005	6
3	$\pm$ 0.0075	6
4	$\pm$ 0.01	4
5	$\pm$ 0.015	2
6	$\pm$ 0.02	2
7	$\pm$ 0.03	2
Continue with increments in θ of 0.01 and perform two cycles in each step		

Table 6.8 Displacements defined by ECCS loading protocol

Load step	Lateral displacement, Δ	Number of cycles, n
1	$\pm 0.25\ \Delta_y$	1
2	$\pm 0.5\ \Delta_y$	1
3	$\pm 0.75\ \Delta_y$	1
4	$\pm\ \Delta_y$	1
5	$\pm 2\ \Delta_y$	3
6	$\pm 4\ \Delta_y$	3
7	$\pm 6\ \Delta_y$	3
Continue with increments in Δ of $2\Delta_y$ and perform three cycles in each step		

Table 6.9 Summary of test results for T-joints under monotonic in-plane bending

Joint	Steel grade	P_{Test} (kN)	Lateral displacement at failure Δ (mm)	M_{Test} (kNm)	Failure mode*	$M_{pl,Rd}$ (kNm)	CIDECT $M_{Rd,1}$ (kNm)	$M_{Test}/ M_{Rd,1}$	EC3 $M_{Rd,2}$ (kNm)	$M_{Test}/ M_{Rd,2}$
T1-C	S355	76.4	107.4	58.1	BF, CP	35.1	49.0	1.18	55.2	1.05
T2A	S690	132.7	76.3	100.9	HAZ	68.7	96.9	1.04	97.1	1.04
T2B	S690	134.2	78.7	102.0	HAZ	68.7	96.9	1.05	97.1	1.05
T3-C	S355	138.5	86.2	105.3	BF,CP	64.2	87.1	1.21	98.2	1.07
T4	S690	234.2	59.8	178.0	HAZ	125.9	172.3	1.03	172.7	1.03
T5	S690	243.3	79.7	184.9	HAZ	212.6	172.3	1.07	172.7	1.07

*Notes: BF denotes failure in the brace

CP denotes plasitification of the chord

HAZ denotes fracture within a heat affected zone.

$M_{Test} = r \times P_{Test}$, where r = 0.76 m

$M_{pl,Rd}$ denotes the design moment resistance of the brace

$M_{Rd,1}$ denotes the design moment resistance determined with CIDECT Design Guide 1

$M_{Rd,2}$ denotes the design moment resistance determined with EN 1993-1-8

Table 6.10 Summary of test results for T-joints under cyclic in-plane bending

Joint	Loading protocol	Maximum positive load +P (kN)	Maximum positive moment +M (kNm)	Strength reduction factor	Maximum negative load -P (kN)	Maximum negative moment -M (kNm)	Strength reduction factor	Maximum interstory drift (rad)	Ductility reduction factor	No. of cycles at failure
T6	SAC	125.9	95.7	0.94	-127.1	-96.6	0.95	0.08	0.67	37
T7	SAC	125.7	95.5	0.94	-127.3	-96.7	0.95	0.07	0.58	35
T8	ECCS	134.9	102.5	1.00	-132.8	-100.9	0.99	0.08	0.67	6
T9	ECCS	132.4	100.6	0.99	-129.2	-98.2	0.96	0.08	0.67	5

Table 6.11 Energy dissipation parameters of T-joints under cyclic in-plane bending

SAC Loading Protocol	Dissipated Energy, E_i (kNm)	
Cycle	**Joint T6**	**Joint T7**
1 to 18	0.01	0.01
19 to 22	0.02	0.02
23	0.04	0.05
24	0.04	0.05
25	0.13	0.16
26	0.12	0.13
27	0.64	0.73
28	0.64	0.73
29	1.74	1.94
30	1.91	2.06
31	3.69	3.93
32	4.03	4.14
33	6.06	6.56
34	6.56	6.75
35	8.72	
36	9.13	
Accumulative energy dissipation E_{sum} (kNm)	43.71	27.49
E_y (kNm)	1.8	1.8
Energy dissipation ratio, η_a	24.23	15.24

ECCS Loading Protocol	Dissipated Energy, E_i ((kNm)	
Cycle	**Joint T8**	**Joint T9**
1	0.04	0.04
2	0.22	0.27
3	0.92	0.94
4	2.33	2.3
5	12.53	
Accumulative energy dissipation E_{sum} (kNm)	16.04	3.55
E_y (kNm)	1.8	1.8
Energy dissipation ratio, η_a	8.91	1.97

Table 6.12 Comparison of measured and predicted moment resistances of T-joints under monotonic in-plane bending

Joint	Steel grade	P_{Test} (kN)	M_{Test} (kNm)	M_{FE} (kNm)	Moment resistance ratio M_{FE}/M_{Test}
T1-C	S355	76.4	58.1	55.9	0.96
T2A	S690	132.7	100.9	100.8	1.00
T2B	S690	134.2	102.0	101.0	0.99
T3-C	S355	138.5	105.3	96.8	0.92
T4A	S690	234.2	178.0	181.9	1.02
T5	S690	243.3	184.9	176.2	0.95
				Mean	0.97

Table 6.13 Comparison of measured and predicted moment resistances of T-joints under cyclic in-plane bending

Joint	M_{Test}^{+} (kNm)	M_{FE}^{+} (kNm)	Moment resistance ratio M_{FE}^{+}/M_{Test}^{+}	M_{Test}^{-} (kNm)	M_{FE}^{-} (kNm)	Moment resistance ratio M_{FE}^{-}/M_{Test}^{-}
T6	95.7	98.9	1.03	-96.6	-99.3	1.03
T7	95.5	98.2	1.03	-96.7	-98.2	1.02
T8	102.5	100.2	0.98	-100.9	-101.0	1.00
T9	100.6	100.6	1.00	-98.2	-100.2	1.02
		Mean	1.01		Mean	1.02

Table 6.14 Parametric studies on T-joints between CFCHS under brace in-plane bending

Parameter	Range of parameter
β	0.2, 0.4, 0.6, 0.8, 1.0
2γ	25, 30, 40, 50

Table 6.15 Geometrical dimensions of FE models for parametric studies

	FE model	Steel grade	d_1 (mm)	d_0 (mm)	β	t_1 (mm)	t_0 (mm)	τ
$2\gamma=25$	T1	S690	50	250	0.2	6	10	0.6
	T2		100	250	0.4	6	10	0.6
	T3		150	250	0.6	6	10	0.6
	T4		200	250	0.8	6	10	0.6
	T5		250	250	1.0	6	10	0.6
$2\gamma=30$	T6		60	300	0.2	6	10	0.6
	T7		120	300	0.4	6	10	0.6
	T8		180	300	0.6	6	10	0.6
	T9		240	300	0.8	6	10	0.6
	T10		300	300	1.0	6	10	0.6
$2\gamma=35$	T11		70	350	0.2	6	10	0.6
	T12		140	350	0.4	6	10	0.6
	T13		210	350	0.6	6	10	0.6
	T14		280	350	0.8	6	10	0.6
	T15		350	350	1.0	6	10	0.6
$2\gamma=40$	T16		80	400	0.2	6	10	0.6
	T17		160	400	0.4	6	10	0.6
	T18		240	400	0.6	6	10	0.6
	T19		320	400	0.8	6	10	0.6
	T20		400	400	1.0	6	10	0.6

CHAPTER SEVEN

CONCLUSIONS AND FUTURE PLAN

7.1 INTRODUCTION

In this research project, a comprehensive experimental and numerical investigation is conducted to study the structural behaviour of S690 cold-formed circular hollow sections (CFCHS). The key findings from this research project are summarized, and recommendations on the work to be done in the future are also discussed in this chapter.

7.2 EXPERIMENTAL INVESTIGATIONS

A comprehensive experimental investigation has been carried out in this research project, including material tests, temperature measurements during welding, residual stress measurements, stocky column tests under axial compression and T-joint tests under various loading conditions. Through this experimental programme, effects of various fabrication processes onto structural behaviour of S690 CFCHS are examined in details. The key findings are summarized as follows:

- *Residual stresses in S690 CFCHS*

Surface temperature history of four S690 CFCHS were measured with thermocouples during longitudinal welding. Detail welding parameters were recorded.

Surface residual stresses in two S690 CFCHS without welding (CFCHS-NW) and two CFCHS were measured using the sectioning method to obtain the residual stresses due to transverse cold-bending and longitudinal welding. For S690 CFCHS-NW, tensile residual stresses are found on the outer surface of the CFCHS while compressive residual stresses are found on the inner surface. Bending residual stresses with an average magnitude of 0.28 f_y are measured, except that very low values are obtained from the strips on the edge.

For CFCHS, residual stresses are shown to be very high in adjacent to the weld seams, where a maximum value is obtained on the outer surface of the CHS. A magnitude of about $0.3f_y$ is measured as the maximum bending residual stress also indicates the effect of cold-forming to the CFCHS.

- *Stocky columns of S690 CFCHS under axial compression*

A total of eight stocky columns of S690 CFCHS with Class 2, 3 and 4 sections were tested under axial compression. All these stocky columns failed in local buckling and full section resistances of these S690 CFCHS have been mobilized. The measured compressive resistances of all these CFCHS are larger than the design resistances according to EN 1993-1-1 by over 5%.

- *T-joints between CFCHS under brace axial compression*

A total of six T-joints between S355 and S690 CFCHS were tested under brace axial compression. All these T-joints failed in an interaction between the local plastification of the chord and overall plastic bending of the chord, and they are found to have sufficient strength and ductility. With the same geometric dimensions, the measured resistances of S690 joints are higher than those of the S355 joints by 58% to 80%.

- *T-joints between CFCHS under brace in-plane bending*

Six tests on T-joints between CFCHS were carried out under monotonic in-plane bending in the braces. Various failure modes have been identified. Local buckling at the compression sides of the chords are found for T-joints between S355 CFCHS while fracture is found within the heat affected zone at brace ends for T-joints between S690 CFCHS. Through the application of a DIC technique, the failure mechanism of those T-joints with S690 CFCHS is identified from the surface principal strain contours. The maximum principal strains in these joints are found to be 19.2% and 33.9% just before fracture.

Four T-joints between S690 CFCHS were conducted under cyclic in-plane bending in the braces with two different loading protocols. They all failed in fracture at the heat affected zones of the braces. A reduction of less than 6% is found in the moment resistances of these T-joints under cyclic loads, when compared with those measured from monotonic tests. While a reduction of about 33% to 42% are found in the ductility of these T-joints under cyclic loads. It is considered not to be influenced by the number of load cycles. Energy dissipation characteristics of these T-joints under cyclic in-plane bending are evaluated by an energy dissipation ratio. These T-joints between S690 CFCHS are shown to have sufficient strength and ductility under both monotonic and cyclic in-plane bending moments, and they are considered to be applied for seismic resistant structures.

7.3 NUMERICAL INVESTIGATIONS

- *Residual stresses in S690 CFCHS*

2D numerical models with plane strain elements are used to simulate the transverse cold-bending of CFCHS. The residual stress distributions due to transverse cold-bending are obtained. 3D numerical models with solid elements are established to carry out sequentially coupled thermomechanical analyses. Measured surface temperature history, recorded welding parameters and measured surface residual stresses are used to calibrate these numerical models. It is shown that residual stress distributions on both the inner and the outer surfaces of S355 and S690 CFCHS are able to be predicted with the proposed numerical models. Simplified residual stress models for S690 CFCHS have been proposed.

- *Structural behaviour of stocky columns of S690 CFCHS*

3D Numerical models with solid elements are established to study the structural behaviour of stocky columns of S690 CFCHS. Residual stresses obtained from sequentially coupled thermomechanical analyses are directly incorporated in these models as initial stress states. Typical failure modes, load-deformation behaviour and compressive resistances of these sections are predicted with these models with a high accuracy. Parametric studies are conducted to study effects of yield strengths of steels, residual stresses and cross-sectional slenderness onto structural behaviour of stocky columns of S690 CFCHS. The residual stress patterns are found to have only a small effect on the section resistances of these stocky columns of S690 CFCHS, but they have some effects onto the initial extensional rigidity of these stocky columns. In general the cross-sectional slenderness has some effects on the section resistances of stocky columns of S690 CFCHS.

- *Structural behaviour of T-joints between S690 CFCHS*

Numerical analyses on T-joints between CFCHS under various loading conditions are also carried out. Test results of these T-joints have been used to calibrate the proposed 3D numerical models with solid elements.

The proposed models are shown to be effective to provide accurate predictions in terms of typical failure modes, load versus chord indentation curves and axial resistances for these T-joints under brace axial compression. For T-joints between CFCHS under brace in-plane bending moments, both the static moment versus rotation curves and the hysteretic behaviour under cyclic loadings of these T-joints are also predicted by the proposed models with a high accuracy.

Hence, these proposed models are adopted for a series of parametric studies to study various geometric parameters on the structural behaviour of T-joints between S690 CFCHS.

7.4 DESIGN RECOMMENDATIONS

- *Residual stresses in S690 CFCHS*

At present, there has been no clear reference provided for design of the residual stress distribution in the S690 CFCHS. In this research project, residual stress distributions on both the inner and the outer surfaces of these S690 CFCHS are proposed. A simplified average residual stress model is also proposed after comparison with existing residual stress models available in literature. The proposed residual stress model is readily employed for numerical investigation into structural behaviour of various structural members made of S690 CFCHS.

- *Structural behaviour of stocky columns of S690 CFCHS*

The applicability of existing section classification rules provided in EN 1993-1-1 is examined through a systematic parametric study. The current slenderness limit of 90 for Class 1 to 3 sections is confirmed to be generally applicable for S690 CFCHS with considerable conservatism. A new slenderness limit of 130 is proposed in the present study.

- *Structural behaviour of T-joints S690 CFCHS*

Current design rules provided in CIDECT Design Guide 1 and EN1993-1-8 are considered to be generally adequate for prediction of the axial resistances of these T-joints between S690 CFCHS. CIDECT Design Guide 1 is shown to provide more accurate prediction in the axial resistances and moment resistances of the T-joints than those design equations provided in EN 1993-1-8.

Current reduction factors of 0.8 in EN 1993-1-12 and 0.9 in CIDECT Design Guide 1 are considered to be too conservative for design of T-joints between S690 CFCHS under brace axial compression, and they are suggested to be removed to improve structural efficiency. However, these reduction factors are considered to be necessary for design of T-joints between S690 CFCHS under brace in-plane bending moments.

7.5 RECOMMENDATIONS FOR FUTURE WORK

The recommendations for future research work are proposed as follows.

- *Experimental investigation*

In the present study, material properties of weld metals and heat affected zone materials are not studied. Further standard coupon tests are suggested to be conducted. They are important material information which can be incorporated into various numerical models to consider the effect of welding in HAZ. Strength reduction of HAZ materials due to various heat energy input are also required to be quantified.

Surface residual stresses in CFCHS are measured with the sectioning method in the present study. Transverse residual stresses in CFCHS are recommended to be measured. Further residual stress measurements for other cross-section types, including cold-formed rectangular hollow sections (RHS) and square hollow sections (SHS) are suggested to be carried out.

Stocky columns of S690 CFCHS are tested under axial compression. More structural tests on slender columns of S690 CFCHS should be carried out to study effects of various manufacturing processes onto buckling behaviour of these columns.

Structural tests on T-joints between S690 CFCHS under brace axial compression and brace in-plane bending moment are conducted. Further experimental investigations on other types of high strength steel tubular joints, including X-joints, K-joints and Y-joints etc. are suggested to be carried out.

- *Numerical investigation*

In the present study, residual stresses in CFCHS is predicted with sequentially-coupled thermomechanical analyses. Material properties of weld metals and heat affect zones, as well as phase transformation of steels at elevated temperature is not considered in the proposed models. These parameters are suggested to be considered in further numerical investigations.

Residual stresses are found to have a minor effect on the compressive resistances of stocky columns of S690 CFCHS. Their effect on structural behaviour of slender columns, beams and other structural members are suggested to be investigated through further parametric studies.

Residual stresses induced by cold-forming and welding are not considered in the numerical investigations on T-joints between CFCHS although they have been reported to have minor influence on the structural behaviour of these T-joints in some literature. It is recommended to conduct further numerical analyses to define the residual stress patterns in these T-joints between CFCHS.

It should be noted that fracture mechanism is not considered in the proposed numerical models for T-joints between CFCHS under in-plane bending moments. Further studies are suggested to be carried out to establish numerical models which incorporate fracture mechanism in order to predict initiation of cracks and their developments.

- *Design of high strength S690 steel structural members*

In the present study, the applicability of current section classification rules for stocky columns of CFCHS under axial compression are examined. Whether these rules are applicable for slender columns, beams and other structural members are necessary to be verified through further investigations.

Current design rules for T-joints between S690 CFCHS under brace axial compression and brace in-plane bending moment are examined. The applicability of the design rules for other types of high strength tubular joints, including X-joints, K-joints and Y-joints etc. are recommended to be investigated.

REFERENCES

ABAQUS (2009). Theory Manual 2009, Providence, US: Dassault Systems Simulia Corp.

AISC. (2016). ANSI/AISC 341-16, Seismic Provisions for Structural Steel Buildings. Chicago, IL: American Institute of Steel Construction.

API. (2002). American Petroleum Institute, Recommended practice for planning, designing, and constructing fixed offshore platforms. RP2a. Washington (DC).

ASTM. E837-01 (2001). Standard method for determining residual stresses by the hole-drilling strain-gage method.

AWS (1995) Specification for Carbon Steel Electrodes for Flux Cored Arc Welding. Structural Welding Code – Steel. Miami, United States: American Welding Society

AWS (2005) Specification for Low-Alloy Steel Electrodes and Rods for Gas Shielded Arc Welding. Structural Welding Code – Steel. Miami, United States: American Welding Society.

Anderson, L.F. (2000). Residual stress and deformations in steel structures. Department of Navel Architecture and Offshore Engineering, Technical University of Denmark.

Ban, H., Shi, G., Shi, Y., & Wang, Y. (2013). Residual stress of 460 MPa high strength steel welded box section: Experimental investigation and modeling. Thin-Walled Structures, 64, 73-82.

Becque, J., & Wilkinson, T. (2017). The capacity of grade C450 cold-formed rectangular hollow section T and X connections: An experimental investigation. Journal of Constructional Steel Research, 133, 345-359.

Brensing, K., & Großrohre, S. (2004). Steel Tube and Pipe Manufacturing Processes.

CEN. (2005). BS EN 1993-1-8, Eurocode 3: Design of steel structures Part 1-8: Design of joints. European Committee for Standardization.

CEN. (2007). BS EN 1993-1-12, Eurocode 3: Design of steel structures Part 1-12: Additional rules for the extension of EN 1993 up to steel grades S700. European Committee for Standardization.

Chen, W. F., & Ross, D. A. (1977). Test of fabricated tubular columns. Journal of the Structural Division, 103(ASCE 12809).

Chukkan, J. R., Vasudevan, M., Muthukumaran, S., Kumar, R. R., & Chandrasekhar, N. (2015). Simulation of laser butt welding of AISI 316L stainless steel sheet using various heat sources and experimental validation. Journal of Materials Processing Technology, 219, 48-59.

Clark, P., Frank, K., Krawinkler, H., & Shaw, R., (1997). Protocol for Fabrication, Inspection, Testing, and Documentation of Beam-Column Connection Tests and Other Experimental Specimens, SAC Steel Project Background Document. October, Report No. SAC/BD-97/02.

Cruise, R. B., & Gardner, L. (2008). Residual stress analysis of structural stainless steel sections. Journal of Constructional Steel Research, 64(3), 352-366.

De, A., Walsh, C. A., Maiti, S. K., & Bhadeshia, H. K. D. H. (2003). Prediction of cooling rate and microstructure in laser spot welds. Science and technology of welding and joining, 8(6), 391-399.

ECCS. (1986). Recommended testing procedure for assessing the behaviour of structural steel elements under cyclic loads. Brussels, Belgium: European Convention for Constructional Steelwork.

Ellobody, E. (2014). Finite element analysis and design of steel and steel–concrete composite bridges. Butterworth-Heinemann.

Gery, D., Long, H., & Maropoulos, P. (2005). Effects of welding speed, energy input and heat source distribution on temperature variations in butt joint welding. Journal of materials processing technology, 167(2-3), 393-401.

Goldak, J., Chakravarti, A., & Bibby, M. (1984). A new finite element model for welding heat sources. Metallurgical transactions B, 15(2), 299-305.

Havula, J., Garifullin, M., Heinisuo, M., Mela, K., & Pajunen, S. (2018). Moment-rotation behavior of welded tubular high strength steel T joint. Engineering Structures, 172, 523-537.

International Institute of Welding (IIW). (1981). Design recommendations for hollow section joints—predominantly statically loaded. IIW Doc. XV-701-89.1st edition.

International Institute of Welding (IIW). (1989). Design recommendations for hollow section joints—predominantly statically loaded. IIW Doc. XV-701-89. 2nd edition.

International Institute of Welding (IIW). (2009). Design recommendations for hollow section joints—predominantly statically loaded. IIW Doc. XV-701-89. 3rd edition.

Jandera, M., Gardner, L., & Machacek, J. (2008). Residual stresses in cold-rolled stainless steel hollow sections. Journal of Constructional Steel Research, 64(11), 1255-1263.

Jiang, W., Yahiaoui, K., Hall, F. R., & Laoui, T. (2005). Finite element simulation of multipass welding: Full three-dimensional versus generalized plane strain or axisymmetric models. The Journal of Strain Analysis for Engineering Design, 40(6), 587-597.

Kim J. H. (2018). Experimental and Analytical Study of RHS X-Joints under Axial Compression (Master dissertation). Seoul National University.

Kim, S. H., Kim, J. B., & Lee, W. J. (2009). Numerical prediction and neutron diffraction measurement of the residual stresses for a modified 9Cr–1Mo steel weld. Journal of Materials Processing Technology, 209(8), 3905-3913.

Lan, X. Y., & Chan, T. M. (2018). Recent research advances of high strength steel welded hollow section joints. Structures. Elsevier.

Lee, C. H., Kim, S. H., Chung, D. H., Kim, D. K., & Kim, J. W. (2017). Experimental and numerical study of cold-formed high-strength steel CHS X-joints. Journal of Structural Engineering, 143(8), 04017077.

Lee, C. K., Chiew, S. P., & Jiang, J. (2012). Residual stress study of welded high strength steel thin-walled plate-to-plate joints, Part 1: Experimental study. Thin-Walled Structures, 56, 103-112.

Lindgren, L. E. (2001). Finite element modeling and simulation of welding. Part 3: Efficiency and integration. Journal of thermal stresses, 24(4), 305-334.

Liu, C., Zhang, J. X., & Xue, C. B. (2011). Numerical investigation on residual stress distribution and evolution during multipass narrow gap welding of thick-walled stainless steel pipes. Fusion engineering and design, 86(4-5), 288-295.

Liu, X., & Chung, K. F. (2018). Experimental and numerical investigation into temperature histories and residual stress distributions of high strength steel S690 welded H-sections. Engineering Structures, 165, 396-411.

Lu, L. H., De Winkel, G. D., Yu, Y., & Wardenier, J. (1994). Deformation limit for the ultimate strength of hollow section joints. 6th International Symposium on Tubular Structures, 341-347.

Ma, J. L., Chan, T. M., & Young, B. (2015). Material properties and residual stresses of cold-formed high strength steel hollow sections. Journal of Constructional Steel Research, 109, 152-165.

Masubuchi, K. (2001). Residual stresses and distortion in welds. Encyclopedia of Materials: Science & Technology. Oxford: Elsevier.

Moen, C. D., Igusa, T., & Schafer, B. W. (2008). Prediction of residual stresses and strains in cold-formed steel members. Thin-walled structures, 46(11), 1274-1289.

Qian, X. D., Choo, Y. S., Van Der Vegte, G. J., & Wardenier, J. (2008). Evaluation of the new IIW CHS strength formulae for thick-walled joints. In Proceedings of the 12th International Symposium on Tubular Structures, Shanghai. Taylor & Francis, London (pp. 271-280).

Quach, W. M., Teng, J. G., & Chung, K. F. (2004). Residual stresses in steel sheets due to coiling and uncoiling: a closed-form analytical solution. Engineering structures, 26(9), 1249-1259.

Rossini, N. S., Dassisti, M., Benyounis, K. Y. & Olabi, A. G. (2012). Methods of measuring residual stresses in components. Materials & Design, 35, 572-588.

Shim, Y., Feng, Z., Lee, S., Kim, D., Jaeger, J., Papritan, J. C., & Tsai, C. L. (1992). Determination of residual stresses in thick-section weldments. Welding Journal, 71(9), 305-312.

Somodi, B., & Kövesdi, B. (2017). Residual stress measurements on cold-formed HSS hollow section columns. Journal of Constructional Steel Research, 128, 706-720.

Sonti, N., & Amateau, M. F. (1989). Finite-element modeling of heat flow in deep-penetration laser welds in aluminum alloys. Numerical heat transfer, 16(3), 351-370.

Tebedge, N., Alpsten, G. & Tall, L. (1973). Residual stress measurement by the sectioning method. Experimental Mechanics, 13(2), 88-96.

Tong, L., Hou, G., Chen, Y., Zhou, F., Shen, K., & Yang, A. (2012). Experimental investigation on longitudinal residual stresses for cold-formed thick-walled square hollow sections. Journal of Constructional Steel Research, 73, 105-116.

Wahab, M. A., Painter, M. J., & Davies, M. H. (1998). The prediction of the temperature distribution and weld pool geometry in the gas metal arc welding process. Journal of Materials Processing Technology, 77(1-3), 233-239.3

Pilipenko, A. (2001). Computer simulation of residual stress and distortion of thick plates in multielectrode submerged arc welding: Their mitigation techniques. (Doctoral dissertation, Norwegian University of Science and Technology).

Van der Vegte, G. J., & Makino, Y. (2005). Ultimate strength formulation for axially loaded CHS uniplanar T-joints. In The Fifteenth International Offshore and Polar Engineering Conference. International Society of Offshore and Polar Engineers.

Van der Vegte, G. J., & Makino, Y. (2010). Further research on chord length and boundary conditions of CHS T-and X-joints. Advanced Steel Construction, 6(2), 879-890.

Vegte, G. V. D., Wardenier, J., Zhao, X. L., & Packer, J. A.(2008) Evaluation of new CHS strength formulae to design strengths. Proceedings of 12th International Symposium on Tubular Structures, Shanghai, China, pp. 313–322.

Wardenier, J., Kurobane, Y., Packer, J. A., Van der Vegte, G. J., & Zhao X. L. (2008). Design guide for circular hollow section (CHS) joints under predominantly static loading. CIDECT.

Wardenier, J., Packer, J. A., Zhao, X. L., & Van der Vegte, G. J. (2002). Hollow sections in structural applications. Rotterdam,, The Netherlands: Bouwen met staal.

Withers, P. J. & Bhadeshia, H. K. D. H. (2001). Residual stress. Part 1– measurement techniques. Materials science and Technology, 17(4), 355-365.

Yang, C., Yang, J., Su, M., & Li, Y. (2016). Residual stress in high-strength-steel welded circular tube. Proceedings of the Institution of Civil Engineers-Structures and Buildings, 170(9), 631-640.

Yura, J. A., Edwards, I. F., & Zettlemoyer, N. (1981). Ultimate capacity of circular tubular joints. Journal of Structural Engineering, 107(10), 1965-1984.

Zheng, B., Shu, G., & Jiang, Q. (2019). Experimental study on residual stresses in cold rolled austenitic stainless steel hollow sections. Journal of Constructional Steel Research, 152, 94-104.